University of Liverpool

Department of Chemistry

UNIVERSITY OF LIVERPOOL

Synthesis and Characterisation of HPLC Stationary Phases on a Molecular Level

Thesis submitted in accordance with the requirements of the University of Liverpool for the degree of Doctor of Philosophy

By

Laura Katherine Clews

2011

Dedication

Dedicated to my mother and father,

Without whom I never would have made it this far.

Acknowledgements

There have been many people throughout my PhD who have supported me both academically and emotionally, though there are a few people who deserve special recognition.

I would like to extend my upmost thanks to Thermo for funding my research, especially Harry Ritchie for all the help and support throughout my PhD.

To Dr. Yaroslav Khimyak, thank-you for giving me opportunity to undertake my PhD studies under your guidance. For all the support and advice over the years in both my research and personal life. We may not have always seen eye to eye, but I imagine this to be difficult when I'm over a foot shorter. Most of all thank-you for making me a YP.

To Prof. Myers, thank-you for taking me into your research group, for all the help and support and most of all for all the times you made me laugh when I was at my lowest. You have been like a second father to me over the years, though I am amazed I'm not two stone heavier after all those jam doughnuts.

I would also like to thank Rob Clowes for all his help with BET, Neil Grant for my SEM images and Charlotte Blythe, Kevin Skinley and Thomas Wray for all their help with HPLC.

To Paul, thank-you does not seem like a big enough word for all the things you have done for me over the years. You have been the person who has picked me up when I was down, celebrated in all my successes and supported me unconditionally throughout the years. Thank you for never complaining about every weekend I worked, every time I turned up late with no make-up on and for every time I fell asleep on the couch. I love you more than anything else in the whole wide world, without you there would be no point.

To my parents, you are both wonderful parents, I can honestly say I would never have made it without your care and support. It is not enough to thank-you for the last three years, I'd like to thank-you both for the last twenty-four. You have always been there

for me, encouraging me to better myself when I needed to work and distracting me when I needed to stop. Most of all I'd like to thank you for letting me live rent free for the last few months (and let's face it even when I did pay rent it was a steal!).

To my sisters, cheese and three bean, I am very lucky to have two sisters with whom I am so close, who have done everything they could to help and support me, who kick me in their sleep and make me laugh, always. An extra special thank-you to Helen for rescuing my thesis when my laptop crashed. I just hope one day you are as proud of me as I am of the both of you.

To my friends and colleagues at the University of Liverpool, a big thank-you to James, Cate, Paul, Andrea and Lucy. I think we all know we have kept each other going, thank-you for all the help and discussions over the years. Most of all thank-you for eating your breakfast in my office every day, for all the girly gossip and stories, for the rubbish music you played and for the secret slow dances in our office (no one will ever know!). To Carly, for all the nights we stayed up until 2 am gossiping. Alex, with whom I have been through every stage at university, thank-you for all the support over the years.

To my friends, most notably the amigos, thank-you for supporting me throughout my PhD. For the endless chats, cups of tea and dinners. Thank-you for never complaining when I was late, when I forgot to call and never pointing out on nights out that my make-up was clearly done in the back of the taxi on the way there. I could never express just how much it has meant to me over the years.

Synthesis and Characterisation of HPLC Stationary Phases

High Pressure Liquid Chromatography (HPLC) is the process of separating multiple analytes by differing affinities toward the stationary phase. The selectivity of a stationary phase is dependent on the surface functional groups, though the majority of research only characterises new phases on a mesoscopic level. Solid-state NMR is a non-invasive technique which can provide detailed analysis on these materials on a molecular level. The technique can be used to determine not only whether a functional group has been successfully incorporated but can analyse whether this group is on the pore surface, able to interact with analytes, or trapped within the pore wall. Furthermore, we can assess whether the organic moiety is homogeneously distributed throughout the stationary phase and the interconnectivity of the silica framework. Analysing new stationary phases on a molecular level is essential to determining their chromatographic applications.

The synthesis of three bi-functionalised PMOs under acidic conditions using combinations of bridging ($-CH_2CH_2-$, -CH=CH-) and tether ($-CH_2C_6H_5$, $-C_6H_5$) functionalities is presented. By incorporating the organic groups into the silica framework we have produced new reversed phase columns containing a high carbon content. The synthesis of each periodic mesoporous organosilica (PMO) was optimised by varying the acid content and analysing the effect on a mesoscopic scale. The bi-functionalised silicas were then assessed on a molecular level to determine the mobility and the homogeneity of the functionalities using 2-D experiments such as ^{1}H-^{13}C Wideline (WISE) NMR and ^{1}H-^{29}Si Heteronuclear correlation (HETCOR) spectroscopy. The most viable stationary phases were analysed chromatographically using PAH and Tanaka tests and the results were compared to commercially available columns.

There are many columns available, though even those containing the same functionality can produce very different separations due to the different synthetic procedures. We have compared two commercially available silicas, 1.7 μm Syncronis (containing monomeric $-C_{18}$) and Spherisorb ODS2 (containing polymeric $-C_{18}$).

Although both stationary phases contain the same functionality we have shown that on a molecular level they are very different. We have tried to relate these differences to the selectivity of the two phases. Using techniques such as ^{1}H Nuclear Overhauser Effect Spectroscopy (NOESY) we have been able to compare how a toluene analyte interacts with two $-C_{18}$ functionalised stationary phases. By also analysing the interactions between a $-CH_2CH_2-$/ $-CH_2C_6H_5$ functionalised PMO and toluene we have shown the way in which the analyte interacts with the stationary phase is dependent on the functionality incorporated.

The synthesis of a new sphere-in-sphere stationary phase to improve the selectivity of larger biomolecules is presented. By sintering silica nanoparticles to the surface of large pore silica the mechanical strength and surface area of the material is improved though the large pores remaining can still facilitate the mass transfer of high molecular weight compounds. We have shown that by grafting $-C_{12}$ moieties onto the surface of the silica the shorter elution time of smaller molecules compared to larger compounds is observed, whereas classical size exclusion chromatography (SEC) elutes larger analytes first. This suggests that the separation may be effected by some reversed-phase characteristics.

Contents

Chapter 1: Introduction

1. Introduction

1.1 Theory of Chromatography

High Pressure Liquid Chromatography (HPLC) is the process of separating multiple analytes contained in a solution. This process is both quantitative and qualitative as the elution time (the point at which the individual compound is detected) is unique for each analyte within an individual set of conditions. The peak height and area are determined by the amount of analyte present.

The separation occurs as the sample mixture is distributed between two phases; a mobile phase and a stationary phase. The stationary phase is usually a porous, surface active material in particle form. For liquid chromatography the mobile phase is a solvent mixture (non-polar solvents are used for normal HPLC and polar solvents are used for reversed-phase HPLC). The retention factor (k') of an analyte or, as it is more commonly called, the capacity factor is a measure of how much time a compound spends in the mobile phase compared to the stationary phase. The equilibrium between the two phases will differ for different analytes. This parameter should be independent of the equipment used being a function of the column and mobile phase.

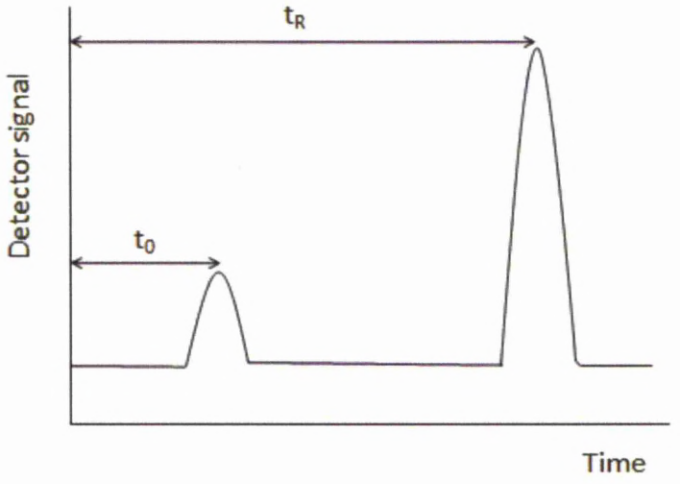

Figure 1.1 Chromatogram illustrating the retention of a compound

The retention time (k') of each compound can be directly measured from the chromatogram assuming a constant flow rate using the equation below.

$$k' = \frac{t_R - t_0}{t_0} \qquad (1.1)^1$$

Wherein t_R is the retention time of the compound and t_0 is the retention time of a compound completely unretained by the column.

As HPLC is used to separate solutes containing multiple compounds the resolution of the peaks becomes an important factor. Two peaks can only be separated if they have different k' values. The degree of separation (known as the separation factor, α) can be calculated using equation 1.2.

$$\alpha = \frac{k_2}{k_1} = \frac{t_{R2} - t_0}{t_{R1} - t_0} \qquad (1.2)^1$$

If α = 1 the retention times of the two compounds are the same and no separation has occurred; there must be a difference in the equilibrium distribution of the two compounds for a separation to occur. There are two ways to increase the separation of analytes; the first is by increasing the efficiency of the column creating a reduction in the band widths of the peaks (reducing band broadening), the second is to increase the retention factor of the analytes.

The efficiency of the column is measured using theoretical plates (N) or Height Equivalent to a Theoretical Plate (HETP), a higher number of plates or a smaller HEPT indicates a more efficient column. For a separation to occur equilibrium of the solute between the two phases has to first be achieved. During the separation the molecules are transferred from the mobile phase to the stationary phase and back to the mobile phase again. The distance taken for this transfer to occur is called a theoretical plate.

The more times the transfer occurs the more efficient the column is; therefore the efficiency of a column can be measured by theoretical plates (Equation 1.3).

$$N = \frac{5.55\, t_R^2}{W_{1/2}^2} \qquad (1.3)$$

$W_{1/2}$ is the peak width at half height.

1.2 Causes of band broadening

As the analyte migrates through the column mass transfer effects cause the target analyte to disperse. The result being the analyte elutes over a longer period of time. This phenomenon is referred to as band broadening. The three mass transfer effects are eddy diffusion (A-term), longitudinal diffusion (B-term) and mass transfer (C-term). By studying the causes of band broadening we can minimise the effects on the separation and increase the number of theoretical plates for the column.

1.2.1 Eddy Diffusion

As the mobile phase moves through the column the solute takes random paths through the column packing which can cause band broadening. The variance in path length, and therefore level of band broadening, is dependent on the geometry of the column packing, the particle size and the irregularity of the particle shapes.

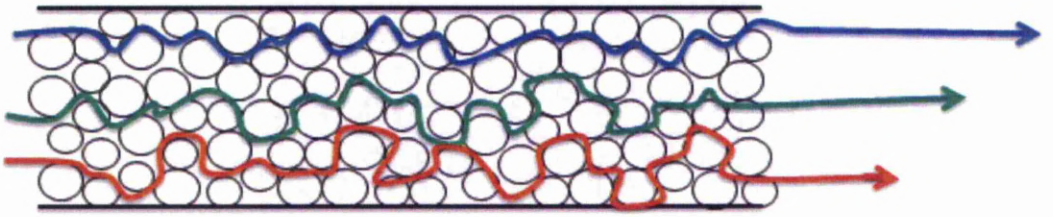

Figure 1.2 The path of the mobile phase through the column effects the time taken for the solute to elute

The column packing has a large influence on the level of eddy diffusion, mainly due to the particle size, regularity of shape and porosity of the beads. The effect of the stationary phase on eddy diffusion (H_F) is shown by equation 1.4.

$$H_F = 2\lambda d_p \qquad (1.4)^2$$

The equation shows that eddy diffusion decreases as the particle size (d_p) of the column packing decrease, which has lead to copious research in the reduction of particle diameters below 5 μm.[3] λ is dependent on the irregularity of the particles (λ is equal to 1 for spherical particles) and the material of the column (*i.e.* glass or steel). The effect of eddy diffusion can be minimised by using a steel column, packed with a small and uniformly spherical packing material, leading to an increase in the number of theoretical plates.

1.2.2 Longitudinal Diffusion

A solute contained in a liquid will naturally diffuse down the concentration gradient along the column. As diffusion occurs randomly this will produce a Gaussian type distribution; the distribution of the solute will increase with increasing time within the column.

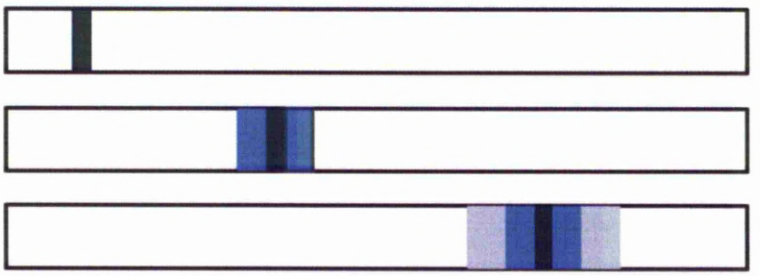

Figure 1.3 Longitudinal diffusion of a solute in a column

Van Deemter *et al.* derived the an equation relating the effects of longitudinal diffusion per column unit length (Equation 1.5).[4] The equation includes the level of diffusion of the solute in the mobile phase (D_m), the linear velocity of the mobile phase (u) and a constant dependent of the quality of the packing (γ).

$$H_L = \frac{2\gamma D_m}{u} \qquad (1.5)^2$$

The equation shows that longitudinal diffusion can be reduced by increasing the linear velocity of the mobile phase. The equation also shows that the quality of column packing, and therefore the shape and uniformity of the stationary phase, also affects the level of longitudinal diffusion.

1.2.3 Mass transfer

The solute within the column is constantly transferred between the mobile and stationary phases. Transfer through diffusion is relatively slow and depending on the velocity of the mobile phase, can cause significant dispersion of the solute band. The band broadening is also dependent on the diffusivity of the solute into the stationary phase. Molecules that remain at the interface between the mobile and stationary phases can transfer quickly between each phase. Whereas molecules which diffuse further into the stationary phase (e.g. into the porous network) have a longer diffusion path compared to molecules at the interface. For a specific analyte the molecules at the interface will move along the column faster eluting before the molecules which diffuse further into the stationary phase, causing band broadening.

$$H_m = \omega \frac{d_p^2}{D_m} u \qquad (1.6)^2$$

Equation 1.6 shows the Van Deemter parameter for mass transfer; which is dependent on the particle diameter (d_p), the coefficient determined by the pore size distribution, pore shape and particle shape of the stationary phase (ω), the diffusion coefficient of the solute in the mobile phase (D_m) and the velocity of the mobile phase (u). The equation shows that the band broadening of the solute for mass transfer can be minimised by reducing the velocity of the mobile phase.

1.3 Van Deemter Curves

As described there are three main causes of band broadening in chromatography, eddy diffusion, longitudinal diffusion and mass transfer. As shown above the factors for minimising the causes can contradict each other. Each individual component will effect the HEPT associated with the column. In order to find the optimum conditions to separate the solute a Van Deemter curve is used.

The overall affect of band broadening is shown by equation 1.7.

$$H = H_F + H_L + H_m \tag{1.7}$$

This equation can be expanded to give the Van Deemter equation, shown below:

$$H = 2\lambda d_p + \frac{2\gamma D_m}{u} + \omega \frac{d_p^2}{D_m} u \tag{1.8}$$

This is commonly simplified to give:

$$H = A + \frac{B}{u} + Cu \tag{1.9}$$

The equation shows that varying the flow rate has differing effects on each term and therefore changes the HETP, though each term follows a general trend. Eddy diffusion (A-term) is unaffected by the flow rate, longitudinal diffusion (B-term) decreases with increasing flow rate and mass transfer (C-term) increases with increasing flow rate. A Van Deemter curve measures how the HETP varies with flow rate to find the optimum conditions for the column.

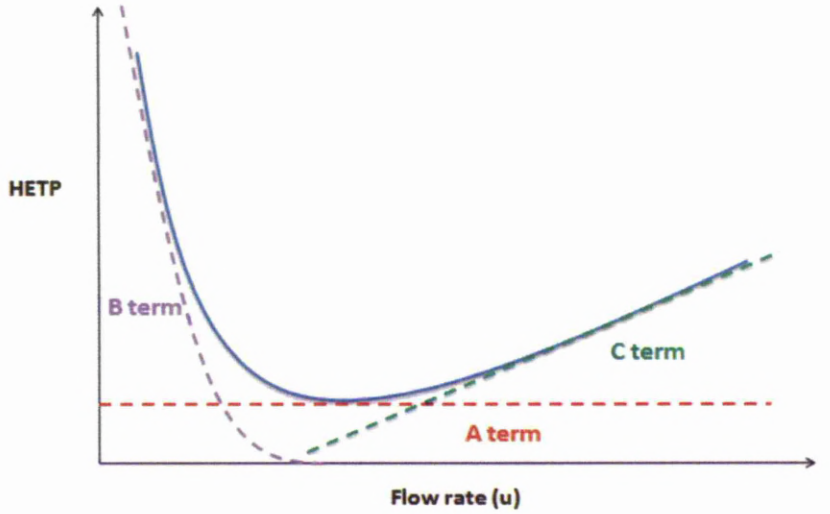

Figure 1.4 Van Deemter Curve

1.4 The Knox Equation

The Knox equation uses dimensionless values to enable the comparison of the efficiency of columns with similar particle sizes. The idea was first proposed by Giddings[5] though Knox and co-workers produced extensive research on the subject [6-9] showing that the A-term is directly affected by the linear velocity. Column efficiency was traditionally measured using the plate height (H):

$$H = L\tau^2/t^2 \tag{1.10}$$

Wherein the plate height is calculated from the column length (L), the standard deviation of the Gaussian (τ) and the retention time of the solute (t). The reduced plate height (h), used in the Knox equation, incorporates the average particle size within the column. The column efficiency now equates to the number of particles corresponding to a single plate and is a dimensionless parameter.

$$h = \frac{H}{d_p} \tag{1.11}$$

The reduced flow velocity:

$$\nu = d_p v/D_m \tag{1.12}$$

Wherein the reduced flow velocity is dependent on the mean cross sectional flow velocity (v) and the diffusion co-efficient of the analyte in the mobile phase. When the Van Deemter equation is modified with these dimensionless values it is called the Knox equation (Equation 1.13).

$$h = Av^{0.33} + \frac{B}{v} + Cv \qquad (1.13)$$

Where A is the eddy diffusion and flow distribution component, B is the longitudinal diffusion component and C is the mass transfer component. By using the Knox equation all geometrically similar columns should produce identical curves of h versus v regardless of the particle size or the mobile phase used.

1.5 Kinetic Plots

Traditionally the efficiency of liquid chromatography columns are measured using the plate height (H) versus the linear velocity of the mobile phase (u) or the reduced values of these parameters. Desmet and co-workers [10-12] produced the kinetic plot method (KPM) which uses experimentally obtained conditions obtained on the efficiency (u_0, H) and the pressure drop of the column (ΔP) allowing the comparison of columns with different particle sizes and shapes (including monoliths). By combining the pressure drop equation (Figure 1.14):

$$U_0 = \frac{\Delta P}{\eta}\frac{K_{v0}}{L} \qquad (1.14)$$

Where η is the viscosity of the mobile phase, K_v is the column permeability and L corresponds to the length of the column, and the equation relating plate number (N), plate height and column length

$$L = NH \qquad (1.15)$$

The two equations can be combined to give an equation for the efficiency of the column regardless of its length and particle size (Equation 1.16).

$$N = \frac{\Delta P}{\eta}\frac{K_{v0}}{u_0 H} \qquad (1.16)$$

1.6 The Nature of Silica

Silica is the most widely used stationary phase in chromatography due to the materials high mechanical strength, control of particle size and pore size and the large surface areas which can be easily modified. Despite these qualities there are still many problems concerning silica based stationary phases. Some problems include peak tailing in the separation of basic compounds, pH instability and irreproducible columns.[13] Many of the columns properties are determined by the materials surface silanol groups. As silica used in chromatography is amorphous it can be difficult to produce well-defined silica. A silicon stationary phase can be synthesised in many ways:

- Hydrolysis of inorganic silicates (though this method produces irregular silica particles containing trace metals such as iron and aluminium).
- Hydrolysis of alkoxysilanes (this method can produces both irregular and spherical silica particles).
- An oil emulsion method (using a silica colloid in a water immiscible solution where upon the size of the silica beads are controlled by stirring velocity).
- Pyrogenic silica (synthesised via high temperature hydrolysis of silicon tetrachloride).

The surface of the silicon stationary phase contains single, geminal or vicinal silanol groups. It is the interaction between these groups and the analytes which creates the chromatographic separation. Free silanols are slightly acid, therefore the adsorption of basic compounds will occur here, often leading to peak tailing. Geminal silanol groups are not acidic. Vicinal (associated) silanols are also non-acidic though they interact strongly with compounds containing OH functional groups [1]. Mass and Englehart showed that the retention capacity of the stationary phase is dependent on the quality of the hydroxyl containing groups on the surface of the silica and free silanol groups are considered the most reactive.

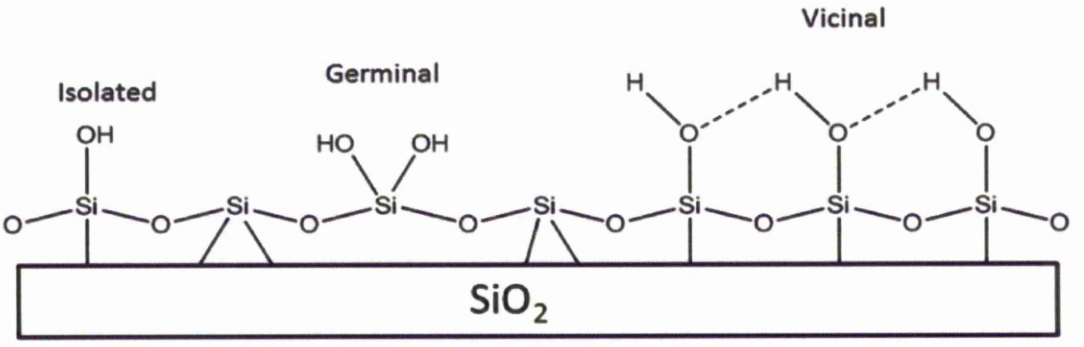

Figure 1.5 Surface of silicon stationary phase [13]

1.7 Synthesis of porous silica beads

1.7.1 Micelle formation

The formation of mesoporous spherical beads has many variables to consider though these can be placed in three main categories. The formation of rod shaped micelles, the hydrolysis of the organosilane precursors and the overall system as we also need to consider the interaction between the secondary building units (SBUs) with the surfactant and the formation of spherical beads containing rod-shaped micelles [14-16].

Surfactants are compounds which contain hydrophobic alkyl chains and hydrophilic polar head groups (Figure 1.6). When dissolved in a polar solution the surfactant monomers are arranged with the non-polar tails at the water surface and the polar head groups submerged in the water. At the critical micelle concentration (CMC) the surfactant unimers become micelles, whereby the hydrophobic tails of the unimers aggregate to expel water.

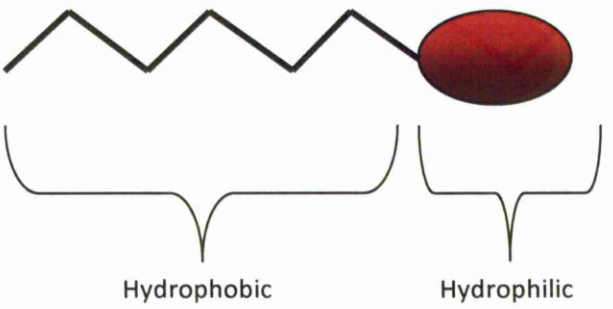

Figure 1.6 Structure of surfactant molecule

Copolymers such as poly(ethylene oxide)-*block* poly (propylene oxide)-*block* poly(ethylene oxide) copolymers (PEO-PPO-PEO) are often used in the synthesis of mesoporous silicas. The formation and structure of the micelles formed is dependent on the packing geometry of the surfactant and the concentration, pH, temperature and addition of salts added to the system. At low temperatures and/or concentration these surfactants remain as unimers. The formation of the thermodynamically stable micelles occurs only with increasing amounts of copolymer and/or temperature. The critical micelle concentration (CMC) and temperature (CMT) are dependent on the surfactant, the temperature /concentration at which micellisation occurs. CMC and CMT decreases as the molecular weight of the hydrophobic PPO block increases. A similar trend is observed for the PEO block, a slight increase is observed for the CMC and CMT with increasing molecular weight of the PEO block though this effect is on a much smaller scale compared to the PPO block indicating the hydrophobic PPO block is a primary factor in the micellisation process.[17]

The process of micellization is entropy driven. The presence of these polymers in water significantly reduces the entropy of the water molecules. When these polymers form micelles the hydrogen bonding between the water molecules is restored increasing the entropy of the system once again. It has been discovered that the hydrophobic PPO block causes the micelle process to occur due to the weaker hydrogen bonding between the surfactant and water at higher temperatures. The point at which the surfactant phase separates from water is referred to as the cloud point.[18,19,17]

1.7.2 The Geometry of Micelles formed

As discussed above it has been shown that the formation of micelles form the subsequent unimers is dependent on the CMC and CMT [15,20,21]. Research by Wanka [22] and Mortensen *et al.*[23-25] has shown that the surfactant concentration and temperature of the system can also effect the geometry of the micelle formed.

At low temperature and concentrations the monomers are fully dissolved in the solution. Around ambient temperatures the hydrophobic nature of the PPO block causes the micelles to aggregate forming spherical micelles with dense PPO cores. As temperature is further increased the interaction between the hydrophobic PPO block and the water molecules are weakened and the PPO chain extends. The radius of the micelle core increases until it is equivalent to a fully stretched PPO chain. At this point the morphology

of the micelles changes from spherical to rod-shaped. Increasing the temperature of the system at lower concentration levels initially creates hard spheres where increasing amounts of monomers are incorporated into the micelle. Further increasing the temperature (60 - 70°C) causes the morphology of the hard spheres to prolate to form an ellipsoid, leading to a decrease in intermicellular interactions. At high concentration and high temperature the large aggregates are ordered in a lamellar (layered) structure. By altering the morphology of the micelles the pore structure of the silica beads synthesised can be tailored.[26-28] Figure 1.7 shows the effect of temperature and concentration on the morphology of the micelle formed.

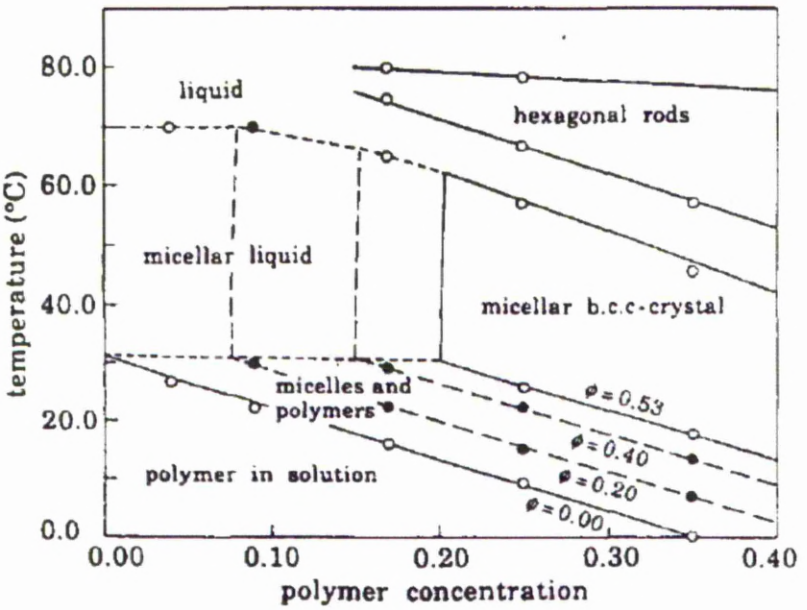

Figure 1.7 Phase diagram of Pluronic 85 (a copolymer type surfactant)[19]

1.7.3 The Addition of Salts

The addition of salts to PEO-PPO-PEO block copolymers has shown to have a direct effect on the cloud point. Depending on the type of salt added the temperature at which the phase separation occurs can be either increased or decreased. As temperature can be used to alter the morphology of the micelles the presence of a salt can help to tune the synthesis. Salts which reduce the temperature of the cloud point cause the micelles to

aggregate together. The extent to which the aggregation occurs is depended on the salt used $F^- > Cl^- > Br^-$ [29] as shown in Figure 1.8.

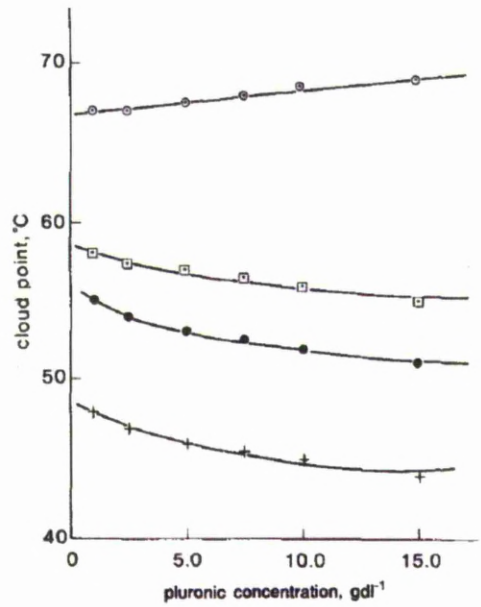

Fig. 2. Cloud point (CP) of pluronic L-64 in 0.5 M aqueous salt solutions as function of polymer concentration. ⊙ KCNS, □ KBr, ● KCl, + KF.

Figure 1.8 The effect of the addition of salts on the temperature and concentration at which cloud point occurs [29]

Prior to the addition of the salt the hydrophilic PEO groups will be surrounded by water molecules. The addition of ions effects the structure of water which will alter the strength of the interaction between the water molecules and surfactant. If the interaction is weakened the primary interaction becomes the van der waals forces between the surfactant molecules, creating phase separation. The extent to which the cloud point is effected and whether it is increased or reduced is dependent on the type of salt present.[30-32]

1.7.4 Hydrolysis and Condensation of the silica precursor

Diffusion is a natural occurrence, for example, particles of a gaseous substance will diffuse down a concentration gradient until equilibrium is established. In a sol-gel reaction a silicon source, such as TEOS (tetraethyl orthosilicate), hydrolyses and

condenses to form silica particles. If the rate of hydrolysis at the surface of the particle is uniform a spherical morphology is achieved. By controlling the rate of hydrolysis of the silica precursor we can control the particle size, particle size distribution and the morphology of the beads produced.[33,34]

As the silica precursor reacts with the surface of the silicon beads it is removed from the solution, this produces a deficit of silicon precursor in the solution surrounding the bead creating a diffusion gradient, as shown in Figure 1.9. The unreacted silica precursor remaining in the solution will move towards the bead down the diffusion gradient continuing the cycle.

If the reaction has a slow hydrolysis rate the silica precursor has time to move down the gradient and react with the surface of the silica beads. This creates larger more uniform silica beads. At higher hydrolysis rates the reaction proceeds faster than the rate of diffusion. This leads to more nucleation points creating a higher number of smaller beads.

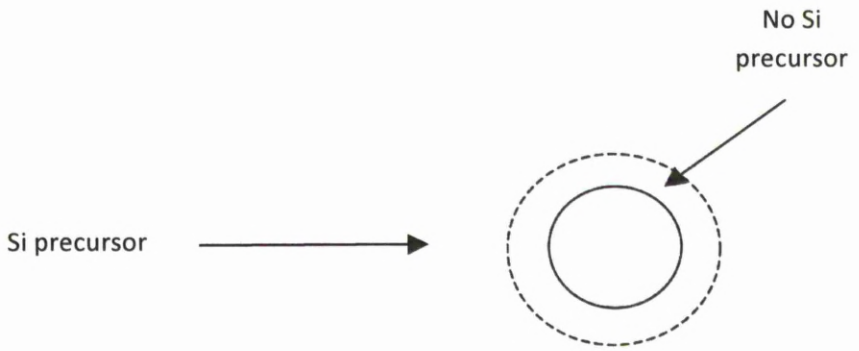

Figure 1.9 Schematic representation of silica precursor concentration gradient

To create porous silica beads, micelles can be incorporated into the sol-gel synthesis. At high concentrations of surfactant the spherical micelles will form rods to conserve space. The secondary building units (SBU) of silica are then attracted to the polar head groups of the surfactant and react with its surface. This causes the polar head group to be neutralised. This neutralisation means the repulsion between the head groups is reduced and can become more compact, causing the shape of the micelle to change.

As the silica condenses around the surfactant its rigid structure traps the micelle, stopping any further changes in morphology. The formation of a porous silica containing an ordered hexagonal array of pores is demonstrated below (Figure 1.10), with the formation of MCM-41 (ordered porous silica). It remains a challenging experiment to trap rod shaped micelles inside a spherical silica bead.[35]

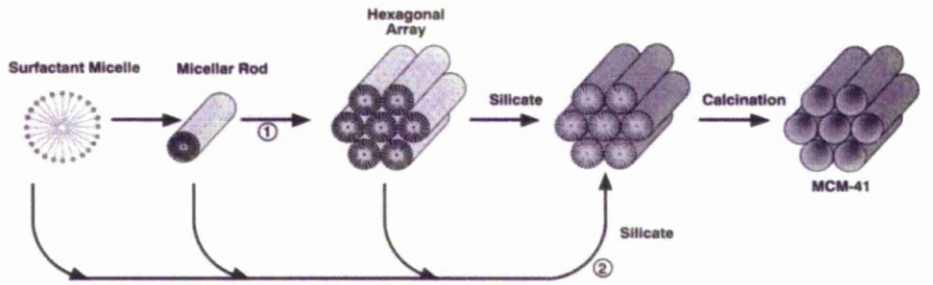

Figure 1.10 Schematic representation of the formation of porous silica [37]

For my synthesis I must also to take into account the addition of the functional groups and their effect on the hydrolysis rate of the silica precursors. Each synthesis contains two different organic moieties. Varying the acid catalyst concentration can be used to optimise the rate of hydrolysis of the organosilane precursors to create spherical morphology and optimise the porous framework.[36] Furthermore, the interaction between the organic groups and the surfactant must be taken into consideration. For HPLC separations the moieties incorporated must be at the pore surface. As the porosity is produced through the removal of the surfactant the organic groups and surfactant must have a favourable interaction.

1.8 Classical Liquid Chromatography

Traditionally, liquid chromatography used irregular shaped silica particles with a diameter between 30-60 μm.[38] As the theory behind chromatography shows, the efficiency of the column is affected by the particle size and the packing of the stationary phase. Approximately 30 years ago the synthesis of smaller (5 – 10 μm) [39,40,3]

and spherical silica beads led to improved column packing and more efficient columns, producing High-performance liquid chromatography (HPLC).

The synthesis of monodisperse silica beads through the hydrolysis and condensation of silicon alkoxides was first reported by Kolbe *et al.* In 1956[41]. Stöber *et al.* systematically examined the synthetic conditions using tetraethyl orthosilicate (TEOS), a low molecular weight alcohol and ammonia as a catalyst and was able to obtain monodisperse silica beads with particle sizes between 0.05 – 2 μm.[42]

Bogush *et al.* extended the research shown by Stöber to determine the range for the concentrations of reagents in which the synthesis of monodisperse silica beads can be produced by this method.[43] The research showed that the monodisperse silica beads can be synthesised using 0.1 – 0.5 M TEOS, 0.5 – 17.0 M H_2O and 0.5 – 3.0 M NH_3. Furthermore, Bogush developed an equation based on over 100 experimental results to correlate the initial reagent concentrations (within the ranges stated) to the final particle size (Equation 1.19):

$$d = A[H_2O]^2$$

$$\exp(-B[H_2O]^{\frac{1}{2}})$$

with

$$A = [TEOS]^{\frac{1}{2}}(82 - 151[NH_3] + 1200[NH_3]^2 - 366[NH_3]^3)$$

and

$$B = 1.05 + 0.523[NH_3] - 0.128[NH_3]^2 \qquad (1.19)^{43}$$

where d is the average diameter in particle size and the reagent concentration are given in mol/L, though this method can only be used to synthesise silica particles with a diameter up to 800 nm.

The synthesis of larger silica particles was produced using a two liquid-phase synthesis by Barder *et al.*[44] The reaction uses two liquid phases (1) a solution containing TEOS and (2) a solution containing NH_3 and an alcohol. Solution (1) was then added to

solution (2) either drop wise or by batch. The initial particle size is determined by the concentration of the reactants (as shown by the equation above). The particle diameter can be further increased by subsequent addition of the silica precursor (TEOS) to produce silica beads of diameters between 0.1 – 10 μm.

1.9 Reversed-Phase Chromatography

The process of reversed-phase (RP) chromatography is a partitioning process similar to normal phase chromatography. Traditional chromatography uses a polar stationary phase and a non-polar solvent whereas reversed-phase chromatography has a non-polar (or hydrophobic) stationary phase and a polar mobile phase.

The idea of using a non-polar stationary phase was first put forward by Boscott[45] wherein the use of cellulose acetate was suggested. Shortly after, research by Boldingh advocated the use of vulcanized rubber[46] though this method proved to be unsuccessful as the degree of swelling varied in each batch of rubber. The degree of swelling will affect the magnitude of retention meaning reproducible results cannot be obtained.[47] The first publication of a non-polar stationary phase similar to that which we use today was in 1950 by Howard and Martin[48] wherein the authors reacted kieselguhr with dimethyldichlorosilane to produce a non-polar stationary phase which could separate C_{12}-C_{18} fatty acids.

1.10 Synthesis of Non-Polar Stationary Phases

The addition of organic groups into the silica stationary phase can be done via grafting, co-condensation or through the synthesis of periodic mesoporous organosilica (PMOs).

1.10.1 Post Synthetic Functionalisation (Grafting)

Post synthetic grafting (as shown in Figure 1.11) is achieved by reacting the silanol groups of the silica with organosilanes ($(R'O)_3Si$-R) under aqueous conditions. This method allows the original mesostructure of the silica to be retained and a variety of organic groups to be incorporated, though the synthesis cannot control where the

organosilanes react. If the reaction occurs preferentially at the pore openings this can hinder access to the pores or in some cases block the pores completely.

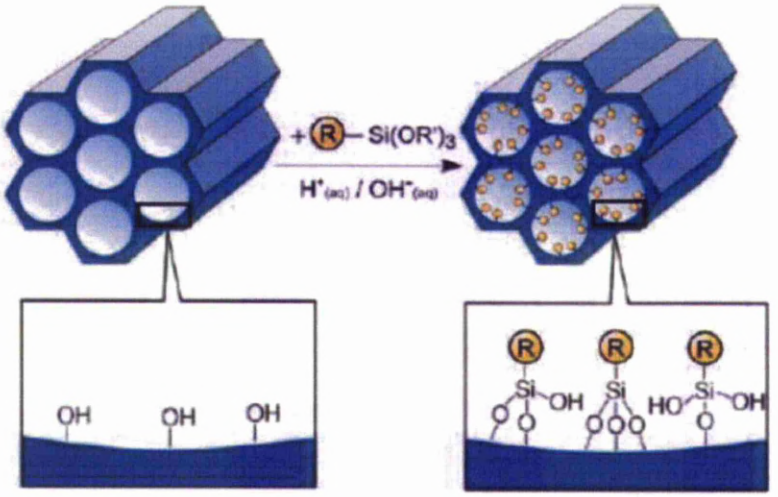

Figure 1.11 post synthetic grafting of organic functionalities [49]

1.10.2 Co-Condensation

An alternative to post-synthetic grafting (as shown in Figure 1.12) is the co-condensation method which is a "one pot" synthesis. This direct method can be used to synthesises mesoporous silica through the co-condensation of tetra-alkoxysilanes (such as tetraethyl orthosilicate, TEOS) and a terminal trialkoxyorganosilane in the presence of a structure directing agent to produce a material with the organic groups at the pore walls. Synthesising the organic-inorganic hybrid materials using this method eliminates the problem of pore blocking and allows more control of the homogeneity of the organic groups incorporated [50] compared to the grafting method. The main disadvantage to this method is that in general the level of mesoscopic ordering decreases with increasing organosilanes precursor.

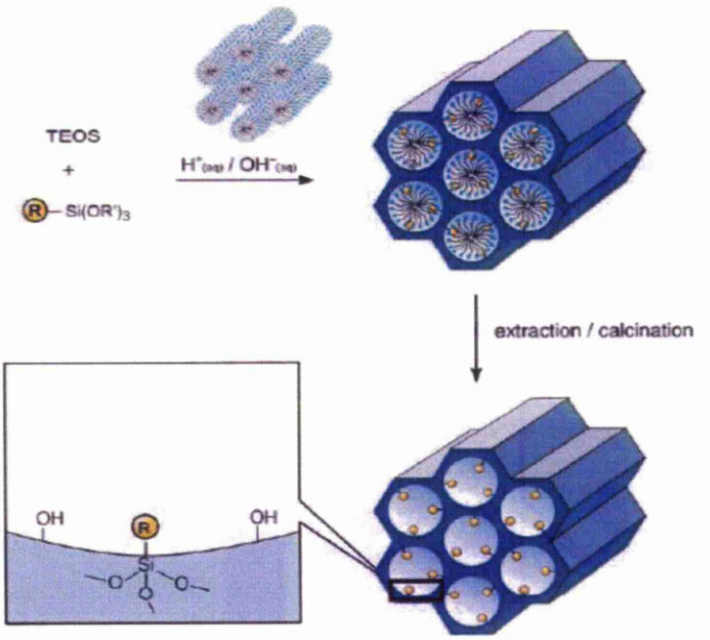

Figure 1.12 Synthesis of organic-inorganic hybrid material *via* a co-condensation method [49]

1.10.3 Periodic Mesoporous Organosilicas (PMOs)

Periodic mesoporous organosilicas are again synthesised through hydrolysis and condensation reactions though bridged organosilane precursors are used as opposed to terminal organosilianes. This produces silica with organic groups in the three-dimensional structure of the silica framework as opposed to projecting into the pore. The first PMOs were synthesised by three independent groups in 1999.[51-53] This method creates hybrid silica with a homogeneous distribution of functional groups throughout the pore wall, (as shown in Figure 1.13) high thermal stability and large surface areas, though most material has a low level of mesoscopic ordering.

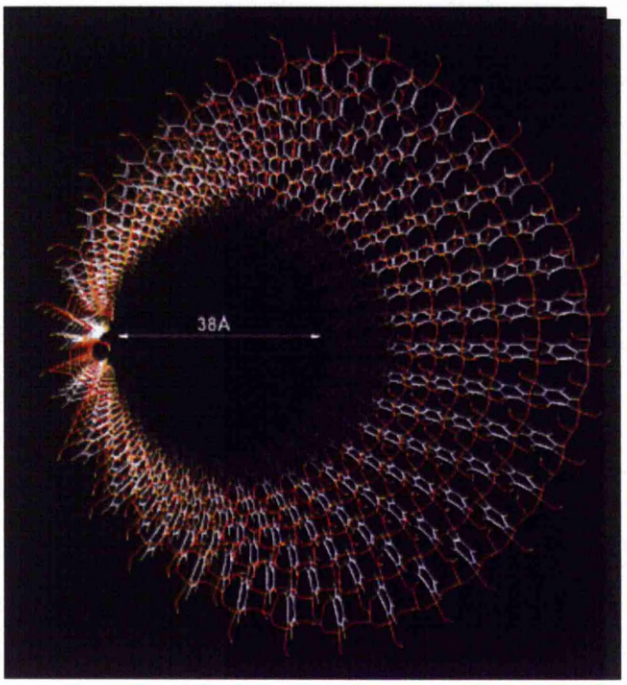

Figure 1.13 Periodic Mesoporous Organosilica (PMO)[54]

1.11 Superficially Porous Silicas

Most forms of liquid chromatography use a totally porous packing material. As the basis of chromatographic separation is dependent on the adsorption of the solute onto the stationary phase, the high surface areas of the porous beads is advantageous. However, for high speed chromatography the mass transfer term becomes a very important factor.[55] Stagnant mobile phase and solute remaining within the pores of the stationary phase limit the speed of the separation. It was first suggested by Golay [56] and Purnell [57] from a theoretical view that a thin porous layer could be used for rapid analysis.

Kirkland first synthesised superficially porous silica in 1969 for liquid-liquid chromatography and soon after superficially porous silica for reversed-phase chromatography. Some literature has shown that rapid analysis can be achieved through using extremely small porous beads (< 2 μm diameter); though this type of stationary phase cannot efficiently separate macromolecules such as proteins. The thin porous layer of the superficially porous silica beads allow fast mass transfer (C-term)

and therefore should be advantageous for the separation of larger molecules which have a much slower diffusion rate.

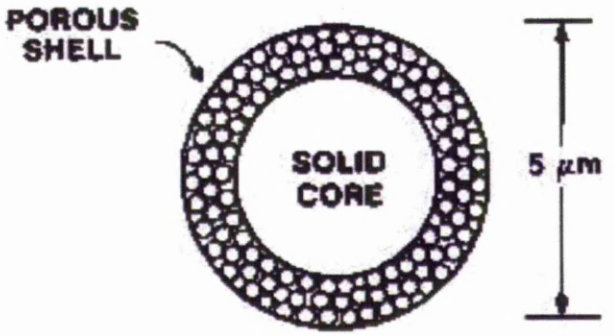

Figure 1.19 Superficially porous silica [58]

Kirkland first used a spray drying method to create superficially porous silica. This method comprised spray-drying a dense silica bead with a 44 nm silica sol solution in dilute ammonium hydroxide to form a uniform porous shell around the solid core. Later he modified the process using smaller beads by a layer-by-layer technique that was first developed by Lvov.

Lvov[59] demonstrated the alternative synthesis using a layer-by-layer adsorption of alternating negatively and positively charged polyelectrolytes on the surface of a solid core wherein the terminal polyelectrolyte contains a positive charge. The material was then submerged into an aqueous dispersion of silica. This process could be repeated creating more control over the size of the bead and thickness of the porous layer.

1.12 Comparison of HPLC Columns

To achieve optimum separations a column with the most suitable selectivity has to be chosen. Often it can be difficult to directly compare columns as manufacturers use non-standardised separation methods to highlight the superiority of one column compared to other commercially available columns. Standardised tests can be used to

directly compare the selectivity of columns from different manufacturers using different bonded phases. Phase selection charts (Figure 1.20) analyse the columns hydrophobicity and polar properties. This allows the user to compare the selectivity of similar columns. The hydrophobicity is measured by the retention time of a hydrophobic analyte (e.g. acenathpthene) and is determined by the strength of hydrophobic interaction and the surface coverage of the bonded phase. The level of polar activity is determined by measuring the difference in relative retention of an analyte that interacts via both hydrophobic and silanolic interactions (e.g. amitriptyline) and an analyte that only has hydrophobic interactions (e.g. acenaphthene).

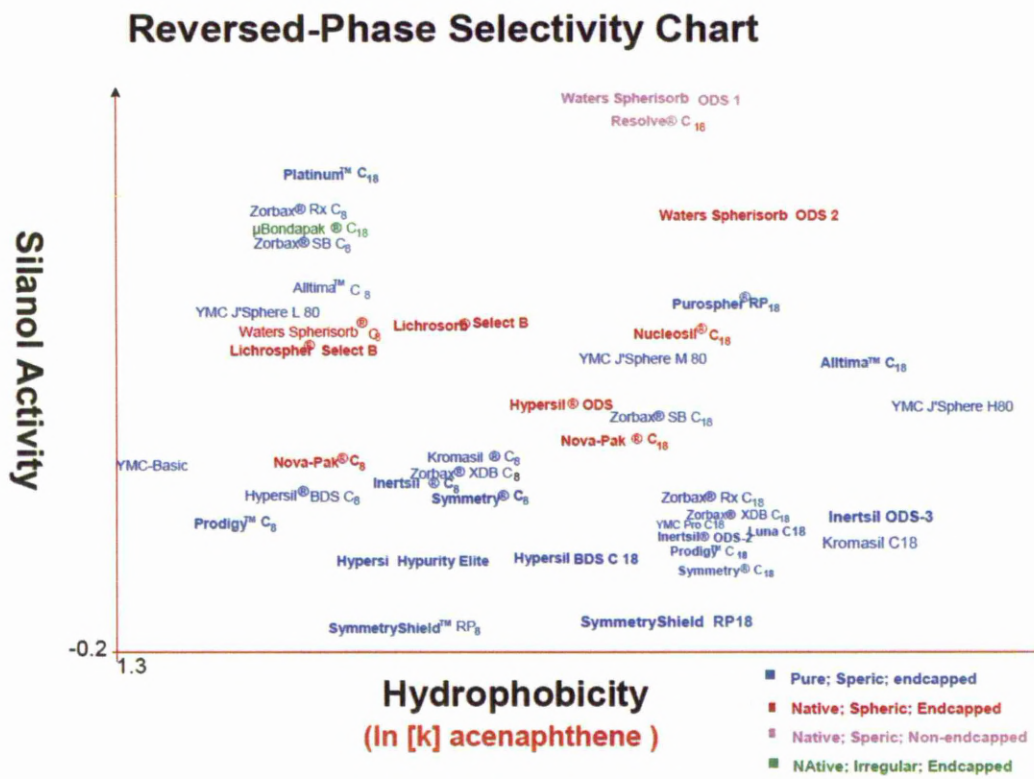

Figure 1.20 Comparison of HPLC Column using a selectivity chart

In this research we have used a more in depth standardised test, the Tanaka test. This can be used to compare the physio-chemical properties of columns through analysing

the retentiviy, hydrophobicity, steric selectivity, silanol capacity and ion exchange capabilities of a phase.

1.13 Characterisation of Functionalised Silica Through Solid-State NMR

The retention mechanisms of reversed-phase chromatography are not fully understood and despite research spanning over 30 years a uniform view has not yet been achieved. Horvath[60] and Karger[61] *et al.* (1976) publish research on the "hydrophobic or solvophobic retention theory" which is a thermodynamic approach to analysing the retention mechanism produced by analysing the retention trends of polar and non-polar analytes. This theory states that the retention time of a non-polar analyte in a polar mobile phase is dependent on the contact area between the solute and mobile phase (wherein higher contact areas produce longer retention times) and the surface tension between the mobile phase and the solute. However, this theory does not explain the differences in retention time for different stationary-phases.

The theory of a "lattice model" was put forward by Dill[62,63] *et al.* which was further researched by Martire[64] *et al.* who analysed the theory using a statistic mechanical model to describe the retention mechanism. This theory suggested that the conformational order of alkyl chains incorporated onto the surface of the stationary phase will affect the retention of analytes. Further research by Wise[65] *et al.* suggested the retention of the analytes was affected by the "length-to-breadth" (L/B) ratio, wherein bulky, square or non-planar analytes are not able to penetrate the alkyl chains. This reduces the interaction between the two compounds creating shorter elution times. Extended planar molecules are able to penetrate between the functional groups of the stationary phase and therefore longer retention times are observed.

Solid-state NMR is a powerful analytical technique which can be used to characterise the reversed-phase stationary phases and their interactions with analytes. Recent research using this technique has been centred on structural and conformational analysis. The more simple techniques such as ^{1}H-^{13}C and ^{1}H-^{29}Si CP/MAS NMR have been used to confirm the incorporation of functional groups bonded to the surface of

the reversed-phase or ion-exchange columns.[66-68] Alternatively, this technique has been shown to be useful in analysing the *trans/gauche* conformation of the alkyl chains incorporated[69] and the bonding between the alkyl groups (i.e. monomeric of polymeric functionalities) which have been shown to effect the chromatographic performance of RP columns.[70]

Few papers have been published analysing chromatographic stationary phases using more complicated NMR techniques. Pursch *et al.*[71] published research analysing the structural differences of monomeric, polymeric and self-assembled monolayer (SAM) docosyl ($-C_{22}$) functionalised silica. This research showed *trans* and *gauche* conformations of alkyl chains could be analysed using 2D ^{1}H-^{13}C WISE NMR techniques, showing the increased mobility of the *gauche* conformation compared to *trans*.

Research by Chagolla *et al.*[72] showed NMR could be used to probe the interactions between solvents and a $-C_{18}$ fucntioanlised stationary phase. As ^{129}Xe is sensitive to changes in environment the element was incorporated into various mobile phases to analyse whether the solvent was incorporated into the porous framework of the functionalised silica beads or whether the solvent remained predominantly in the inter-particulate spaces. The research indicated polar solvents such as ethylene glycol do not mix with the non-polar stationary phase though non-polar solvents such as cyclohexane mix well.

Although the research to present has given an insight into the possibilities available using solid-state NMR techniques, full structural analysis of the silicate structure, incorporation of the functional groups, bonding between the functional groups and the mobility and homogeneity of these groups incorporated on the surface has not yet been shown. Further it would be beneficial to link the structural and conformational information obtained through the analysis with the chromatographic performance of different columns. Furthermore although the research by Chagolla gave insight into the interactions between reversed-phase columns and polar/ non-polar solvents, these results were obtained *via* the analysis of ^{129}Xe. It would be beneficial to obtain information directly between the solvent and/or analyte and the stationary phase. Although Chagolla was able to show non-polar solvents mix well with RP columns, no

insight was given into how these two compounds interact. If further information can be obtained regarding how the solvent/ analyte and the functional groups incorporated onto the silica interact, this may provide vital information about how the retention mechanism of reversed-phase chromatography works.

Solid-state NMR is a useful technique for analysing functionalised silica on a molecular level and can be used to create a detailed understanding of the structure of different stationary phases. By analysing the silicas on this level and linking the structural difference to the efficiency and selectivity of the stationary phases we can further understand and therefore improve chromatographic columns.

The majority of research available uses only single pulse or cross-polarisation (CP) experiments to analyse and compare stationary phases.[73,70,74-78] The mobility of the organic groups present can be analysed using single pulse experiments such as ^{1}H MAS NMR. ^{1}H-^{29}Si CP/MAS NMR can be used to determine the degree of cross-linking and therefore can be used to determine the amount of silanol groups present on the surface. ^{1}H-^{29}Si CP/MAS NMR spectra can also provide information about the type of surface modifications, whether monomeric or polymeric coverage of alkyl chains is present and the degree of polymerisation on the surface. ^{1}H-^{13}C CP/MAS NMR experiments have been used to analyse the chemical structure of the organic groups present and analyse the mobility of these functionalities.

More complicated NMR sequences can provide much more detailed information about the framework though there is little research available linking 2D NMR experiments and chromatographic performance [79,80].

To the best of our knowledge no research has been published which provides a full analysis of new stationary phases and their interactions with analytes. Furthermore, more advanced NMR techniques can be used to analyse this type of material such as ^{1}H–^{13}C wide-line separation experiments (WISE) which correlate molecular structure and mobility. This can determine whether the functionality incorporated is on the surface of the silica and able to interact with the eluent or whether the functional groups are within the pore wall and therefore ineffective. ^{1}H–^{29}Si heteronuclear correlation (HETCOR) CP/MAS NMR and ^{1}H NOESY NMR techniques are used to examine the homogeneity of the silica precursors and moieties incorporated. A

homogeneous distribution of the two functional groups is paramount as this will give a uniform interaction between the stationary phase with the eluent throughout the column, whereas domain type functionality could cause band broadening. As this technique is dependent on distance it can also be used to study how analytes interact with different stationary phases. As the mobility, location and homogeneity of the functional groups incorporated affect the performance of the column, it is vital to analyse and understand these properties to produce/develop quality stationary phases.

Chapter 2: Characterisation Techniques

2. Nuclear Magnetic Resonance Spectroscopy (NMR)

The method of using nuclear magnetic resonance to analyse molecules on a molecular level was first put forward by Rabi *et al*[81] in 1938. The research published showed the detection of both lithium and chloride atoms by applying a small oscillating field at right angles to a larger constant field wherein the frequency of the oscillating field is varied until a resonance was observed. This method used radiofrequency pulses applied at the larmour frequency of the nuclei to observe the change in nuclear transition states. Further research by Bloch[82] and Purcell *et al.*[83] showed applying a small radio-frequency pulse perpendicular to the main field could cause a considerable change in the orientation of the nuclear moments. This research also highlighted that the detection of different nuclei through the measurement of the electromagnetic induction would also be possible for solid and liquid samples. Bloch used radiofrequency to detect the reorientation of the moments wherein the signals, cause by the electromagnetic induction produced by the reorientation of the nuclear moments, were produced as a voltage.[84] It is on the basis of the discoveries and theories presented that modern solid-state NMR is based; using radio-frequency pulses to measure the small oscillations occurring of the interactions between the magnetic moment (μ) of an atomic nuclei and an external magnetic field (B_0).

2.1 Basic NMR Theory

2.1.1 Angular momentum

The nuclei of atoms have four main physical properties; mass, charge, magnetism and spin. The physical properties of spin and magnetism make it possible for materials to be analysed, non-destructively, on a molecular level. [85]

Nuclei can have a spin quantum number of 0, ½, 1, $^3/_2$, 2 *etc.* which are determined by the number of unpaired protons and neutrons. Nuclei with no-unpaired protons or neutrons ($I = 0$), such as ^{12}C, posses no nuclear spin and cannot be analysed using NMR.

Nuclei with non-zero quantum numbers have magnetic moments (μ) which are dependent on the angular momentum (**I**) and the gyromagnetic ratio (γ):

$$\mu = \gamma I \tag{2.1}$$

Where the angular momentum (I) is calculated by:

$$I = \frac{mh}{2\pi} \tag{2.2}$$

in which the magnetic quantum number (m) has 2I+1 integral steps between –I and +I and h is planck's constant.

2.1.2 Nuclear Magnetisation

The nucleus producing the magnetic field can be thought of as a bar magnet. If this bar magnet is placed in a external magnetic field (B_0) the magnet will align preferentially with the magnetic field, wherein the energy associated with the magnetic moment is:

$$E = -\mu_z B_0 = -m\hbar\gamma B_0 \tag{2.3}$$

In the presence of B_0 the spin the energy levels split into (2I+1) energy levels with transitions occurring only between adjacent energy levels ($\Delta m = \pm 1$), this is called nuclear Zeeman splitting.

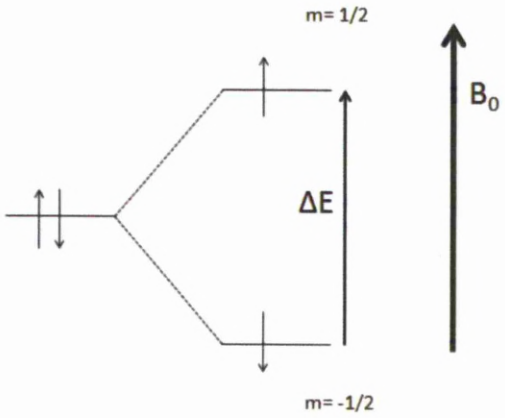

Figure 2.1 Zeeman Splitting

The extent of splitting between energy levels is dependent of the strength of the external field (B_0) and gyromagnetic ratio:

$$\Delta = \hbar\gamma B_0 \tag{2.4}$$

Figure 2.1 shows that the spins can align with (α) or against (β) the external field. When a collection of spins are placed in a magnetic field the spins will align preferentially with the field. The orientation parallel to the applied field, α, has slightly lower energy than the antiparallel orientation, β, so at equilibrium there will be an excess of nuclei in the α state as defined by the Boltzmann distribution:

$$\frac{P_{-1/2}}{P_{+1/2}} = e^{\Delta E/kT} \qquad (2.5)$$

Wherein P represents the fraction of particles in the population state, ΔE is the energy difference between the transition states, k is the Boltzmann constant and T the temperature.

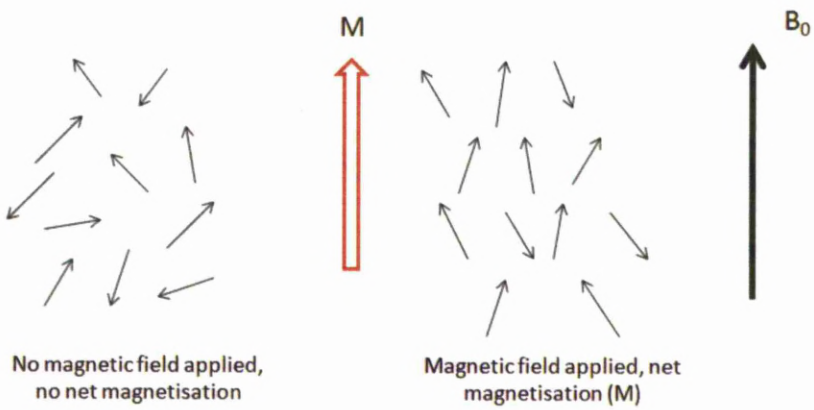

Figure 2.2 Effect of an external magnetic field on net magnetisation of a sample

Due to the small energy difference in populations; the signal is weak, the small population excess can be represented by bulk magnetisation shown in Figure 2.2. This magnetisation precesses around the external field.

2.1.3 Larmor Frequency and the Vector Model

The spin in a magnetic field will precess around the external field at a constant angle. The frequency of the precession, ω_0, is referred to as the Larmor frequency and is proportional to the external field.

$$\boldsymbol{\omega_0 = -\gamma B_0} \tag{2.5}$$

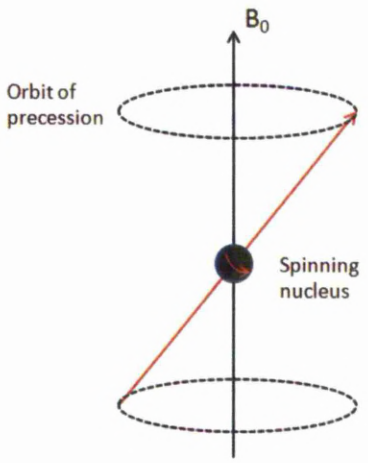

Figure 2.3 Schematic representation of the precession of a nucleus in an external field

The Larmor frequency has a defined sign which can provide information regarding the direction of the spin precession. NMR active elements with a positive gyromagnetic ratio will give a negative value of ω_0. These nuclei will rotate clockwise (if viewed down the axis of the B_0 field). Finally, NMR occurs when the resonance condition is met:

$$\boldsymbol{\Delta E = h\nu = \frac{\gamma B_0}{2\pi}} \tag{2.6}$$

2.1.4 Relaxation

Relaxation in NMR is the process by which the spins return to equilibrium after the application of an rf pulse. There are two forms of relaxation, spin-lattice relaxation (T_1) and spin-spin relaxation (T_2).

2.1.4.1 Spin-Lattice Relaxation

Spin-lattice relaxation is derived from the movement of spin populations back to the normal distribution of α and β spin states. Nuclei in the lattice have vibrational and rotational motions which create a magnetic field referred to as the lattice field. Due to these motions the lattice can interact with the nuclei causing a loss of energy in the form of thermal heat. This causes a gradual break down of the constant angle precession. The anisotropic distribution in of the field created by the nucleus is referred to as thermal equilibrium. Spin-lattice relaxation can also be referred to as T_1 relaxation or longitudinal relaxation.

2.1.4.2 Spin-Spin Relaxation

If a radio-frequency (rf) pulse is applied to the system the net magnetisation can be rotated by $\pi/2$ radians. Individual spins will continue to precess. The frequency of the precession for each nucleus is dependent on the local environment and so small differences in frequency will occur. Eventually the synchronicity of the spins breaks down and the magnetisation decays. This can also be referred to as T_2 relaxation or transverse magnetisation. Although pure spin-spin relaxation is produced through the molecular interactions described, variations in the external B_0 field can also infer T_2 relaxation.

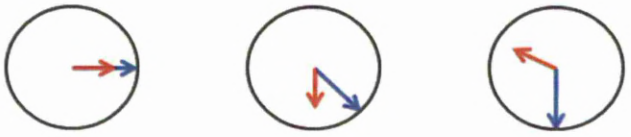

Figure 2.5 Schematic representation of T_2 relaxation

2.1.5 Chemical Shift and Shielding

The frequency (ν) of a nucleus is dependent on γ and B_0, therefore in the same field different nuclei will resonate at different frequencies.

$$\nu = \frac{\gamma B_0}{2\pi} \tag{2.7}$$

In a 9.4 T field ^{1}H resonates at *ca* 400.1 MHz and ^{13}C *ca* 100.6 MHz. However, not all ^{1}H and ^{13}C nuclei have identical resonance frequencies; the frequency of resonance depends, in part, on the position of a nucleus in a molecule, or the local electron distribution associated with that nucleus. The slight deviation in frequencies is known as the *chemical shift* and allows chemists to distinguish different nuclei environments in molecules.

The magnetic field at the nucleus is not equal to the applied magnetic field. Surrounding electrons shield the nucleus and alter the field strength at the nucleus, this is called shielding. The torque generated by the external magnetic field also causes the surrounding electrons to precess, creating a magnetic field (B') in the opposite direction to B_0. The field produced by the electrons shields the nucleus from the external field.

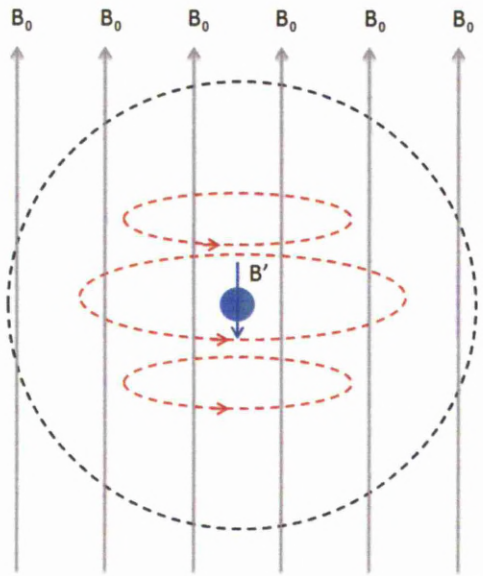

Figure 2.4 Shielding effects

The net effect can be described using the shielding constant (σ):

$$B = B_0 - B' = B_0(1 - \sigma) \tag{2.8}$$

therefore the frequency of the nucleus becomes:

$$\nu = \frac{\gamma B_0(1-\sigma)}{2\pi} \tag{2.9}$$

2.1.6 NMR Signal

The rotating magnetic moments creates a small oscillating frequency which can be detected by the coils located in the x-y axis. This current created at the frequency of the nucleus can be transformed into an NMR signal.

2.2 Solid-State NMR

Solid-state NMR can be used to analyse insoluble materials such as zeolites and mesoporous silica, on a molecular level. In liquids rapid molecular tumbling averages anisotropic interactions resulting, in general, in isotropic resonances. However in the solid-state, molecular motion is slower and anisotropic interactions dominate, causing severe line broadening.[86] A typical nuclear spin Hamiltonian can be expressed as:

$$\hat{H} = \hat{H}_Z + \hat{H}_{RF} + \hat{H}_D + \hat{H}_{CSA} + \hat{H}_Q + \hat{H}_J \qquad (2.10)$$

The nuclear spins experience a range of interactions including Zeeman interactions ($\hat{H}_Z$), interactions with the RF field ($\hat{H}_{RF}$), magnetic dipolar interactions ($\hat{H}_D$), chemical shift anisotropy ($\hat{H}_{CSA}$), quadrupolar coupling ($\hat{H}_Q$) for nuclei with spin quantum numbers I > 1 and spin-spin interactions ($\hat{H}_J$). $\hat{H}_Z$ and $\hat{H}_{RF}$ are referred to as the external part of the Hamiltonian:

$$\hat{H}_{ext} = \hat{H}_Z + \hat{H}_{RF} \qquad (2.11)$$

The remaining Hamiltonians are referred to as the internal Hamiltonians ($\hat{H}_{Int}$). For spin ½ nuclei the dominant interactions are the chemical shift anisotropy and the dipolar interactions.

2.2.1 Chemical Shift Anisotropy

The external field perturbs the electrons surrounding a nucleus, generating a small magnetic field (B') which shields the nucleus, altering the field experienced by the nucleus. As the frequency of the nucleus is dependent on B_0 the shielding effect will create a chemical shift. As the electron cloud density of atoms within molecules is not uniformly distributed (*i.e.* more commonly an ellipsoidal shape not spherical), the level of shielding, and therefore the frequency, of the nucleus is dependent on the orientation of the molecule with respect to B_0. Chemical shift anisotropy (CSA) can be as large as 120 – 140 ppm for ^{13}C nuclei [87].

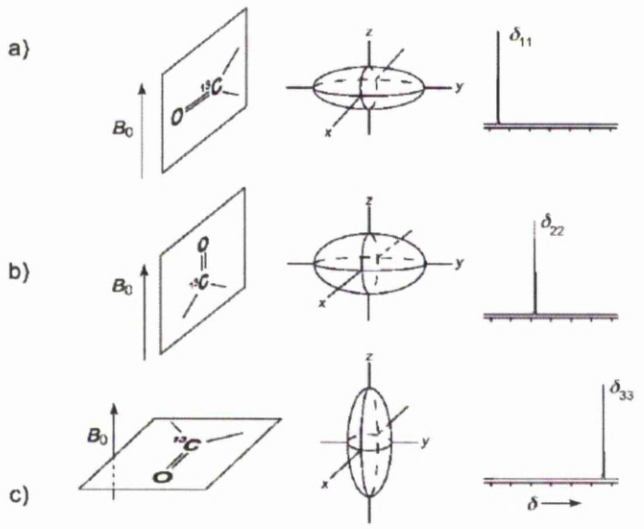

Figure 2.6 The effect of molecular orientation on chemical shift [87]

Figure 2.6 shows only three orientations but in reality numerous orientations are possible each with a different spectra reference with respect to B_0. Collectively the different frequencies create a powder pattern [88] (Figure 2.7).

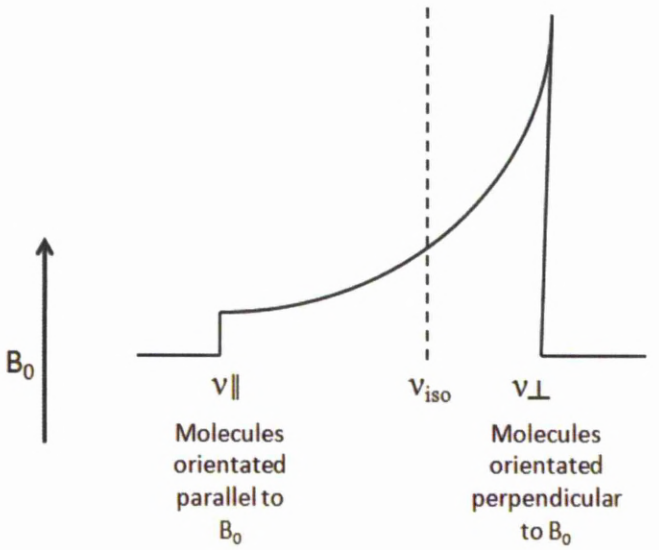

Figure 2.7 Chemical anisotropy powder pattern

The chemical shift Hamiltonian can be written as:

$$\hat{H}_{CSA} = \gamma B_0 I_Z \left[\delta_{iso} + \frac{1}{2}\delta_{CSA}(3cos^2\theta - 1)\right] \quad (2.12)$$

wherein the isotropic chemical shielding factor (δ_{iso}) is the average of the resonance frequencies:

$$\delta_{iso} = \frac{1}{3}(\delta_{11} + \delta_{22} + \delta_{33})$$

$$\delta_{CSA} = \delta_{33} - \delta_{iso} \quad (2.13)$$

The angle θ is given by the orientation of the axis ellipsoid electro cloud with respect to the external field and δ_{CSA} is the magnitude of CSA which is calculated by the chemical shift produced when the widest part of the electron cloud is orientated along B_0 minus the average chemical shift.

2.2.2 Dipolar Interactions

Dipolar coupling is the interactions which occur between two spin systems relatively close in space (< 10Å). These interactions can occur between either two different spin systems (Heteronuclear dipolar coupling) or two spin systems of the same form (Homonuclear dipolar coupling).

2.2.2.1 Heteronuclear Dipolar Coupling

Heteronuclear dipolar coupling occurs between the magnetic moments of two different spins. Commonly one spin is an abundant spin (I) such as ^{1}H and the other a rare spin (S) such as ^{13}C or ^{14}N. When placed in a magnetic field the IS spins will align parallel or anti-parallel to the B_0 field. The magnetic field produced by the I spin will alter the local magnetic field at the S spin, the frequency of the S spin will vary depending on the strength of this interaction. The extent to which the S spin is affected is dependent on the orientation the I spin with respect to the external field and the strength of the dipolar coupling. The heteronuclear dipolar interactions can be described by:

$$\hat{H}_{IS} = -d(3cos^2\theta - 1)I_Z S_Z \quad (2.14)$$

The strength of the dipolar coupling is dependent of the dipolar coupling constant (d), the orientation of the internuclear vector relative to the external magnetic field (θ) and the z components of the nuclear spin angular momentum operators I and S (I_zS_z). The dipolar coupling constant is dependent of the gyromagnetic ratio of the two spins and the internuclear distance (r):

$$d = \left(\frac{\mu_0}{4\pi}\right)\frac{\hbar\gamma_I\gamma_S}{r_{IS}^3} \qquad (2.15)$$

For crystalline samples, in which all possible orientations are present, a "pake doublet" is formed corresponding to the parallel and anti-parallel alignment of the IS spins producing positive and negative I_zS_z components respectively.

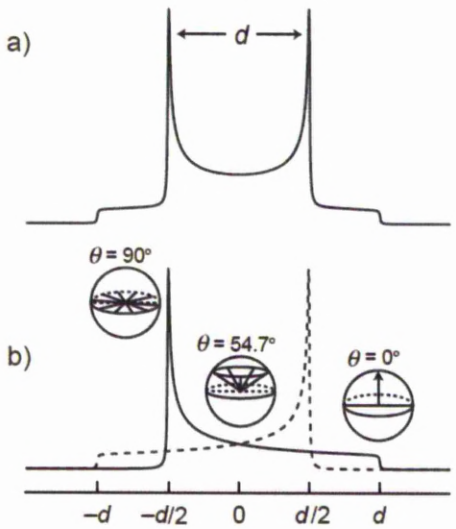

Figure 2.8 Pake doublet due to heteronuclear dipolar coupling in a crystalline solid [87]

2.2.2.2 Homonuclear Dipolar Coupling

The interaction of the magnetic fields of two spins from the same type of nucleus (e.g. ^1H-^1H) is referred to as homonuclear dipolar coupling. As both spins resonate at the same frequency the Zeeman splitting of the energy level will be equivalent. This enables the "flip-flop" effect of the transition states between the two spins (i.e. when one spin flips up the other spin flips down). The homonuclear dipolar coupling can be described by:

$$\hat{H}_{II} = -d_{\frac{1}{2}}^{1}(3cos^2\theta - 1)\left(2I_{1Z}I_{2Z} - \tfrac{1}{2}(I_1^+I_2^- + I_1^-I_2^+)\right) \quad (2.16)$$

Raising the operator I^+ increases the angular momentum causing a spin to flip from the "down" orientation to the "up" orientation. The lowering operator I^- decreases the angular momentum causing a spin to flip from the "up" orientation to the "down" orientation. These two effects create an energy conserving exchange of magnetisation.

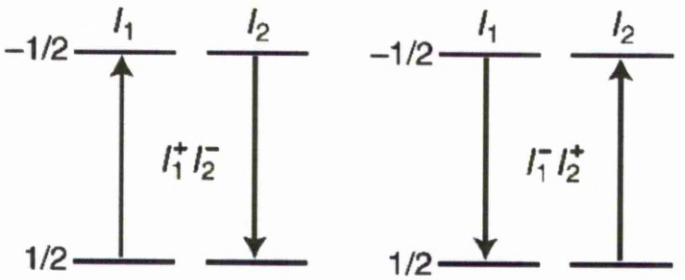

Figure 2.9 "Flip-flop" transitions occurring between two spins of the same form of nuclei

The homonuclear coupling for nuclei with low gyromagnetic values and natural abundances such as ^{13}C and ^{15}N can simply be removed using magic angle spinning (MAS). However, ^{1}H NMR spectra are usually broad and featureless due to the high abundance and gyromagnetic ratio. Even at high MAS rates of 60 kHz, the homonuclear interaction cannot be completely averaged. Nuclei such as ^{1}H have much stronger homonuclear dipolar interactions due to the higher γ value and the large abundance of spins. These interactions cannot be removed using only MAS.

2.3 Experimental Techniques in Solid-State NMR

2.3.1 Magic Angle Spinning (MAS)

Due to the rapid molecular tumbling in liquids the orientation dependent nuclear spin interactions, chemical shift anisotropy and dipolar coupling, are averaged producing sharp resonances.[89] These molecular motions are absent for solids and so the presence of all the possible orientations create line broadening (powder patterns). For solid samples the effect of these interactions can be removed through magic angle spinning. By spinning the sample at the magic angle (54.74°) the orientation dependent section of the CSA and dipole coupling Hamiltonians becomes zero ($3\cos^2(54.74^\circ) - 1 = 0$). In order to produce narrow linewidths the rotation frequency must be in the order of the CSA linewidth (a few kilohertz). The frequency observed is the isotropic (average) chemical shift.

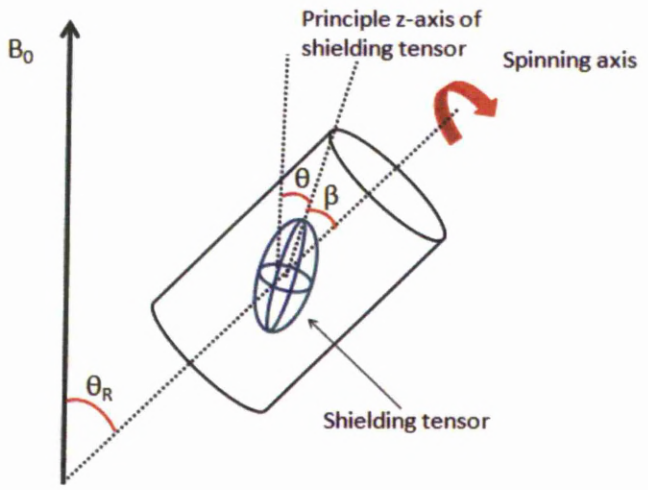

Figure 2.10 Magic angle spinning experiment

The sample is spun about an axis inclined at an angle (θ_R), θ is the angle between the principle z-axis of the shielding tensor and the applied external field and β is the angle between the z-axis of the shielding tensor and the spinning axis of the tensor (this is fixed for a given nucleus in a rigid solid but can take on all possible values).

2.3.2 Decoupling and r.f.pulses

Strong heteronuclear dipolar coupling can cause line broadening even under MAS conditions. These coupling effects can be removed using r.f. pulses. By applying high powered irradiation at the frequency of the proton resonances during the acquisition of the free induction decay (FID) of the dilute (S) spin produces high resolution spectra. The r.f. pulse does not have to be applied directly on resonance, due to the strong homonuclear coupling for ^{1}H nuclei if the r.f. pulse is applied to any part of the ^{1}H spectrum the effect is transmitted to all coupled protons. The effect of the close to resonance r.f. irradiation is to cause the ^{1}H spins to undergo repeated transitions ($\alpha \leftrightarrow \beta$) at a rate determined by the power of the r.f. irradiation. The strength of the dipolar interaction is dependent on m_H, the z-component of the ^{1}H spin, as shown by the heteronuclear dipolar coupling Hamiltonian. Due to the rapid transitions of the ^{1}H spin ($\pm½$) this part of the Hmailtonian will average to zero, removing the effect of the dipolar coupling. There are many heteronuclar decoupling sequences that have been devised to be used in conjunction with MAS. The most common of which are the Two Pulse Phase Modulation (TPPM) which uses continuous irradiation of two pulses with flip angles (θ_P) differing between 10-70°, the second being X inverse X (XiX) which again uses continuous irradiation of two pulses but for this sequence the pulses differ by a phase of 180°.

The pulse sequences above are only applicable to heteronuclear couping, the effects of homonuclear dipolar coupling can be removed by reorienting the direction of the spins averaging the spin vectors. Frequency-switched Lee-Goldburg (FSLG) homonuclear decoupling uses alternating 360° pulses ($\pm\Delta\omega$). These pulse sequences, which are often collectively referred to as multiple pulse sequences, have windows in which the homonuclear dipolar Hamiltonian is averaged to zero. If the FID is collected at these points the effect of the homonuclear dipolar coupling is not observed. The earliest of these sequences are a WAHUHA (named after Waugh, Huber and Haberlen) and MREV-8 (after Mansfield, Rhim, Elleman and Vaughan). Both sequences use a series of 90° pulses (-x, y, -y,x) throughout acquisition decaying the magnetisation in the x-y plane. WAHUHA is a four pulse sequence and MREV-8 an eight pulse sequence.

Homonuclear decoupling is often used in conjunction with MAS to average anisotropic effects, though the averaging effect of MAS interferes with the homonuclear decoupling sequence. These two averaging methods are synchronised using a Combined Rotation And Multiple Pulse Sequence (CRAMPS).

2.4 Cross Polarisation (CP)

Cross-polarisation (CP) is a technique used to observed low abundant spins such as ^{13}C (1.1 %), ^{29}Si (4.7 %) and ^{15}N (0.03 %). As very few spins are detected using the conventional pulse-acquire solid-state NMR experiment (Bloch decay experiment) these spins produce poor signal-to-noise ratios. The absence of the strong homonuclear decoupling interactions which can stimulate spin-lattice relaxation means long delays between scan are required (minutes for ^{29}Si framework silica). CP NMR can be used to overcome these problems associated with low abundant spins.

2.4.1 Cross Polarisation Theory

Magnetisation will naturally flow from highly polarised spins to spins of lower polarisation. The transfer of magnetisation between abundant (^{1}H) and rare spins (^{13}C) is facilitated by heteronuclear dipolar interactions. Commonly the Hartmann-Hahn (H/H) method is used to create a connection between the energy levels of the heteronuclear spins.

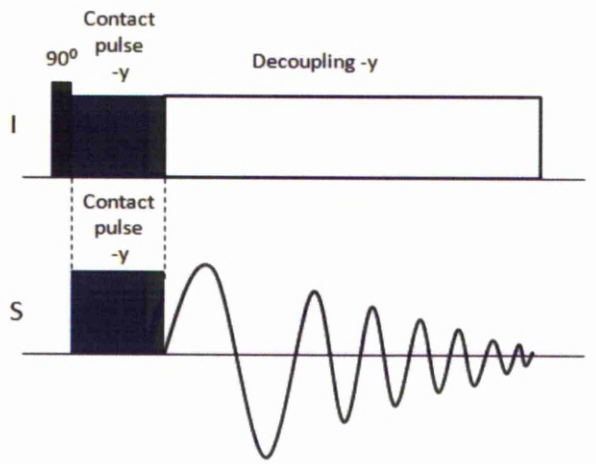

Figure 2.11 Pulse program for the cross polarisation NMR experiment

The CP experiment uses a doubly rotating frame in which the ^{1}H and X spins are in two different frames, each processing at its own Larmor frequency. By applying a ^{1}H 90_x^{o} pulse the magnetisation is transferred along the –y axis in the rotating frame. A –y

contact pulse ($B_1(^1H)$) can then be applied to "hold" the magnetisation at –y. Two r.f. fields are applied simultaneously; one at the frequency of the I spin and one at the frequency of the S spin. The rotation frequency of each spin can be controlled as it is dependent on the frequency and amplitude of the r.f. pulse applied.

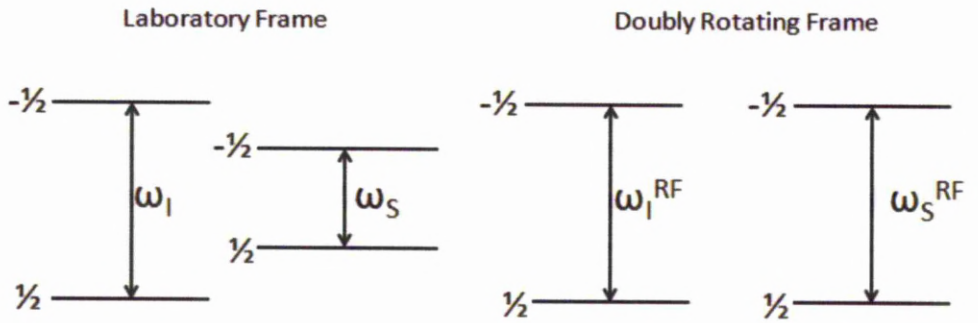

Figure 2.12 Energy differences of I and S spins in the laboratory frame and the doubly rotating frame

When the nutation frequency of both spins are equal, and therefore have equivalent Zeeman splitting, polarisation can be transferred. The Hartmann-Hahn conditions are met when:

$$\gamma_I B_1(I) = \gamma_S B_1(S) \qquad (2.17)$$

This phenomenon can be described using the dipolar coupling operator (Equation 2.17):

$$\hat{H}_{HX} = -\sum_i di\,(3cos^2\theta_i - 1)\hat{I}_{iZ}^{H}\hat{S}_Z^X \qquad (2.18)$$

where d_i corresponds to the coupling constant between the I and S spin. The equation is invariant when transformed into a doubly rotation frame as it only contains $\hat{I}_z$ and $\hat{S}_z$ which are unaltered by rotations about the z-axis. As the ^{1}H/X magnetisation is parallel to the z-axis the dipole-dipole coupling operator does not affect the net energy of the spin system. The energy of the spin system is dependent of the r.f. fields applied (B_1) and the magnetisation of the spins which are parallel to the quantization axis. When

the H/H requirements are met the energy gaps between transition states are equal for both spins. Transition absorbing energy at the I spin is compensated by transition releasing energy at the S spin and vice-versa so the net polarisation remains constant.

2.4.2 Kinetics of Cross Polarisation

The rate at which magnetisation is transferred between I and S spins during cross-polarisation varies depending on the local structure and mobility of the S spin. Whilst a single CP experiment can provide information about molecular structure, the dynamics and mobility of different environments cannot be analysed by a spectrum recorded with an arbitrarily chosen contact time. Recording a series of spectra varying the contact time allows us to monitor and compare the build-up and relaxation of different peaks.

The CP kinetics can be described using different models. The I-S model assumes that spin diffusion is sufficient to allow all I spins to behave as a single spin system. When the homonuclear dipolar interactions are not sufficient to allow the I spins to behave as one system the I-I*-S model can be used to explain the dynamics within the sample. Magnetisation is transferred primarily from abundant spins in close proximity to the S spin (I*) and then from the remaining surrounding I spins.

2.4.2.1 I-S Model

The CP kinetics of a system can be simplified by describing the system thermodynamically. If we assume that the system consists of a lattice with a huge heat capacity and two subsystems I and S, in which I has a much larger heat capacity than S. In the rotating frame the inverse of these spin temperatures are used. At the point of cross polarisation the hot dilute S spins are cooled through contact with the reservoir of cool I spins.

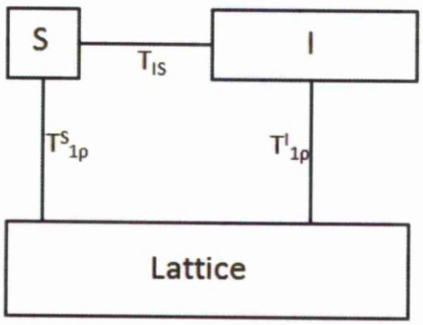

Figure 2.13 Diagram of CP thermodynamics

Cross polarisation between dilute and abundant spin ½ nuclei can be described by the kinetic equation:

$$I(t) = I_0\left(1 + \frac{T_{IS}}{T^S_{1\rho}} - \frac{T_{IS}}{T^I_{1\rho}}\right)^{-1}\left\{exp\left(-\frac{t}{T^I_{1\rho}}\right) - exp\left[-t\left(\frac{1}{T_{IS}} + \frac{1}{T^S_{1\rho}}\right)\right]\right\} \quad (2.19)^{90}$$

I_0 is the absolute intensity, T_{IS} corresponds to the CP time constant which described the rate at which magnetisation is transferred from the I spin to the S spin, $T^I_{1\rho}$ and $T^S_{1\rho}$ are the relaxation constant of the I and S spins respectively in the rotating frame. This equation can be further simplified when $T_{IS}/T^S_{1\rho} \approx 0$, to give:

$$I(t) = I_0\left(1 - \frac{T_{IS}}{T^I_{1\rho}}\right)^{-1}\left[exp\left(-\frac{t}{T^I_{1\rho}}\right) - exp\left(-\frac{t}{T_{IS}}\right)\right] \quad (2.20)^{90}$$

The rate at which magnetisation is transferred and then decays is characteristic of the local structure and mobility of the observed nuclei. The dipolar interactions which facilitate the transfer of magnetisation is strongly dependent on the internuclear distances ($1/r^3$). The bulid-up of magnetisation is dependent on the number of protons in close proximity. The mobility of the nuclei will also affect T_{IS}, higher levels of mobility will average the out the dipolar interactions reducing T_{IS}. As CP is also used to induce relaxation of low abundance nuclei, higher numbers of protons surrounding the nuclei will reduce $T^S_{1\rho}$. Due to the averaging effect more mobile groups have much longer relaxation times. For example a rigid group with many surrounding protons will have a fast build-up of magnetisation and a short relaxation time.

2.4.2.2 I-I*-S Model

The I-I*-S model can be used to describe systems in which the homonuclear dipolar coupling is not efficient enough to allow the abundant I spins to act as one spin system. The transfer of magnetisation takes place in two stages. Primarily magnetisation is transferred rapidly by bonded or surrounding protons (I*). In the second stage magnetisation is transferred from the remaining protons (I) *via* the directly bonded protons through spin diffusion interactions. This process can be described through the kinetic equation:

$$I(t) = I_0 exp\left(-\frac{t}{T_{1\rho}^I}\right)\left[1 - \lambda exp\left(-\frac{t}{T_{df}}\right) - (1-\lambda) exp\left(-\frac{3}{2}\frac{t}{T_{df}}\right) exp\left(-\frac{1}{2}\frac{t^2}{T_2^2}\right)\right] \quad (2.21)^{90}$$

Wherein T_{df} is the ^1H spin diffusion time constant, which is dependent on the strength of the homonuclear dipole interactions, λ is the number of protons (n) directly bonded to the observed I spin (λ = 1/n+1) and T_2 corresponds to the spin-spin relaxation time.

2.5 2D NMR Experiments Based on CP

Cross-polarisation is the basis of many 2-dimentional experiments which can be used to determine more than just structural information from the solid.

2.5.1 Wideline Spectroscopy (WISE) NMR

^1H lineshapes can be used as a qualitative measure of the mobility of groups. Strong ^1H-^1H dipolar coupling can give rise to very broad ^1H resonances. Under these conditions magic-angle spinning has very little effect on the resolution of the spectrum. Molecular motion within the sample can average out the dipolar interactions present significantly reducing the linewidths, though inevitably due to the broad ^1H lines the resonances overlap. 2D WISE NMR techniques can be used to correlate the mobility of the sample (through ^1H linewidths) and structure (^{13}C or ^{29}Si frequencies).

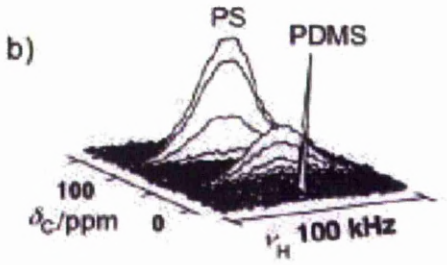

Figure 2.14 ^{1}H-^{13}C WISE NMR experiment of polystyrene-b-polydimethylsiloxane (PS-b-PDMS) block copolymer, highlighting the rigid polystyrene and mobile polydimethylsiloxane components [87]

A ^{1}H 90° pulse is applied to transfer the magnetisation into the x-y plane. The magnetisation is then allowed to evolve during a time period t_1. The remaining magnetisation t_1 is transferred to a dilute spin (^{13}C or ^{29}Si). The time given for cross polarisation is kept short (50 – 100 μs) to only allow magnetisation to be transferred from directly bonded protons

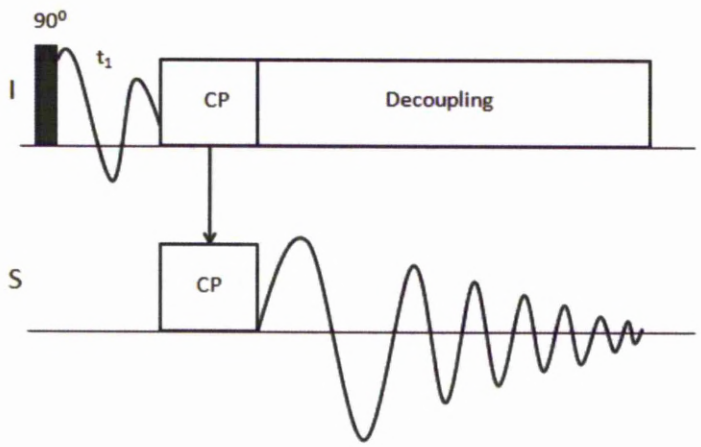

Figure 2.15 Pulse sequence for WISE NMR experiements

2.5.2 Heteronuclear Correlation (HETCOR) NMR

2D ^{1}H-X HETCOR NMR experiments correlate the ^{1}H chemical shifts in the indirect dimension to the X chemical shifts in the direct dimension. The pulse program of the

HETCOR experiment is identical to that of WISE NMR experiment apart for the incorporation of ^{1}H homonuclear dipolar decoupling during the t_1 evolution period. This means that the ^{1}H magnetisation evolves only under their own chemical shift. As the correlation experiment is based on CP, the variation of the length of the contact pulse will alter what resonances are observed. For short contact times magnetisation will only be transferred from directly bonded protons, by increasing the contact time magnetisation can be transferred from other surrounding protons. A series of HETCOR experiments using increasingly longer contact times can be used to build a full picture of the molecular structure of the sample.

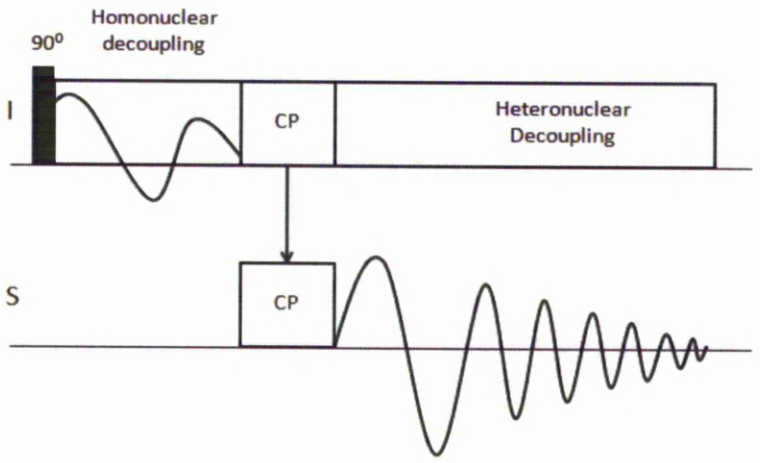

Figure 2.16 Pulse programme for the HETCOR NMR experiment

2.6 X-ray Diffraction [91-94]

2.6.1 Introduction

X-ray diffraction is a characterisation technique commonly used to determine the crystalline structure of solid materials. The use of x-rays in determining the lattice structure of crystalline solids was first shown by Max von Laue in 1912.[95] As x-rays impinge upon a material the electrons associated with the atoms or ions of the material scatter the x-rays. By studying the scattering effect of the material we can determine structural information.

The x-rays needed for this technique are generated by accelerating electrons with a metal plate (Cr, Fe, Co, Cu, Mo). The impact of the electron with the metal plate (assuming the electron has sufficient energy) causes the ejection of an electron from a core electron orbital of the metal atom. The vacant orbital can be filled by an electron in a higher energy orbital through the emission of radiation (x-rays).

Metals such as copper can fill the vacant orbital from numerous higher energy orbitals. Each different transition will emit radiation with a different wavelength, producing a spectrum of x-rays as shown in Figure 2.17

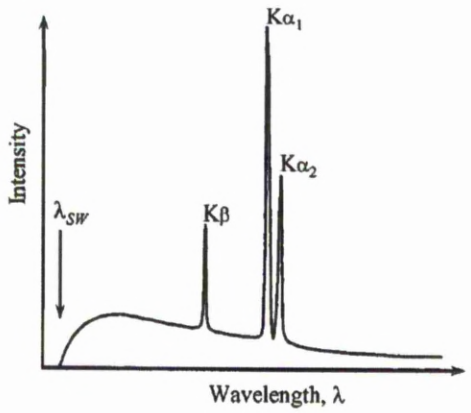

Figure 2.17 Spectrum of X-rays[92]

The lines are labelled with respect to the electron shells involved in producing the radiation. For example the filling an S orbital (quantum number one) is shown by the symbol K. This orbital can be filled from either a 2p or a 3p orbital. In order to

differentiate between the two the 2p → 1s transition is denoted as K_α whereas the 3p → 1s transitions denoted as K_β. The K_α transition produces two wavelengths due to the multiplicity of the p orbitals in Copper (total angular momentum quantum numbers of ½ or $^3/_2$), though both wavelengths are very similar, $K_{\alpha1}$ = 1.5406 Å and $K_{\alpha2}$ = 1.5444 Å.

X-rays can also be produced through the deceleration of electrons as they enter the metal target (bremsstrahlung). This affect produces a continuous curve of radiation as shown in Figure 2.17.

An x-ray diffraction experiment uses a single x-ray wavelength. As multiple wavelengths are often produced from the metal plate the spectrum of x-rays must be filtered before it reaches the target material. Modern difractometers use either a crystal monochromator or a filter. A crystal monochromator is comprised of a crystal set at a chosen, fixed orientation to the x-ray. At the chosen angle only one wavelength can be diffracted from the crystal. By adjusting the angle the most intense wavelength can be selected ($K_{\alpha1}$). Alternatively a metal with an atomic number one or two below the metal used to produce the x-rays can be used to eliminate any unwanted wavelengths. Due to the reduced nuclear charge of the filter, the transition between energy levels require slightly less energy than the metal used to produce the x-rays, the K adsorption edge lies between K_α and K_β. The filter will strongly adsorb the higher energy wavelength K_β leaving only K_α.

The reflected x-ray can be considered as a sine wave repeating periodically. The intensity of the reflected x-ray (*I*) is proportional to the amplitude (A) squared. If two sine waves are not aligned they have a phase shift ($\delta\Psi$) with respect to one another. When more than one point is affect by the same incident x-ray the overall amplitude is affected by the interference between the reflected x-rays, the intensity is now dependent on the phase shift of these waves.

$$I(\varphi) \propto \frac{sin^2 N\varphi}{sin^2 \varphi} \qquad \textbf{(2.22)}$$

2.6.2 Bragg's Law

As an x-ray source impinges an atom or ion the x-rays are scatted. The x-ray source will produce many x-rays in parallel, all of which will be scattered by the material. The scattered x-rays will interfere with other x-rays scattered by atoms or ions in close proximity. The reflected x-rays from points A and D will either be in phase (constructive interference) or out of phase (destructive interference). Bragg's law determines the geometrical conditions needed to produce constructive interference.

Figure 2.18 shows that the two point of reflection within the crystal are separated by the interplanar distance (d_{hkl}). The path length of the second wave has increased from wave one by BC + CD. For an integral wavelength path length difference BC + CD must be a whole number.

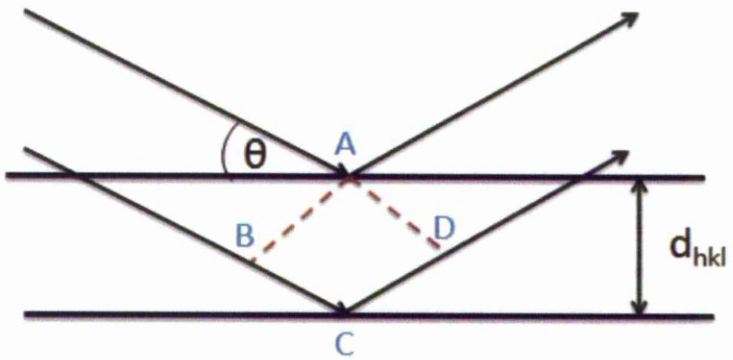

Figure 2.18 X-ray reflection at angle θ

Wherein Bragg's law is dependent on the incidence angle of the x-ray beam (θ) and the lattice spacing (d_{hkl}).

$$BC + CD = 2d_{hkl} \sin\theta = n\lambda \qquad (2.23)$$

2.6.3 Detecting the reflected X-rays

The reflected x-rays are scattered in all possible directions producing a cone of diffraction for each lattice point. In order for the data to be analysed the position of the cones needs to be determined. Powder x-ray diffractometers use either a Geiger-muller tube or a scintillation detector, whereupon the detector moves along a circumference around the sample in order to cut through the diffraction cones at different diffraction maxima. The scattered x-rays are detected and presented as a function of the detector angle, 2θ.

The scattered x-rays are detected as an electrical current which can be easily digitised and analysed by computer. Modern diffractometers use either a racemeter or a true counter detector. A racemeter detects the electrical current and produces a reading which is proportional to the flux of photons entering the detector. True counter detectors register each individual photon entering the detector window.

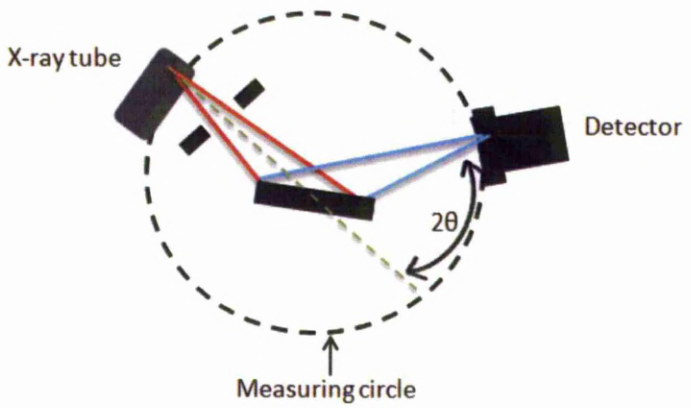

Figure 2.19 Schematic picture of a powder diffractometer

2.6.4 X-ray Diffraction of Amorphous Silica

X-ray diffraction is most commonly used to determine the crystal structure of materials. More recently it has been shown as a useful characterisation tool for certain types of amorphous silica. Normally, mesoporous materials have an irregular pore

structure; MCM-41 contains unidimensional pore channels in a regular hexagonal array.

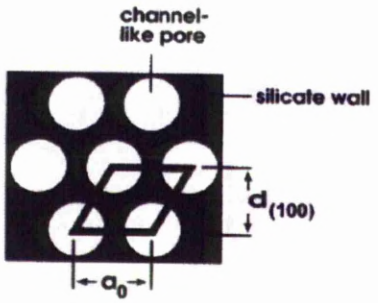

Figure 2.20 Hexagonal array of pores in MCM-41[96]

It is due to the regularity of the pores that these materials can be analysed through x-ray diffraction[96,97]. The reflection indexes arise from the regular variation in electron density as opposed to the lattice structure. As shown in Figure 2.21 the hexagonal arrangement of the pore channels gives rise to a reflection index corresponding to a hexagonal symmetry.

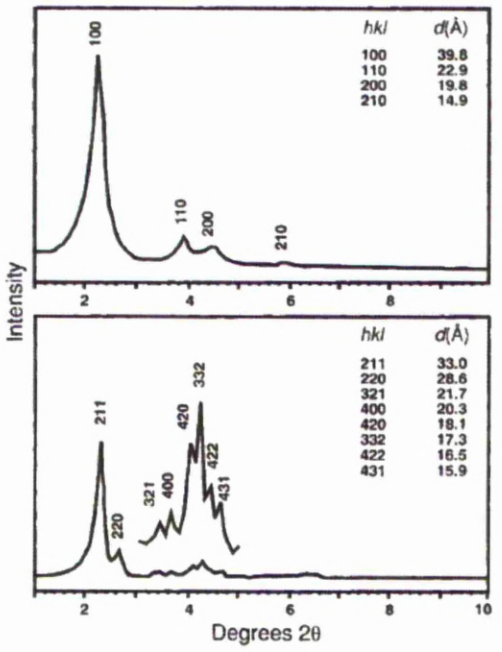

Figure 2.21 XRD reflections of MCM-41in the hexagonal (top) and cubic (bottom) phase[98]

2.7 Adsorption-desorption Isotherms

2.7.1 N_2 Adsorption-Desorption analysis

Nitrogen adsorption at 77 K (boiling temperature of N_2) can be used to determine the surface area and pore structure of materials. The fractional cover of the gas (θ) is dependent on pressure. At lower pressures monolayer coverage of the surface can be used to calculate the surface area (A_s) of the sample. As pressure is further increased the gas condenses in the pores. The volume of condensed gas (V_m) can be used to analyse the pore texture. Measuring the volume of gas adsorbed (V_m) with varying pressures at a chosen temperature is called an adsorption isotherm.

$$\theta = \frac{\textit{Number of adsorption sites occupied}}{\textit{Number of adsorption sites available}} \qquad (2.24)$$

2.7.2 Types of Pores

The shape of the adsorption isotherm is dependent on the shape and size of the pores. Pores can either be regular or irregular in shape. Pore shape is often described using the most similar geometrical shape, which falls into three main categories: cylinders, slits or voids (space occurring between spherical solids).

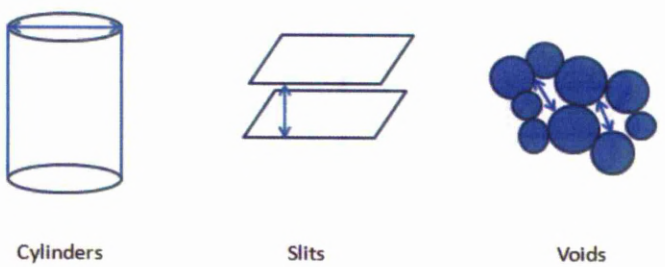

Figure 2.22 Common pore shapes

The models used to analyse the adsorption-desorption data all assume a uniform size along the pores but commonly they are either ink bottle shaped (pore body larger than the pore mouth) or funnel shaped (pore mouth larger that the pore body).

2.7.3 Adsorption-Desorption Isotherms

The adsorption-desorption isotherms are classified according to the six IUPAC types, of which the four shown below are the most common [99].

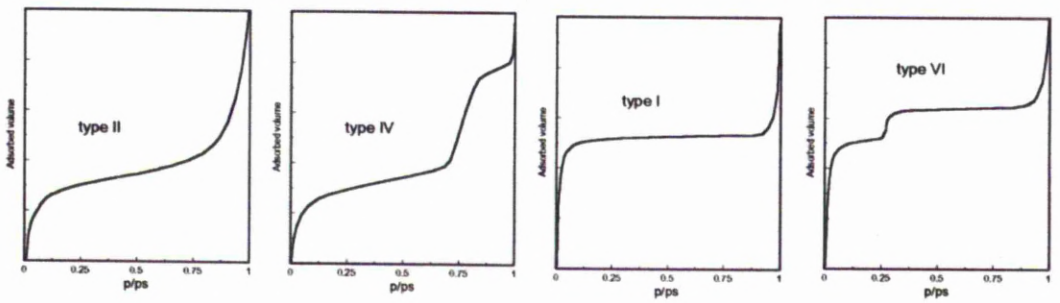

Figure 2.23 Most common N_2 isotherms

Type I isotherms are observed for a microporous solid (pore size <2nm). The adsorption occurs at relatively low pressure ($p/p^0 < 0.3$) and increases as limiting value of p/p^0 approaches one. The limiting value is due to the accessibility of the micropores. *Type II* isotherms are characteristic of non-porous or macroporous solids (pore size >50 nm) wherein the isotherm shows unrestricted monolayer adsorption. *Type IV* isotherms are attributed to mesoporous solids (2 nm < pore size < 50 nm). The initial part of the isotherm is a consequence of the monolayer coverage of the sample. A characteristic feature of type IV isotherms is the hysteresis observed which is associated with the process of capillary condensation occurring in the pores at higher p/p^0 values. A *Type VI* isotherm is obtained through stepwise multi-layer adsorption on a uniform non-porous solid, whereby the sharpness of the steps observed are dependent of the temperature of the system.

2.7.4 Hysteresis

Hysteresis loops, which are observed for mesoporous solids, appear in the multilayer region of isotherms and are associated with capillary condensation. The shape of the hysteresis loops can be used to provide information about the pore structure [100].

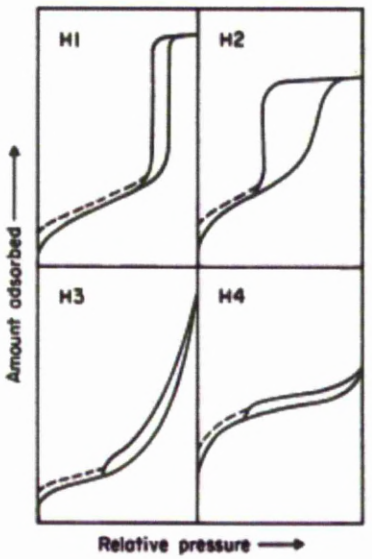

Figure 2.24 Types of hysteresis loops

H1 and H2 hysteresis loops are produced by near cylindrical pores or channels made from agglomerated or aggregated particles. Materials which produce H1 hysteresis loops contain pores of a more uniform size and shape whereas materials which produce H2 hysteresis loops contain a much wider pore size distribution. Hysteresis loops 3 and 4 are produces by materials containing slit type pores. H4 type hysteresis loops are representative of material with uniform porosity whereas material with pores of non-uniform size and shape will produce a H3 hysteresis loop.

2.7.5 Calculating the Surface area of Porous Materials

2.7.5.1 Langmuir Isotherms

There are several models used to calculate the surface area of porous materials, of which the Langmuir isotherm is the simplest. This model is based on three assumptions:

1) adsorption cannot proceed beyond a monolayer coverage
2) all sites are equivalent and the surface is uniform (the adsorption site is flat on a microscopic scale)
3) the ability of a molecule to adsorb at a specific site is independent of the occupation of neighbouring sites.

As discussed above the adsorption of nitrogen molecules on to the surface of mesoporous solids proceeds beyond a monolayer coverage and so this model is not often used for the characterisation of such solids.

2.7.5.2 Kelvin Equation

Most calculations for mesoporous solids are based on the Kelvin equation (Equation 2.25). As the partial pressure of the system increases the pore space is filled with condensed N_2 vapour. Once the pore is filled a meniscus is formed at the liquid-vapour interface. The Kelvin equation can be used to relate the liquid/ vapour equilibrium to pore volume.

$$ln\frac{P_V}{P_{Sat}} = -\frac{2H\gamma V_l}{RT} \qquad (2.25)$$

The ratio of the vapour pressure (P_v) and saturation pressure (P_{Sat}) is related to the mean curvature of the meniscus (H), the liquid/vapour surface tension (γ), the liquid molar volume (V_l), the ideal gas constant (R) and the temperature of the system (T).

2.7.5.3 BET Method

The BET model was developed by Brunauer, Emmet and Teller in the 1940s to calculate the surface area and pore size of porous solids.[101] This model is based on the assumptions that:

1) the heat of adsorption of the first monolayer is constant (i.e the adsorption surface is flat)
2) the interaction between neighbouring adsorbed molecules is negligible

3) the adsorbed monolayer can act as a new adsorption surface
4) the heat of adsorption of all the monolayers (excluding the first monolayer) is equal to the heat of condensation.

The monolayer volume of pores (V_m) and surface area (A_S) of these solids can be calculated using the equation below:

$$A_S = \left(\frac{V_m}{22414}\right) N_a \sigma \tag{2.26}$$

where N_a corresponds to avagadro's number and σ is the area covered by one N_2 molecule (generally accepted as 0.162 nm). V_m can be estimated using the three parameter BET equation (Equation 2.27).

$$V_{ads} = V_m \frac{c\, p/p_s}{1-p/p_s} \frac{1-(n+1)(p/p_s)^n+n(p/p_s)^{n+1}}{1+(c-1)(p/p_s)-c(p/p_s)^{n+1}} \tag{2.27}$$

Wherein the adsorbed volume (V_{ads}) is dependent on the relative pressure (p/p_s), the parameter c is related to the heat of adsorption and liquification (where upon high values indicate strong adsorbate-adsorbent interactions) and the parameter n is related to the mean number of layers adsorbed. If $n \rightarrow \infty$ the equation can be further simplified to give:

$$V_{ads} = V_m \frac{cp/p_s}{(1-p/p_s)(1+(c-1)p/p_s)} \tag{2.28}$$

though this equation is only suitable for macroporous or large mesoporous material where $n > 6$.

2.7.5.4 BJH Model

The model developed by Barrer, Joiyner and Halenda is based in the capillary condensation region ($p/p_s > 0.4$) and is used to explain the caplillary-condensation process.[102,103] The model states an increase in the partial pressure creates an increase in the thickness of the adsorbed layer and the condensation in a pore with a core radius of r_c.

$$\ln\left(\frac{p}{p_s}\right) = -(2\gamma W_m \cos\theta)/RTr_c \quad (2.29)$$

The radius of a cylindrical pore or the distance between two sheets for slit pores (r_c) can be calculated from the surface tension (γ), the molar volume (W_m) and the contact angle (θ) of the nitrogen molecules. As the model assumes either cylindrical or silt geometry for pores it is possible to calculate the pore volume form the core volume and the pore size form the radius.

2.7.6 Mercury Porosimetry

Mercury porosimetry is used to analyse macropores which cannot be studies through vapour adsorption techniques (pore sizes 7.5 – 15000 nm). The behaviour of Hg is the opposite to that of N_2. N_2 isotherms create a monolayer coverage after which capillary condensation occurs at higher pressures whereas Hg progressively fills the finer pores as pressure increases. Hg only enters the pores when forced by pressure and a plot of Hg volume against pore size is used to analyse these materials. This model follows the Washburn equation:

$$P = (2\gamma \cos\theta)/r_p \quad (2.30)$$

Wherein the applied pressure (P) is related to the surface tension, the contact angle of Hg (θ, generally accepted to be 140^0) and the pore size (r_p).

2.8 SEM Imaging

Scanning electron microscopes use a beam of high energy electrons to generate 2-dimensional images of samples. SEM imaging can be used to provide information such as morphology, topography, chemical composition and crystalline structure [104,105].

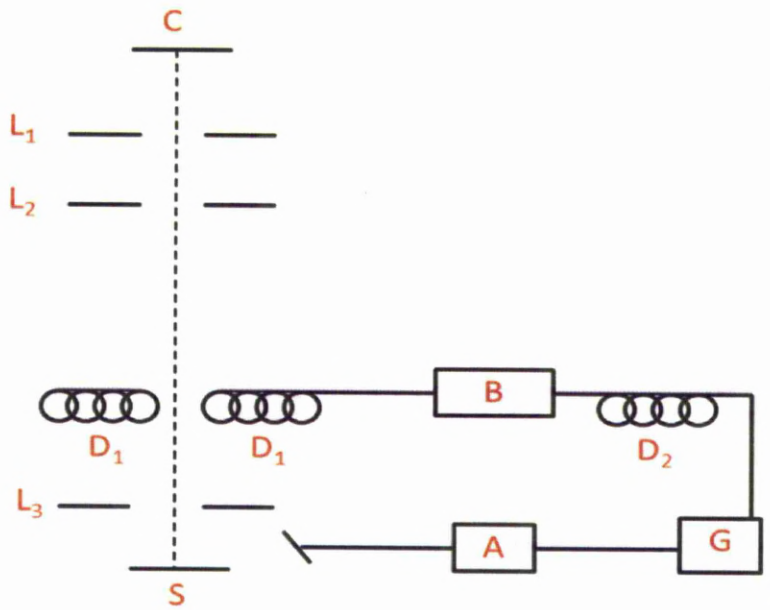

Figure 2.25 Diagrammatic representation of SEM imaging

A cathode, most commonly made of tungsten, produces a narrow stream of electrons (C). These electrons are then focused by a series of lenses (L_1, L_2 and L_3) onto the sample (S). A current from a generator (B) passes through a coil (D_1) and deflects the beam of electrons; the current also passes through a second coil (D_2) to deflect the beam of a second cathode ray. The two beams scan the sample in a raster scan pattern. The secondary and backscattered electrons produced by the sample are collected, producing a current. The current controls the potential of the grid (G) and therefore brightness at each point, creating an image of the sample.

2.9 Dynamic Light Scattering (DLS)

2.9.1 Introduction

Dynamic light scattering is used to determine particle size and particle size distribution of small beads in suspension. Brownian motion is the random movement of the suspended particles due to bombardment by the solvent molecules.[106] When light impinges on a small particle, a fraction of the right is re-directed; this is referred to as light scattering. The angle at which the light is scattered and the intensity of the scattered light is dependent on the size, shape orientation and composition of the particle.[107] The scattered light is dependent on the position of the particle, the rate at which the particle moves. Since large molecules have a slower Brownian motion compared to smaller particles, the velocity of the Brownian motion (D) can be used to determine the radius of the particles:

$$d(H) = \frac{KT}{3\pi\eta D} \qquad (2.31)$$

wherein d(H) is the diameter of the particle, K is the Boltzman constant, T the temperature and η is the viscosity of the solution.

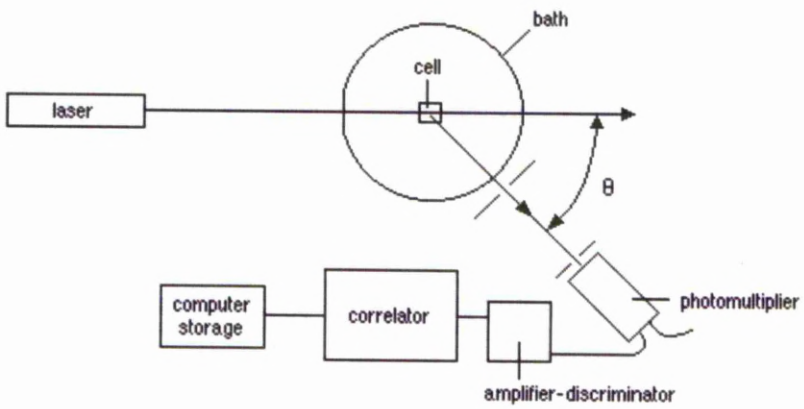

Figure 2.26 Schematic representation of a dynamic light scattering instrument

There are two main models used for light scattering, the Rayleigh model and the Mie model.[108]

2.9.2 The Rayleigh Model

The model produced by Lord Rayleigh (1881) is used for particle which are small in relation to the wavelength of the laser (d = λ/10). For small particle the scattering of light is isotropic. This theory assumes that the entire particle responds instantaneously to the change in electric field (i.e. the velocity of light does not decrease once it has come into contact with the particle. The Rayleigh equation:

$$I \propto d^6 \tag{2.32}$$

Shows how the intensity of the scattered light (I) varies with the diameter of the particle (d). In accordance with this equation a particle with a diameter of 50 nm will scatter a million times more light compared to a 5 nm particle.

2.9.3 Mie Model

This method is commonly used for particles with diameters which are large in relation to the wavelength, though this model can be used for particles with diameters from $0 \rightarrow \infty$.

2.10 Elemental Analysis

Elemental analysis is a technique which can be used to determine qualitatively and quantitatively the composition of an unknown sample. The amount of carbon, hydrogen and nitrogen within the sample is determined through combustion of the sample. Full combustion is guaranteed by providing a plentiful supply of oxygen; creating carbon dioxide (CO_2), water (H_2O) and nitric oxide (NO). The mass of the combustion products is then used to create an imperial formula for the unknown sample [109].

Chapter 3: Experimental Conditions

3. Experimental Section

Synthetic Conditions

3.1 Materials

With the exception of TEOS; all materials were used as received without any further purification: 1,2-bis(triethoxysilyl)ethane (BTSE, Gelest), benzyltriethoxysilane (BTES, Gelest), bis(triethoxysilyl)ethylene (BTSEY), phenyltrimethoxysilane (PTMS), Pluornic 123 ($HO(CH_2CH_2O)_{20}(CH_2CH(CH_3)O)_{70}(CH_2CH_2O)_{20}$, Aldrich), cetyltrimethylammonium bromide (CTAB, Aldrich), ethanol (Aldrich), hydrochloric acid (Aldrich), 1.7 μm Syncronis column (C_{18} functionalised, Thermo Scientific), Spherisorb ODS2 column (C_{18} functionalised, Waters), Hypersil GOLD (C_{18} functionailised 150 x 4.6mm, 5μm, ThermoScientific), Hypersil GOLD Phenyl ($-C_6H_5$ functionalised 150 x 4.6mm, 5μm, ThermoScientific), magnesium metal, anhydrous, non-denatured ethanol, mercury chloride, tetraethylorthosilicate (TEOS), poly(diallyldimethylammonium chloride) (PDDA), poly(styrene sulfonate) (PSS), sodium hydroxide (NaOH)

3.2 Synthesis of Bi-functionalised PMOs – used to synthesise the PMOs in Chapter 4

3.2.1 Synthesis of $-CH_2CH_2-$/ $-CH_2C_6H_5$ (BTSE/BTES) functionalised PMOs

In a typical synthesis of $-CH_2CH_2-$/$-CH_2C_6H_5$ PMO, P123 (0.36 g) and CTAB (0.06 g) were dissolved in DDI water (21.0 mL), ethanol (3.0 mL) and 2M HCl (3.96 mL) whilst stirring under room temperature. When the surfactant had dissolved BTSE (0.371 mL) and BTES (0.064 mL) were added to the solution. The solution was stirred for 30 minutes at room temperature and then transferred to an oven and heated at 100°C for 16 hours. The white precipitate which formed was then filtered, washed with deionised water and dried at 60°C. The final composition of the synthesis mixture was P123 (0.0495): H_2O (1068.5): EtOH (41): HCl (5.26): BTSE (0.80): BTES (0.20): CTAB (0.131). The synthesis was also repeated with ratios of BTSE : BTES of 0.90 : 0.10, 0.95 : 0.05 and 1 : 0. P123 was removed from the PMO by stirring 0.4 g of the material in 100 mL 1M HCl/ EtOH overnight at 50°C. The product was then washed thoroughly with EtOH and dried at room temperature.

The synthetic procedure for $-CH_2CH_2-$/ $-CH_2C_6H_5$ 80/ 20 PMO was optimised by varying HCl 1.5 – 0.05 M to improve the ordering of the material.

3.2.2 Synthesis of –CH=CH-/ $-CH_2C_6H_5$ (BTSEY/BTES) functionalised PMOs

In a typical synthesis of $-CH_2CH_2-$/$-CH_2C_6H_5$ PMO, P123 (0.36 g) and CTAB (0.06 g) were dissolved in DDI water (21.0 mL), ethanol (3.0 mL) and 2M HCl (3.96 mL) whilst stirring under room temperature. When the surfactant had dissolved BTSEY (0.369 mL) and BTES (0.064 mL) were added to the solution. The solution was stirred for 30 minutes at room temperature and then transferred to an oven and heated at 100°C for 16 hours. The white precipitate which formed was then filtered, washed with deionised water at dried at 60°C. The final composition of the synthesis mixture was P123 (0.0495): H_2O (1068.5): EtOH (41): HCl (5.26): BTSEY (0.80): BTES (0.20): CTAB (0.131). The synthesis was also repeated with ratios of BTSEY : BTES of 0.90 : 0.10, 0.95 : 0.05 and 1 : 0. P123 was removed from the PMO by stirring 0.4 g of the material in 100 mL 1M HCl/ EtOH overnight at 50°C. The product was then washed thoroughly with EtOH and dried at room temperature.

The synthetic procedure for –CH=CH-/ $-CH_2C_6H_5$ 80/ 20 PMO was optimised by varying HCl 1.0 – 0.031 M to improve the ordering of the material.

3.2.3 Synthesis of $-CH_2CH_2-$/ $-C_6H_5$ (BTSE/PTMS) functionalised PMOs

In a typical synthesis of $-CH_2CH_2-$/$-C_6H_5$ PMO, P123 (0.36 g) and CTAB (0.06 g) were dissolved in DDI water (21.0 mL), ethanol (3.0 mL) and 2M HCl (3.96 mL) whilst stirring under room temperature. When the surfactant had dissolved BTSE (0.253 mL) and PTMS (0.047 mL) were added to the solution. The solution was stirred for 30 minutes at room temperature and then transferred to an oven and heated at 100°C for 16 hours. The white precipitate which formed was then filtered, washed with deionised water and dried at 60°C. The final composition of the synthesis mixture was P123 (0.0495): H_2O (1068.5): EtOH (41): HCl (5.26): BTSE (0.80): PTMS (0.20): CTAB (0.31). The synthesis was also repeated with ratios of BTES : PTMS of 0.90 : 0.10, 0.95 : 0.05 and 1 : 0. P123 was removed from the PMO by stirring 0.4 g of the material in 100 mL

1M HCl/ EtOH overnight at 50°C. The product was then washed thoroughly with EtOH and dried at room temperature.

The synthetic procedure for $-CH_2CH_2-$/ $-C_6H_5$ 80/ 20 PMO was optimised by varying HCl 0.5 – 0.008 M to improve the ordering of the material.

3.3 Calculation of Surface Coating of Toluene for Reversed-Phase columns – used in Chapter 5.

The stationary phases were loaded with toluene in order to study the interaction between the analyte and stationary phase. In order to guarantee a surface coating the toluene was added in slight excess of the surface area of each silica. To calculate the amount of toluene needed we have taken the surface area of toluene to be 25.18 Å. From this we can determine the volume of toluene need for 1.5 times the surface area.

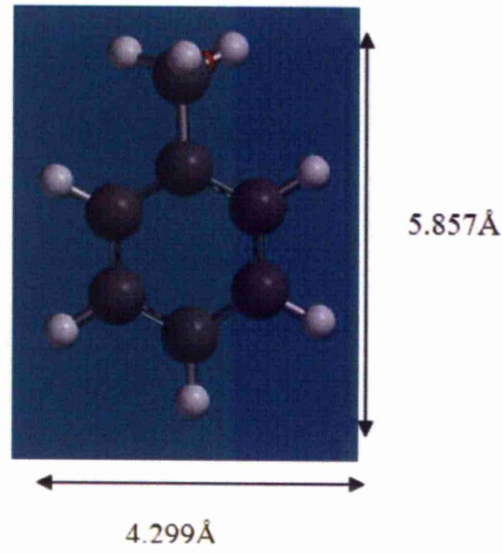

Figure 3.1 Approximate size of Toluene

Table 3.1 Calculation of toluene loading for the reversed-phase silica

Sample	Surface area (m^2/g)	Volume of toluene (ml/g)
1.7 µm Syncronis	238.2	0.250
Spherisorb ODS2	110.0	0.116
$-CH_2CH_2-$/ $-CH_2C_6H_5$ PMO	782.8	0.825

3.4 - Synthesis of Sphere-in-Sphere (SIS) Silica – used in Chapter 6

3.4.1 Distillation of TEOS

In a typical synthesis magnesium metal (0.0165 g) and anhydrous, non-denatured ethanol (0.106 mL) were mixed in a round bottom flask. A trace amount of $HgCl_2$ was added to the mixture. When the metal was reacting vigorously, TEOS (50 mL) was added with a slow stream of N_2 bubbled through the solution. The product was then collected at a temperature of 166 - 167°C.

3.4.2 Synthesis of 16 nm Silica Particles Used in the Synthesis of SIS Silica Beads

In a typical synthesis DDI water (13.3 mL), methanol (101.04 mL) and ammonium hydroxide (28%) solution (0.91 mL) were mixed at 40°C to form the hydrolysis solution. To this solution TEOS (4.47 mL) was added and the solution was stirred for 5 minutes before being left overnight at room temperature.

3.4.3 Synthesis of SIS silica

In a typical synthesis the pH of PDDA and PSS were altered to pH10 using NaOH. The large pore silica beads used were Biggles silica manufactured through a property spray drying route developed by Peter Myers at the University of Liverpool. The large pore silica beads were first immersed in the PDDA solution for 15 minutes, followed by PSS and finally PDDA again. After each coating of polyelectrolyte the material was washed with DDI water. The final silica product was then immersed in the solution of 16 nm silica particles (4.5 mg mL^{-1} in methanol) for 15 minutes. The final silica product was washed with DDI water. The polyelectrolytes were removed by calcining the silica at 330°C for 8 hours.

3.5 Characterisation Conditions

3.5.1 Powder X-ray Diffraction

The powder XRD patterns were recorded using a Panalytical X-pert pro which uses a Co-$K_{\alpha 1}$ with a wavelength λ = 1.789 Å. Using a bracket and a sample stage the samples were recorded with an anti-scatter slit of 5.5 mm and ½, a divergence slit of ¼ and a 10 mm mask. The patterns were recorded in Bragg-Brentano reflection geometry between 0.7 – 5.0 2θ.

3.5.2 Nitrogen Adsorption-Desorption Isotherms

The surface area and pore size distribution was measured using a Micromeretics ASAP 2420 adsorption analyzer. The samples were degassed for 10 hours at 110°C before analysis using BET and BJH at 77.3 K. The surface areas were calculated from the linear part of the BET plot (p/p_0 = 0.05 – 0.15). Pore volume was calculated by the amount of N_2 adsorbed at p/p_0 = 0.98 and pore size distribution calculated using the adsorption branch of the Barrett-Joyner-Halenda (BJH) method.

3.5.3 Dynamic Light Scattering

The Dynamic Light Scattering (DLS) experiments were carried out in ethanol using a Visoteck 802 DLS spectrometer using a 50mW fibre coupled diode laser with a wavelength λ = 830 nm.

3.5.4 Scanning Electron Microscopy

The images were produced using a Hitachi – S4800 Scanning Electron Microscope (SEM). The samples were transferred onto the studs using an ethanol suspension. Prior to analysis the samples were then coated with gold using a EMITECH K550X sputter coater for 3 minutes at 35 mA.

3.5.5 HPLC Separation

All separations were performed using a Thermo Accela U-HPLC system using a UV diode array detector set at 250 nm. Unless otherwise stated separations were conducted using a water (A)/ methanol (B) mobile phase at a flow rate of 1 mL/ min and a column over temperature of 30°C.

3.5.5.1 PAH test

The PAH analysis was performed using a mobile phase gradient of:

Time (Minutes)	%B
0	35
22	35
27	45
45	85
45.01	35
55	35

The test mixture was composed of acenaphthene (1 mg/mL, 50 µL of test mixture), acenaphthylene (1 mg/mL, 100 µL test mixture), anthracene (1 mg/mL, 1 µL test mixture), benzo(a)anthracene (0.1 mg/mL, 100 µL test mixture), benzo(k)fluoranthene (1 mg/mL, 50 µL test mixture), fluorene (1 mg/mL, 5 µL test mixture), fluoranthene (1 mg/mL, 10 µL test mixture), indeno(1,2,3-cd)pyrene (1 mg/mL, 50 µL test mixture), napthalene (1 mg/mL, 10 µL test mixture) and methanol (300 µL).

3.5.5.2 Tanaka Test

The retention capacity, hydrophobicity and steric selectivity were measured using a 10 µl injection of a test mix composed of uracil (as a non-retained marker), butlybenzene (0.2 mg/mL), o-terphenyl (0.05 mg/mL), pentylbenzene (0.2 mg/mL) and triphenylene (0.01 mg/mL).

The silanol capacity was measured using a 10 µl injection volume of the test mixture composed of uracil (as a non-retained marker), caffeine (0.5 mg/mL) and phenol (0.5 mg/mL). The separation was conducted using a H_2O/ MeOH (70/20) at a flow rate of 1.0 mL/min.

The Ion exchange capacity of the columns were analysed using a 10 µL injection of the test mixture composed of uracil (as a non-retained marker), benzylamine (0.5 mg/mL) and phenol (0.5 mg/mL). A mobile phase of 20mM potassium phosphate buffer (pH 2.7)/ MeOH 70/30 and 20mM potassium phosphate buffer (pH 7.6)/ MeOH 70/30 was used at a flow rate of 0.6 mL/min.

3.5.6 Solid-State NMR

All solid-state NMR experiments were measured at 9.4 T using a Bruker DSX-400 spectrometer using a 4 mm 1H/X/Y commercial probehead operating at 79.49, 100.61 and 400.13 MHz to analyse ^{29}Si, ^{13}C and ^{1}H respectively. All chemical shifts are quoted in ppm and referenced to TMS.

3.5.6.1 One dimensional NMR

All one dimensional NMR experiments used a simple pulse-acquire sequence and were recorded using magic angle spinning (MAS) to improve resolution.

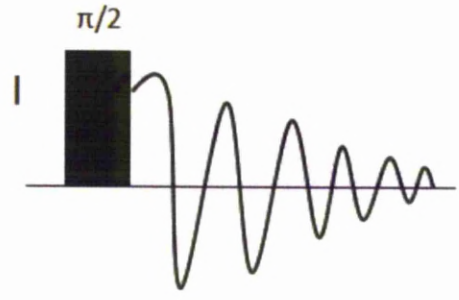

Figure 3.2 1-D NMR pulse sequence

^{1}H MAS NMR spectra were acquired using a ^{1}H π/2 pulse length of 3.40 μs at an MAS rate of 10 kHz using a delay of 8.0 seconds.

^{13}C{^{1}H} MAS NMR spectra were acquired using a ^{13}C π/3 pulse length of 2.60 μs at an MAS rate of 10 kHz using a delay of 20.0 seconds.

^{29}Si{^{1}H} MAS NMR spectra were acquired using a ^{29}Si π/3 pulse length of 3.00 μs at an MAS rate of 4 kHz using a delay of 240.0 seconds.

3.5.6.2 Cross Polarisation NMR

All CP/MAS NMR experiments were conducted using ramped contact pulse and two pulse phase modulation (TPPM) heteronuclear dipolar decoupling with 15° phase difference applied during acquisition.

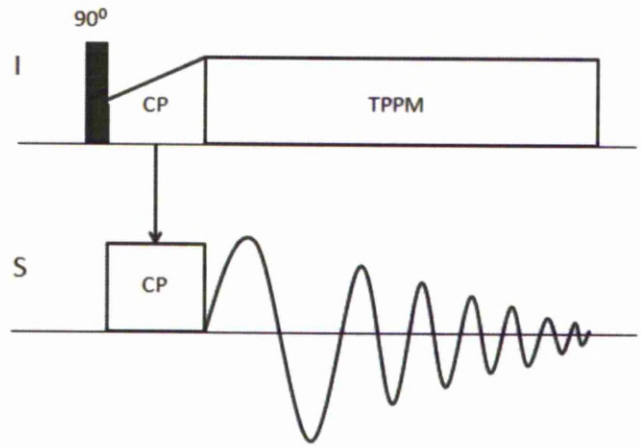

Figure 3.3 Cross-Polarisation pulse sequence

^{1}H-^{13}C CP/MAS NMR spectra were acquired using a ^{1}H π/2 pulse length of 3.40 μs and a contact time of 1.00 ms at an MAS rate of 8.0 kHz using a delay of 6.00 seconds. After the addition of toluene to the HPLC columns (Chapter 5) the contact time was increased to 3.00 ms due to the high mobility of the solvent. Variable contact time (VCT) ^{1}H-^{13}C CP/MAS NMR spectra were recorded using contact times between 0.01 – 12 ms.

^{1}H-^{29}Si CP/MAS NMR spectra were acquired using a ^{1}H $\pi/2$ pulse length of 3.00 μs and a contact time of 2.00 ms at an MAS rate of 4.0 kHz using a delay of 10.0 seconds.

3.5.6.3 Two Dimensional ^{1}H-^{29}Si Heteronuclear Correlation (HETCOR) NMR

2D ^{1}H-^{29}Si HETCOR NMR spectra were collected using a similar pulse programme to CP NMR though with an additional evolution period in which FSLG Homonuclear decoupling is applied.

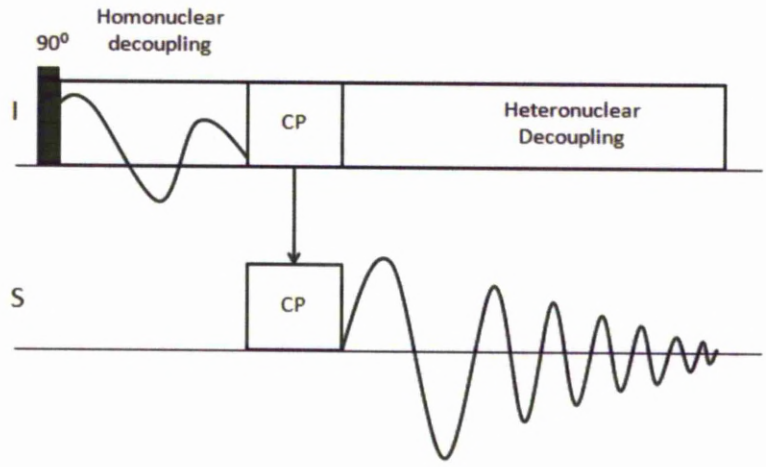

Figure 3.4 ^{1}H-X HETCOR NMR pulse sequence

The ^{1}H-^{29}Si HETCOR NMR spectra were acquired at an MAS rate of 10 kHz using FSLG decoupling with a ^{1}H r.f. field of 76.9 kHz. A contact pulse of 2.00 ms was used after which the TPPM Heteronuclear decoupling was applied during acquisition using a ^{1}H r.f. field of 76.9 kHz. The spectra were collected using 592 scans with 256 increments recorded in t_1 using a spectral width of 23047.920 MHz corresponding to a dwell time of 12.525 μs.

3.5.6.4. ^{1}H-^{13}C Wideline Spectroscopy (WISE) NMR

The ^{1}H-^{13}C Wideline Spectroscopy (WISE) NMR pulse sequence is again similar to CP NMR though with an additional time (t_1) before the transfer of magnetisation for the evolution of the magnetisation.

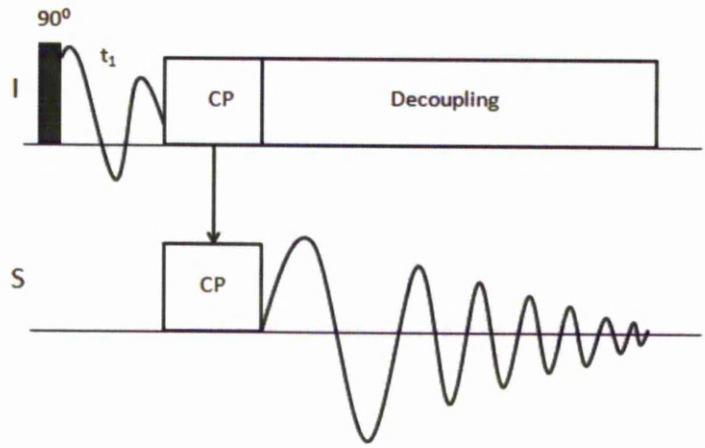

Figure 3.5 ^{1}H-^{13}C WISE NMR pulse program

The ^{1}H-^{13}C WISE NMR spectra were acquired at an MAS rate of 8 kHz. A ^{1}H $\pi/2$ pulse length of 3.40 µs was used. A short contact pulse of 1.00 ms was used to ensure magnetisation is only transferred to directly bonded nuclei. After which the TPPM Heteronuclear decoupling was applied during acquisition using a ^{1}H r.f. field of 73.5 kHz. The spectra were collected using 632 scans with 256 increments recorded in t_1 using a spectral width of 39920.160 MHz corresponding to a dwell time of 12.525 µs.

3.5.6.5 ^{1}H-^{1}H Nuclear Overhauser Effect Specroscopy (NOESY)

^{1}H-^{1}H NOESY NMR pulse sequence consists of three 90° pulses separated by a fixed delay (τ_m) during which magnetisation is transferred through dipolar interactions. As the strength of the dipolar interactions are dependent of distance ($1/r^3$) magnetisation is only transferred between nuclei close in space (10 Å).

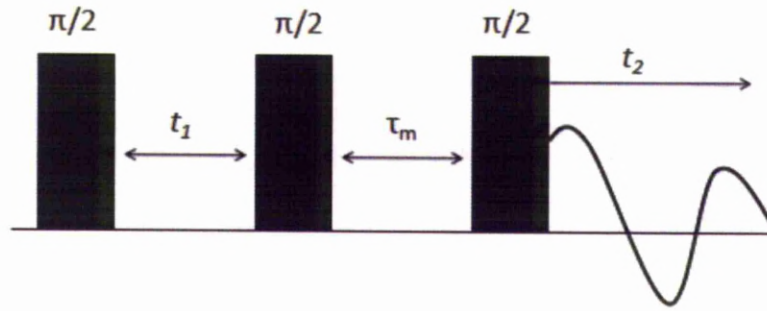

Figure 3.6 ^{1}H-^{1}H NOESY NMR pulse program

^{1}H-^{1}H NOESY NMR spectra were acquired at an MAS rate of 10 kHz. A ^{1}H π/2 pulse length of 3.40 μs and a delay of 2.00 seconds were used. The mixing time (τ_m) was varied between 5 -550 ms to gain a full picture of the molecular structure. 512 increments were used to cover the whole ^{1}H spectral width of 998.040 MHz which corresponds to a dwell time of 50.1 μs.

Chapter 4:

Synthesis of Bi-Functionalised Mesoporous Organosilicas For Use as New Chromatographic Stationary Phases

4. Synthesis of Bi-Functionalised Mesoporous Organosilicas For Use as New Chromatographic Stationary Phases

4.1 Introduction

Silica is the most commonly used stationary phase in chromatography. This preference is due mainly to its highly favorable properties, which include mechanical resistance to high pressures, rapid mass transfer during separations and facile surface functionalisation of the surface silanol groups.[110,111] The performance and development of chromatographic columns have been the subject of extensive research over the past forty years. Improved efficiency has been achieved by reducing the size of the silica beads to improve packing [112], increasing monodispersity of the beads [113,114] and increasing pore sizes.[115-117] Recent advances include new chiral stationary phases for enantiomeric separations.[118-121] A variety of functional groups can be incorporated and the column can be tailored to the analytes being separated. The most common functional groups incorporated are; C_8, C_{18}, phenyl moieties [122-125,110], amino containing functionalities (such as C_3H_6-NH_2, C_3H_6-NH-C_2H_4-NH-C_2H_4-NH_2)[126,127] and polymer chains (using monomers such as styrene, 2-hydroxyethyl methacrylate and methyl methacrylate).[128,113]

The presence of functional groups can increase the mechanical and thermal stability of the silica and improve the separation of non-polar compounds. For porous silica beads the incorporation of organic groups, often through grafting, reduces the pore size of the material. An alternative approach, first reported by Inagaki *et al.*[129,54] utilised a "one-pot" method. In this method organic functional groups are incorporated into the inorganic framework *via* the condensation of organosilanes containing bridging functional groups $(R'O)_3$-Si-R-Si-$(OR')_3$. Functionalised silicas produced through the one pot method are referred to as periodic mesoporous organosilicas (PMOs).

The synthesis procedure used here was optimised to create silica beads which produce an optimum performance for HPLC columns. Spherical morphology and a uniform size distribution have been shown to create a more condensed packing of the stationary phase, improving column performance.[130,131] There has been an emphasis on reducing the size of the silica particles to the sub-micron range as this will further improve the packing of the material and give a higher surface area for the column, though these columns often show a large pressure drop (Equation 4.1).[38,3]

$$\Delta P = \frac{\eta L v}{\theta d_p^2} \qquad (4.1)$$

The pressure drop (ΔP) is dependent on solvent viscosity (η), column length (L), flow velocity (v) and particle diameter (d_p), θ is a dimensionless constant. Alternatively, large surface areas can be produced through using porous silica. Higher surface areas improve the retention of the individual compounds, giving a better separation, though this is only applicable if the surface is accessible.[132] By using a large surfactant, such as a block copolymer pulronic, the pore diameters of the silica are increased improving the accessibility for the analytes compared to those produce using smaller surfactants such as cetyltrimethyl ammonium bromide (CTAB). Larger pore sizes also improve the mass transfer rates of the compounds being separated, producing narrower peaks and improving the separation of the different analytes.

There has been in depth research into the control of morphology, surface area and the porosity of silica and hybrid silicas but little research dedicated to understanding these materials on a molecular level.[133,134,117] Herein, we report the synthesis of three different periodic mesoporous organosilicas (PMOs) containing -CH_2CH_2-/ -$CH_2C_6H_5$, -CH=CH-/ -$CH_2C_6H_5$ and -CH_2CH_2-/ -C_6H_5 bridging and tether groups. Using solid-state NMR we have been able to analyse the organosilanes on a molecular level and the results used to determine their applicability for reversed-phase chromatography. The –CH_2CH_2-/ -$CH_2C_6H_5$ PMO was chosen to be packed into a column due to the high surface area and spherical morphology observed. Also this material showed a homogeneous distribution of the two functionalities which predominantly reside at the pore surface. The efficiency and selectivity of the column was then compared to

commercially available RP columns (Hypersil GOLD and Hypersil GOLD phenyl) using the PAH and Tanaka tests.

4.2 Results and discussion

4.2.1 Analysis of Mesoscopic ordering

The silica precursors used contained different functional groups and therefore have different hydrolysis/condensation rates. Initially, we investigated the effect of using multiple silica sources on the mesoscopic ordering by varying the precursor ratios. The synthetic parameters for the PMO's containing the highest tether loading were then acid optimised to improve mesoscopic ordering. These samples were chosen as they have the highest carbon loading, improving the selectivity of a reversed-phase HPLC column. By varying the acid concentration the effect of the acid catalyst (HCl) on the formation of surfactant micelles and the hydrolysis of silica precursors were investigated.

Periodic mesoporous organosilicas can be synthesised using either the alkaline (using methods similar to stöber process) or acidic synthetic routes.[49] The formation of silicates through the alkaline synthesis is governed by strong electrostatic interactions between the silicate and surfactant (S^+I^-), the kinetics of which have been well researched.[135,136] Due to these interactions the mesostructure of the silicate can be controlled through the choice of template.[137,138] The acidic route, which uses a counter ion ($S^+X^-I^+$) contains much weaker silicate/ surfactant interactions, as the precursor and surfactant are not directly interacting, this synthetic pathway is more influenced by the synthetic conditions. The different rates of silica co-condensation compared to the rate of surfactant self-assembly produces various morphological and topological constructions.[139] Synthetic parameters such as acid concentration[16,33], anion concentration[33], co-solvent [140], synthetic temperature [27,135,134], SiO_2: surfactant ratio[135,134] and even stirring[136] have been shown to affect the morphology and ordering of the silica. Templating using non-ionionic surfactants such as Pluoronic

123 is dependent on hydrogen bonding between the surfactant and silica precursor, and so are strongly influenced by the acid concentration. As pH varies the micellular structure changes. Below the optimum [H^+] non-uniform rod shaped micelles are formed, at optimum H^+ the micelles have rod like morphology. Upon futher increase of the acid concentration the micelles can form discoids and spherical shapes.

Research by Vercaemst *et al.*[141] has shown that catalyst concentration affects the surface area and pore volume of the organosilica produced. The conditions used must allow both the optimum interaction between the silica precursors and surfactant and also give similar rates of hydrolysis/condensation for the individual silica precursors. At the optimum conditions the co-condensation of the silica precursors creates a uniform coverage around the surfactant micelles, producing an ordered mesostructure. At low catalyst concentrations the surface area and pore volume decrease due to insufficient hydrogen bonding (H^+) between the non-ionic surfactant (X^0) and the silica precursor ($X^0H^+X^-$). Increasing the acidity beyond the optimum concentration can also create excessive polycondensation of the silica precursor producing low ordered material and can also create a pore blocking effect. As the acidic synthetic route uses anions to create an intercolliodal interaction between the positive charge of the organosilane and the hydrophilic (PEO) groups of the non-ionic surfactant the assembly of the mesoporous silica is also dependent on the concentration of the counter ion. Increasing the concentration promotes strong silicate/ surfactant interactions producing ordered silica, though further increasing the anion concentration reduces electrostatic repulsion between the silica particles causing aggregation.[142] For our research we aim to optimise acid concentration to create ordered bi-functionalised silica with spherical morphology. For this the acid must be optimised for the formation of rod shaped micelles and the hydrolysis rate of both precursors creating comparable SBUs to condense around the surfactant. The effects are monitored using XRD, N_2 adsorption/ desorption isotherms and SEM imaging.

4.2.1.1 Analysis of Mesoscopic Ordering Using X-ray Diffraction (XRD)

Research by Martin *et al.* has shown that increasing the ordering of the silica can improve the efficiency of the column by comparing the retention coefficient of MCM-41 to silica gels. The uniform pore structure creates homogeneous molecular diffusion of the solute throughout the column allowing faster separations without reducing column efficiency.[133] It is also worthy to note that long range ordering is uncommon in this type of material as increasing mesoscopic ordering of silica causes a reduction in the thickness of the pore walls (0.8-1.2 nm) decreasing their mechanical strength.[143]

The $-CH_2CH_2-$ functionalised PMO displays a broad reflection (d_{100} = 89.0 Å) which indicates a low level of mesoscopic ordering. The d_{100} value decreases with the introduction of the $-CH_2C_6H_5$ tether group (d_{100} = 80.5 Å at the highest loading of $-CH_2C_6H_5$ tether). The degree of mesoscopic ordering is reduced with increasing content of $-CH_2C_6H_5$ which is shown by the broader low angle reflection.

Replacing the $-CH_2CH_2-$ functionalised precursor with the -CH=CH- precursor leads to a decrease ordering as shown in Figure 4.1. The XRD reflections are at a lower angle (d_{100} = 75.4 and 73.9 Å) and are much broader compared to the $-CH_2CH_2-/-CH_2C_6H_5$ functionalised PMOs. The narrowing of the (100) reflections with increasing of the content of $-CH_2C_6H_5$ precursor indicates a slight increase in mesoscopic ordering. N_2 adsorption/ desorption isotherms indicate the narrowest pore size distribution to corresponds to the –CH=CH- /$-CH_2C_6H_5$ (90/10) PMO.

The $-CH_2CH_2-/-C_6H_5$ PMOs also display broad d_{100} reflections suggesting a low level of mesoscopic ordering. In contrast to the $-CH_2CH_2-$/ $-CH_2C_6H_5$ PMOs, the reflection for the $-CH_2CH_2-/-C_6H_5$ PMOs slightly increases and becomes narrower with increasing levels of $-C_6H_5$ functionalised silica precursor.

The XRD patterns show that in most cases the addition of a second precursor decreases the mesoscopic ordering of the material (although a slight increase has been observed

for low levels of a second silica precursor). This may be due to the different hydrolysis rates of the two silica precursors creating different sized SBUs. The XRD patterns show that the overall level of ordering decrease for the PMOs $-CH_2CH_2-$/ $-CH_2C_6H_5$ > -CH=CH- / $-CH_2C_6H_5$ > $-CH_2CH_2-$/ $-C_6H_5$. This may be due to a reduced level of condensation of the silica precursors, as evident from the ^{1}H-^{29}Si CP/MAS NMR.

The hydrolysis and condensation of alkoysilanes has been widely investigated, research has shown factors such as reaction medium, H_2O/ Si ratio, concentration of silica precursor, catalysts, time and temperature all effect the size, connectivity and morphology of the silica produced.[144,145] The incorporation of organic groups into the silane precursors creates a shift in the distribution of electrons throughout the molecule. This creates a $^{\delta-}C$-$^{\delta+}Si$ bond due to the lower electronegativity of the silicon atom compared to carbon.[146] The partial charge of the silicon atom makes it more susceptible to nucleophilic attack by water molecules (hydrolysis). The reactivity of the organosilane is therefore dependent on the organic group incorporated. In this synthesis we use four different organic moieties, $-CH_2CH_2-$, -CH=CH-, $-CH_2C_6H_5$ and $-C_6H_5$. The aromatic ring directly bonded to silicon ($-C_6H_5$) has a much stronger inductive effect compared to the benzyl tether. This increases the positive charge on silicon making it more prone to nucleophilic attack.[147,146] Therefore the rate of hydrolysis of the silicon atom bonded to $-C_6H_5$ is much faster compared to the $-CH_2C_6H_5$ functionalised precursor. Similarly the double bond of the –CH=CH- bridging group is more electron withdrawing compared to $-CH_2CH_2-$. It follows that the silicon atom of the –CH=CH- functionalised silica precursor has a more positive charge and therefore hydrolyses at a faster rate.

The methylene group of the $-CH_2C_6H_5$ moiety drastically decreases the electronegativity of the functionality. It is based on these facts that I would suggest that the rate of hydrolysis for the organosilanes precursors used are as follows – CH_2CH_2-< $-CH_2C_6H_5$< -CH=CH-< $-C_6H_5$.

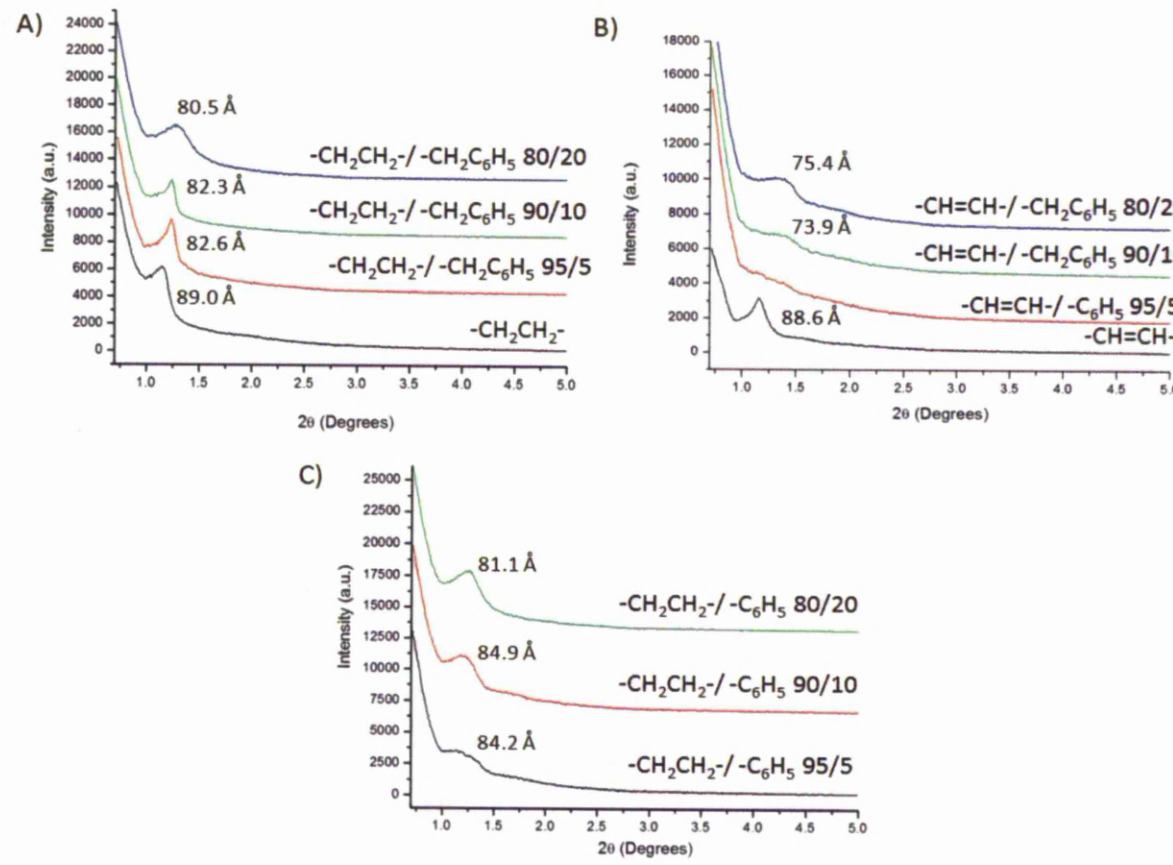

Fig.4.1 Powder XRD patterns of bi-functionalised silica hybrids a) $-CH_2CH_2-/-CH_2C_6H_5$ b) $-CH=CH-/-CH_2C_6H_5$ and c) $-CH_2CH_2-/-C_6H_5$

As these bi-functionalised silicas are intended for chromatographic purposes the ordering of the products must be improved. We have used acid optimisation to find the optimum synthesis composition for each silica.

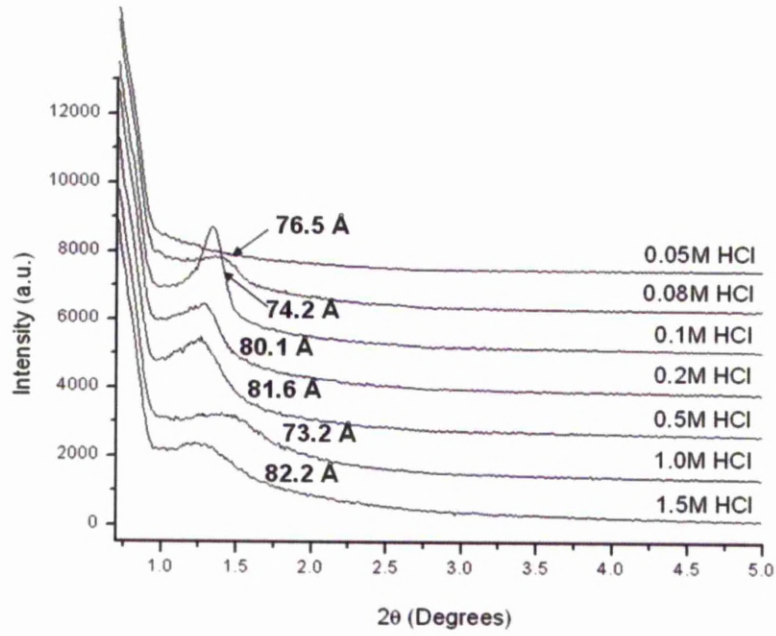

Figure 4.2 XRD patterns of acid optimisation for the synthesis of 80/ 20 – CH_2CH_2-/ -$CH_2C_6H_5$ functionalised PMO

The mesoscopic ordering of the –CH_2CH_2-/ -$CH_2C_6H_5$ (80/20) functionalised PMO can be improved through optimising the acid content of the synthesis mixtures. As the acid content of the synthesis solution increases from 0.05 to 0.1M HCl the pore mesostructure of the –CH_2CH_2/ -$CH_2C_6H_5$ PMO becomes more ordered which is shown by an increase in intensity of the (100) peak and the peak becoming narrower (Figure 4.2). Further increasing the acid concentrations of the solution subsequently decreases the mesoscopic ordering of the PMO.

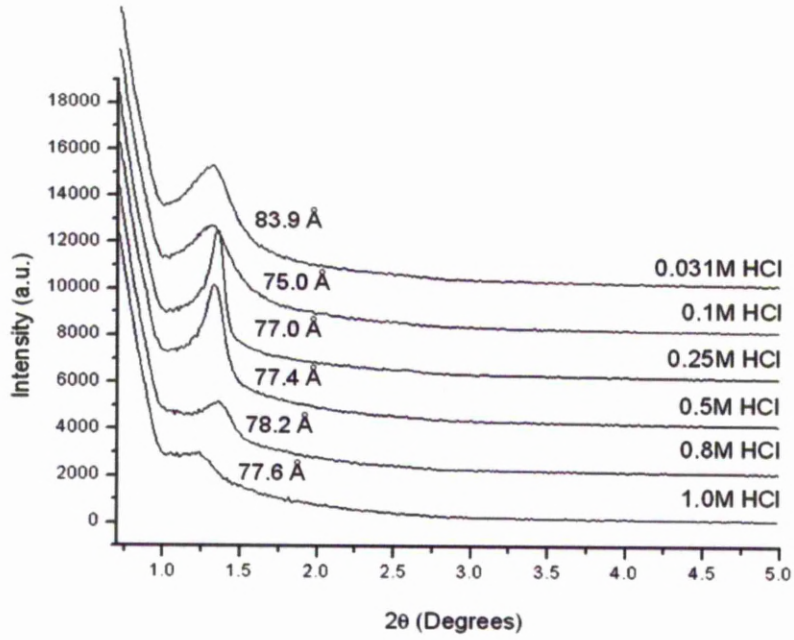

Figure 4.3 XRD patterns of 80/20 –CH=CH-/ -$CH_2C_6H_5$ functionalised PMO obtained at different acid contents

The acid optimisation of the -CH=CH-/ -$CH_2C_6H_5$ PMO follows the same trend as the previous PMO though the optimum synthesis is at a slightly higher acid concentration (0.25M HCl). As the PMOs differ only by the organic functionality incorporated in the silica precursors, the optimum acid concentration must be related to these moieties incorporated (-CH_2CH_2- or –CH=CH-) altering the hydrolysis rate.

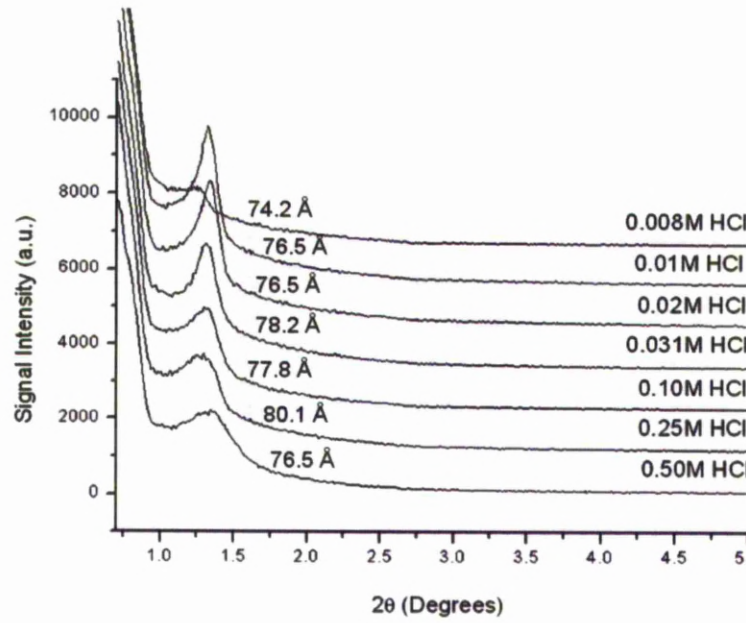

Figure 4.4 XRD patterns of 80/ 20 $-CH_2CH_2-$/ $-C_6H_5$ functionalised PMO obtained at different acid contents

The optimum acid content for the $-CH_2CH_2-$/$-C_6H_6$ functionalised PMO is much lower (0.01M HCl), compared to the $-CH_2CH_2-$/$-CH_2C_6H_5$ functionalised PMO suggesting the $-C_6H_5$ functionality increases the hydrolysis rate of the precursor.

It is worthy to note that the synthesis conditions for the silica with the highest level of ordering are different for each PMO, which has been confirmed through N_2 adsorption/ desorption analysis. The different functional groups affects the hydrolysis rate of the individual precursors.

4.2.1.2 Analysis of Textural Properties Using N_2 Adsorption- Desorption Isotherms

The N_2 adsorption/desorption isotherms of $-CH_2CH_2-$/$-CH_2C_6H_5$ PMOs can be described as a type IV with a H2 hysteresis loop. This indicates that the PMOs contains mesopores of non-uniform ink bottle shape.[50,148] The variation of pore size

distribution can be seen in Figure 4.6. The -CH_2CH_2- PMO has the highest level of mesoscopic ordering, which is confirmed by the sharper capillary condensation step. The capillary condensation step is still relatively broad which suggests a wide range of pore size distributions. The functionalised PMOs have high surface areas (between 750 and 1000 m^2/g) and large pore diameters (4.4–5.3 nm). Silica with higher loading levels of the tether functionality still produce a type IV isotherm indicating that at increased levels of the second organosilane silica precursor some mesoscopic ordering remains.

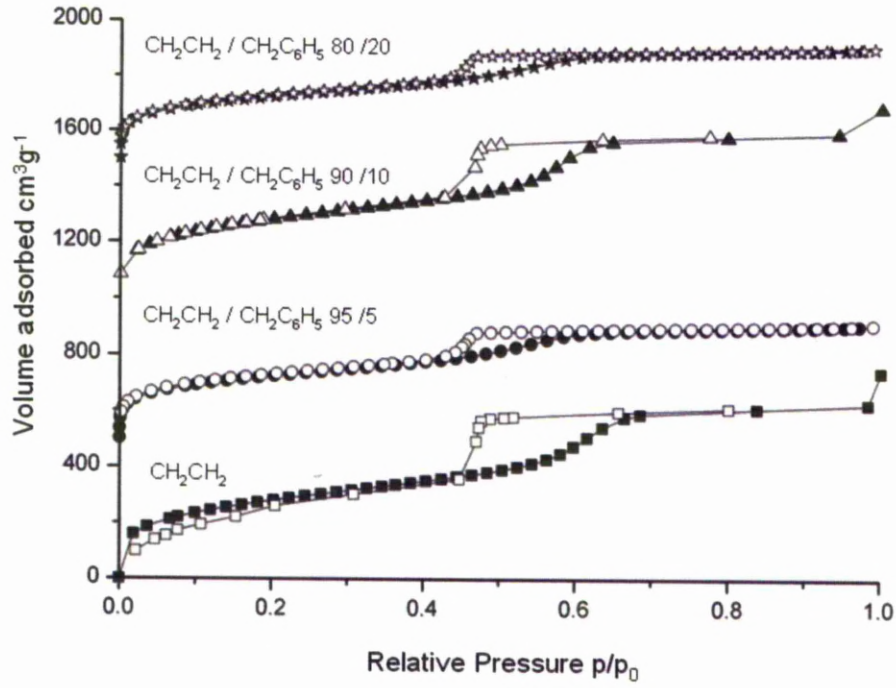

Figure 4.5 N_2 adsorption-desorption isotherms of surfactant extracted -CH_2CH_2-/-$CH_2C_6H_5$ PMOs (the isotherms above are offset by 500 cm^3g^{-1}) wherein the adsorption branch is represented by the filled markers and the desorption branch the empty markers

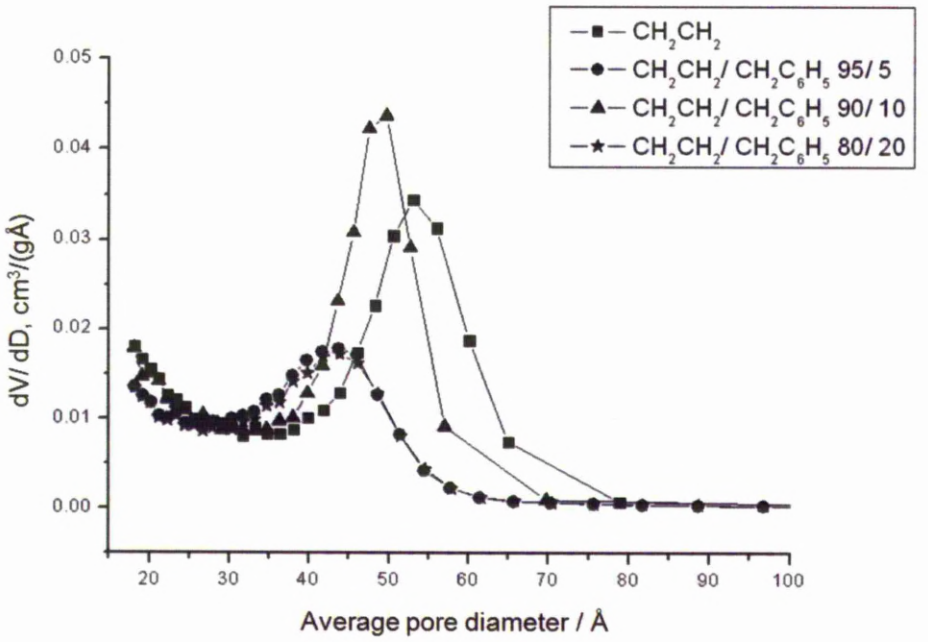

Figure 4.6 Pore size distribution plots calculated from the adsorption branch of the N_2 isotherms

Table 4.1 Mesoscopic properties of surfactant extracted -CH_2CH_2-/-$CH_2C_6H_5$ PMOs

-CH_2CH_2- / -$CH_2C_6H_5$	S_{BET}, (m^2/g)	D_{AV}^{ads} (nm)	V_{ads} (cm^3g^{-1})	a, Å	W, Å
-CH_2CH_2-	990.9	5.3	0.950	103	50
95 : 5	807.4	4.4	0.543	95	51
90 : 10	988.5	5.0	0.835	95	45
80 : 20	765.1	4.4	0.498	93	49

Unit cell parameter *a* determined from *d*100 values using $a = 2d_{100}/\sqrt{3}$ and the wall thickness (W) is determined by $W = a - D_{AV}^{ads}$.

The adsorption/desorption isotherms for the -CH=CH-/-$CH_2C_6H_5$ PMOs can also be described as a type IV with a H2 hysteresis loop. The -CH=CH- PMOs exhibit broader pore-size distributions compared to their ethane counterparts. This is consistent with the low ordering of the material as shown by the PXRD patterns.

The pore volumes of the PMOs decrease with the addition of the benzyl tether suggesting that the moiety is projecting into the pore. The products with the highest loading level of the $-CH_2C_6H_5$ functionality show a type IV isotherm though the hysteresis loop is very small which suggests a much smaller pore size due to pore blocking by the benzyl ring or, more likely, due to poorly ordered material.

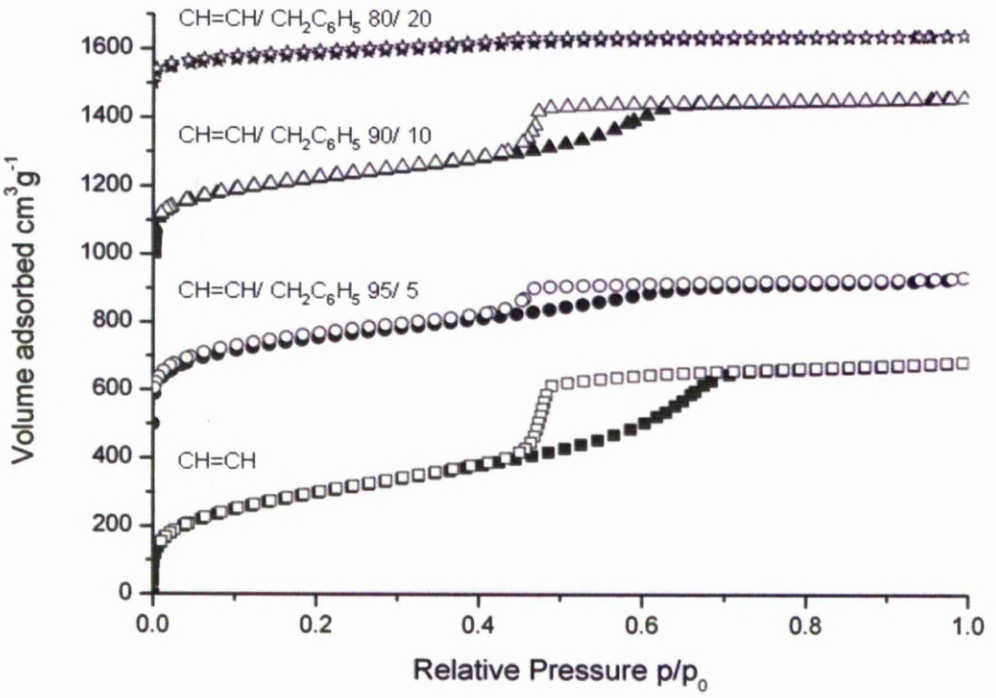

Figure 4.7 N_2 adsorption-desorption isotherms of surfactant extracted -CH=CH-/ $-CH_2C_6H_5$ PMOs (the isotherms above are offset by 500 cm^3g^{-1})

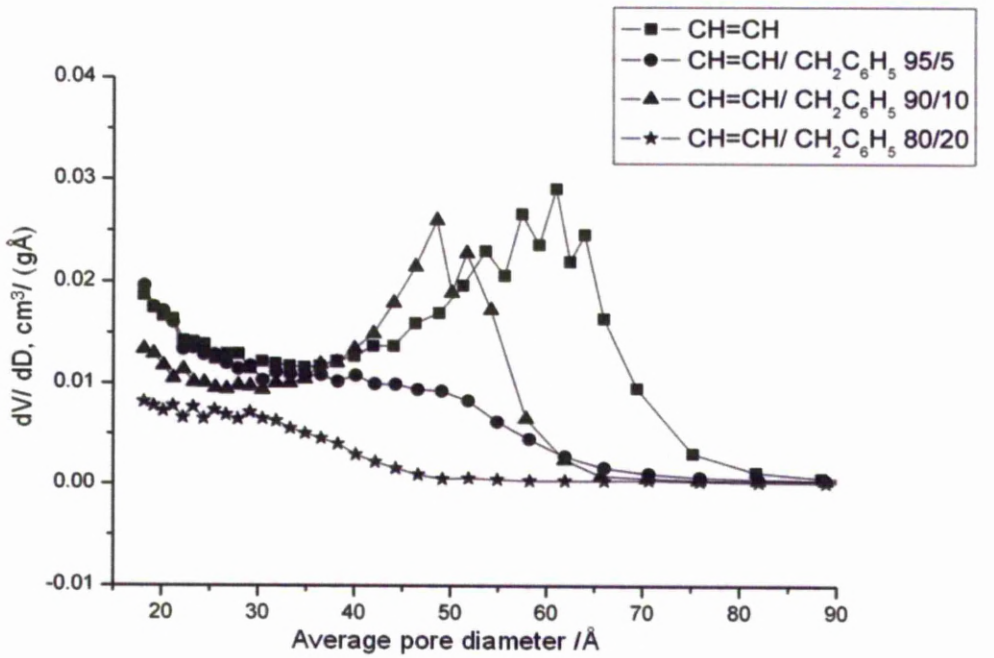

Figure 4.8 Pore size distribution plots calculated from the adsorption branch of the N_2 isotherms

Table 4.2 Mesoscopic properties of surfactant extracted -CH=CH-/ -$CH_2C_6H_5$ PMOs

-CH=CH-/ -$CH_2C_6H_5$	S_{BET} (m^2/g)	D_{AV}^{ads} (nm)	V_{ads} (cm^3g^{-1})	a, Å	W, Å
-CH=CH-	1058	6.1	0.963	102	41
95 : 5	878	5.5	0.660	-	-
90 : 10	764	4.9	0.625	85	36
80 : 20	305	1.8	0.214	87	69

Unit cell parameter a determined from $d100$ values using $a = 2d_{100}/\sqrt{3}$ and the wall thickness (W) is determined by $W = a - D_{AV}^{ads}$.

The adsorption/desorption isotherms for the $-CH_2CH_2-/-C_6H_5$ PMOs show an increase in the sharpness of the capillary step with increasing amounts of $-C_6H_5$ tether. The N_2 adsorption/ desorption data are consistent with the PXRD results which also suggest the PMO's become more ordered with increasing content of the tether functionality.

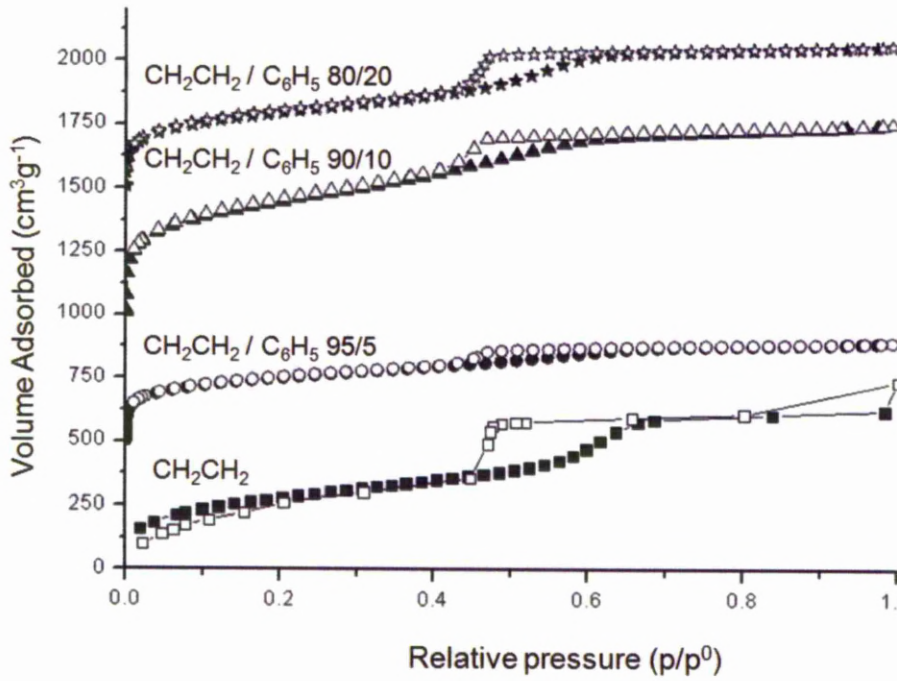

Figure 4.9 N_2 adsorption-desorption isotherms of surfactant extracted $-CH_2CH_2-/-C_6H_5$ PMOs (the isotherms above are offset by 500 cm^3g^{-1})

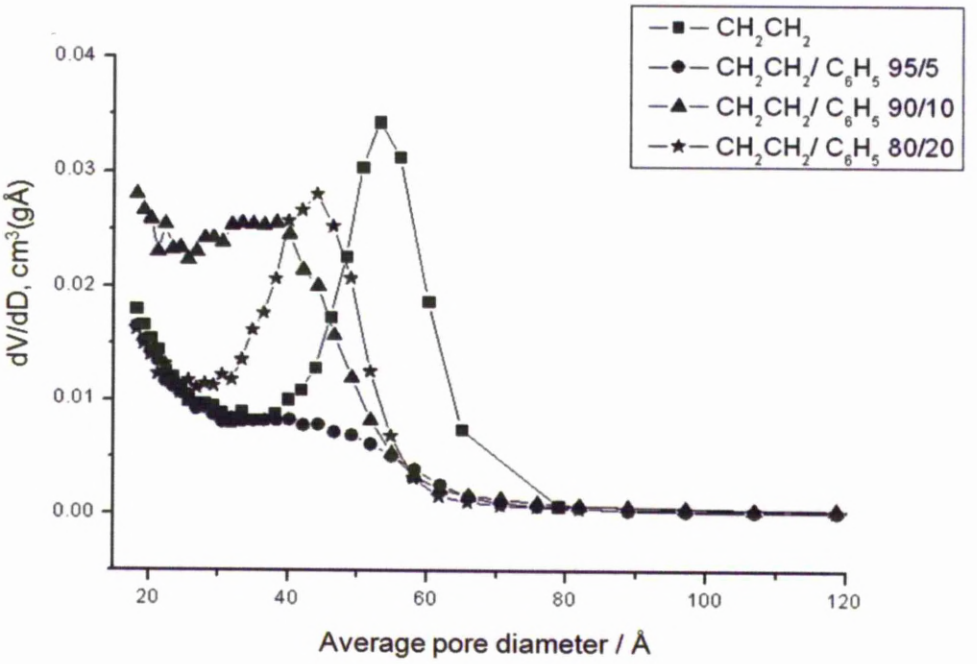

Figure 4.10 Pore size distribution plots calculated from the adsorption branch of the N_2 isotherms

Table 4.3 Mesoscopic properties of surfactant extracted -CH_2CH_2-/ -C_6H_5 PMOs

-CH_2CH_2-/ -C_6H_5	S_{BET} (m^2/g)	D_{AV}^{ads} (nm)	V_{ads} (cm^3g^{-1})	a, Å	W, Å
-CH_2CH_2-	990.9	5.3	0.950	103	50
95 : 5	844	4.0	0.414	97	57
90 : 10	1547	3.8	0.887	98	60
80 : 20	1017	4.4	0.712	94	50

Unit cell parameter *a* determined from *d*100 values using $a = 2d_{100}/\sqrt{3}$ and the wall thickness (W) is determined by $W = a - D_{AV}^{ads}$.

4.2.1.3 Analysis of Carbon Loading

As carbon content is an important factor for reversed-phase chromatography the samples containing the highest raitios of $-CH_2C_6H_5$ and $-C_6H_5$ were chosen to be optimised and further characterised.

Table 4.4 Microanalysis of 80/20 ratios of the functionalsed PMOs

Sample (80/20)	%C	%H
$-CH_2CH_2-$/ $-CH_2C_6H_5$	21.56	3.98
$-CH=CH-$/ $-CH_2C_6H_5$	20.66	3.37
$-CH_2CH_2-$/ C_6H_5	22.67	3.81

4.3 Optimisation of Synthetic Parameters Through Varying Acid Concentration

The mesophase of the micelles formed, silicate/ surfactant interactions and the hydrolysis and condensation rates (and therefore the morphology of the silica beads) are affected by the acid concentration. The template-silicate interactions are dependent on electrostatic forces, hydrophobic/ hydrophilic interactions and hydrogen bonding.[149] The functionality incorporated alters the hydrophobicity/ hydrophilicity of the organosilane precursors and therefore each precursor will have a unique rate of hydrolysis/ condensation. It is therefore evident that the optimum acid concentration for the synthesis of each PMO will differ and therefore need to be optimised individually.

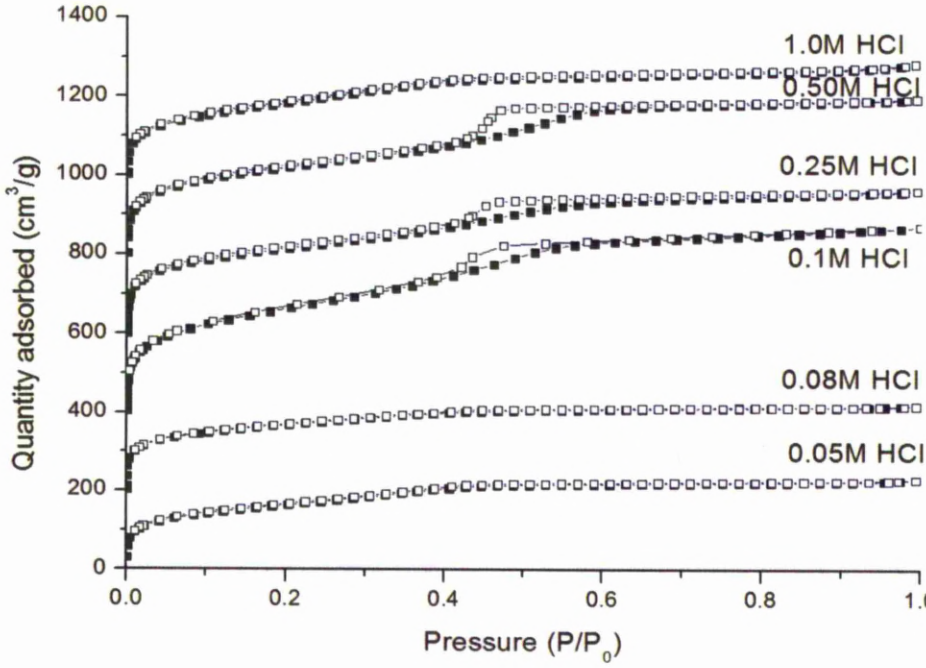

Figure 4.11 N_2 adsorption-desorption isotherms of surfactant extracted -CH_2CH_2-/-$CH_2C_6H_5$ PMOs with varying acid concentrations (the isotherms above are offset by 200 cm^3g^{-1})

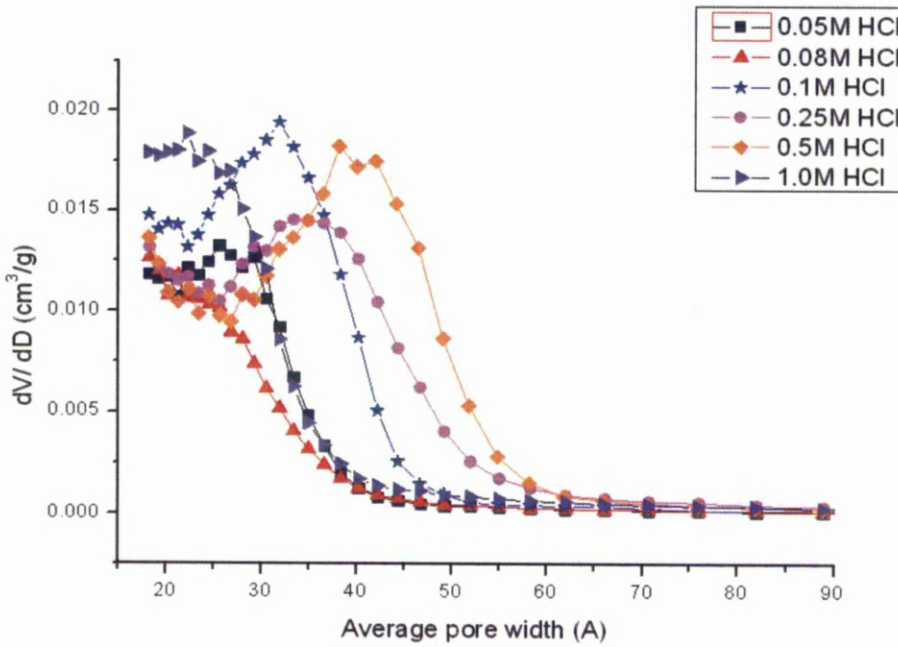

Figure 4.12 Pore size distribution plots of -CH_2CH_2-/ -$CH_2C_6H_5$ PMOs with varying acid concentrations, calculated from the adsorption branch of the N_2 isotherms

Table 4.5 Mesoscopic properties of $-CH_2CH_2-$/ $-CH_2C_6H_5$ functionalised PMO with varying acid concentrations

Concentration of HCl (M)	S_{BET}, (m^2/g)	D_{AV}^{ads} (nm)	V^{ads} (cm^3g^{-1})	a, Å	W, Å
0.05	568.1	2.6	0.234	-	-
0.08	569.3	2.1	0.189	88	67
0.1	782.8	3.2	0.407	86	64
0.25	740.1	3.3	0.432	92	59
0.5	761.9	4.0	0.497	94	56
1.0	666.0	2.1	0.339	85	63

Unit cell parameter a determined from $d100$ values using $a = 2d_{100}/\sqrt{3}$ and the wall thickness (W) is determined by $W = a - D_{AV}^{ads}$.

The XRD patterns indicate that the optimum acid concentration for the synthesis of $-CH_2CH_2-$/ $-CH_2C_6H_5$ functionalised PMO is 0.1M HCl. At these conditions the silica precursors all have similar hydrolysis rates and are able to form around the rod-shaped micelles. The level of mesoscopic ordering shown by the N_2 adsorption/ desorption isotherms of the bi-functionalised silica varies with acid concentration and coincides with the level of ordering observed in the XRD patterns. At the optimum acid concentration, 0.1M HCl, the silica synthesised has the highest surface area. Furthermore the pore size distribution of the acid optimised silicas (Figure 4.12) indicates that the pore diameter of the PMOs is also dependent on the catalyst concentration of the reaction. The pH of the solution effects the size and formation of the micelles and the rate at which the organosilane precursors condense around the micelles.

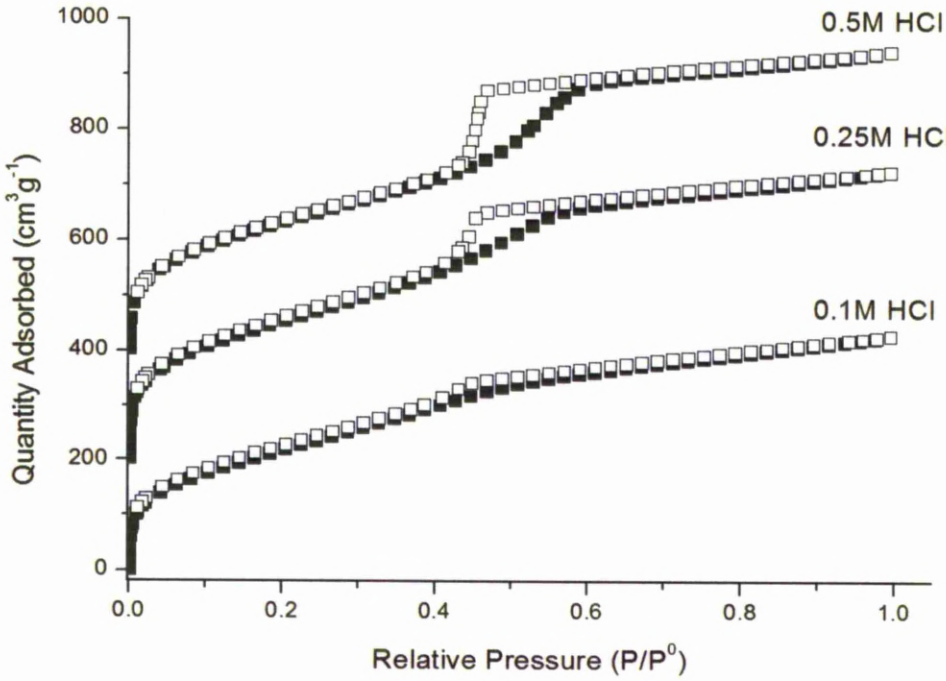

Figure 4.13 N_2 adsorption-desorption isotherms of surfactant extracted –CH=CH-/-$CH_2C_6H_5$ PMOs with varying acid concentrations (the isotherms above are offset by 200 cm^3g^{-1})

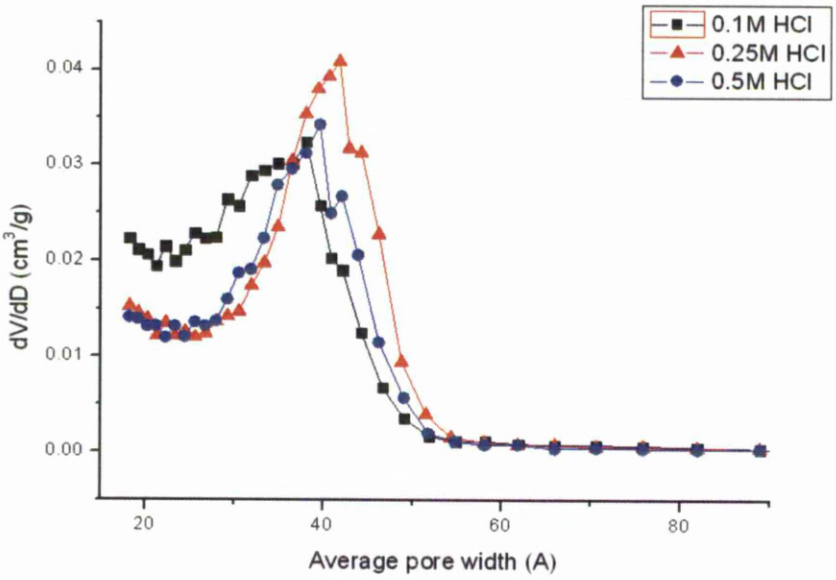

Figure 4.14 Pore size distribution plots of –CH=CH-/ -$CH_2C_6H_5$ PMOs with varying acid concentrations, calculated from the adsorption branch of the N_2 isotherms

Table 4.6 Mesoscopic properties of –CH=CH-/ -$CH_2C_6H_5$ functionalised PMO with varying acid concentrations

Concentration of HCl (M)	S_{BET}, (m^2/g)	D_{AV}^{ads} (nm)	V^{ads} (cm^3g^{-1})	a, Å	W, Å
0.1	1176	3.8	0.755	87	49
0.25	961.9	4.2	0.757	89	47
0.5	842.0	4.0	0.656	89	49

Unit cell parameter a determined from $d100$ values using $a = 2d_{100}/\sqrt{3}$ and the wall thickness (W) is determined by $W = a - D_{AV}^{ads}$.

The –CH=CH-/-$CH_2C_6H_5$ PMOs display high surface areas and large pore volumes (Table 4.6). The isotherms for the -CH=CH-/ -$CH_2C_6H_5$ PMOs are consistent with the XRD results, indicating the synthesis mixture with 0.25 M HCl produces an organosilica with the highest degree of mesoscopic ordering. This is shown by the sharpest capillary condensation step ($p/p_0 \approx 0.55$). The N_2 adsorption/desorption isotherms corresponding to the -CH=CH-/-$CH_2C_6H_5$ PMOs can all be described as type IV with an H2 type hysteresis. A type H2 hysteresis is produced by material with non-uniform cylindrical pores.

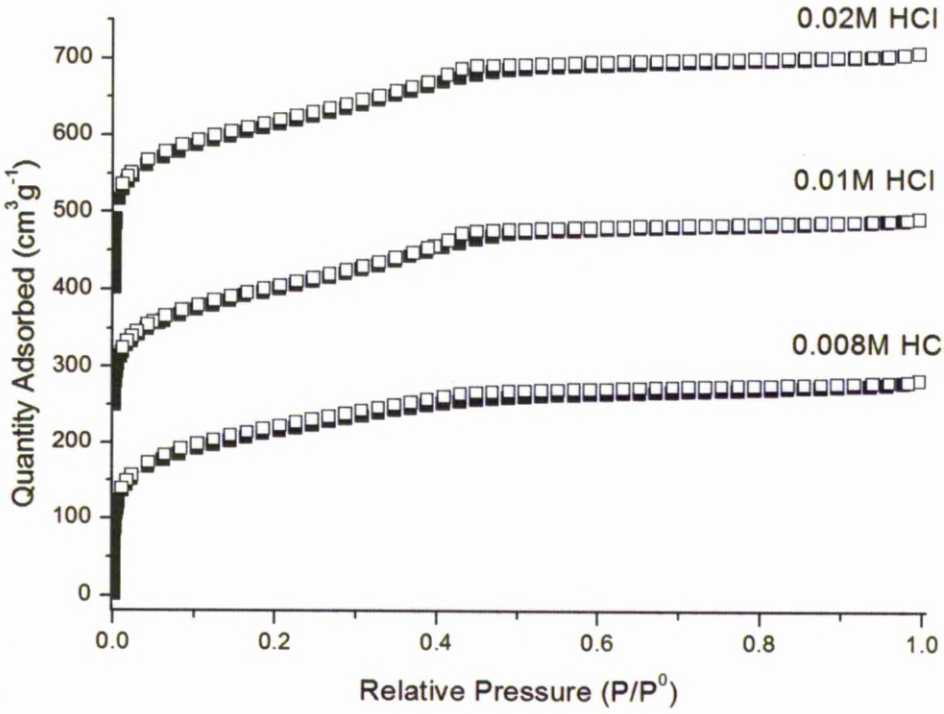

Figure 4.15 N_2 adsorption-desorption isotherms of surfactant extracted $-CH_2CH_2-$/ $-C_6H_5$ PMOs with varying acid concentrations (the isotherms above are offset by 200 cm^{3}g^{-1})

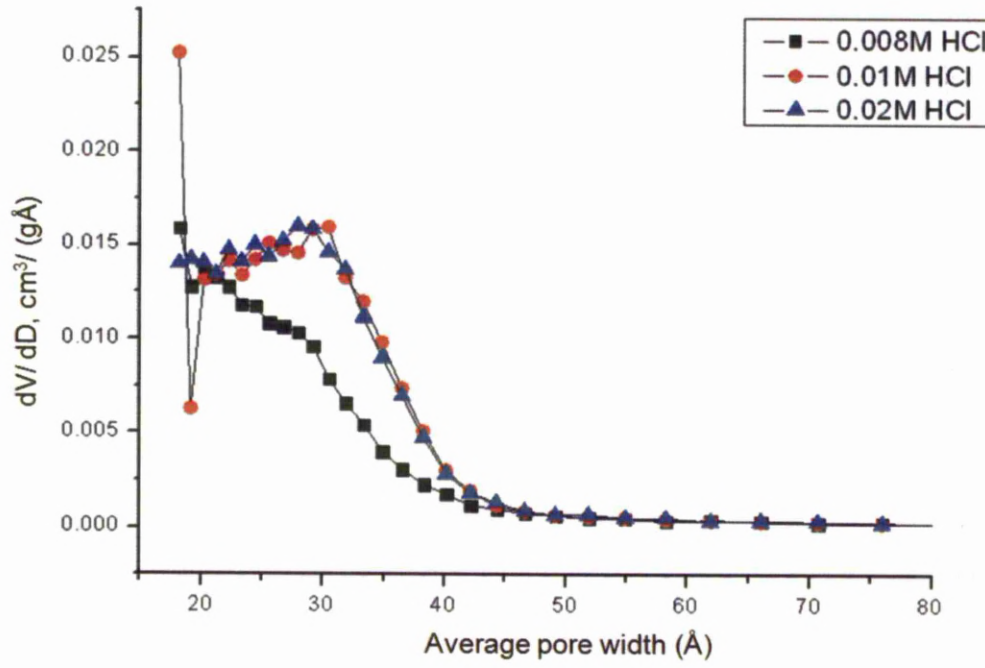

Figure 4.16 Pore size distribution plots of $-CH_2CH_2-$/ $-C_6H_5$ PMOs with varying acid concentrations, calculated from the adsorption branch of the N_2 isotherms

Table 4.7 Mesoscopic properties of $-CH_2CH_2-$/ $-C_6H_5$ functionalised PMO with varying acid concentrations

Concentration of HCl (M)	S_{BET}, (m^2/g)	D_{AV}^{ads} (nm)	V^{ads} (cm^3g^{-1})	a, Å	W, Å
0.008	721.4	2.0	0.237	86	66
0.01	699.1	3.0	0.316	88	58
0.02	740.8	2.8	0.320	88	60

Unit cell parameter a determined from $d100$ values using $a = 2d_{100}/\sqrt{3}$ and the wall thickness (W) is determined by $W = a - D_{AV}^{ads}$..

The optimum acid concentration is much lower for the $-CH_2CH_2-$/ $-C_6H_5$ (0.01M HCl) PMO, which was analysed by comparing the intensity and breadth of the (100) peak. The N_2 adsorption/desorption isotherms have a flatter capillary condensation step ($p/p_0 \approx 0.40$), which is indicative of a broad range of pore sizes. The XRD patterns for these PMOs indicate the silica synthesised using 0.01M HCl produced the highest mesoscopic ordering. Though analysis of these materials using N_2 adsorption/ desorption isotherms show that the $-CH_2CH_2-$/ $-C_6H_5$ functionalised PMOs remain at a low level of mesoscopic ordering subsequent to optimisation procedure. The disparity of the hydrolysis rates ($-CH_2CH_2-$ <- $-CH_2C_6H_5$ <- $-CH=CH-$ <- C_6H_5) for the two precursors, due to the functionalities incorporated, may be too vast to produce a PMO with short range ordering.

4.4 Morphology of the PMOs

The synthesis of mesoporous silica beads with spherical morphology is difficult to achieve due to many varying factors. To synthesise silica beads with a spherical morphology a uniform hydrolysis and condensation rate of the silica precursors on the surface of the bead is needed. The water content, alcohol content and type/ concentration of the acid catalyst will affect the hydrolysis rate and, therefore, the morphology of the silica bead.[150,151]

In this work we have used organosilane precursors with different organic groups. As discussed the type of organic group will alter the hydrophobicity of the precursor which would affect the hydrolysis rate and, therefore, the morphology of the silica beads. As each synthesis uses two different functionalised precursors it becomes more challenging to match their hydrolysis rates to create a uniform growth on the surface of the silica beads.

Another challenge of the synthesis is directing spherical beads around cylindrical micelles. Incorporating rod-shaped micelles within a spherical silica bead can hinder the production of the desired morphology. The optimal reaction conditions must be suitable both for the formation of the surfactant micelles and the required rate of hydrolysis/condensation of organosilane precursor.

The porogenic role of the surfactants is based on suitable non-covalent interactions (i.e. H-bonding and ionic interactions) of their head-groups and organosilane interphases. Again, by using several organosilane precursors, the optimisation of the template/framework interactions becomes more complicated. The addition of different organic groups within the silica precursors will lead to local variation in the strength of such interactions which could disrupt the morphology, ordering, pore size and surface area of the hybrid beads formed.

4.4.1 SEM Imaging

The SEM images of the 90/10 $-CH_2CH_2-/-CH_2C_6H_5$ PMO (Figure 4.17a) show spherical morphology indicating an optimal synthetic procedure. The comparable hydrolysis and condensation rate of the two precursors is also indicated by the narrow d_{100} peak corresponding to the 90/10 $-CH_2CH_2-/-CH_2C_6H_5$ silica (Figure 4.1a) compared to the broader resonances of the other PMOs.

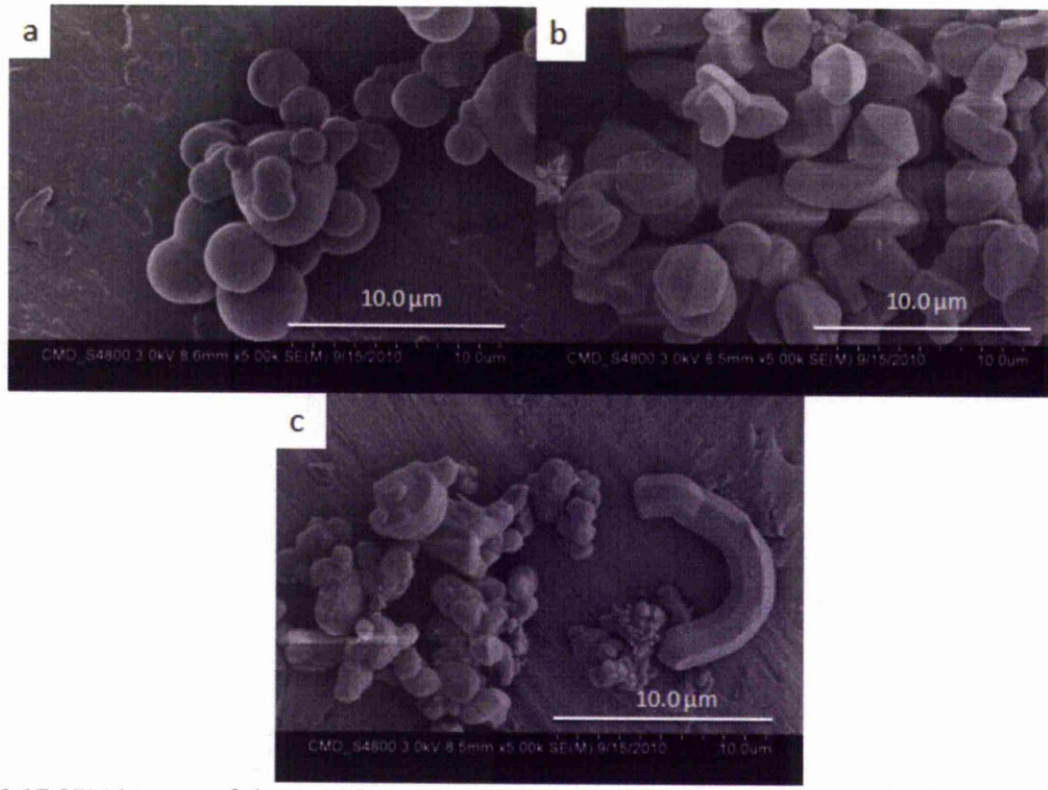

Figure 4.17 SEM images of the template extracted PMOs a) $-CH_2CH_2-/-CH_2C_6H_5$ (90/10); b) $-CH=CH-$ / $-CH_2C_6H_5$ (90/10); and c) $-CH_2CH_2-$ / $-C_6H_5$ (90/10)

The morphology of the $-CH=CH-/-CH_2C_6H_5$ PMO (Figure 4.17b) is non-spherical with a polydisperse particle size. The $-CH_2CH_2-/-C_6H_5$ products exhibit a rod-shaped morphology (Figure 4.17c). This indicates that the acid concentration is not appropriate for these reactions. Due to the irregular shapes and larger particle size distributions of the $-CH=CH-/-CH_2C_6H_5$ and $-CH_2CH_2-/-C_6H_5$ PMOs, the packing of this material into a chromatographic column would create voids in the column. These voids will allow the mobile phase to re-combine, potentially giving a poor separation.

Morphology of the Silica beads after acid optimisation

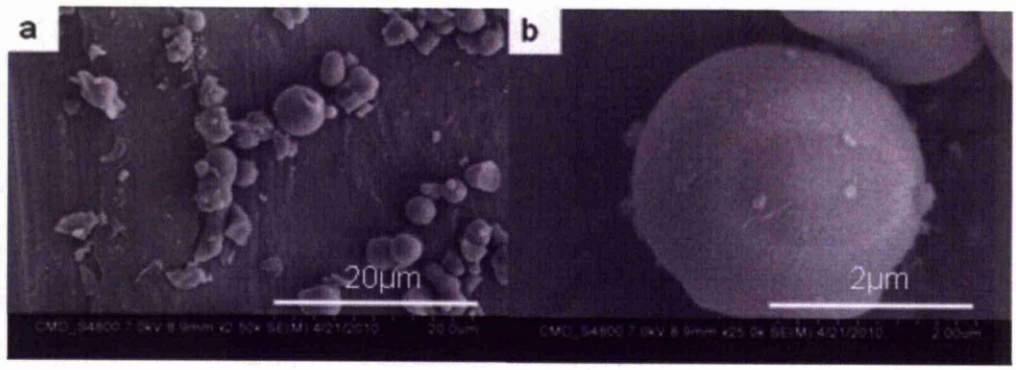

Figure 4.18 SEM images of $-CH_2CH_2-$/ $-CH_2C_6H_5$ 80/ 20 of bifunctionalised silica before acid optimisation (0.28 M HCl)

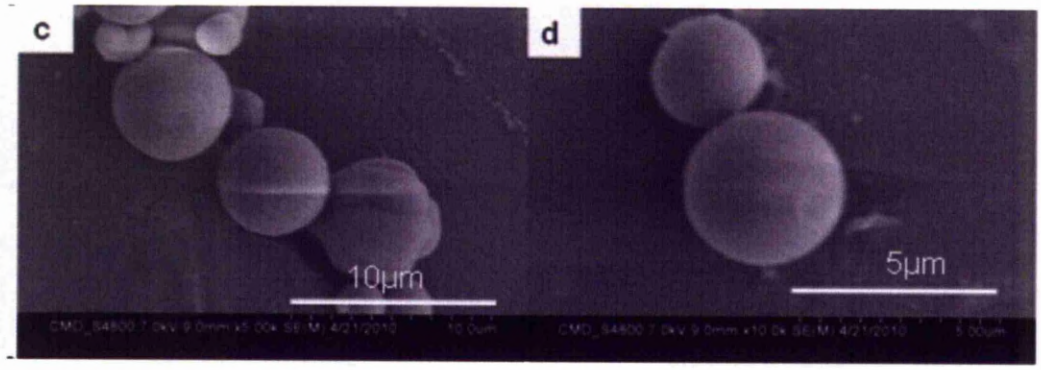

Figure 4.19 SEM images of $-CH_2CH_2-$/ $-CH_2C_6H_5$ 80/ 20 bifunctionalised silica using 0.1 M HCl

The SEM images of the $-CH_2CH_2-$/ $-CH_2C_6H_5$ functionalised PMO synthesised under higher acidity conditions (0.28M HCl) (Figure 4.18) show the silica beads synthesised display spherical morphology. The SEM images also indicate a large particle size range, aggregation between the beads and rough surfaces. At the optimum acid concentration (0.1M HCl) the $-CH_2CH_2-$/ $-CH_2C_6H_5$ PMOs (Figure 4.19) still display a spherical morphology and smoother surface. The XRD patterns and N_2 adsorption/desorption isotherms (Figure 2 and Figure 4.12) show that at the optimum catalyst concentration the silica forms around the surfactant micelles producing an ordered mesostructure. The reduction of the particle size distribution (Figure 4.24)

suggest that at the optimised acid concentration the formation of the silica clusters should occur at similar rates for both precursors forming similar sized SBUs, improving the morphology.[152]

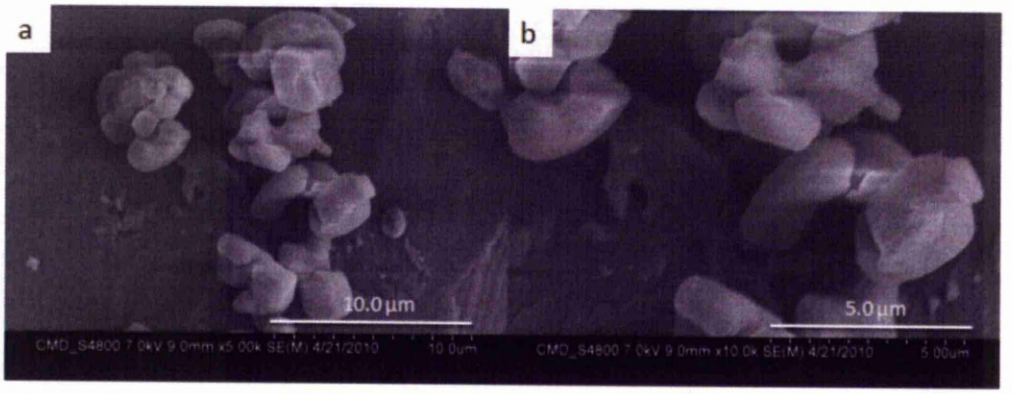

Figure 4.20 SEM images of -CH=CH-/ -$CH_2C_6H_5$ (80/20) PMO before acid optimisation (0.28 M HCl)

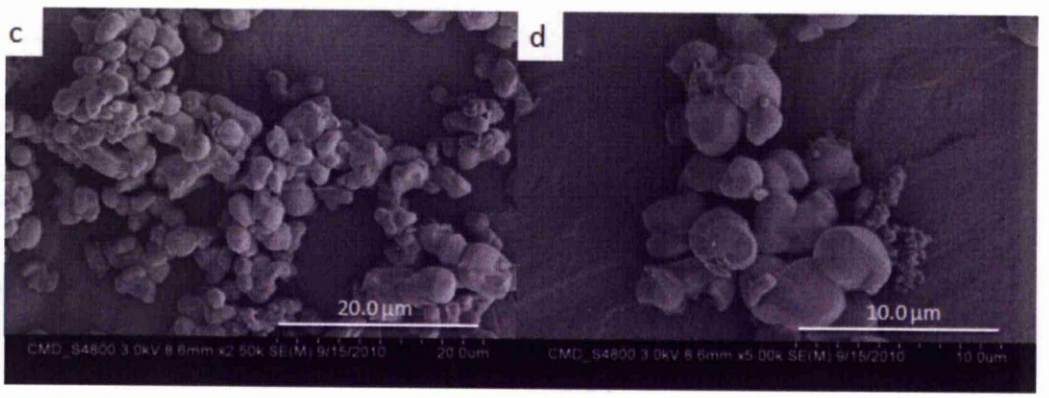

Figure 4.21 SEM images of -CH=CH-/ -$CH_2C_6H_5$ 80/20 bifunctionalised silica using 0.25 M HCl

Before acid optimisation the SEM images show the -CH=CH-/ -$CH_2C_6H_5$ 80/20 PMO to have large particle size distribution of rod and gyroid shaped silica (Figure 4.20). When using the optimised conditions (0.25 M HCl), the SEM images of -CH=CH-/ -$CH_2C_6H_5$ PMO show the silica to have a narrower particle size distribution (Figure 4.21), which is confirmed through particle size measurements (shown below). The shape of the

particles appear to be smoother after acid optimisation. As discussed above the hydrolysis rate of –CH=CH- is faster than $-CH_2C_6H_5$. The slightly higher catalyst concentration (0.28 M HCl) accentuates the difference in hydrolysis rates between the two precursors producing the disordered morphological structures. The double bond of the ethylene group incorporated makes the precursor more susceptible to nucleophilic attack, whereas the benzene ring is only slightly polar creating a much slower hydrolysis rate. It is likely that the more spherical morphology is due to the decrease in H^+ concentration reducing the hydrolysis rate of the ethene functionalised precursor making the rates of the two organosilicas more comparable.

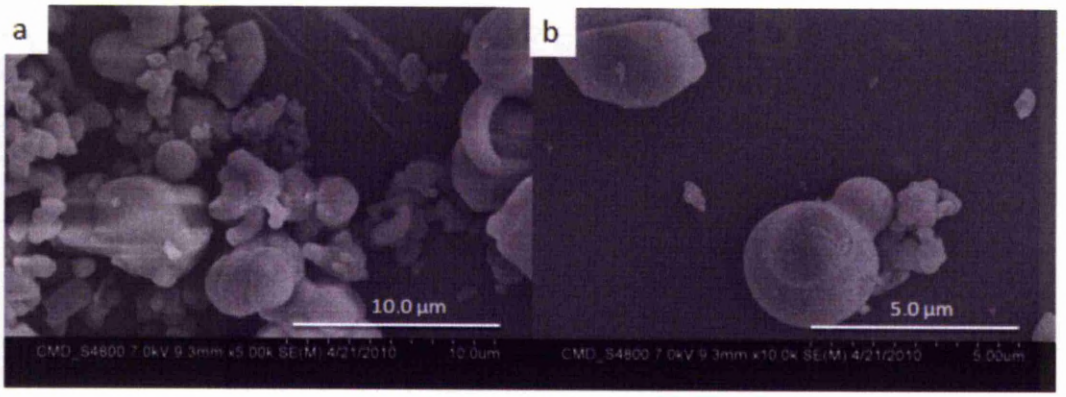

Figure 4.22 SEM images of $-CH_2CH_2-$/ $-C_6H_5$ (80/20) PMO synthesised before acid optimisation (0.28 M HCl)

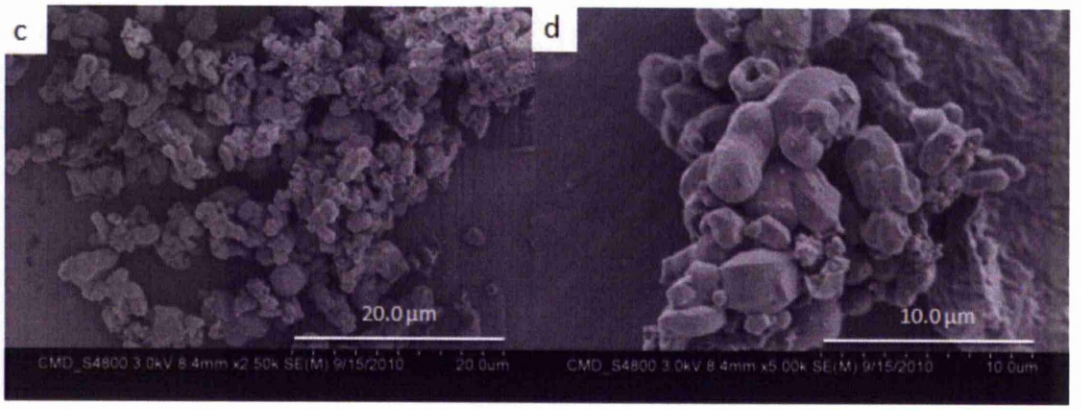

Figure 4.23 SEM images of $-CH_2CH_2-$/ $-C_6H_5$ (80/20) PMO synthesised using 0.01M HCl

The XRD patterns and N_2 adsorption/ desorption isotherms indicated that the -CH_2CH_2- / -C_6H_5 PMO is the least ordered (Figure 4.4 and Figure 4.15). The SEM images show a very large particle size distribution with varying morphology including rods, aggregated spheres and gyroids (Figure 4.22). After acid optimisation the SEM images for the -CH_2CH_2-/ -C_6H_5 PMO indicate a more consistent morphology throughout the silica (Figure 4.23). The PMO appears more spherical, though aggregation has occurred between the beads. The overall morphology is much less consistent compared to the –CH_2CH_2-/ -$CH_2C_6H_5$ PMO. As discussed previously this may be a consequence of the reaction rates of the two silica precursors being incompatible.

The dispersity of the silica particles also affects the performance of the column as similar sized beads produce more densely packed silica. This can be determined by measuring the particle size distribution.

4.4.2 Particle Size Distribution

Particle size analysis was used to examine the effect of acid optimisation on the particle size distribution of the PMOs. A narrower particle size distribution will enhance the packing of the column improving the efficiency.

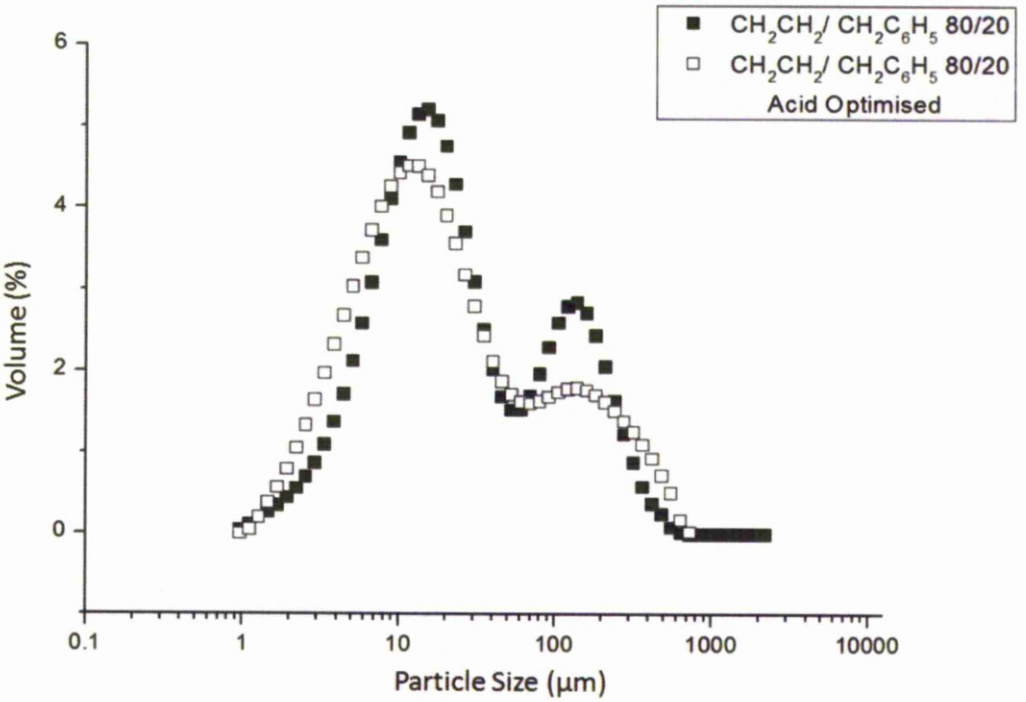

Figure 4.24 Particle size distribution of -CH_2CH_2- / -$CH_2C_6H_5$ before (0.28 M HCl) and after (0.1 M HCl) acid optimisation

The particle size distribution of the -CH_2CH_2-/ -$CH_2C_6H_5$ functionalised PMOs (Figure 4.24) show that the particles become smaller after acid optimisation. The average particle size was reduced from ~ 13 μm to ~ 7 μm; the range of particle sizes has also been reduced after optimisation. Larger particles are present though these are due to aggregation. The results shown are consistent with the SEM images which show less aggregation between the silica beads at the optimised acid content.

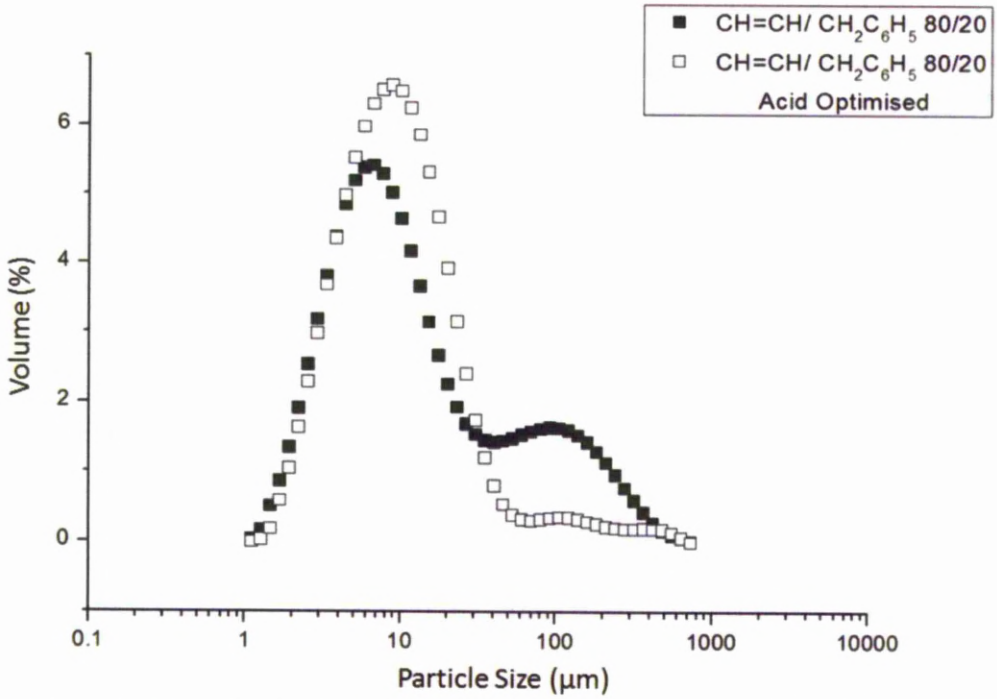

Figure 4.25 Particle size distribution of -CH=CH- / -$CH_2C_6H_5$ before (0.28 M HCl) and after (0.25 M HCl) acid optimisation

The particle size distribution for the -CH=CH-/ -$CH_2C_6H_5$ PMOs shows the average particle size is slightly increased after acid optimisation. The average size of the silica beads increases from 7 to 10 µm, though the number of aggregates in the sample is dramatically reduced. Although the silica particle size appears to be smaller before acid optimisation the presence of aggregates will create large voids within the column creating band broadening and poorly separated compounds. The SEM images show a more uniform morphology is produced using 0.25 M HCl. Before acid optimisation; the faster hydrolysis rate of ethylene functionalised silica will produce numerous smaller silica beads and the slower rate of the benzyl functionalised silica precursor creates larger more monodisperse particles. The combination of these two precursors would create an array of sizes. It is likely that the narrower particle size distributions are due to the decrease in H^+ concentration which will reducing the hydrolysis rate of the ethene functionalised precursor to make the rates of the two organosilicas more comparable.

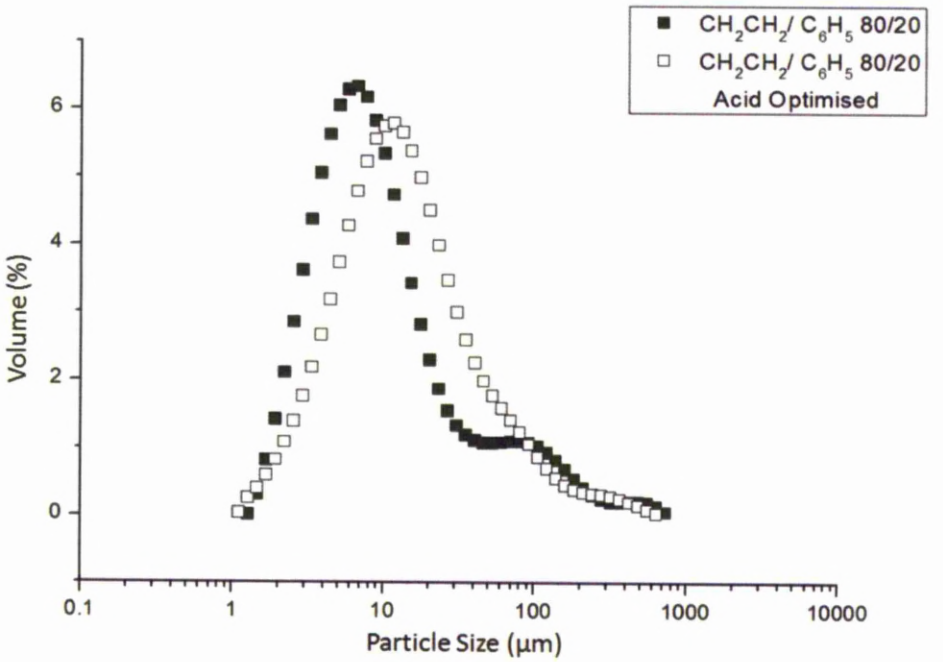

Figure 4.26 Particle size distribution of -CH_2CH_2- / -C_6H_5 before (0.28 M HCl) and after (0.01 M HCl) acid optimisation

The particle size distribution for the -CH_2CH_2-/ -C_6H_5 PMO broadens after acid optimisation which is unexpected as the SEM images (Figure 4.26) indicate a more uniform particle size. The Mastersizer assumes spherical morphology when measuring particle size distribution and so the increase in particle size distribution may simply be marking the change in morphology from rod to more spherical like silica particles.

The SEM imaging shows the -CH_2CH_2-/ -C_6H_5 PMO before acid optimisation contains rods and aggregated beads, which reduces the accuracy of the determination of particle size. The SEM images show the -CH_2CH_2-/ -C_6H_5 PMO to have a more spherical morphology after acid optimisation producing a more accurate particle size distribution (Figure 4.23).

The -CH_2CH_2-/ -$CH_2C_6H_5$ functionalised PMO shows a much higher level of ordering compared to the -CH=CH-/-$CH_2C_6H_5$ and -CH_2CH_2-/ -C_6H_5 functionalised PMOs. This

suggests the $-CH_2CH_2-$ and $-CH_2C_6H_5$ functionalised silica precursors have the strongest interaction with the surfactant and create similar sized SBUs which can condense around the micelles. Although the high density of electrons within the –CH=CH- bond should increase the electrostatic interactions between the positively charged surfactant (under acidic conditions) the rigidity of the double bond may restrict the formation of the organosilanes precursor around the micelles, reducing the mesoscopic ordering of the material. The low ordering observed for the $-CH_2CH_2-$/ $-C_6H_5$ is due to the different hydrolysis rates of the two precursors. The inductive effect of the phenyl ring creates a larger δ^+ charge associated with the silicon atom making it more susceptible to nucleophilic attack by water molecules. The $-CH_2CH_2-$ group has a lower electron withdrawing effect and therefore a slower hydrolysis rate. The different reaction rates of the two precursors means they do not condense uniformly around the micelles.

The kinetics of hydrolysis and condensation of the organosilanes precursors also affects the morphology of the silica. The $-CH_2CH_2-$/ $-CH_2C_6H_5$ functionalised silica shows spherical morphology whereas the other PMOs have rod or gyroid type morphology. For the $-CH_2CH_2-$/ $-CH_2C_6H_5$ PMO silicon environment of each of the organosilanes precursors used are similar. Both silicas are directly bonded to a CH_2 group creating similar inductive effects on the silicon atom. Both organosilanes will produce similar hydrolysis and condensation kinetics. It is therefore simpler to optimise the synthetic parameters to produce spherical beads. The kinetics of the -CH=CH-/ $-CH_2C_6H_5$ and $-CH_2CH_2-$/ $-C_6H_5$ PMOs are too different to create spherical morphology through optimisation of the acid content.

The mesoscopic ordering of the three PMOs were increased through varying the acid content of the sol-gel synthesis. The XRD patterns corresponding to the $-CH_2CH_2-$/ $-CH_2C_6H_5$ PMOs showed the optimum acid concentration to be 0.1M HCl. At lower acid concentrations the pH of solution may not be below the isoelectric point of silica (pH 2). Under these conditions insufficient amounts of Si-OH groups are protonated ($Si-{}^+OH_2$). There is insufficient hydrogen bonding between the positive silica species and the positive surfactant *via* a mediator ($S^+X^-I^+$).[49] Above 0.1M HCl the hydrolysis of the two silica precursor is too rapid, creating large SBUs which cannot form around the

surfactant. High acid concentrations will hinder the formation of the surfactant creating ink bottle-shaped pores as opposed to rod shaped pores.

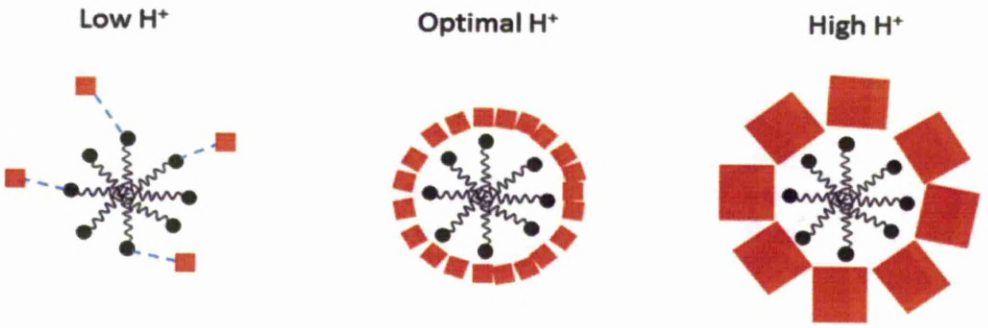

Figure 4.27 Schematic representation of effect of the acid concentration on ordering

By replacing the $-CH_2CH_2-$ bridging group with –CH=CH- the mesoscopic ordering of the silica is reduced (Figure 4.1). The incorporation of the –CH=CH- group produces a more positive silicon atom, this in turn creates more acidic –OH groups. The increase in acidity creates stronger interactions with the surfactant. If the strength of this interaction is too high the formation of the rod-shaped micelles can be hindered.

The optimum acid content for the $-CH_2CH_2-$/ $-C_6H_6$ functionalised PMO is much lower, 0.01M HCl, compared to the $-CH_2CH_2-$/ $-CH_2C_6H_5$ functionalised PMO. It is more challenging to optimise the synthetic parameters for this PMO as the hydrolysis and condensation kinetics of the precursors are very different. At very low acid concentrations the P123 forms smaller micelles with higher polydispersity [153] which can be observed from the pore size distribution (Figure 4.16). Furthermore the H^+ provided by the acid creates hydrogen bonds between the micelles causing aggregation. At low acid concentrations these hydrogen bonds are not present and so the rod shaped micelles are not packed in an ordered array.

4.5 Local structure of the Pore Walls

NMR spectroscopy can be used to probe functionalised silicas on a molecular level. ^{1}H-^{29}Si CP/MAS has been used to assess the degree of framework condensation. ^{1}H-^{13}C CP/MAS kinetics provides qualitative insight into location of organic functional groups and their mobility.

4.5.1 Composition of Pore Walls

^{1}H MAS NMR

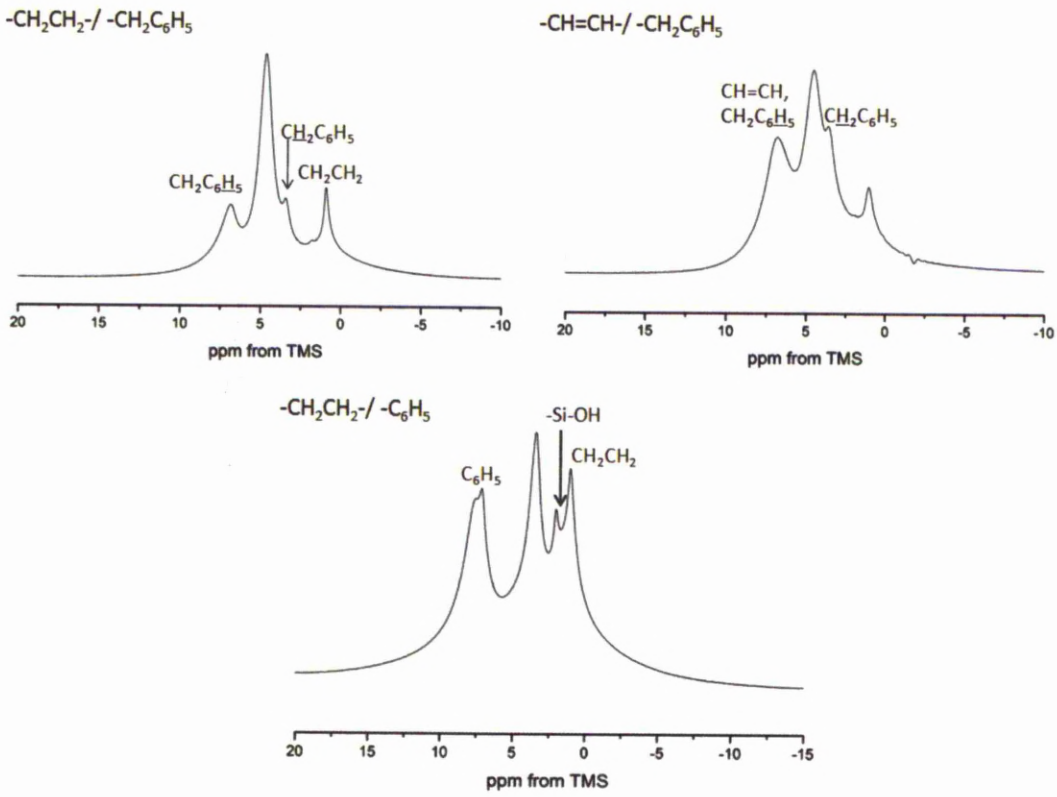

Figure 4.28 ^{1}H MAS NMR spectra of a) $-CH_2CH_2-$/ $-CH_2C_6H_5$ 80/20, b) $-CH=CH-$/$-CH_2C_6H_5$ 80/20 and c) $-CH_2CH_2-$/$-C_6H_5$ 80/20 functionalised silica at an MAS rate of 10 kHz

The ^{1}H NMR MAS spectra confirms the presence of the different functionalities incorporated into the PMOs. The $-CH_2CH_2-$ bridging group resonates *ca.* 0.95 ppm. The aromatic ring of the benzyl tether incorporated into both the $-CH_2CH_2-$/ $-CH_2C_6H_5$ and the $-CH=CH-$/ $-CH_2C_6H_5$ functionalised silica can be observed as a broad resonances at *ca.* 6.9 ppm. The $C\underline{H}_2C_6H_5$ group resonates *ca.* 3.5 ppm for both PMOs. The resonance corresponding to the $-CH=CH-$ bridging group cannot be observed directly as the resonance frequency at which this group resonates is the same as the aromatic ring. The resonances observed at 7.14 and 7.54 ppm correspond to the phenyl ring. For each PMO a resonance at *c.a.* 4.00 ppm is observed, this corresponds to water molecules hydrogen bonded to the surface silanol groups of the silica. An additional resonances is observed for the spectrum of the $-CH_2CH_2-$/ $-C_6H_5$ functionalised silica, this corresponds to the presence of surface silanol (Si-OH) groups.[154]

$^{1}H - ^{13}C$ CP/MAS NMR Spectra

The $^{1}H-^{13}C$ CP/MAS NMR spectra of the $-CH_2CH_2-/-CH_2C_6H_5$ PMOs show a resonance at 5.3 ppm corresponding to the $-CH_2CH_2-$ bridge. The peaks due to the aromatic functionality are observed at 120 – 140 ppm (Figure 4.29). The resonance at 22.3 ppm (A) corresponds to $-\underline{C}H_2C_6H_5$ sites. The additional peaks observed at 16.7 and 58.4 ppm are due a small amount of remaining surfactant.

Similarly, the $-CH=CH-/-CH_2C_6H_5$ functionalised silicas (Figure 4.29) show resonances corresponding to the benzyl functionality and an intense resonance at 146.8 ppm which corresponds to the $-CH=CH-$ bridge. For the $-CH_2CH_2-/-C_6H_5$ organosilicas (Figure 3c) the resonance at 128.5 ppm corresponds to carbon A and C of phenyl ring, the resonances at 131.5 and 134.4 ppm can be attributed to carbons D and B respectively.[155] The intense resonance at 5.2 ppm corresponds to the $-CH_2CH_2-$ bridging functionality. For all three types of PMOs the intensity of the resonances corresponding to $-CH_2C_6H_5$ and $-C_6H_5$ increases with their increased loading levels.

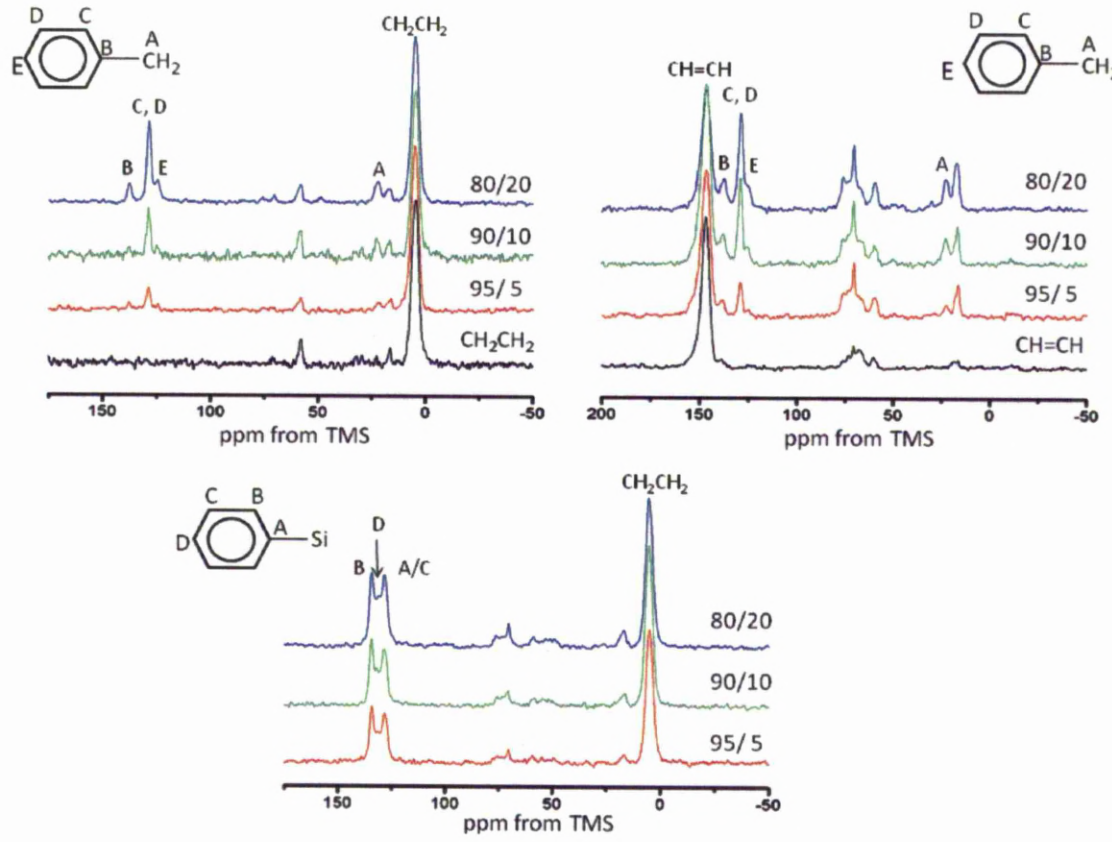

Figure 4.29 $^{1}H - {}^{13}C$ CP/MAS NMR spectra of template extracted PMOs: a) -CH_2CH_2- / -$CH_2C_6H_5$ b) -CH=CH- / -$CH_2C_6H_5$ and c) -CH_2CH_2- / -C_6H_5.

$^{1}H - {}^{29}Si$ CP/ MAS NMR Spectra

^{1}H-^{29}Si CP/MAS NMR is sensitive to surrounding proton environments and therefore can be used to qualitatively determine the silicon environments present in the PMOs. These experiments can be used to analyse the effect of acid concentration on the molecular structure of the silica pore walls. The ^{1}H-^{29}Si CP/ MAS NMR spectra show the presence of T^3 (R-Si(OSi)$_3$), T^2 (R-Si(OSi)$_2$(OH)) and T^1 (R-Si(OSi)(OH)$_2$) sites at -64.2, -56.3 and -48.0 ppm respectively. The absence of any Q^n sites in the region from -90 to -120 ppm indicates no Si-C bond cleavage occurred during acidic surfactant extraction or high-temperature synthesis. The level of condensation can be determined using the formula $(T^1 + T^2)/T^3$; the lower the ratio, the more condensed the silica network.

The ^{29}Si T-sites corresponding to both condensed organosilane precursors of the -CH_2CH_2-/-$CH_2C_6H_5$ PMO have similar chemical shifts. Therefore, individual levels of condensation for each silica precursor cannot be calculated and an overall level of framework condensation is shown. The ^{1}H-^{29}Si CP/MAS NMR spectra show an increase in the degree of framework condensation with increasing levels of -$CH_2C_6H_5$ silica precursor.

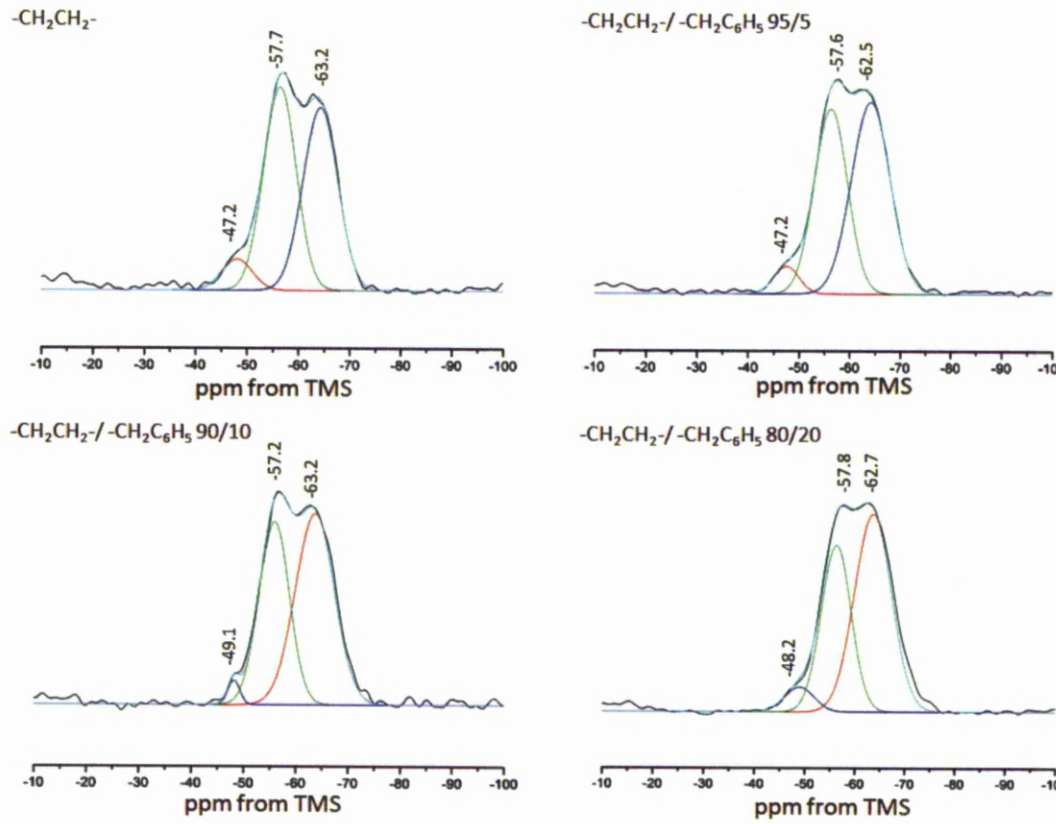

Figure 4.30 ^{1}H-^{29}Si CP MAS NMR spectra of template extracted PMOs a) -CH_2CH_2- b) -CH_2CH_2-/ -$CH_2C_6H_5$ (95 : 5) c) -CH_2CH_2-/ -$CH_2C_6H_5$ (90 : 10) and d) -CH_2CH_2-/ -$CH_2C_6H_5$ (80 : 20)

Table 4.8 Degree of framework condensation of $-CH_2CH_2-$/ $-CH_2C_6H_5$ PMOs determined from ^1H-^{29}Si CP/MAS NMR spectra

Sample	Peak Area (a.u.)			
	$-CH_2CH_2-$ / $-CH_2C_6H_5$			
	T^1	T^2	T^3	$(T^1 + T^2)/T^3$
$-CH_2CH_2-$	1.03 ± 0.23	7.28 ± 0.55	7.00 ± 0.39	1.19
95 : 5	0.77 ± 0.12	6.93 ± 0.51	8.40 ± 0.46	0.916
90 : 10	0.33 ± <0.01	6.08 ± 0.25	8.21 ± 0.26	0.781
80 : 20	0.86 ± 0.05	5.90 ± 0.35	8.75 ± 0.35	0.773

As the condensed precursors containing –CH=CH- and $-CH_2C_6H_5$ functionality resonate at slightly different frequencies the ^1H-^{29}Si CP/MAS NMR spectra for -CH=CH-/ $-CH_2C_6H_5$ PMOs show the presence of two different T^2 (R-Si(OSi)$_2$(OH)) sites at -73.0 and -60.0 ppm (R = -CH=CH- and $-CH_2C_6H_5$ respectively). The spectra show an initial decrease in overall condensation due to the incorporation of an additional silica precursor, differences in rates of hydrolysis will effect the overall connectivity of the silica framework. This further suggests that for these synthesis conditions the hydrolysis and condensation rates of the two precursors are mis-matched. Further increase of the second precursor creates a slightly more condensed framework.

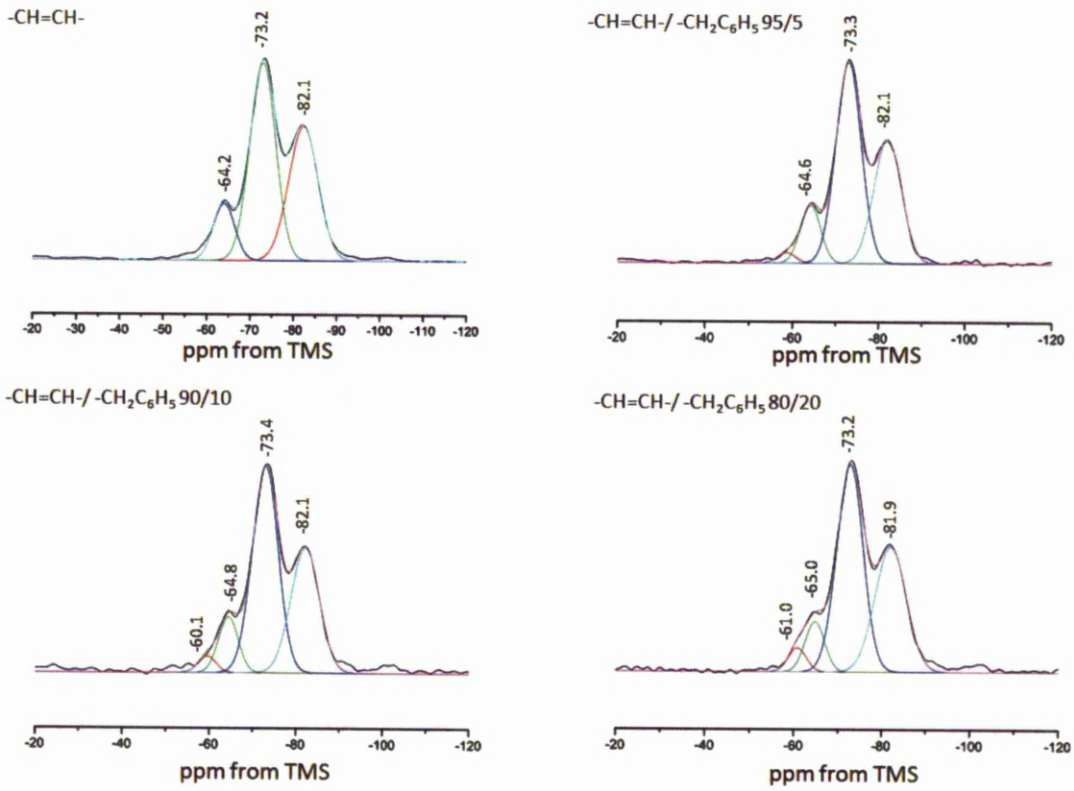

Figure 4.31 ^{1}H-^{29}Si CP/MAS NMR spectra of the template extracted PMOs: a) –CH=CH- b) -CH=CH-/ $-CH_2C_6H_5$ (95 : 5) c) -CH=CH-/ $-CH_2C_6H_5$ (90 : 10) and d) -CH=CH-/ $-CH_2C_6H_5$ (80 : 20)

Table 4.9 Degree of framework condensation of -CH=CH-/ $-CH_2C_6H_5$ PMOs

Sample	Peak area (a.u.)				
	-CH=CH-			$-CH_2C_6H_5$	
	T^1	T^2	T^3	T^2	$(T^1+T^2)/T^3$
100 : 0	1.70 ± -	7.12 ± 0.02	5.63 ± 0.02		1.57
95 : 5	1.58 ± 0.09	7.02 ± 0.08	4.61 ± 0.05	0.25 ± 0.07	1.92
90 : 10	1.50 ± 0.19	7.27 ± ±0.11	4.83 ± 0.07	0.40 ± 0.16	1.90
80 : 20	1.30 ± 0.40	7.20 ± 0.12	5.13 ± 0.07	0.56 ± 0.35	1.77

As the resonances of the two silica precursors used to synthesised the $-CH_2CH_2-$/ $-C_6H_5$ resonate at different frequencies ($-CH_2CH_2-$ *ca.* -63, -48, -56 and -63 ppm whereas $-C_6H_5$ *ca.* -66 and -78 ppm). The ^1H-^{29}Si CP/MAS NMR spectra for $-CH_2CH_2-$/$-CH_2C_6H_5$ PMOs indicate the presence of T^3 ($R-Si(OSi)_3$) at -63.0 and -78.0 ppm (R= $-CH_2CH_2-$ and $-C_6H_5$ respectively), T^2 ($R-Si(OSi)_2(OH)$) sites at -56.0 and -66.0 ppm (R = $-CH_2CH_2-$ and $-C_6H_5$ respectively) and T^1 ($R-Si(OSi)(OH)_2$) sites at -48.0.0 ppm (R= $-CH_2CH_2-$).

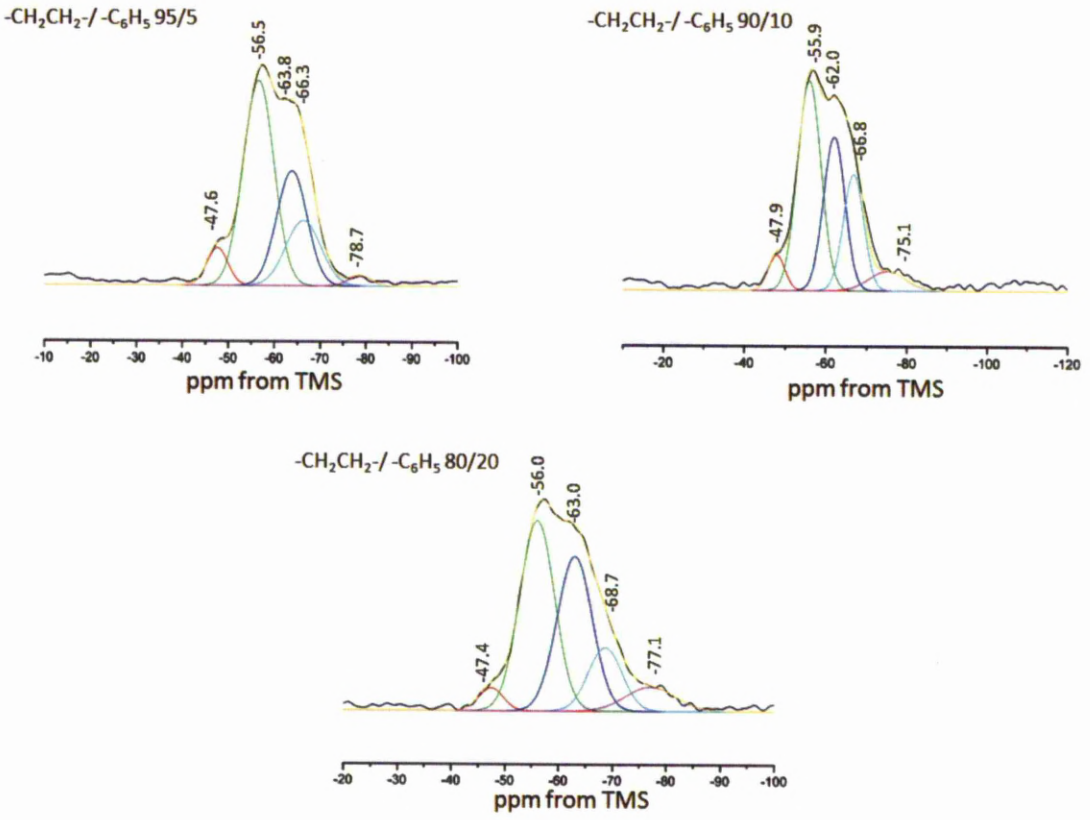

Figure 4.32 ^1H – ^{29}Si CP MAS/NMR spectra of template extracted PMOs : a) $-CH_2CH_2-$/ $-C_6H_5$ (95 : 5) b) $-CH_2CH_2-$/ $-C_6H_5$ (90 : 10) and c) $-CH_2CH_2-$/ $-C_6H_5$ (80 : 20)

Table 4.10 Degree of framework condensation of $-CH_2CH_2-$/ $-C_6H_5$

Sample	Peak area (a.u.)							
	$-CH_2CH_2-$				$-C_6H_5$			Total
	T^1	T^2	T^3	$(T^1 + T^2)/T^3$	T^2	T^3	T^2/T^3	$(T^1 + T^2)/T^3$
95 : 5	0.83 ± 0.03	6.67 ± 0.06	4.86 ± 0.07	1.54	2.75 ± 0.05	0.08 ± 0.02	34.4	2.07
90 : 10	0.80 ± 0.05	6.80 ± 0.53	4.53 ± 1.40	1.68	3.29 ± 1.03	1.00 ± 0.12	3.29	1.97
80 : 20	0.62 ± 0.14	7.29 ± 2.28	6.00 ± 6.52	1.32	2.35 ± 4.91	1.35 ± 0.58	1.74	1.40

The framework of the three $-CH_2CH_2-/-C_6H_5$ PMOs is condensed to a lesser degree compared to the previous two samples. For this sample the level of condensation of the $-C_6H_5$ dramatically increases with increasing levels of the precursor. This may be due to a secondary effect of co-condensation occurring more readily between the same precursors. For all three types of PMOs the overall level of condensation increases with increasing amounts of the tether functionalised precursor. The co-condensation of the silica precursors around the surfactant is depended on the coulombic interactions between the two groups ($^-$O-Si-R-Si-O$^-$ / $^-$O-Si-R with the surfactant head group H_2O^+-CH_2CH_2-) which will vary depending on the organic groups incorporated.[156,157] Furthermore the incorporation of a second silica precursor will disrupt the charge distribution between the surfactants and surfactant polar head groups, as shown by the initial decrease in silica co-condensation. Strong interactions between the surfactant and silicate species incourages strong co-opertaive binding, increasing framework interconnectivity.[158] The hydrophobicity of the organic groups must also be taken into account as variations in this parameter will effect co-assembly.

4.6 Mobility of the Functional Groups

In order to determine whether the PMOs synthesised are viable candidates for a new stationary phase, these materials have been probed on a molecular level to determine the position and mobility of the organic groups incorporated. It is imperative that the organic groups incorporated are located on the surface of the material and are able to interact with and, therefore, separate analytes in the mobile phase. This can be determined by studying the mobility of these groups through the CP dynamics.

The Classical I-S model assumes strong heteronuclear (I-S) dipolar coupling and sufficient spin diffusion between the abundant spins (I) for them to act as a single spin source. For a system in which both the abundant and dilute nuclei are spin-½, the general kinetic equation is:

$$I(t) = I_0\left(1 - T_{IS}/T_{1\rho}^{I}\right)^{-1}\left[\exp\left(-t/T_{1\rho}^{I}\right) - \exp\left(-t/T_{IS}\right)\right] \qquad \textbf{(4.2)}$$

The strength of heteronuclear dipolar coupling (T_{IS}) is dependent on internuclear distance (r) by a factor of $1/r^3$. If coupling is not sufficient for ^{1}H's to act as a single spin system, the magnetisation transfer from the abundant spins comes from two sources as described by the I-I*-S model. Magnetisation is initially transferred to S-spins from directly attached abundant I*-spins followed by the remaining I-spins in close proximity.

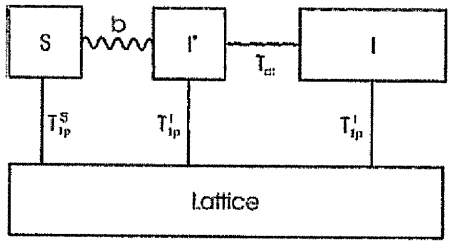

Figure 4.33 block diagram of I-I*-S CP thermodynamics

$^{1}H-^{13}C$ CP/MAS kinetics for the bi-functionalised PMOs

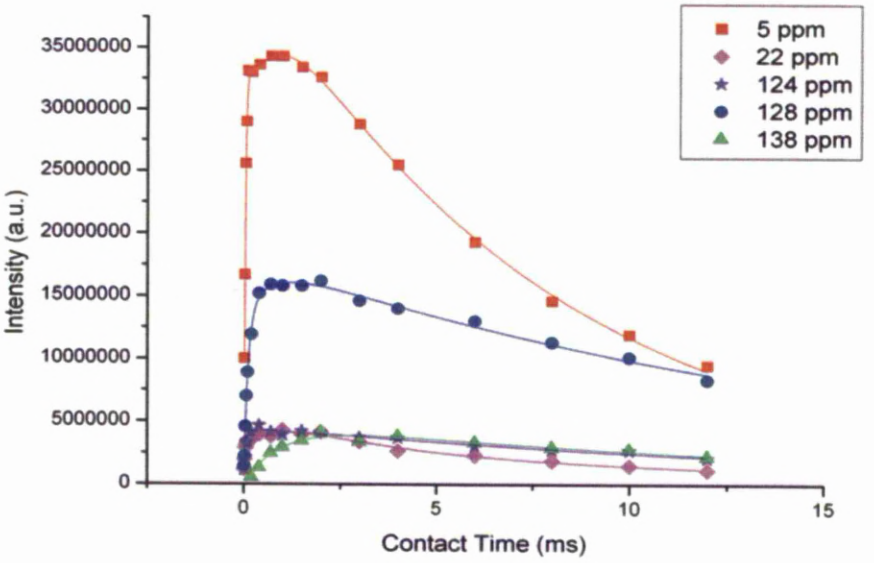

Figure 4.34 $^{1}H - ^{13}C$ CP/MAS kinetics curves of template extracted PMO - CH_2CH_2-/ -$CH_2C_6H_5$ (80 : 20)

Table 4.11 $^{1}H-^{13}C$ CP/MAS kinetics parameters for -CH_2CH_2- /-$CH_2C_6H_5$ PMO

^{13}C site/ppm	Model		Intensity / 10^7	T_{IS} / ms	$T_{1\rho}{}^{H}$ / ms	λ	T_{df} / ms	T_2 / ms	R^2
-CH_2CH_2- 5 ppm	I-S (Two components)	Fast	3.08 ± 0.12	0.029 ± 0.003	0.258 ± 0.089				0.995
		Slow	3.94 ± 0.058	0.35 ± 0.085	8.03 ± 0.296				
-$\underline{C}H_2$– C_6H_5 23 ppm	I-I*-S		0.484 ± 0.024		8.21± 0.76	0.411 ± 0.04	0.418 ± 0.153	0.013 ± 0.001	0.960
-C_6H_5 125 ppm (para)	I - S		0.442 ± 0.011	0.061 ± 0.005	17.50 ± 1.79				0.956
-C_6H_5 129 ppm (ortho/ meta)	I - S		1.69 ± 0.027	0.142 ± 0.008	19.11 ± 1.29				0.989
-C_6H_5 137 ppm (Quaternary carbon)	I - S		0.461 ± 0.034	0.951 ± 0.147	15.79 ± 3.25				0.934

The CP-kinetics of resonances at 125, 129 and 137 ppm assigned to the benzyl carbons were fitted using the I-S model (Table 4.11). These sites display longer T_{IS} and $T_{1\rho}$ times compared to those for the $-CH_2CH_2-$ bridging group. Longer relaxation times usually suggest that the functionality is more mobile[50], which is to be expected from a tether group. The quaternary carbon shows a slower build up of magnetization due to no directly bound protons.

The CP kinetics for the $-\underline{C}H_2C_6H_5$ peak was fitted using the I-I*-S model as the magnetization can be transferred from both the directly bound protons and those from the aromatic ring. As the value of the parameter λ falls within the expected range ($\lambda \sim 1/3$)[90] for the $-CH_2-$ group we can assume that the I-I*-S model provides an accurate description of the magnetisation transfer for the $-\underline{C}H_2-C_6H_5$ environment. The CP dynamics of the bridging functionality, $-CH_2CH_2-$, can be fitted using two components with different T_{IS} and $T_{1\rho}$ times, suggesting this functionality resides in two different environments. The fast build up of magnetisation and fast relaxation is indicative of a more rigid environment, which most likely corresponds to $-CH_2CH_2-$ groups trapped within the bulk of the silica. The slow build up of magnetisation and relaxation suggests a more mobile environment corresponding to the $-CH_2CH_2-$ groups at the surface of the silica[159,50,143,142] . Although the measurement of CP kinetics is not a quantitative technique, by comparing the intensity of the slow and fast components (I_S/I_F) components of the same resonance we can determine the ratio of bridging groups at the pore surface to the pore wall.[14] The CP kinetics show the I_S/I_F ratio for the $-CH_2CH_2-$ moiety is 1.28.

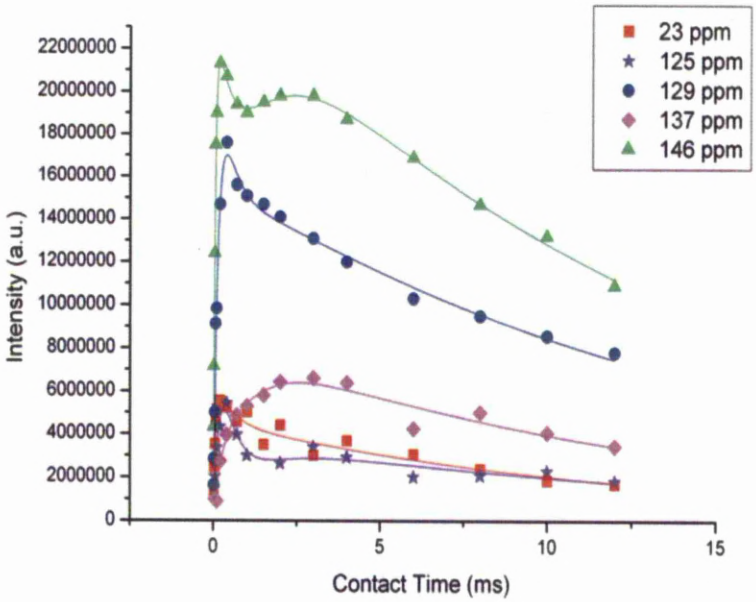

Figure 4.35 $^{1}H - {}^{13}C$ CP/MAS kinetics curves of template extracted PMO -CH=CH-/ $-CH_2C_6H_5$ (80 : 20)

Table 4.12 $^{1}H-{}^{13}C$ CP/MAS kinetics parameters for –CH=CH- :$-CH_2C_6H_5$ PMO

^{13}C site	Model		Signal Intensity / 10^7	T_{IS} / ms	$T_{1\rho}{}^{H}$ / ms	R^2
-CH=CH-	I-S	Fast	2.23 ± 0.050	0.052 ± 0.003	0.618 ± 0.087	0.9963
146 ppm	(Two components)	Slow	2.38 ± 0.055	1.01 ± 0.139	14.51 ± 0.913	
$-\underline{C}H_2-C_6H_5$	I-S	Fast	0.480 ± 0.054	0.038 ± 0.009	0.370 ± 0.075	0.9186
23 ppm	(Two components)	Slow	0.448 ± 0.023	0.263 ± 0.041	12.3 ± 1.87	
$-C_6H_5$	I-S	Fast	0.847 ± 0.303	0.181 ± 0.081	0.400 ± 0.176	0.8830
125 ppm (para)	(Two components)	Slow	0.348 ± 0.052	1.07 ± 0.322	15.90 ± 6.56	
$-C_6H_5$	I-S	Fast	1.73 ± 0.185	0.138 ± 0.021	0.453 ± 0.062	0.9905
129 ppm (ortho / meta)	(Two components)	Slow	1.51 ± 0.038	0.516 ± 0.034	16.26 ± 1.30	
$-C_6H_5$	I –S		0.711 ± 0.044	0.545 ± 0.089	16.81 ± 3.38	0.9247
137 ppm (Quaternary)						

The CP-kinetics for the bridging -CH=CH- groups was fitted using a two component IS model indicating the bridging moiety resides at both the pore surface and within the pore wall.[49,50] Unlike for the $-CH_2CH_2$-/-$CH_2C_6H_5$ PMO, the kinetic data for the carbons of the benzyl ring were also fitted using a two component IS model. This suggests some tether functionality is trapped within the pore wall and so fewer benzyl groups reside at the pore surface. The quaternary carbon of the benzyl group was fitted using the I-S model not a double exponential model. As this carbon contains no directly bonded protons the magnetisation is transferred from an ensemble of surrounding protons averaged out by ^1H-^1H spin diffusion. The calculated I_S/I_F ratio for the –CH=CH- bridging group has decrease (1.07) compared to the $-CH_2CH_2$- group (1.28). This suggests increased amounts of the –CH=CH- functionality reside within the bulk of the frame work.

By replacing the $-CH_2CH_2$- group with a –CH=CH- the increased charge density of the silicate anion may increase the electrostatic interactions between the –CH=CH- functionalised precursor and the surfactant head group.[156] This could create a preferential interaction between the micelles and –CH=CH- group, causing more tether groups to be trapped in the silica walls. The relative hydrolysis rates of the two bridging functionalities may also effect the molecular structure of the PMO. The more polar –CH=CH- moiety will alter the hydrolysis and condensation rate of the precursor. The different organic groups incorporated will affect the nucleation and growth of the precursors which may cause the $-CH_2C_6H_5$ functionalised silica to be encased by the –CH=CH- precursor.[160,161]

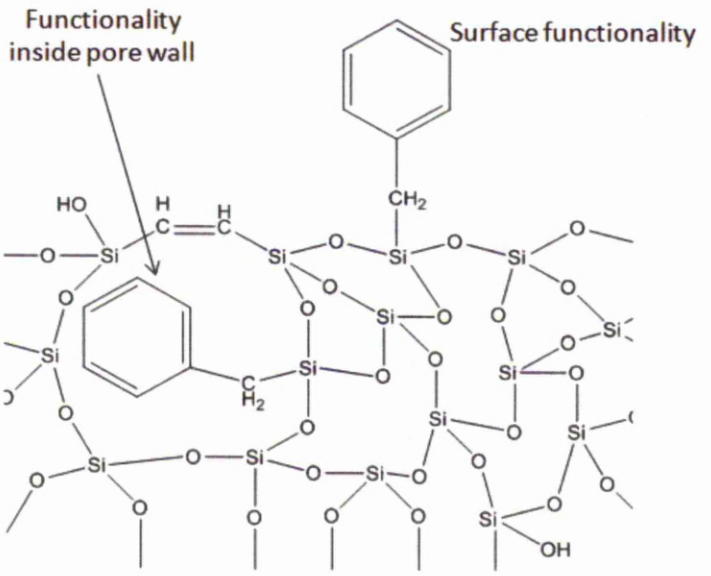

Figure 4.36 Representation of the silica pore wall containing –CH=CH- and $-CH_2C_6H_5$ functional groups

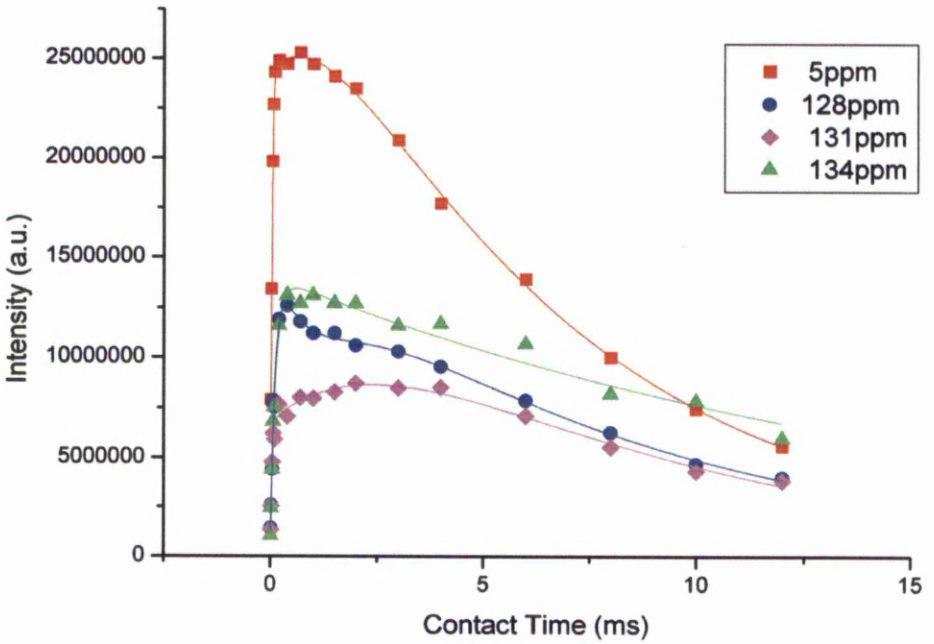

Figure 4.37 $^{1}H - {}^{13}C$ CP/MAS kinetics curves of template extracted $-CH_2CH_2-/-C_6H_5$ PMO (80 : 20)

Table 4.13 $^{1}H - {}^{13}C$ CP/MAS kinetics fitting parameters for $-CH_2CH_2-$/ $-C_6H_5$ PMO

^{13}C site	Model		Signal Intensity / 10^7	T_{IS} / ms	$T_{1\rho}{}^{H}$ / ms	R^2
$-CH_2CH_2-$	I-S	Fast	2.42 ± 0.013	0.025 ± 5.1 x 10^{-4}	5.27 ± 0.08	0.9984
5 ppm	(Two components	Slow	0.972 ± 0.053	1.37 ± 0.128	9.17 ± 0.93	
$-C_6H_5$	I-S	Fast	1.34 ± 0.086	0.108 ± 0.012	0.695 ± 0.068	0.9827
128 ppm (ortho / para)	(Two components	Slow	1.39 ± 0.075	1.15 ± 0.112	8.44 ± 0.830	
$-C_6H_5$	I-S	Fast	0.686 ± 0.033	0.042 ± 0.005	0.890 ± 0.083	0.9751
131 ppm (meta)	(Two components	Slow	1.21 ± 0.074	1.46 ± 0.146	8.56 ± 0.915	
$-C_6H_5$	I-S		1.39 ± 0.026	0.112 ± 0.007	16.61 ± 1.25	0.9834
134 ppm (Quaternary)						

The resonances attributable to the phenyl functionality show much shorter $T_{1\rho}{}^{H}$ relaxation times in comparison to the benzyl tether. The mobility of the phenyl tether would be reduced as the benzene ring is directly attached to the silicon atoms. The CP kinetics of the phenyl ring can be described by the two component IS model indicating the organic group resides in two different environments. As explained above, altering the organic groups incorporated affects the micelle/ precursor coulombic interactions and the relative hydrolysis rates of the two silica precursors. If the electrostatic interactions between the surfactant and phenyl functionalised precursor are altered, tether functionalities can become trapped within the silica pore wall. The CP kinetic data for the $-CH_2CH_2-$ bridging group indicates that the organic group resides in two environments. The majority of the $-CH_2CH_2-$ bridging groups for this PMO are contained within the pore walls as opposed to the pore surface (I_S/I_F = 0.40).

The ^{1}H-^{13}C CP kinetics show increasing levels of bridging functionality within the pore walls for the –CH=CH-/ -$CH_2C_6H_5$ and –CH_2CH_2-/ -C_6H_5 (I_S/I_F = 1.07 and 0.40 respectively) compared to –CH_2CH_2-/ -$CH_2C_6H_5$ functionalised PMO (I_S/I_F = 1.28). Furthermore the CP kinetics data for the –CH_2CH_2-/ -$CH_2C_6H_5$ tether groups were fitted using the I-S model indicating a uniform transfer of magnetisation and the long relaxation times. This suggests the organic groups are in a mobile environment at the pore surface. The tether moieties of the –CH=CH-/ -$CH_2C_6H_5$ and –CH_2CH_2-/ -C_6H_5 PMOs were fitted using a two component IS model. This indicates the tether functionalities are located at both the pore surface and in the pore wall. This implies changing the organic group of the silica precursors alters the homogenous distribution of the functionalities within the PMO either through the varying electrostatic interactions between the precursors and the surfactant or through different hydrolysis and condensation rates. The mobility, accessibility and homogeneity of the functionalities will affect the selectivity of the column as trapped organic groups are not able to interact with an analyte. The decreasing ordering of mis-matched precursors is also observed through x-ray diffraction as the incompatible silica precursor/ micelle and precursor/ precursor intermolecular interactions will create lower ordered material.

The ^{1}H–^{13}C CP/MAS kinetics data has shown that the bridging groups and tethers are accessible to analytes within a mobile phase. As the –CH_2CH_2-/ -$CH_2C_6H_5$ contains the greatest amount of surface organic groups it is likely that this material will produce a higher degree of selectivity. To determine whether the PMO contains a homogeneous distribution of the two moieties throughout the silica, the samples have been analysed using ^{1}H NOESY and ^{1}H-^{29}Si HETCOR 2D NMR experiments.

4.7. ^{1}H-^{29}Si HETCOR NMR

The ^{1}H-^{29}Si CP/MAS NMR spectra have shown the T sites of the separate precursors are only distinguishable for the $-CH_2CH_2-$/ $-C_6H_5$ functionalised organosilica. It is on this basis that we have chosen the $-CH_2CH_2-$/ $-C_6H_5$ PMO to be analysed using ^{1}H-^{29}Si HETCOR NMR experiments.

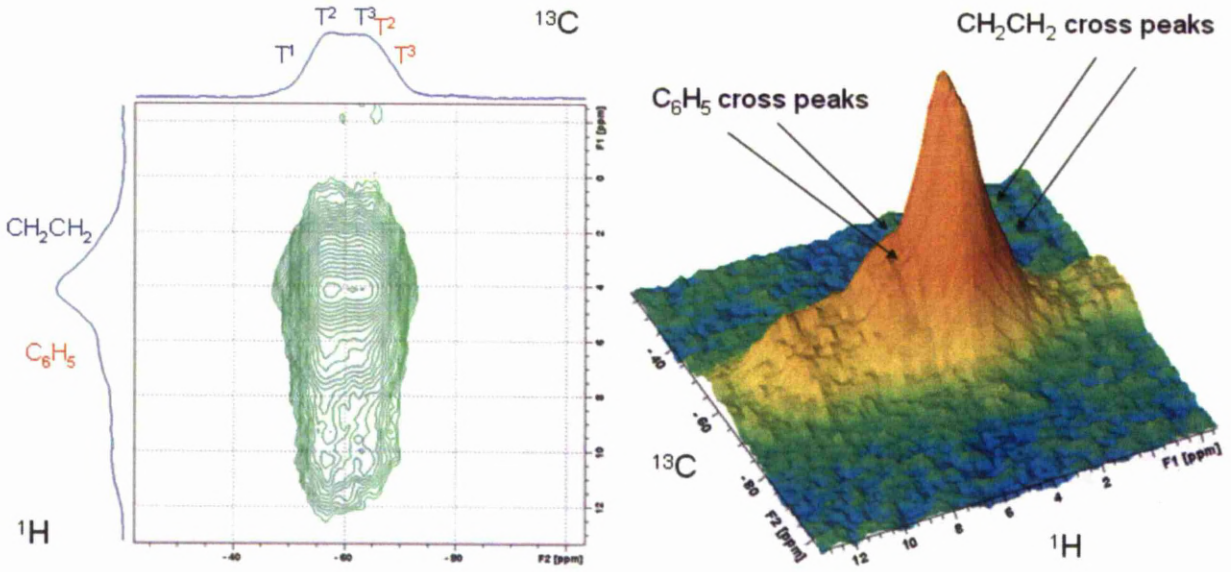

Figure 4.38 ^{1}H-^{29}Si HETCOR NMR spectra of $-CH_2CH_2-$/ $-C_6H_5$ functionalised PMO at 10 kHz

2D ^{1}H-^{29}Si HETCOR experiments can provide information on the spatial proximity between different ^{29}Si sites within the bi-functionalised silica. The intensity of the correlations for this experiment are derived from cross-polarisation and therefore are dependent on internuclear distances. Correlations between the silicon T sites of the $-CH_2CH_2-$ bridging groups (-47.9, -55.4 and -62.0 ppm) with the proton resonances also corresponding to the bridging group (1.8 ppm) are expected and referred to as auto-correlation peaks. Auto peaks are also observed for the $-C_6H_5$ functionalised orgaosilane. The ^{1}H resonance at 1.8 ppm is assigned to the $-CH_2CH_2-$ bridging functionality. The 2D ^{1}H-^{29}Si HETCOR spectrum shows that this

resonance correlates with the T sites form the $-C_6H_5$ tether at -68.7 and -77.1 ppm. Likewise, the ^1H resonance at 7.1 ppm, attributed to the $-C_6H_5$ tether, is correlated to the T sites corresponding to the $-CH_2CH_2-$ organic bridge at -47.4, -56.0 and -63.0 ppm. The presence of cross peaks is indicative of a homogeneous distribution of organic functionalities throughout the framework. The intensity of the cross peaks (Table 4.14) relative to the auto peaks also suggest a random distribution of the organic groups instead of domain type functionality.[50] The conclusions derived from the ^1H-^{29}Si HETCOR experiment can be confirmed using ^1H NOESY NMR.

Table 4.14 Intensity of Cross-peaks in the ^1H-^{29}Si HETCOR spectra. Intensities normalised to those of the $-CH_2CH_2-$ T^3 resonance.

^{29}Si Resonance / ^1H Resonance	$-CH_2CH_2-$			$-C_6H_5$	
	T^1	T^2	T^3	T^2	T^3
$-CH_2CH_2-$	0.31	0.69	1.0	0.61	0.31
$-C_6H_5$	0.85	2.06	1.76	1.09	0.49
(Auto peak T^2+T^3)/ (Correlation peak T^2+T^3)	0.44			1.72	

4.8 ^1H NOESY NMR

In solids ^1H spin diffusion can occur through dipolar interactions when protons are reasonably close in space, up to 5Å.[162] Nuclear Overhauser Effect SpectroscopY (NOESY) experiments can be used to detect cross relaxation between two spins and therefore determine which spins are close in space. The intensity of the cross peaks is dependent on the distance between the two spins as the rate of ^1H spin diffusion decreases with distance ($1/r^6$). This technique can be used to investigate the homogeneity of the two functionalities incorporated. Both $-CH_2CH_2-$/ $-CH_2C_6H_5$ and $-CH_2CH_2-$/ $-C_6H_5$ PMOs were analysed using ^1H NOESY NMR, though as –CH=CH- and

$-CH_2C_6H_5$ resonate at similar frequencies the PMO containing both moieties could not be unequivocally analysed using this technique.

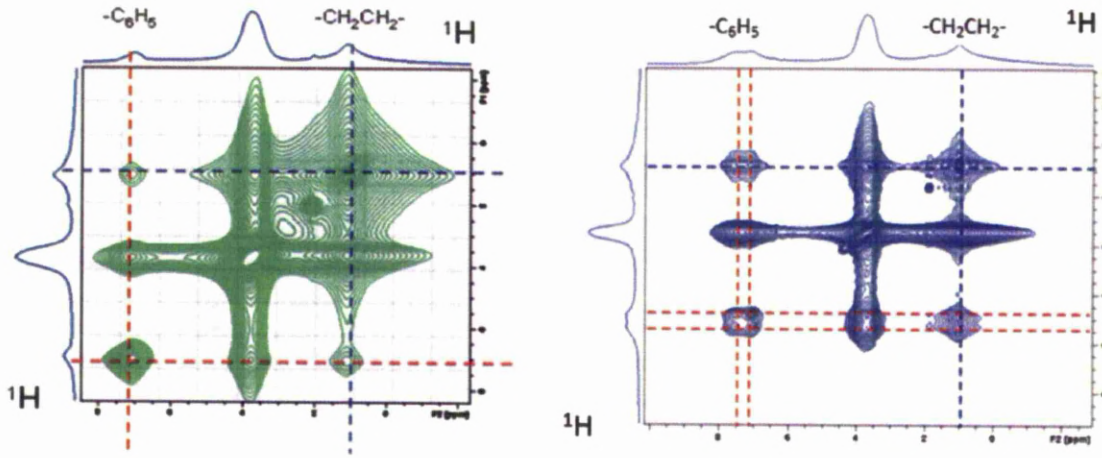

Figure 4.39 ^1H NOESY NMR spectra of template extracted PMO $-CH_2CH_2-$/ $-CH_2C_6H_5$ (80 / 20) (left) using a contact time of 20 ms at a spinning speed of 30kHz and $-CH_2CH_2-$/ $-C_6H_5$ (80/20) (right) using a contact time of 20 ms at a spinning speed of 10 kHz

The ^1H MAS NOESY spectra shows the presence of cross-peaks between the $-CH_2CH_2-$ and $-CH_2\underline{C}_6H_5$ functionalities at mixing times ≥ 20 ms for both PMOs. Magnetisation transferred at shorter mixing times, such as 20 ms, indicates the two functionalities are in close proximity[163,164] and there for homogeneously distributed throughout the silica framework. As the experimental time for the 2D ^1H NOESY NMR is much shorter compared to the ^1H-^{29}Si HETCOR we can analyse the build-up of magnetisation by varying the mixing time.

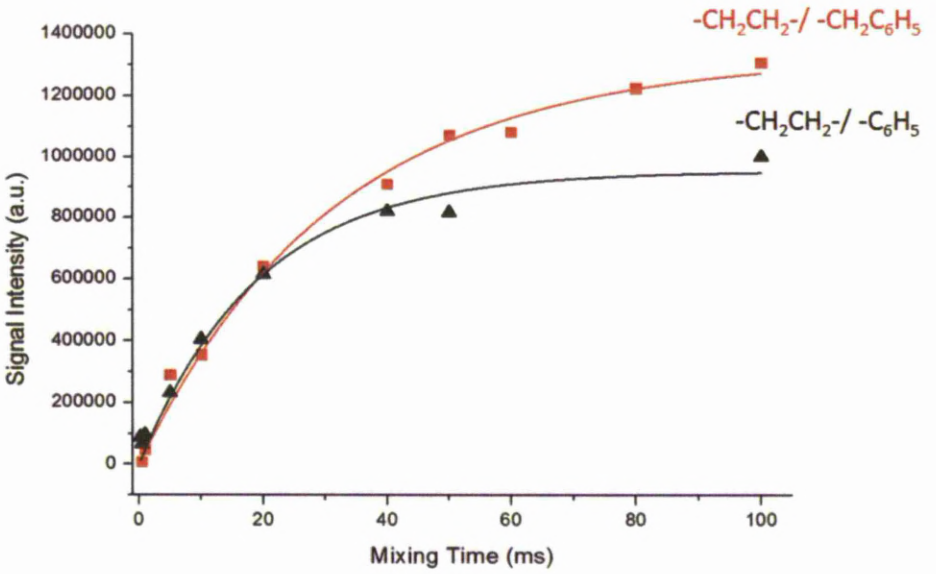

Figure 4.40 Intensity of cross peaks as a function of mixing time

Figure 4.40 shows a higher signal intensity of the $-CH_2CH_2-$/ $-CH_2C_6H_5$ functionalised silica at the longer mixing times. This suggests that the two organic groups are in closer proximity compared to the moieties within the $-CH_2CH_2-$/ $-C_6H_5$ PMO. This coinsides with the ^1H-^{13}C CP/MAS kinetics data which indicate the $-CH_2CH_2-$/ $-CH_2C_6H_5$ silica contains higher ratios of organic groups clustered at the surface. Both organosilanes show fast build-up of magnetisation (rate of transfer of magnetisation for $-CH_2CH_2-$/ $-CH_2C_6H_5$ is 31.8 ms and $-CH_2CH_2-$/ $-C_6H_5$ is 19.4 ms). The $-CH_2CH_2-$/ $-C_6H_5$ functionalised silica plateaus at a much faster rate, wherein magnetisation dissipates back to the lattice. This is indicative of a more rigid environment. Again these results agree with the ^1H-^{13}C CP/MAS kinetics data which suggests a greater amount of the functionality is trapped within the bulk of the silica pore walls.

4.9 ^{1}H-^{13}C WISE NMR

The ^{1}H-^{13}C CP kinetics data were used to analyse the mobility of the organic groups incorporated. These results indicate that the $-CH_2CH_2-$ bridges reside within the pore walls of the silica and the benzyl functionality projects into the pores for the $-CH_2CH_2-$/ $-CH_2C_6H_5$ functionalised silica. The CP kinetics data also indicated a significant amount of the tether functionalities of the $-CH=CH-$/ $-CH_2C_6H_5$ and $-CH_2CH_2-$/ $-C_6H_5$ PMOs were trapped within the pore walls. This could be due to the lower molecular ordering of these materials observed through XRD.

The mobility of the functionalities can be further analysed using 2D WIdeline SEparation (WISE) experiments. The ^{1}H-^{13}C WISE spectrum correlates the structure and mobility of the sample through the ^{13}C chemical shift and the ^{1}H line shapes respectively.[165] The mobility is estimated through the ^{1}H line widths, narrower ^{1}H line widths observed for more mobile environments.

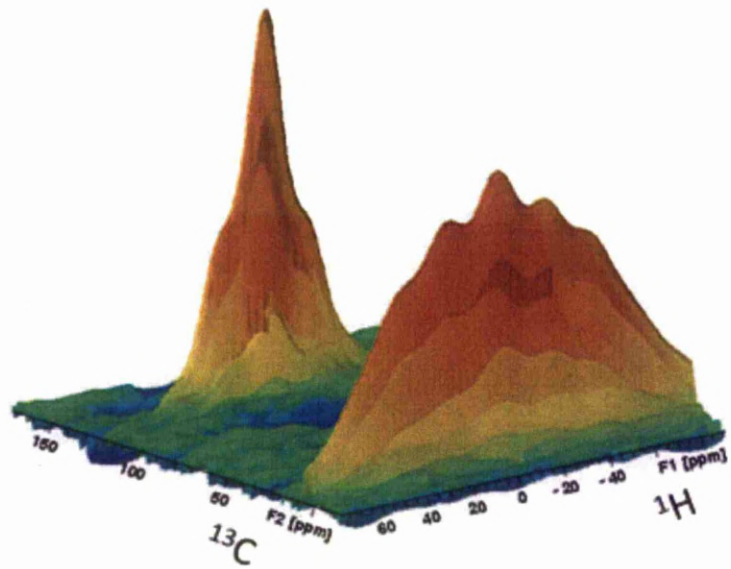

Figure 4.41 $^{1}H-^{13}C$ WISE NMR spectrum of $-CH_2CH_2-/-CH_2C_6H_5$ PMO using a contact time time of 200 μs and an MAS rate of 8 kHz

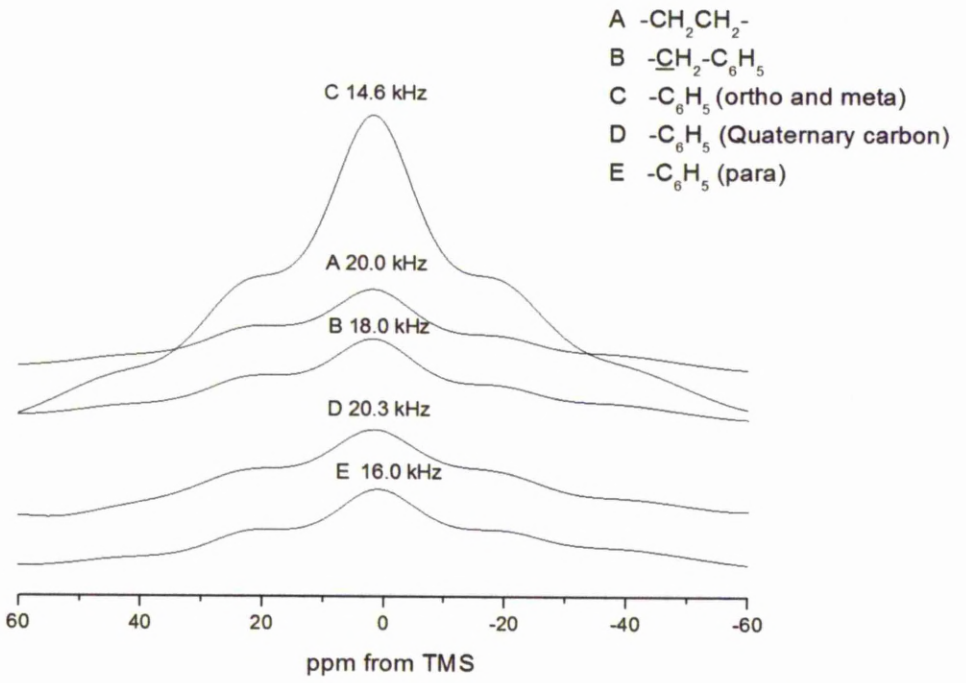

Figure 4.42 ^{1}H projection for ^{1}H-^{13}C WISE NMR $-CH_2CH_2-$/ $-CH_2C_6H_5$ functionalsied PMO

A broad ^{1}H line width is observed for the $-CH_2CH_2-$ functionality (20.0 kHz) indicating the moiety is in a rigid environment. Conversely, the narrow ^{1}H line widths observed for the benzyl functionality (14.0 – 18.0 kHz) indicates a more mobile environment. These results correlate with CP kinetic data which suggests the $-CH_2CH_2-$ bridging group resides in the pore wall and the $-CH_2C_6H_5$ tether projects into the pore.

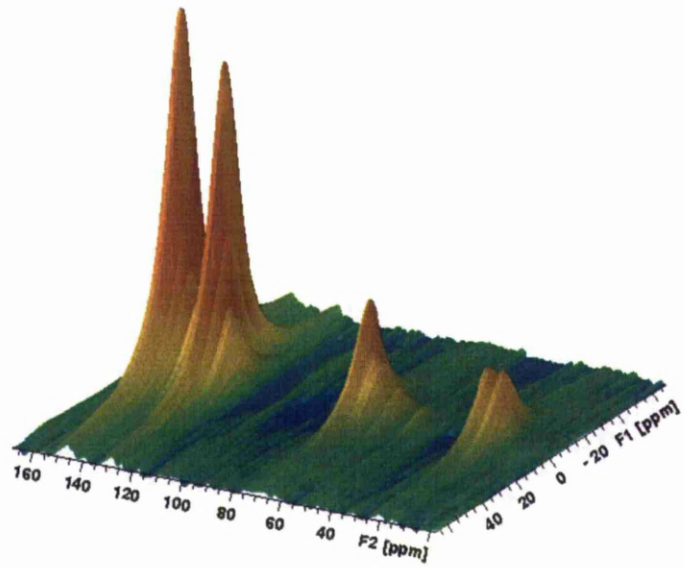

Figure 4.43 $^{1}H-^{13}C$ WISE NMR spectrum of -CH=CH-/-$CH_2C_6H_5$ PMO using a contact time time of 200 μs and an MAS rate of 8 kHz

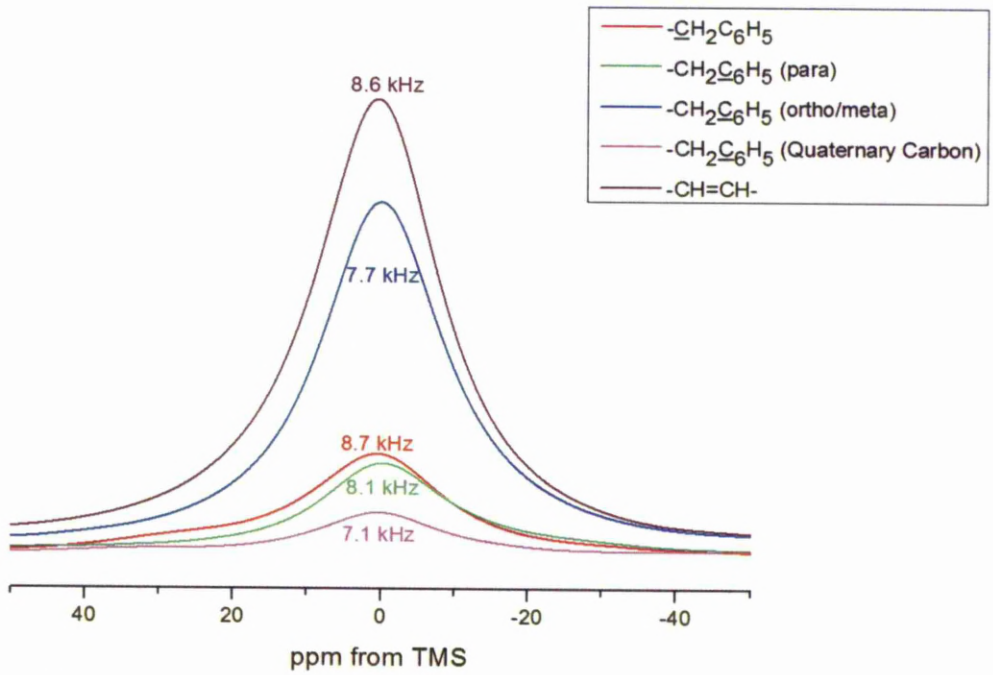

Figure 4.44 ^{1}H projection for $^{1}H-^{13}C$ WISE NMR –CH=CH-/ -$CH_2C_6H_5$ functionalsied PMO

The ^{1}H-^{13}C CP kinetics show slightly longer $T_{1\rho}$ times indicating a more mobile environment compared to the $-CH_2CH_2-$/ $-CH_2C_6H_5$ functionalised silica, this is unexpected as the rigid –CH=CH- bond should produce a shorter $T_{1\rho}$ time. The ^{1}H projection for the –CH=CH-/ $-CH_2C_6H_5$ functionalised silica show similar peak widths for both the bridging and tether functional groups. Similarly to the CP kinetics data this suggests the $-CH_2C_6H_5$ tether group is in a more rigid environment. The narrowing of the peak widths may be due to the efficient spin diffusion which may be caused by the increased rigidity of the –CH=CH- group increasing the residual dipolar coupling present. This allows magnetisation to be transferred between the two organic groups allowing at very low contact times (200 μs). The overall ^{1}H-^{13}C kinetic curve for the –CH=CH-/ $-CH_2C_6H_5$ functionalised silica differs from the other two organosilanes. The initial rate of magnetisation transfer is much faster indicated by the sharp rise in signal intensity.

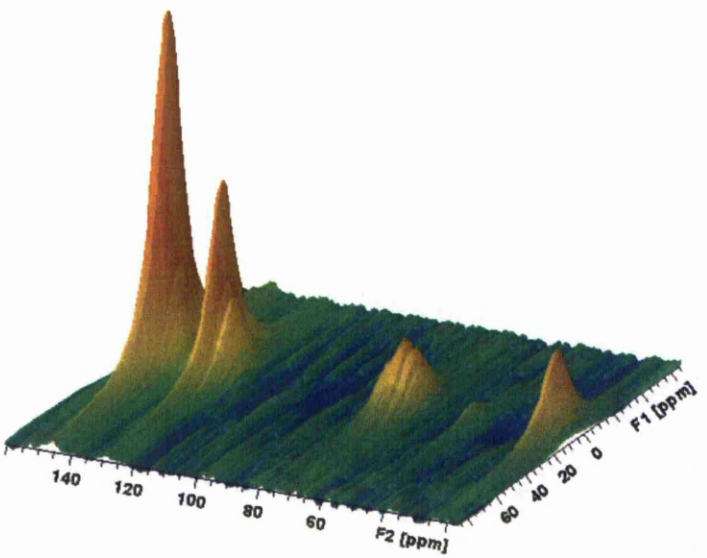

Figure 4.45 ^{1}H–^{13}C WISE NMR spectrum of -CH=CH-/-$CH_2C_6H_5$ PMO using a contact time time of 50 μs and an MAS rate of 8 kHz

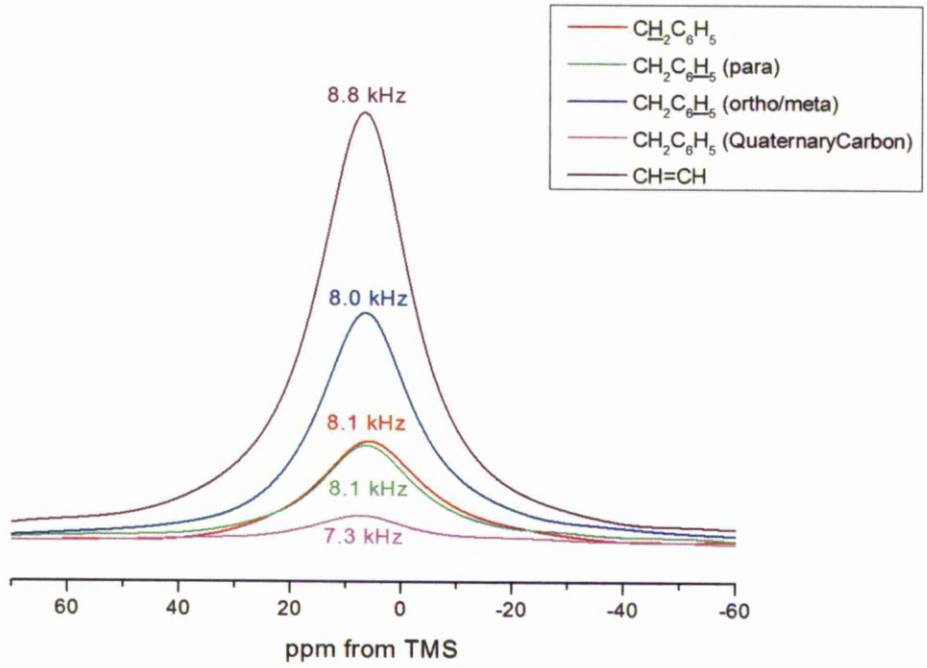

Figure 4.46 ^{1}H projection for ^{1}H-^{13}C WISE NMR –CH=CH-/ -$CH_2C_6H_5$ functionalsied PMO

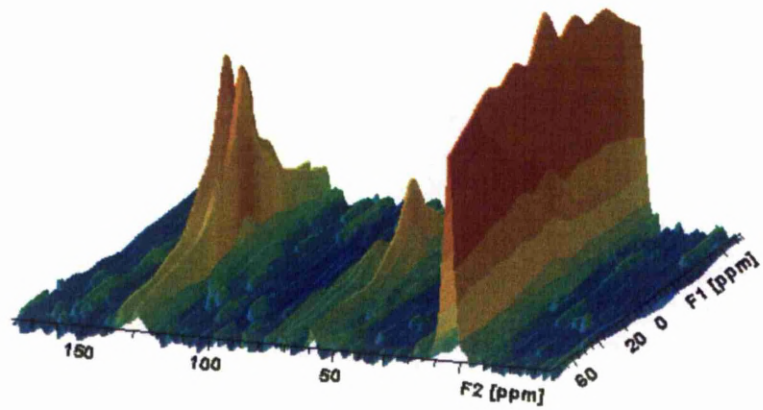

Figure 4.47 ^{1}H–^{13}C WISE NMR spectrum of –CH_2CH_2-/-C_6H_5 PMO using a contact time time of 200 µs and an MAS rate of 8 kHz

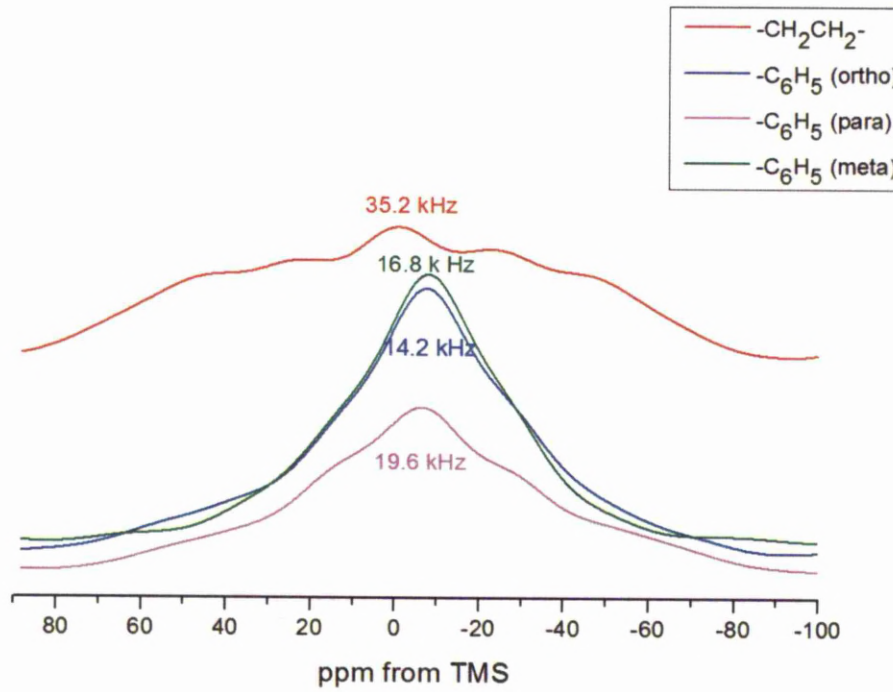

Figure 4.48 ^{1}H projection for ^{1}H-^{13}C WISE NMR $-CH_2CH_2$-/ $-C_6H_5$ functionalsied PMO

The broader resonance corresponding to the $-CH_2CH_2$- bridging group (35.2 kHz) indicates the functionality is in a more rigid environment compared to the $-CH_2CH_2$-/ $-CH_2C_6H_5$ silica (20 kHz). This coinsides with the ^{1}H-^{13}C CP kinetics data which shows a much larger proportion of the bridging tether resides in the bulk of the pore wall. The I_S/I_F value for $-CH_2CH_2$-/ $-CH_2C_6H_5$ is 1.28 indicating the majority of the bridging group is projecting into the pore, whereas, $-CH_2CH_2$-/ $-C_6H_5$ gives a value of 0.40 implying the majority of the group riside within the pore wall. Slightly broader resonances corresponding to the benzene ring are aslo observed compared to the tether groups of the $-CH_2CH_2$-/$-CH_2C_6H_5$ PMO. This may be due a higher ratio of the tether groups residing in the pore wall as opposed to the pore surface.

By analysing the three PMOs on a mesoscopic and molecular level we have shown that the most selective silica for chromatographic separations is synthesised using the $-CH_2CH_2$- and $-CH_2C_6H_5$ functionalised silica precursors. On a mesoscopic level the spherical morphology will produce the densest packing of the column. The high surface areas and large pore sizes should provide good mass transfer and high stationary phase-analyte interactions to produce and efficient column. Analysis

through solid state NMR has shown the $-CH_2CH_2-$/ $-CH_2C_6H_5$ functionalised silica precursors produce the most condensed silica which will reduce the number of acidic surface silanol groups. The two functionalities are distributed homogeneously throughout the materials and we have shown that for this material the tether moiety is projecting out into the pore and therefore is able to interact with and separate analytes.

4.10 Chromatographic Separation

Polycyclic aromatic hydrocarbons (PAHs) are environmental contaminants produced through industrial combustion processes, burning wood and fossil fuels. PAHs have carcinogenic and mutagenic properties and so the presence of these compounds are tested in air, water, soil and tissue samples. Chromatography has been used to detect these compounds from its inception. In 1971 research by Schmit *et al.* showed improved separation of the PAH compounds could be achieved through using a chemically bonded octadecylsilane stationary phase.[166] Reversed-phase columns have become the most commonly used method for the separation of PAH compounds, though not all columns provide the same level of selectivity. In fact, only a small number of columns are able to separate all 16 standard PAH compounds.[167]

There are numerous reversed-phase columns available today though it is often difficult to compare stationary phases. Manufacturers use non-standard separation methods optimised specifically to show the column produced has a superior efficiency compared to other stationary phases.[168] The PAH (poly aromatic hydrocarbon) compounds are used as a standardised test to compare the retentively and selectivity of different columns.

Acetonitrile is the most commonly used mobile-phase for reversed-phase chromatography as the physical properties such as UV adsorption, viscosity and boiling point are well suited to HPLC. Acetonitrile is a bi-product in the manufacturing of acrylonitrile, which is used in the synthesis of plastics and resins, therefore the volume of acetonitrile available is not constant but depended on the demand of plastic. As a solvent acetonitrile is toxic and disposed through chemical waste.[169] We have shown that the $-CH_2CH_2-$/ $-CH_2C_6H_5$ functionalised stationary phase is able to produce sufficient separation using a water/ methanol mobile phase to provide a more eco-friendly separation process.[170]

The PAH solution contains the 16 compounds shown in Figure 4.49. The $-CH_2CH_2-$/ $-CH_2C_6H_5$ (80/20) organosilica was able to separate nine of these compounds. Of the nine compounds separated anthracene, fluoranthene, benzo(a)anthracene, benzo(k)fluoranthene and indeno(1,2,3-cd)pyrene show well resolved peaks using this stationary phase. The remaining analytes were retained on the column.

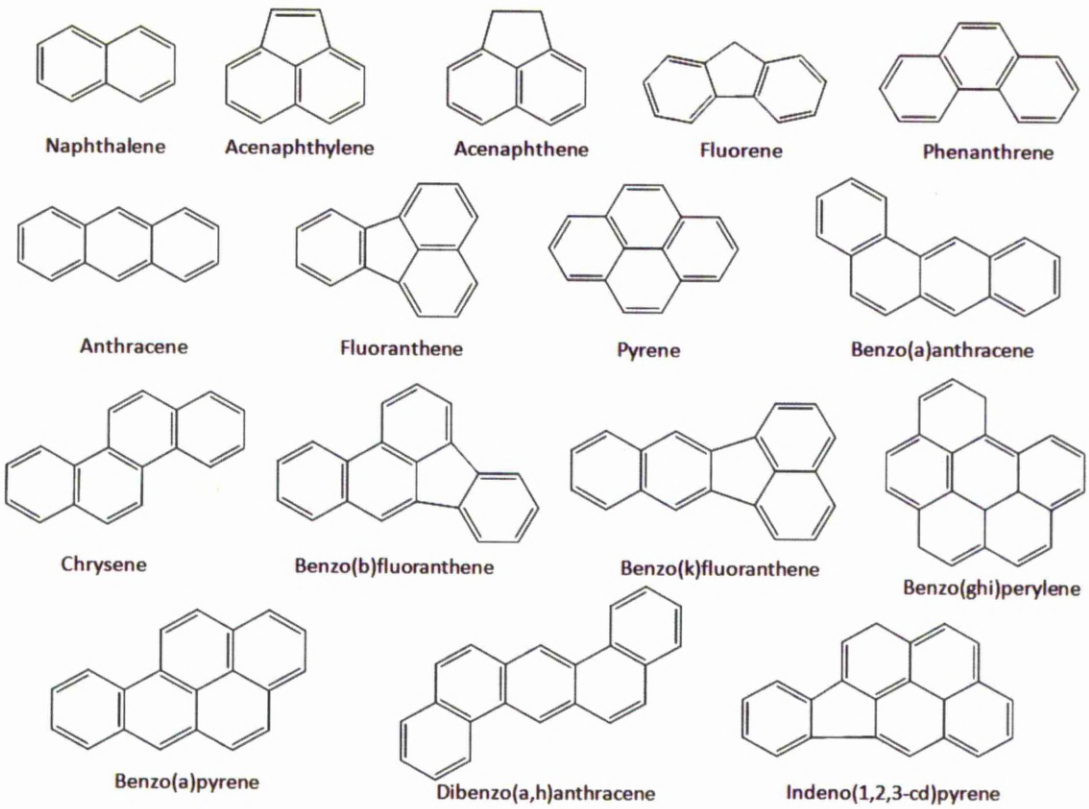

Figure 4.49 Chemical compounds used in the PAH test

Some of the larger compounds do not elute under these conditions, this could either be due to the high carbon content of the column having a stronger interaction with the larger hydrocarbons or the compound becoming trapped within the smaller pores of the stationary phase. As the larger hydrocarbons can be eluted, but not separated, by using 100% methanol as a mobile phase the retention is more likely due to the strong hydrophobic interactions between the analytes and stationary phase.

4.10.1 PAH Test

Research by Wise and May,[65,167] whom developed the PAH test, showed the separation of the polyaromatic hydrocarbons is dependent on several factors. The pore diameter and surface area of the silicate, the type of bonded phase and the density of coverage all effect the selectivity of the phase. The chromatogram for the $-CH_2CH_2-$/ $-CH_2C_6H_5$ PMO shows the separation of nine of the PAH compounds. The elution order of the compounds was determined by running each compound individually and comparing the retention times to the PAH mixture. The stationary phase produces resolved peaks for these compounds. Reversed-phase columns which produced well resolved peaks for Benzo(ghi)perylene and Indeno(1,2,3-cd)pyrene are considered to have high selectivity.[171] As shown in Figure 4.50 Indeno(1,2,3-cd)pyrene is separated into a resolved peak though Benzo(ghi)perylene remains on the column. As discussed above, increasing the organic content of the mobile phase removes the compound so it is unlikely that the analyte is trapped within the pores.

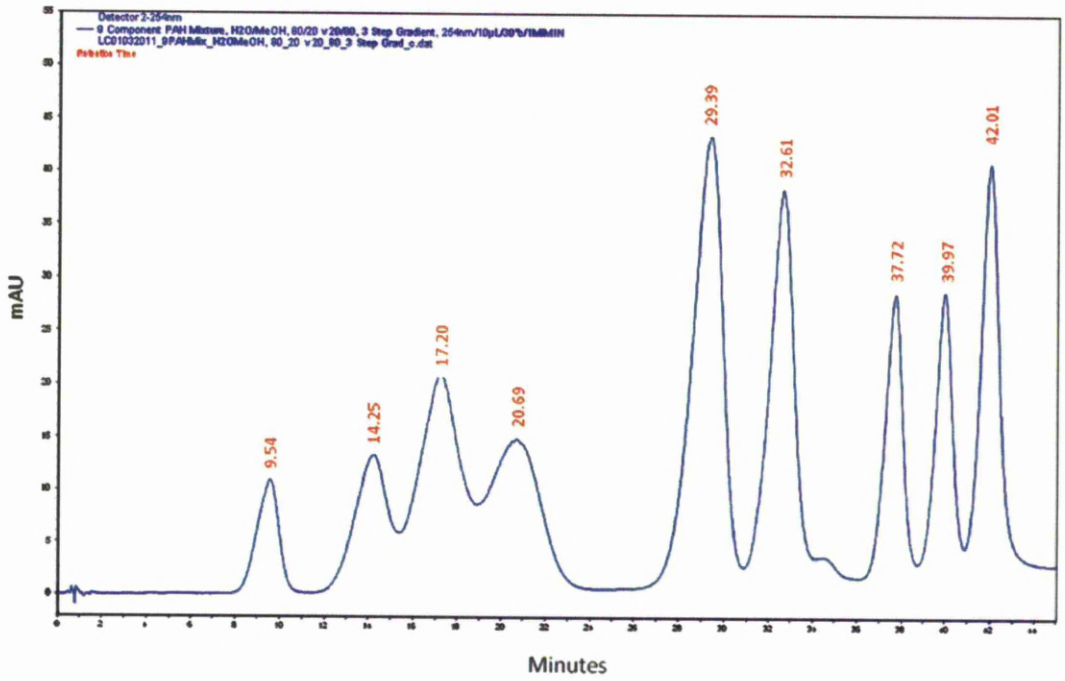

Figure 4.50 Chromatogram of the separation of PAH chemical using the $-CH_2CH_2-$/ $-CH_2C_6H_5$ functionalised column

Table 4.15 Results of PAH test for $-CH_2CH_2-$/ $-CH_2C_6H_5$ functionalised column

Analyte	Elution order	Retention Time (minutes)	Stock solution concentration (mg/mL)	Volume (µL)
Napthalene	1	9.54	1	10
Acenaphthylene	2	14.25	1	100
Acenaphthene	3	17.20	1	50
Fluorene	4	20.69	1	5
Anthracene	5	29.39	1	1
Fluoranthene	6	32.61	1	10
Benzo(a)anthracene	7	37.72	0.1	100
Benzo(k)fluoranthene	8	39.97	1	50
Indeno(1,2,3-cd)pyrene	9	42.01	1	50

Research by Wise and Jinno *et al.* [172,173] has shown planar molecules have a stronger interaction with the bonded phase and therefore are more strongly retained. The incorporation of a five membered ring in the Indeno(1,2,3-cd)pyrene compound creates a slight puckering effect. This reduces the retention of the analyte compared to the planar Benzo(ghi)perylene allowing the analyte to elute (as shown in Figure 4.51).

The elution of benzo(a)anthracene is also observed though the isomer chrysene is not. Research by Wise and Jinno *et al.* observed that retention of polyaromatic compounds was also effected by the length-to-bredth (L/B) ratio. A mixture of isomers will elute in order of increasing L/B. Benzo(a)anthracene has an L/B value of 1.58 will elute before chrysene (1.72).[174] It is thought that analytes which are long and narrow can be dispersed in between the bonded phases of the silica stationary phase and therefore increases their interaction with the stationary phase. More "square like" molecules are not able to penetrate in-between the surface organic groups. Due to the high carbon loading the interaction between the bonded phase and chrysene may have been sufficient to impede elution.

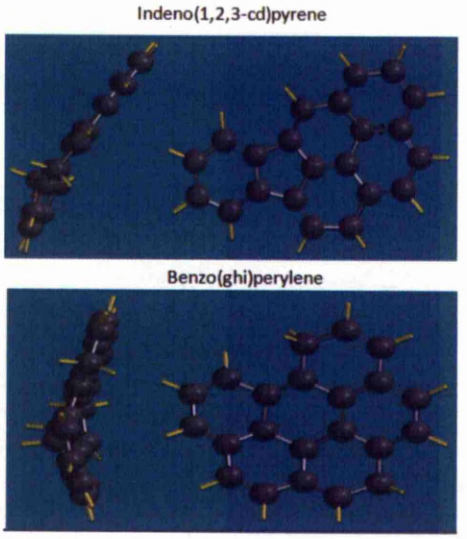

Figure 4.51 Molecular structure of Indeno(1,2,3-cd)pyrene and Benzo(ghi)perylene

4.10.2 Tanaka Test

As mentioned above it can be difficult to select a column with the optimum properties for the user's needs. This is due to manufacturers using non-standard separations to highlight the columns selectivity making it difficult to compare different columns. The Tanaka test is another standardised test used to assess and compare the physio-chemical properties of columns through analysing the retention, hydrophobicity, steric selectivity, silanol capacity and ion exchange capabilities of a column. The test compares the relative capacity factors of set molecules, the k' factors are then normalised and presented in a radar plot allowing users to easily compare several columns.[168,175,176]

Retention capacity, hydrophobicity and steric selectivity.

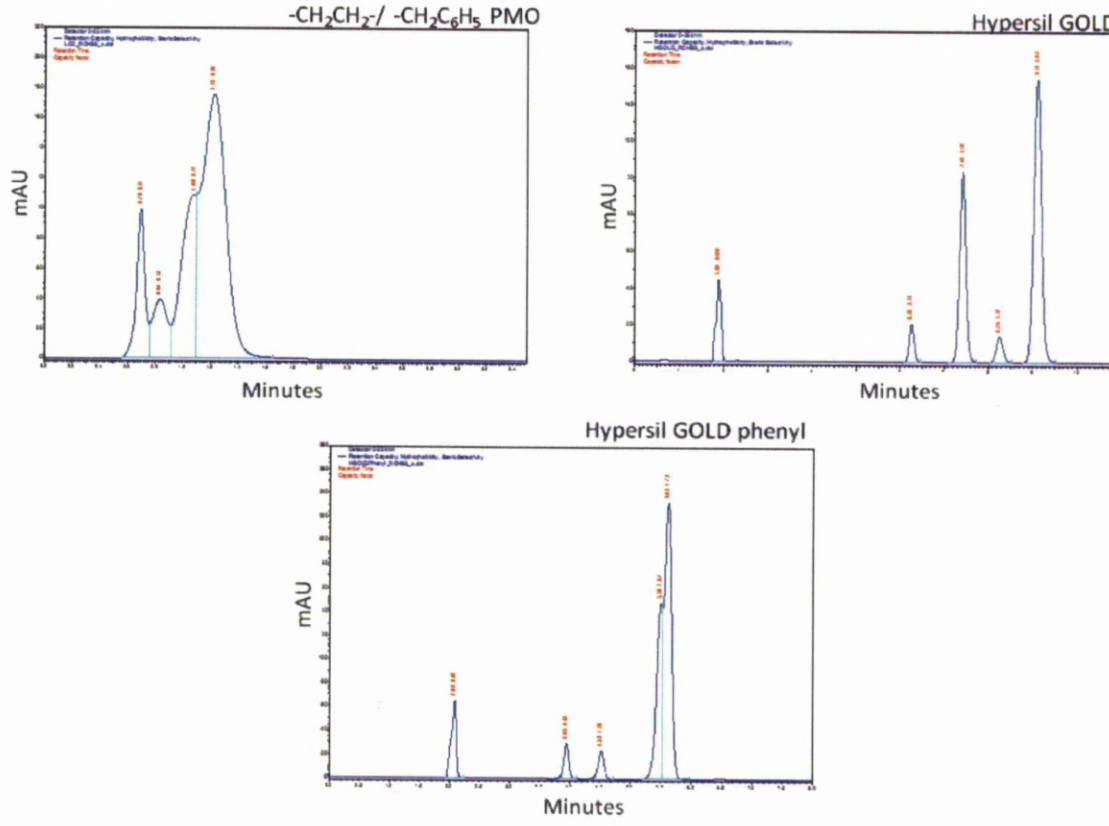

Figure 4.52 Chromatograms comparing the retention capacity, hydrophobicity and steric selectivity of the reversed phase columns

Table 4.16 Capacity factor for the reversed phase columns

Column	Capacity factor (k)			
	Butylbenzene	o-Terphenyl	Pentylbenzene	Triphenylene
$-CH_2CH_2-$/ $-CH_2C_6H_5$	0.31	0.68	0.34	0.96
Hypersil GOLD	2.32	2.96	3.41	3.87
Hypersil GOLD phenyl	0.91	1.68	1.19	1.74

The retention capacity (K') of pentylbenzene is dependent on the porous structure of the silica and the type and density of the bonded phase. This technique can

therefore be used to analyse the surface area of the silica and level of surface coverage with bonded organic groups. The capacity factor, which describes the migration rate of an analyte, for the $-CH_2CH_2-$/ $-CH_2C_6H_5$ functionalised silica is much lower compared to the C_{18} and phenyl functionalised columns. Microanalysis shows high levels of organic present (21.6%) so it is unlikely that the low capacity factor is due to the surface coverage. It is more plausible that the retention capacity is reduced because of the small pores (<25 Å) as shown by the N_2 adsorption/ desorption isotherms. These smaller pores will restrict the mass transfer of analytes increasing band broadening. Furthermore if the pores are of comparable size to the analytes, this can restrict access within the porous network reducing the surface area available. The pore size distribution (Figure 4.12) shows there are a range of pore sizes within this material, some of which will be too small for pentylbenzene to permeate.

The hydrophobicity is measured by comparing the retention times of butylbenzene and pentylbenzene, which differ by CH_2. The most hydrophobic column was the Hypersil GOLD. Although the retention time of pentylbenzene and butylbenzene on the $-CH_2CH_2-$/ $-CH_2C_6H_5$ PMO was shorter, compared to the other columns the selectivity ($\alpha = K'_B/K'_A$) of the two compounds (1.10) are similar to those observed for the Hypersil GOLD phenyl column (1.31).

The steric selectivity of the column is determined by the ratio of the capacity factor of triphenylene and o-terphenyl (Figure 4.52). The mobile and non-planar structure of o-terphenyl prevents strong interaction with the bonded phase and so elutes before the more rigid, planar triphenylene. The retention of these analytes is affected by the spacing of the organic groups and the type of functional group incorporated. The retention time of the two analytes where highest using the C_{18} and phenyl functionalised Hypersil columns. However the selectivity (α) of the analytes is greater for the $-CH_2CH_2-$/ $-CH_2C_6H_5$ functionalised PMO (1.41) compared to HypersilGOLD (1.31) and HypersilGOLD phenyl (1.04). As the $-CH_2CH_2-$/ $-CH_2C_6H_5$ functionalised silica does not contain any end-capping groups, unlike the Hypersil columns, this could explain the reduced retention. We have shown that our column

produces the optimum selectivity for steric hindrance, though does not display high efficiency compared to the Hypersil columns. The high selectivity may be produced by using a stationary phase with the organic groups incorporated into the framework, which creates a more homogenous distribution of the functional groups.

Silanol Capacity

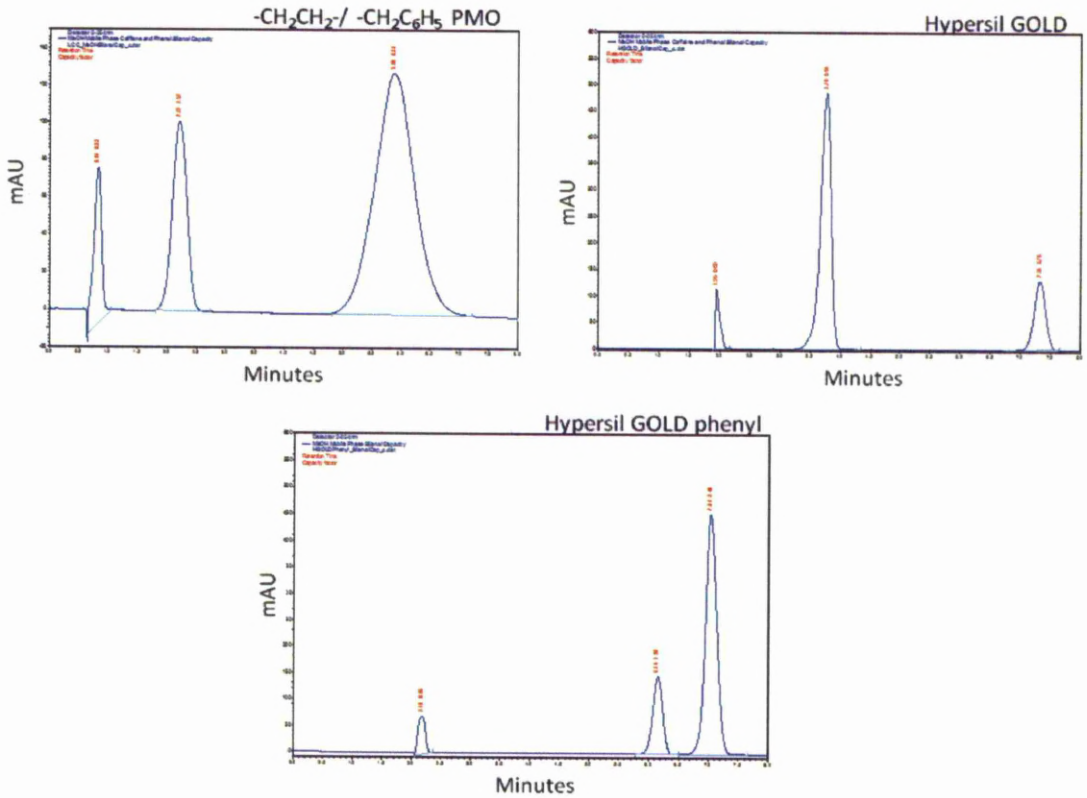

Figure 4.53 Chromatograms comparing the silanol capacity of the reversed-phase columns

Table 4.17 Capacity factors

Column	Capacity factor (k)	
	Phenol	Caffeine
$-CH_2CH_2-$/ $-CH_2C_6H_5$	2.51	8.37
Hypersil GOLD	2.77	0.95
Hypersil GOLD phenyl	1.98	2.40

The silanol capacity determines the level of hydrogen bonding within the material and is determined by the number of free silanol groups. The $-CH_2CH_2-$/ $-CH_2C_6H_5$ PMO shows a much higher silanol capacity compared to the other columns. This is to be expected as the Hypersil columns have a reduced number of silanol groups due to end-capping procedures, whereas the $-CH_2CH_2-$/ $-CH_2C_6H_5$ contains no end-capping groups. The ^{1}H-^{29}Si CP/MAS NMR spectrum of the $-CH_2CH_2-$/ $-CH_2C_6H_5$ organosilane (Figure 4.30) shows the material is predominantly comprised of T^2 and T^3 sites. This suggests large number of silanol groups remain. Despite the increased number of silanol groups the stationary phase still has comparable levels of hydrophobicity. It is also important to note the elution order of caffeine and phenol. The C_{18} functionalised Hypersil GOLD column elutes caffeine first followed by phenol whereas both the phenyl functionalised Hypersil GOLD and $-CH_2CH_2-$/ $-CH_2C_6H_5$ functionalised silica elute phenol before caffeine. The reversed elution order may be due to stronger electrostatic interactions between caffeine which is more polar due to the amide groups present, and the bonded aromatic groups on the silica surface. $-CH_2CH_2-$/ $-CH_2C_6H_5$ functionalised column has selectivity similar to Hypersil GOLD phenyl.

Ion Exchange

Ion Exchange Capacity at pH 2.7

The ion exchange capacity is determined by measuring the retention capacity of a

basic compound (benzylamine) and a slightly acidic compound (phenol). At pH 2.7 the majority of silanol groups are undissociated and do not interact with the analytes (isoelectric point of silica is pH 1.7-3.5). Therefore the retention capacity is determined purely on the loading level and type of organic groups incorporated. At pH 7.6 most silanol groups are deprotonated (SiO^-). The deprotonated silanol groups cause ion exchange interactions with the phenol analyte. The retention time of phenol can be compared to non-ionic benzylamine which should be unretained.

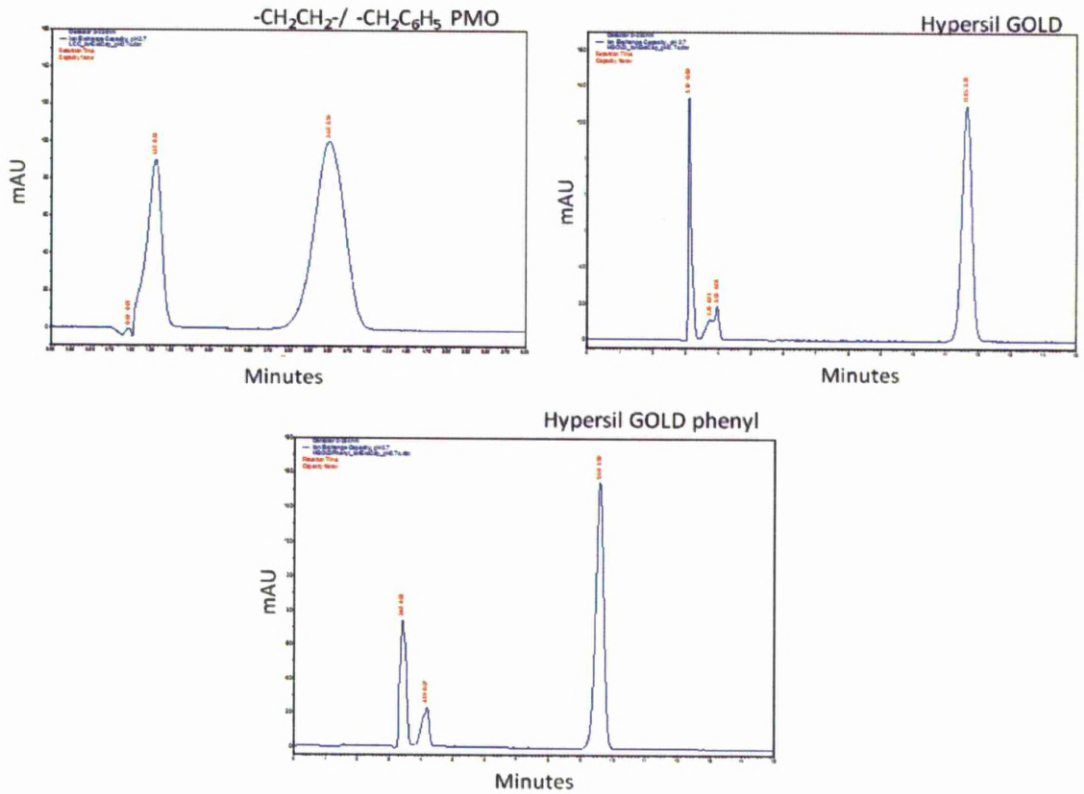

Figure 4.54 Chromatograms comparing the ion exchange capacity of the reversed-phase columns at pH 2.7

Table 4.18 Capacity factors

Column	Capacity factor (k)		K_b/K_p
	Benzylamine	Phenol	
$-CH_2CH_2-$/ $-CH_2C_6H_5$	0.23	2.53	0.091
Hypersil GOLD	0.25	2.77	0.090
Hypersil GOLD phenyl	0.27	1.90	0.142

Although all three columns show very similar capacity factors for benzylamine, however the retention of phenol differs. The ratio of the capacity factors (benzylamine/ phenol) show an optimum for the $-CH_2CH_2-$/ $-CH_2C_6H_5$ and Hypersil GOLD. As the silanol groups do not affect retentivity, the longer retention times are due to the high loading level of organic groups and the long alkyl chains.

Ion exchange Capacity (pH 7.6)

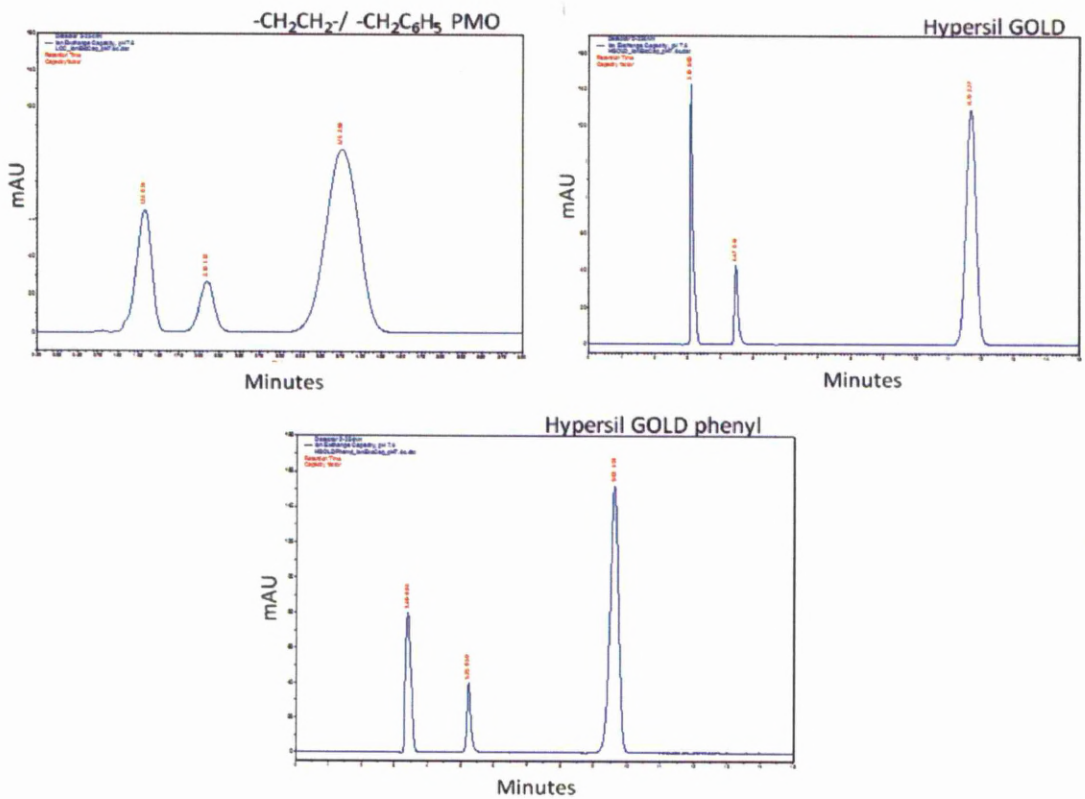

Figure 4.55 Chromatograms comparing the ion exchange capacity of the reversed-phase columns at pH 7.6

Table 4.19 Capacity factors

Column	Capacity factor (k)		K_b/K_p
	Benzylamine	Phenol	
$-CH_2CH_2-/-CH_2C_6H_5$	1.12	2.76	0.406
Hypersil GOLD	0.44	2.77	0.159
Hypersil GOLD phenyl	0.58	1.91	0.307

A large increase in capacity factor for benzylamine is observed for the $-CH_2CH_2-/-CH_2C_6H_5$ functionalised column. This is due to the higher number of silanol groups for this stationary phase as shown by the high silanol capacity factor and the ^{1}H-^{29}Si CP/MAS NMR spectrum. This can simply be reduced through end-capping. Though the $-CH_2CH_2-/-CH_2C_6H_5$ functionalised stationary phase contains a high number of silanol groups, the ion exchange capacity at pH 7.6 is similar to that of the Hypersil GOLD column.

Radar plots

The results of the separations are normalised and presented using a radar plot to allow easy comparison of the selectivity properties of different columns. The radar plots illustrate the selectivity of the columns for each Tanaka test relative to the other columns.

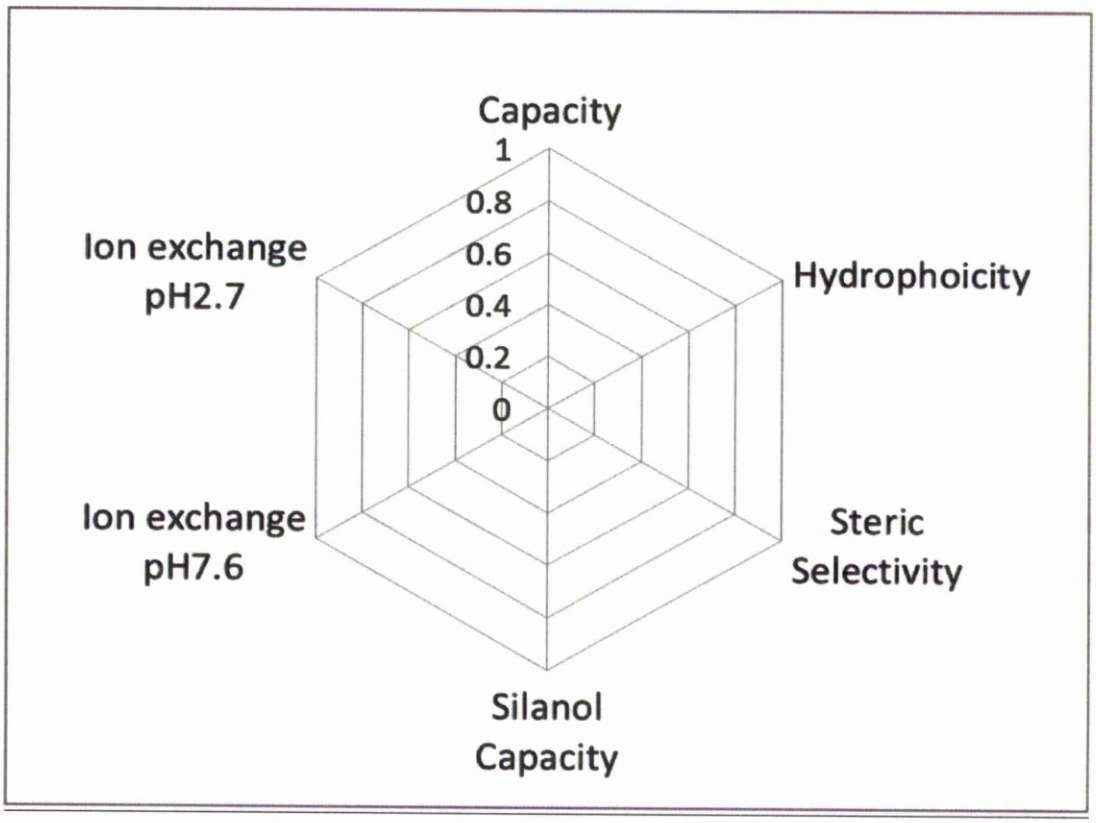

Figure 4.56 Tanaka test radar plots

The radar plots show the selectivity properties of $-CH_2CH_2-/-CH_2C_6H_5$ functionalised silica compared to the C_{18} and phenyl functionalised commercially available columns. The plot highlights that the PMO shows good selectivity, or at least comparable selectivity with the commercially available columns, in all areas with the exception of capacity factor. Due to the incorporation of the aromatic compounds the selectivity is more comparable with Hypersil GOLD phenyl than Hypersil GOLD. Both columns contain aromatic compounds which are able to act as a lewis base facilitating ion exchange. The radar plots show that both columns perform well in this area though Hypersil GOLD phenol showed improved selectivity for pH 2.7 wherein the retention capacity is determined purely on the loading level and type of organic groups incorporated whereas the $-CH_2CH_2-/-CH_2C_6H_5$ column is more efficient at pH 7.6 wherein the unprotonated silanol groups facilitate ion-exchange. This may be due to the increased number of surface silanol groups present on the surface of the $-CH_2CH_2-/CH_2C_6H_5$ silica.

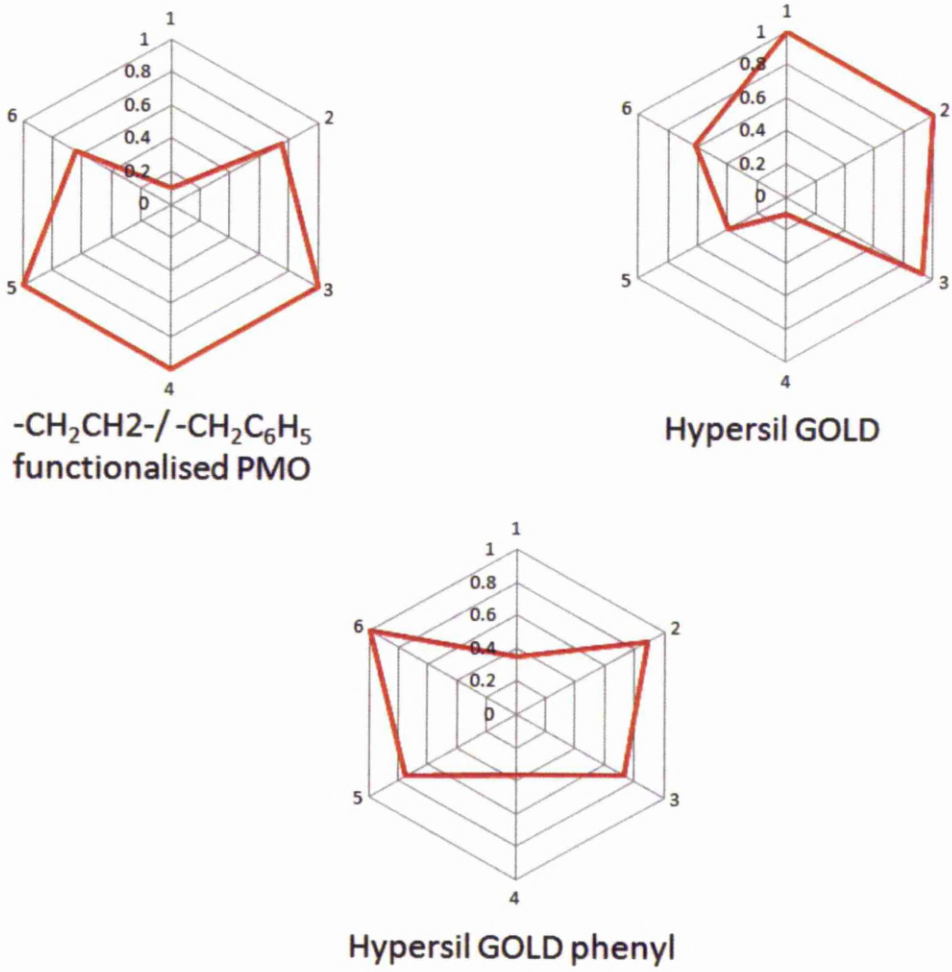

Figure 4.57 Tanaka Radar plots of the $-CH_2CH_2-$/ $-CH_2C_6H_5$ functionalised PMO and two commercially available columns.

The radar plot produce by the $-CH_2CH_2-$/$-CH_2C_6H_5$ functionalised stationary phase shows similar selectivity preferences to commercially available Resolve C18 and Spherisorb ODSB.[168] The radar plots not only highlight the key areas where the $-CH_2CH_2-$/$-CH_2C_6H_5$ functionalised column will perform best such as hydrophobicity, steric selectivity, silanol capacity and ion exchange (pH 7.6), but it has also shown that the column made is comparable with commercially available columns. The Tanaka test has shown the PMO has enhanced efficiency for the steric selectivity compared to HypersilGOLD and HypersilGOLD phenyl (Figure 4.57).

Through the use of organosilanes precursors we have synthesised a reversed-phase

stationary phase with high carbon content (21.56 %). ^{1}H-^{13}C CP kinetics has shown that the majority of the functionality incorporated resides at the pore surface, and so can interact with the analytes. This has been shown by the well resolved separation of nine of the PAH compounds. The radar plots indicate the incorporation of aromatic moieties increases the ion exchange selectivity of the column. The performance of the $-CH_2CH_2$-/ $-CH_2C_6H_5$ PMO is similar to HypersilGOLD phenyl which uses a grafting procedure to incorporate the organic groups. As the selectivity for these two columns are similar this suggests the $-CH_2C_6H_5$ tether is projecting into the pore and interacting with the analytes which is indicated through the ^{1}H-^{13}C CP kinetics and ^{1}H-^{13}C WISE NMR spectra. The Tanaka test has also highlighted the high silanol selectivity and the low capacity of the $-CH_2CH_2$-/ $-CH_2C_6H_5$ functionalised silica. The presence of the surface silanol groups is shown by the ^{1}H-^{29}Si CP/MAS spectrum, however these polar groups cause a reduction in the capacity factor of the column. End-capping the silanol groups will improve the capacity factor and increase the carbon loading of the silica.

The analyte peaks of the $-CH_2CH_2$-/ $-CH_2C_6H_5$ PMO are much broader compared to the HypersilGOLD and HypersilGOLD phenyl columns. This is due to the broader particle size distribution of the PMO column as shown by the SEM images and particle size analysis. Sizing of the silica beads which is applied to the commercially available Hypersil columns will improve the packing density of the column and reduce band broadening.

4.11 Conclusions

In this chapter we have presented the synthesis for three new RP columns containing high levels of carbon loading (*ca.*22%). We have demonstrated how the acid optimisation of the synthesis can improve the silica on a mesoscopic scale (larger surface area, increasing pore size, formation spherical silica beads with a narrower particle size distribution). These phases were then compared on a mesoscopic and molecular level to determine which material was most suitable for reversed-phase separations.

Highly ordered silica is required for HPLC analysis as this is indicative of a uniform porous structure. Additionally it is desirable to produce small spherical beads as these create a more densely packed column, thus improving the efficiency of the stationary phase. The ordering and morphology of the PMOs varied depending on the organic group incorporated. The silica precursors used effect the formation of the silica around the micelles and the hydrolysis rate (and therefore the size, size distribution and morphology) of the silica. The materials produced were optimised by varying the acid concentration.

Figure 4.58 schematically shows the optimisation methods, and their effect on the final structure of the bi-functionalised silicas produced.

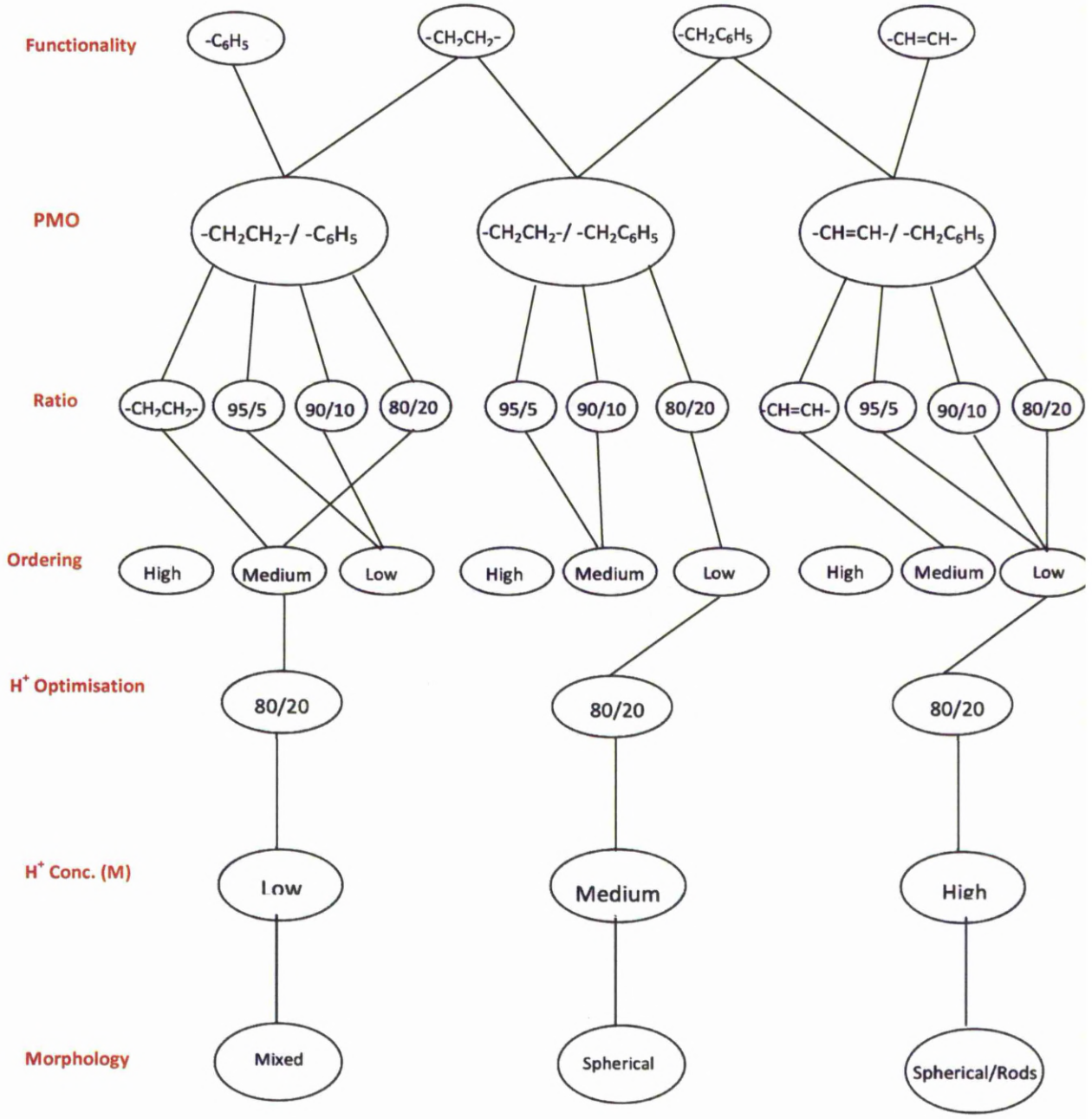

Figure 4.58 Schematic showing the acid optimisation process for the synthesis of the bi-functionalised PMOs.

All three PMOs showed type IV N_2 adsorption/ desorption isotherms indicating pore sizes in the mesoporous range high surface areas (700-1000 m^2/g). The morphology of the silica produced was very varied due to the different synthetics procedures. The -CH_2CH_2-/-$CH_2C_6H_5$ PMO has spherical morphology which is ideal for column packing, though the SEM images showed a range of particle sizes. The morphology of –CH=CH-/ -$CH_2C_6H_5$ PMO was improved after the optimisation though still contained a mixture of rods and spheres. The –CH_2CH_2-/ -C_6H_5 PMO contains a mixture of rods and aggregated spheres and gyroids, this will create a very poorly packed column and inefficient separations.

NMR spectroscopy was successfully used to determine not only the presence of the two different organic groups but could also determine whether the functionality was on the pore surface and able to interact with analytes or trapped within the pore walls. ^{1}H-^{13}C WISE NMR and ^{1}H-^{13}C CP/MAS kinetics experiments indicated a higher ratio of tether groups have restricted mobility for the –CH=CH-/ -$CH_2C_6H_5$ and –CH_2CH_2-/ -C_6H_5 functionalised silica, which is caused by the tether groups becoming trapped within the pore walls of the lower ordered material. We were also able to confirm the homogeneity of the two functionalities to ensure uniform interaction between the stationary phase and analyte, thus reducing band broadening.

The –CH_2CH_2-/ -$CH_2C_6H_5$ PMO showed greater potential as a new stationary phase due to the high surface area, spherical morphology and the higher ratio of organic moieties at the silica surface. This column was chosen to be packed and compared to commercially available RP columns.

PAH and Tanaka tests we used to demonstrate the efficiency and selectivity of the new stationary phase. Good separation of nine PAH analytes indicates the column works effectively for non-polar compounds. The selectivity could be further improved by refining the particle sizes to produce a more monodisperse particle size distribution.

The Tanaka tests showed the $-CH_2CH_2-$/ $-CH_2C_6H_5$ functionalised silica had comparable selectivity to commercially available columns. As the silica had not undergone an end-capping procedure many surface silanol groups will remain unlike the Hypersil silica columns. These groups reduce the selectivity of a reversed phase column, so the results appear very promising. The functionalised PMO shows enhanced performance within ion exchange and steric selectivity.

Chapter 5 -

Investigating the Interactions between a Hydrophobic Phase Bonded onto silica and Toluene

Chapter 5. - Investigating the Interactions between a Hydrophobic Phase Bonded onto silica and Toluene

5.1 Introduction

Adsorption chromatography depends on the interaction between the analyte and the groups chemically bound to the surface of the stationary phase. For reversed-phase (RP) chromatography these moieties are commonly n-alkyl chains (C_{18}, C_{12}) [177-179] and aromatic groups (phenyl or benzyl) [180-182] which separate mixtures of analytes through solvophobic interactions.[60,183] The strength of these interactions is dependent on the type and number of non-polar moieties within the analytes.

Initially both the analyte in the mobile phase and the organic groups of the stationary phase are surrounded by ordered water molecules. As the analyte partitions to the surface of the stationary phase the amount of surrounding water molecules is reduced as water molecules return to the bulk disordered phase. Therefore the adsorption process of analytes in reversed-phase chromatography is entropically favourable.[184]

The selectivity of the column is determined predominantly by the type of ligand bound to the stationary phase. Table 5.1 lists the numerous columns available, though at present there is no rational way to predict which ligand should be used to give the best separation for a specific group of analytes. As a rule of thumb; the more hydrophilic (polar) the target analyte, the more hydrophobic (non-polar) the ligand needs to be.

Table 5.1 Common stationary phases available

Column Name	Manufacturer	Functionality	Particle Size (µm)	Pore Size (Å)	Surface Area (m^2/g)	Reference
Kromasil	Kromasil	C_{18}/ C_8	2.5, 5	100, 300	330	[185-187]
LiChrosorb RP 18	Merck	C_{18}	5, 7, 10		300	[188,186]
Spherisorb ODS	Waters	C_{18}	3, 5	80	220	[189]
Purospher	Merck	C_{18}				[185,187]
µBondapak	Waters	C_{18}	10-20	125	330	[187,190]
LiChroCART superspher	Merck	C_{18}/ C_8	4			[191]
Zorbax	Agilent	C_8	1.8, 5, 7	70		[189,191]
Nucleosil	Macherey-Nagel	C_{18}	3, 5, 10	100, 120	350	[191,192]
Hypercarb	Thermo Scientific	Porous graphitic Carbon (PGC)	3, 5, 7	250		[188]
Hypersil	Thermo Scientific	C_{18}/ C_8	3, 5, 10	120, 130, 190		[192]
Hypersil Phenyl BDS	Thermo Scientific	Phenyl	3, 5, 10	120		[193]

It is commonly known that due to different synthetic methods nominally identical RP materials can provide significantly different selectivity.[194,195] Reversed-phase materials are predominantly compared through chromatographic methods and analysis of the retention times of specific analytes. Standard tests such as the Englehardt, Tanaka and polyaromatic hydrocarbon (PAH) test provide information about column parameters such as hydrophobic selectivity, shape selectivity, hydrogen bonding capacity, ion exchange capacity and aromatic selectivity.[196,197,168,198,199,180,200,177,201] Although these tests enable users to determine which column will provide the optimum selectivity, they do not provide insight into how these slight chemical differences affect analyte/ stationary phase interactions.

The efficiency of a column is affected by many variables such as surface area, pore size, type of organic group incorporated, level of silica co-condensation, the particle size and how these particles are packed within the column.[38,133,202-204,132,205] Whilst the

mesoscopic properties are often analysed, very little research has been published comparing RP columns on a molecular level. Solid-state NMR can be used to provide structural information about these amorphous materials.[79] The majority of research analysing RP columns on a molecular scale use ^{1}H-^{13}C or ^{1}H-^{29}Si/CP MAS NMR techniques.[206-214] ^{1}H-^{13}C CP/MAS NMR can be used to confirm the chemical modification of the stationary phase and provide information about the conformation and mobility of the organic groups present. ^{1}H-^{29}Si CP/MAS NMR can be used to analyse the degree of co-condensation of the silica and the level of polymerisation between grafted alkyl chains. To the best of our knowledge previous research analysing RP silica on a molecular level examines only one or two of these aspects. To fully understand how RP columns function, a comprehensive study and comparison of the structural framework, conformation and mobility of multiple stationary phases is needed.

In this work, we have undertaken detailed structural analysis of three stationary phases on both a mesoscopic and molecular level. We have also studied the interactions between toluene and 1.7 µm Syncronis (containing monomeric $-C_{18}$ chains), Spherisorb ODS2 (containing polymeric C_{18} chains)[215] and a $-CH_2CH_2-/-CH_2C_6H_5$ 80/ 20 functionalised PMO (discussed in the previous chapter).

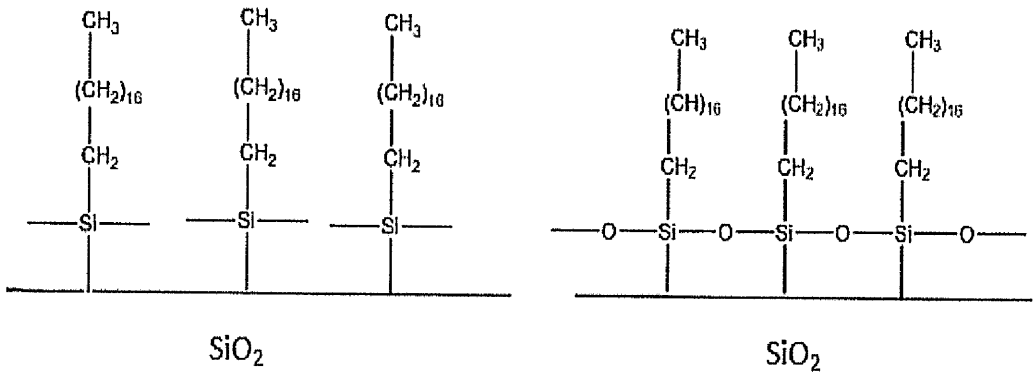

Figure 5.1 Schematic representation a monomeric (left) and a polymeric (right) $-C_{18}$ functionalised silica

The majority of HPLC stationary phases are synthesised *via* the sol-gel process. This uses the reaction of alkoxides to produce a silicate gel through a hydrolysis and condensation reaction which was first published by Dearing and Reid.[216] The reaction occurs through two step synthesis. First the alkoxides are hydrolysed to form hydroxyl groups. Then, the solid SiO_2 is formed through the polycondensation of these hydroxyl groups.[217-219]

Hydrolysis:

$$Si(OR)_4 + H_2O \leftrightarrow (HO)Si(OR)_3 + ROH$$

$$(HO)Si(OR)_3 + H_2O \leftrightarrow (HO)_2Si(OR)_2 + ROH$$

$$(HO)_2Si(OR)_2 + H_2O \leftrightarrow (HO)_3Si(OR) + ROH$$

$$(HO)_3Si(OR) + H_2O \leftrightarrow Si(OH)_4 + ROH \qquad \textbf{(5.1 to 5.4)}$$

Alcohol condensation (Alcoxolation):

$$\equiv Si - OR + HO - Si \equiv \leftrightarrow \equiv Si - O - Si \equiv + ROH \qquad \textbf{(5.5)}$$

Water Condensation (Oxolation):

$$\equiv Si - OH + HO - Si \equiv \leftrightarrow \equiv Si - O - Si \equiv + H_2O \qquad \textbf{(5.6)}$$

The hydrolysis and condensation reactions can occur simultaneously once the hydrolysis reaction is initiated, though alkoxides are not always fully hydroxylated and many intermediates are possible (shown by Equations 5.1 to 5.4). The type of polymer networks formed and the morphology are dependent on the synthetic conditions. Variations of the alkoxides, water/ alkoxide ratio, catalyst, temperature and aging time all alter the product formed.[220]

By using organoalkoxysilanes the sol-gel method can be altered to incorporate organic groups to create hybrid materials. Alternatively, post-synthetic functionalisation can be used to graft organic groups onto a pure silica surface by reacting organosilanes

with surface silanol group. However, this can lead to an inhomogeneous distribution of the functionality.[49,221] Stationary phases which are functionalised under anhydrous conditions using monofunctional silanes (for example **Cl**-Si$(CH_3)_2$-R), such as monochloro or monoalkoxy, are more commonly referred to as "monomeric" whereas trifunctionalsied silanes (for example **Cl**$_3$-Si-R) prepared in the presence of water are called "polymeric".[222]

The C_{18} chain of the 1.7 µm Syncronis silica was grafted post-synthetically using octadecyldimethylchlorosilane. (Trimethylsilyl)imidazole was then used to end-cap any remaining free silanol groups. The C_{18} group of Spherisorb ODS2 silica was bonded using octadecyltrimethoxysilane. The O-CH_3 groups can condense, thereby polymerising the grafted functionality (Figure 5.1). This reaction produces a denser coverage of the alkyl and shows greater selectivity (shown by increased α values) compared to monomeric phases. [222,223] A combination of hexamethyldisilazane and trimethylchlorosilane end-capping groups was used (approx. 50/50 mixture) to react with any remaining silanol groups.

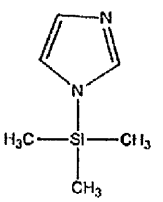

(Trimethylsilyl) Imidazole

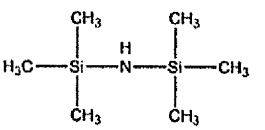

Hexamethyldisilazane

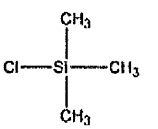

Trimethylchlorosilane

Figure 5.2 End-capping groups

Research by Yang *et al.* has shown that (trimethylsilyl)imidazole can be up to five times more efficient as an end-capping agent when compared to hexamethyldisilazane. The imidazole functionality is a better leaving group compared to NH_3 making the conjugate acid ($(CH_3)_3$-Si^+) more readily available. [224]

5.2 Characterisation of 1.7 µm Syncronis and Spherisorb Silica

The efficiency and selectivity of a column is determined not only by the loading level of organic functionality but is also dependent on the type of organic group and the mesoscopic parameters such as surface area, pore size, pore volume and the density of the column packing.[225,6,226,133,227,195,3]

5.2.1 Mesoscopic Properties of the Stationary Phases

The N_2 adsorption/ desorption isotherms for the 1.7 µm Syncronis and Spherisorb ODS2 stationary phases can be described as type IV isotherms with H2 hystereses loops. This indicates that both materials contain mesopores which are irregular in size and shape. The pore size distribution plots show the 1.7 µm Syncronis silica to have a slightly narrower pore size distribution (Syncronis – 40-120 Å, Spherisorb - 40-130 Å) though the average pore size for both materials are similar (Syncronis has an average pore size of 6.54 nm whereas Spherisorb ODS2 has an average pore size of 7.00 nm). The surface area of the 1.7 µm Syncronis is approximately double that of the Spherisorb stationary phase.

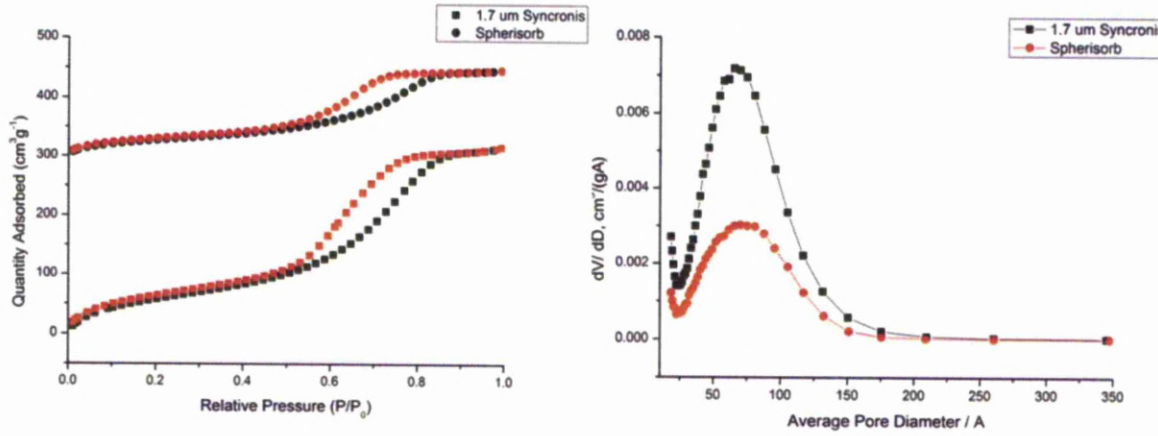

Figure 5.3 N_2 adsorption/ desorption isotherms and pore size distributions of 1.7 µm Syncronis and Spherisorb ODS2 silica (offset by 300 cm^3g^{-1})

Table 5.2 Mesoscopic properties of the stationary phases

Stationary Phase	S_{BET} (m^2/g)	D_{AV}^{ads} (nm)	V_{ads} (cm^3g^{-1})
1.7 µm Syncronis	238.2	6.54	0.534
Spherisorb ODS2	110.0	7.00	0.247

The 1.7 µm Syncronis silica has a smaller particle size (~1.7 µm) compared to the Spherisorb silica beads (~4.5 µm) and will therefore have larger external surface area for a given weight. The N_2 adsorption/ desorption isotherms confirm that the surface area of the two silicas are not solely dependent on particle size. As $p/p_0 \rightarrow 1$ the quantity of nitrogen adsorbed begins to plateau. This indicates that the isotherms observed are also produced by the internal porosity of the silica beads and not inter-particulate spacing. The surface area is therefore dependent on the internal porous structure. Both Syncronis and Spherisorb have similar pore sizes though Syncronis silica has a significantly larger pore volume. The larger volume will consequently reduce the overall surface area of the silica, reducing the capacity of the column.

5.2.2 Morphology

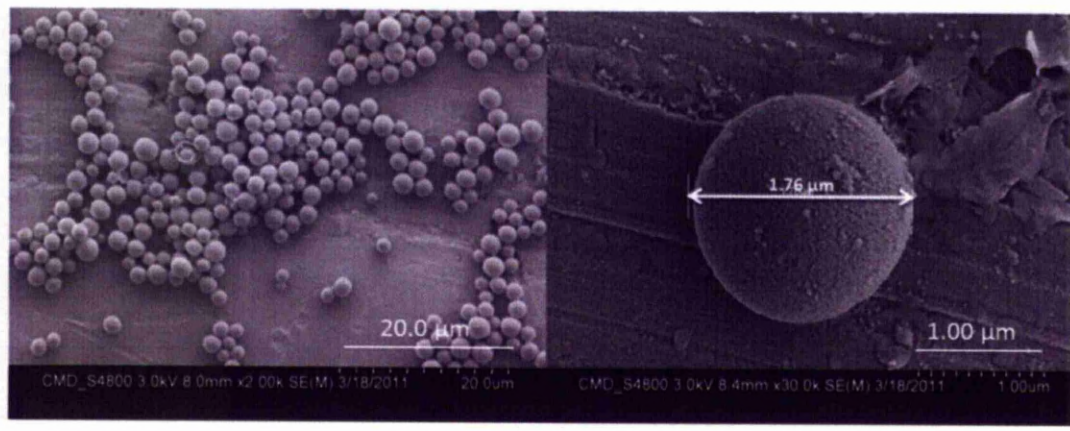

Figure 5.4 SEM Images of 1.7 µm Syncronis silica

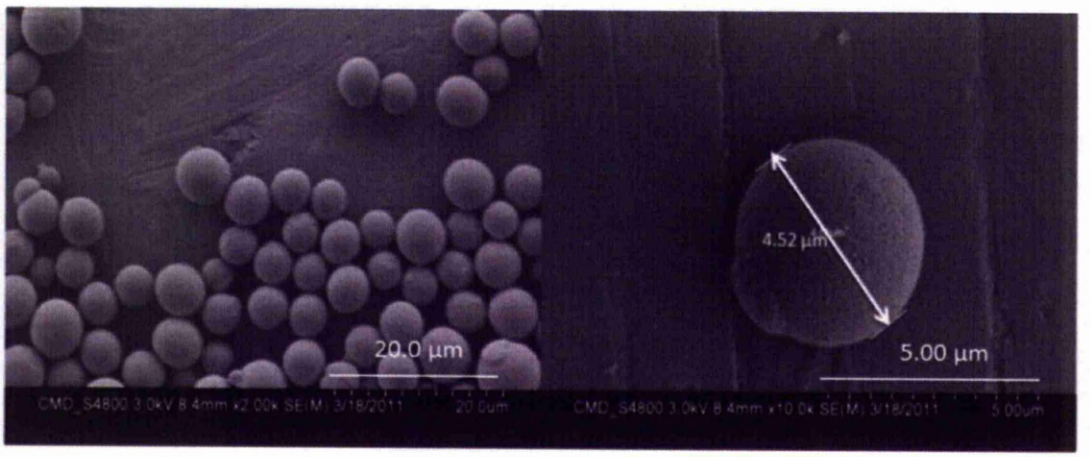

Figure 5.5 SEM Images of Spherisorb ODS2 silica

The SEM images (Figures 5.4 and 5.5) show that both stationary phases have spherical morphology, allowing the particles to be packed closer together in the column. The 1.7 µm Syncronis silica having a smaller average particle size (*ca.*1.7 µm) compared to Spherisorb ODS2 (*ca.* 4.5 µm) can produce a more densely packed column. The optimum packing combined with the higher surface areas indicate that, from a morphological approach, the 1.7 µm Syncronis silica should exhibit higher efficiency.

5.2.3 Carbon Loading

Parent silica sourced from different manufacturers can have significantly different surface areas, therefore, comparing the carbon loading of two materials does not give any insight into the density of the coverage of the bonded phases. By calculating the surface coverage (Equation 5.4) the surface area of the materials is incorporated and allows direct comparison between columns.

$$\alpha = \frac{\%C * 10^6}{12.011 n_c S\left[100 - \left(\frac{\%C}{12.011 n_c}\right)(M - 36.5)\right]} \qquad (5.7)^{228}$$

In this equation, α is the surface coverage, %C is the percentage carbon, n_C is the number of carbons on the silane ligand, S is the surface area of the silica and M is the

molecular weight of the grafted ligand and 36.5 is the molecular weight of chlorine which is released during the grafting process.[228]

Table 5.3 Carbon loading and surface coverage of C_{18} chains

Sample	%C	%H	Surface area of silica before grafting (m^2/g)	Surface area of silica after grafting (m^2/g)	Surface coverage ($\mu mol/ m^2$)
1.7 µm Syncronis	14.87	3.11	320	238.2	2.81
Spherisorb ODS2	10.91	2.32	220	110.0	2.77

The process of RP chromatography is dependent on the interactions between the analytes and the non-polar groups bonded to the surface of the stationary phase. Although the carbon loading of 1.7 µm Syncronis is higher, the densities of the C_{18} chains are similar. As Spherisorb ODS2 contains some level of polymerisation on the surface a denser coverage was expected, although this is dependent on the extent of the polymerisation. This indicates the C_{18} functionality is composed of clusters sporadically distributed on the surface of the silica which might create deviations in the strength of interaction between the analyte and stationary phase throughout the column.

As both silicas contain C_{18} functionalities and have used the same end-capping groups ($Si\text{-}(CH_3)_3$) the selectivity will be dependent on the method used to bond the phase (monomeric/ polymer), density of the coverage and the efficiency of the end-capping. The density of the organic groups is slightly higher for the Syncronis silica which contains the monomeric coverage of C_{18} chains. It is not possible at this stage to determine which column would have a higher level of selectivity as it is also dependent on the efficiency of the end-capping, the silicon framework connectivity, the conformation and mobility of the C_{18} chains and how the analyte interacts with the bonded phase (is this interaction restricted to the terminal methyl groups or does it occur along the whole chain?). To determine how the selectivity of these two columns and the $-CH_2CH_2-/-CH_2C_6H_5$ functionalised stationary phase are affected further investigation is required on a molecular level.

5.3 Characterisation of the Stationary Phases on a Molecular Level

5.3.1 ^{1}H MAS NMR Spectra

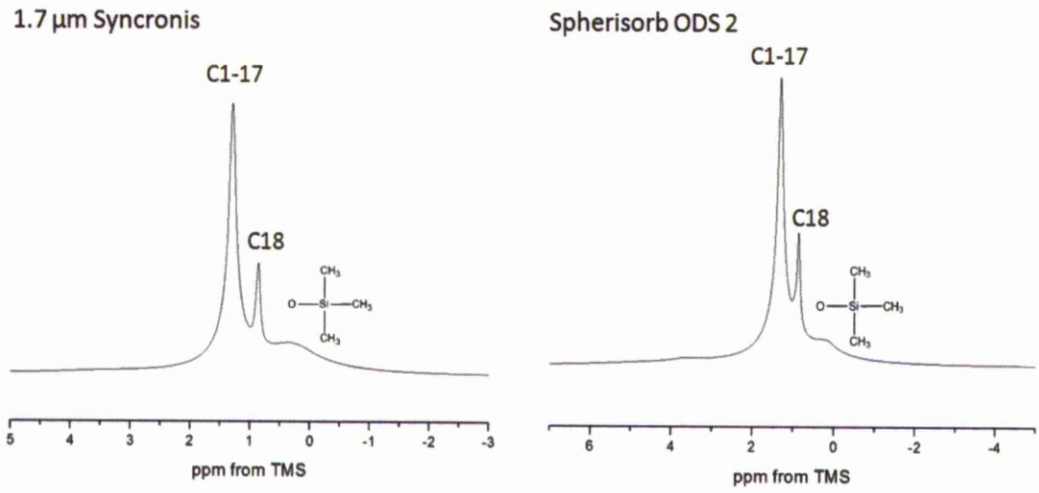

Figure 5.6 ^{1}H MAS NMR spectra of 1.7 µm Syncronis silica (left) and Spherisorb (right) acquired at an MAS rate of 10 kHz

The resonances at *ca.* 1.3 ppm corresponds to the main body of the C_{18} chain. The terminal methyl group resonates at *ca.* 0.85 ppm whereas the methyl end-capping groups correspond to the resonance at *ca.* 0.35 ppm. The ^{1}H MAS NMR spectra for the C_{18} functionalised stationary phases confirmed the presence of the grafted alkyl chain and the methyl end-capping groups, though it has not displayed the differences between the grafted organic groups bonded to the 1.7 µm Syncronis and Spherisorb ODS2 silica.[229]

5.3.2 Characterisation of the C_{18} Chain

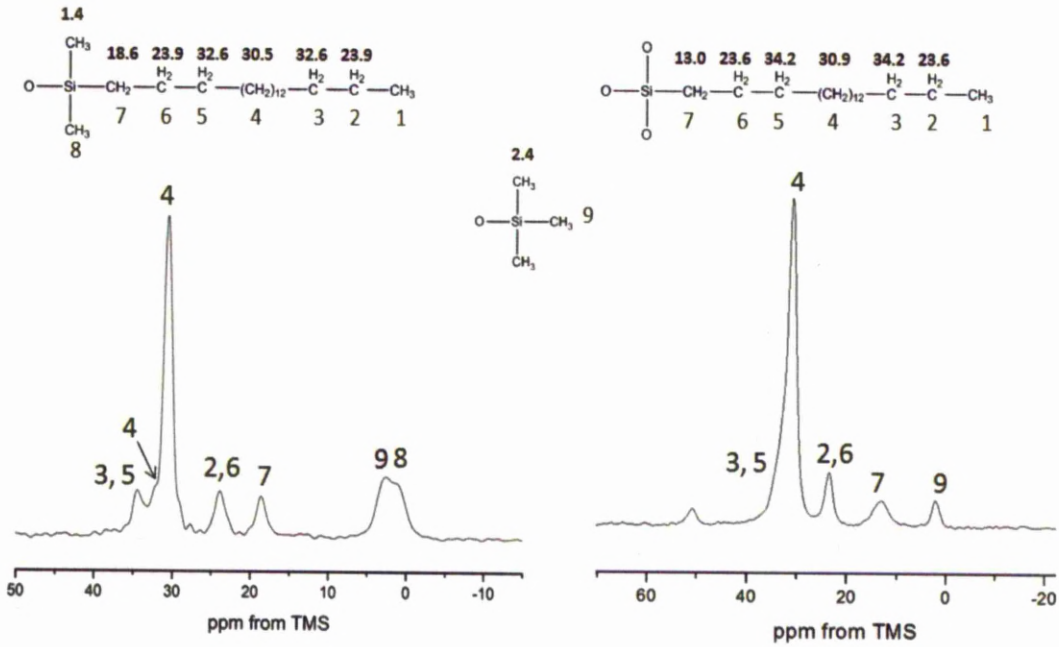

Figure 5.7 ^{1}H-^{13}C CP/MAS NMR spectra of 1.7µm Syncronis silica (left) and Spherisorb ODS2silica (right) acquired at 8 kHz

A resonance at *ca.* 30 ppm corresponding to C4-C15. The resonances at 24 and 32 ppm correspond to C2/ 17 and C3/ 6 respectively. C1 (labelled as 7 on Figure 5.7), which is directly bonded to silicon can be observed at 18.6 ppm. The methyl groups of the end-capping functionality are observed at 2.5 ppm. Additional resonances are observed for the ^{1}H-^{13}C CP/MAS NMR spectrum of the 1.7 µm Syncronis stationary phase at 1.3 and 34 ppm. The resonance at 1.3 ppm corresponds to the methyl groups bonded to the monomeric –Si-C_{18}. As the monomeric C_{18} chains are less densely packed it can be in either *trans* or *gauche* position, the resonance at 30.6 ppm corresponds to the gauche conformation whereas the resonance at 32.2 ppm corresponds to the *trans* conformation of carbons 4-15. The resonance at 34 ppm corresponds to carbons 3 and 15. This not observed for the polymeric Spherisorb stationary phase due to the broad resonance corresponding to the main body of the C_{18} chain. This broadening is caused by the restriction of mobility of the polymeric bonded phase. An additional resonance for the Spherisorb silica is observed *ca.* 50 ppm; this is most likely due to a small amount of Si-OCH_3 groups which remain unpolymerised.[230,231,210]

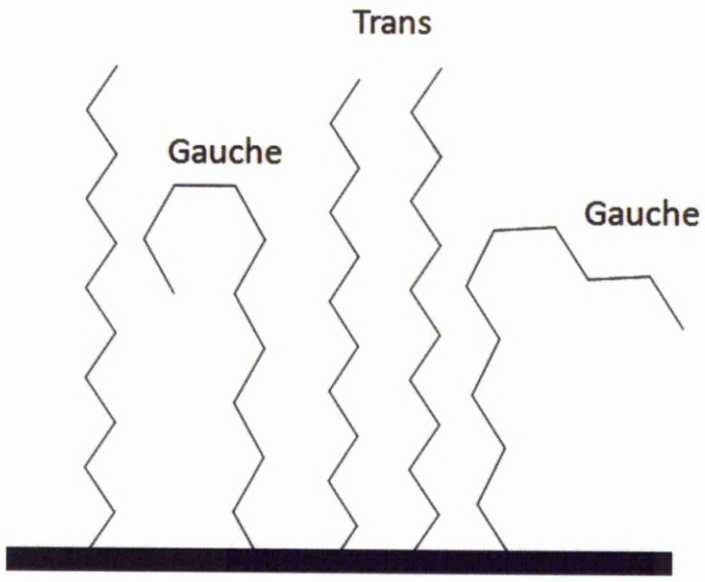

Figure 5.8 Schematic representation of *trans* and *gauche* conformations of alkyl chains

The ^{1}H-^{13}C CP/MAS NMR spectra show that although the two stationary phases contain the same functional groups they are distinctly different wherein one stationary phase comprises a monomeric coverage and other a polymeric.

The level of interaction between the C_{18} chain and the analyte will vary depending on the conformation of the chain (*trans/ gauche*), whereby the C_{18} chain in the extended trans position are more exposed to the analyte or can indicate a more densely packed reversed-phase on the surface of the silica creating a stronger interaction. The dominant conformation of the alkyl chain is determined by its mobility, which is dependent on temperature and the density of packing of the alkyl chains. To correlate the interactions between the analytes and the bonded phases we have used ^{1}H NOESY NMR method. Due to the high mobility of toluene, the homonuclear (^{1}H-^{1}H) dipolar interactions used in ^{1}H NOESY NMR spectra are averaged out. By recording the spectra at 233 K the mobility of the toluene is reduced and the homonuclear interactions can be observed. As these experiments are acquired at low temperatures it is imperative to first investigate any effect of temperature on the conformation of the alkyl chains.

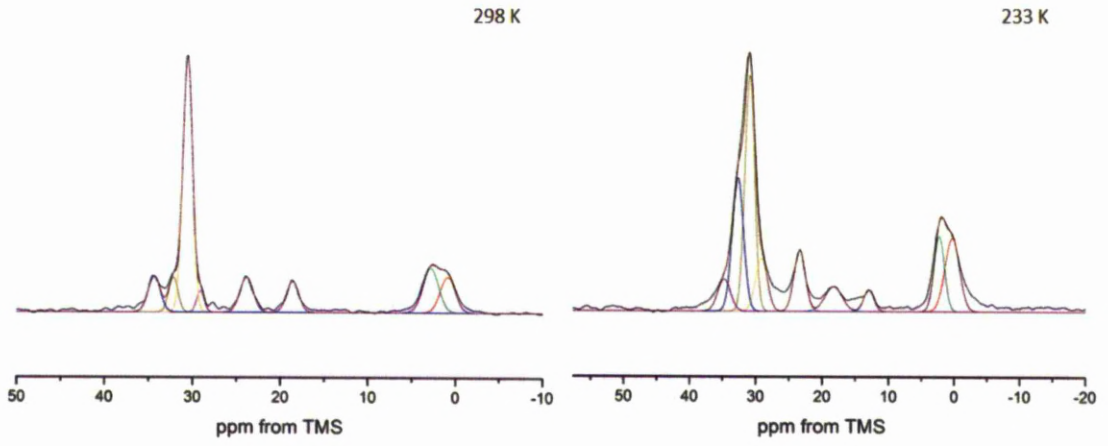

Figure 5.9 ^{1}H-^{13}C CP/MAS NMR spectra of 1.7 µm Syncronis silica containing $(-CH_3)_2Si-C_{18}H_{37}$ functional groups at varying temperatures

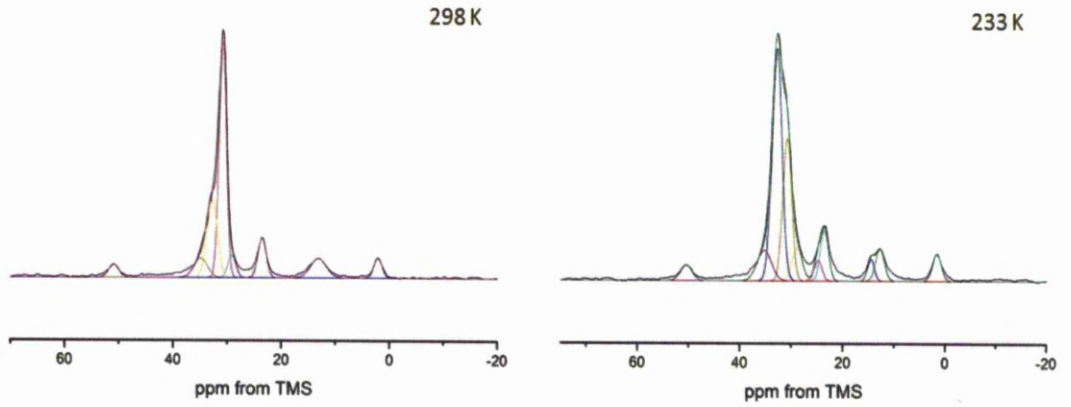

Figure 5.10 ^{1}H-^{13}C CP/MAS NMR spectra of Spherisorb ODS2 silica containing $-(EtO)_2Si-C_{18}H_{37}$ functionality at varying temperatures

Table 5.4 *Trans/ gauche* ratio of the C_{18} chains at 298 and 233 K

Sample	Temperature (K)	Peak area- *gauche* (30.6 ppm)	Peak area- *trans* (32.2 ppm)	*trans/ gauche*
1.7 µm Syncronis	298	1.36	0.182	0.13/ 1
1.7 µm Syncronis	233	1.65	1.1	0.67/ 1
Spherisorb ODS2	298	1.58	0.75	0.47/1
Spherisorb ODS 2	233	1.23	2.23	1.8/1

At room temperature both silica show the dominant *gauche* conformation of the alkyl chains. The ^{1}H-^{13}C CP/MAS NMR spectra show 1.7 µm Syncronis silica to have a much lower proportion of *trans* C_{18} chains compared to Spherisorb ODS 2. This is a consequence of the denser packing of the alkyl chains in the polymeric phase. As expected, both silicas show an increase of the *trans* conformation at decreasing temperatures due to a reduction in mobility.[232,233,110] At 233 K a change in the dominant conformation from the *gauche* to *trans* can be observed for Spherisorb ODS 2. At lower temperatures there is an increase in the ordering of the C_{18} chains. The lower temperatures have a more pronounced effect on this chain conformation due to the already restricted motions of the polymerised phase on the silica surface.

At the lower temperatures the spectra corresponding to the Spherisorb ODS2 stationary phase show an additional peak at 13.0 ppm. This resonances is assigned to the to the terminal methyl group of the C_{18} chain which can now be observed as the lower temperatures will reduce the mobility of this group. This resonance is not observed for the 1.7 µm Syncronis silica at the lower temperature of 233 K. This is due to the higher mobility of the monomeric phase compared to the C_{18} chains of the Spherisorb ODS2 phase which are more clustered together.

5.3.3 Analysis of the Silica Framework

^{1}H-^{29}Si CP/MAS NMR can be used to determine the level of co-condensation for each stationary phase. This will affect the efficiency of the column as residual surface silanol groups will decrease its hydrophobic nature. Furthermore, ^{1}H-^{29}Si CP/MAS NMR can be used to confirm the monomeric/ polymeric nature of the surface bonded organic groups and can be used to determine the extent of polymerisation on the silica surface.

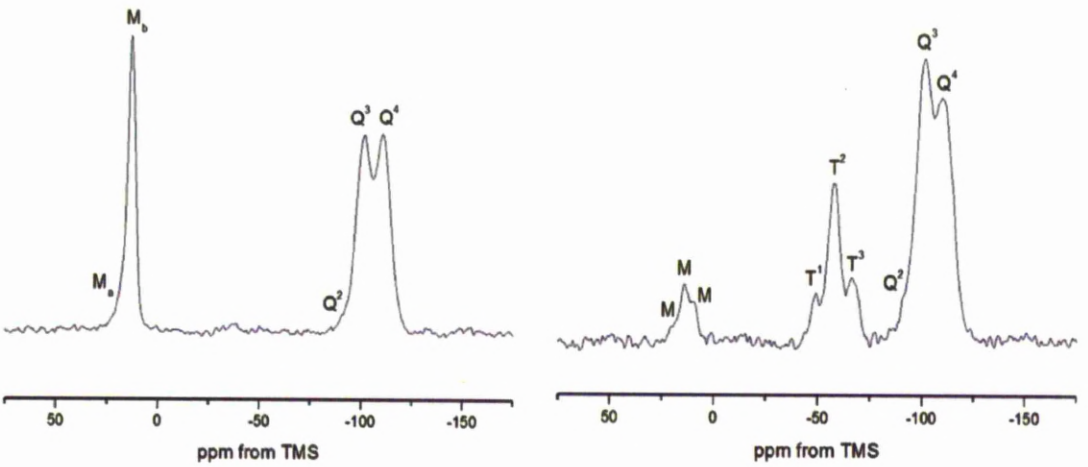

Figure 5.11 ^{1}H-^{29}Si CP/MAS NMR spectra of 1.7 µm Syncronis silica (left) and Spherisorb ODS2 (right) acquired at 4 kHz

The ^{1}H-^{29}Si CP/MAS NMR spectra for both 1.7 µm Syncronis and Spherisorb show resonances corresponding to Q^2 ($SiO_2(OH)_2$), Q^3 ($SiO_3(OH)$) and Q^4 (SiO_4) sites at *ca.* -98, -101 and -110 ppm respectively.

The spectrum of 1.7 µm Syncronis silica shows a further two resonances, M_a and M_b corresponding to –O-Si-($\underline{C}H_3)_3$ and –O-Si-$(CH_3)_2$-$\underline{C}_{18}H_{37}$ respectively.

The T sites are observed for the spectrum corresponding to Spherisorb ODS2. Wherein, T^3 ($-O_3$-Si--$C_{18}H_{37}$), T^2 ($-O_2$-Si-(OCH_3)-$C_{18}H_{37}$) and T^1 (-O-Si-$(OCH_3)_2$-$C_{18}H_{37}$) sites resonate at -65.9, -57.4 and -48.4 ppm respectively. Resonances directly bonded to three carbon groups are denoted as M sites. The resonances between 9.1, 14.0 and 19.5 ppm correspond to the end-capping of free silanol groups and -(O-Si-$(CH_3)_2$-$C_{18}H_{37}$.[215]

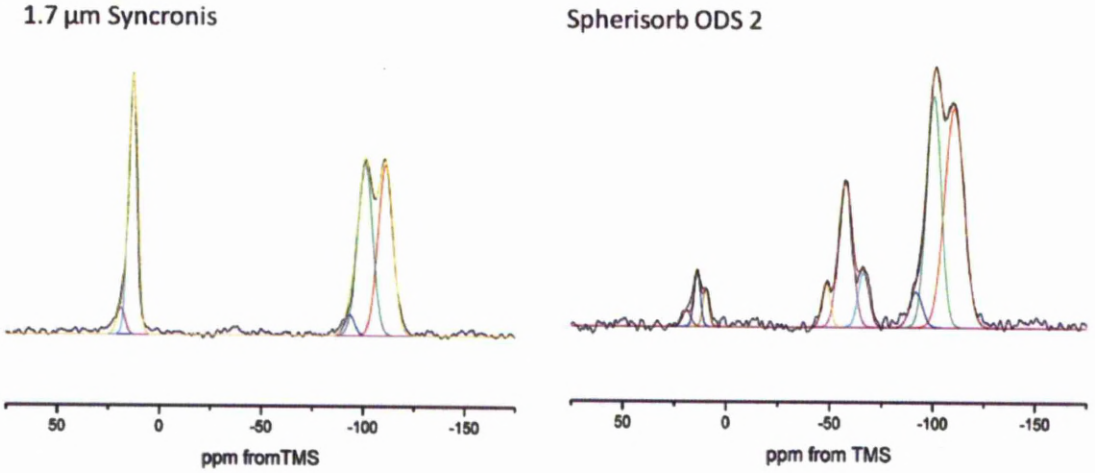

Figure 5.12 Deconvoluted $^{1}H–^{29}Si$ CP/MAS NMR spectra of 1.7 µm Syncronis silica (left) and Spherisorb ODS (right)

Table 5.5 Peak areas of $^{1}H–^{29}Si$ CP/MAS NMR spectrum 1.7 µm Syncronis silica

	Peak area (a.u.)				Peak area (a.u.)			
Sample	Q^2	Q^3	Q^4	$(Q^2+Q^3)/Q^4$	M_a	M_b	Total M	M/ Q
1.7 µm Syncronis	0.48	5.9	5.9	1.08	0.51	5.3	5.81	0.47/ 1

The deconvoluted spectra indicate a relatively high level of condensation for the 1.7 µm Syncronis stationary phase which is mostly comprised of Q^3 and Q^4 sites. The M/Q ratio (0.47/1) suggests a high level organic functionality has been incorporated.

Table 5.6 Peak areas of $^{1}H–^{29}Si$ CP/MAS NMR spectrum Spherisorb ODS 2

	Peak area (a.u.)				Peak area (a.u.)				Peak area (a.u.)			
Sample	Q^2	Q^3	Q^4	$(Q^2+Q^3)/Q^4$	T^1	T^2	T^3	$T^3/(T^1+T^2)$	M^1	M^2	M^3	M/T/Q
Spherisorb ODS2	1.03	7.54	9.58	1.12	0.8	4.44	1.30	0.25	0.5	0.78	0.3	0.09/0.36/1

The ^{1}H-^{29}Si / CP MAS NMR spectrum for Spherisorb ODS2 indicates a slightly lower level of co-condensation compared to the Syncronis stationary phases, though again comprises essentially of Q^3 and Q^4 sites. To determine the level of carbon loading for

this material both the T and M sites have to be taken into consideration. The deconvoluted areas of the T and M sites compared to the Q sites give a similar ratio as Syncronis which coincides with the similar bonding densities calculated. The level of polymerisation of the grafted functionality, calculated by comparing the peak areas of the T sites ($T^3/(T^1+T^2)$), is shown to be fairly low (0.248). As the ^1H-^{29}Si CP/MAS NMR experiments have shown the T-sites are predominantly T^2 sites it is likely the sample mainly consists of dimers with some polymerisation. As the surface coverage is comparable to the monomeric C_{18} chains of the 1.7 µm Syncronis this would again imply that the dimer chains are more sporadically dispersed for Spherisorb ODS2. ^1H-^{29}Si CP/MAS NMR experiments are not quantitative, though the experiment is sensitive to changes in the silicon environment and can be used to highlight the structural differences between the two stationary phases.

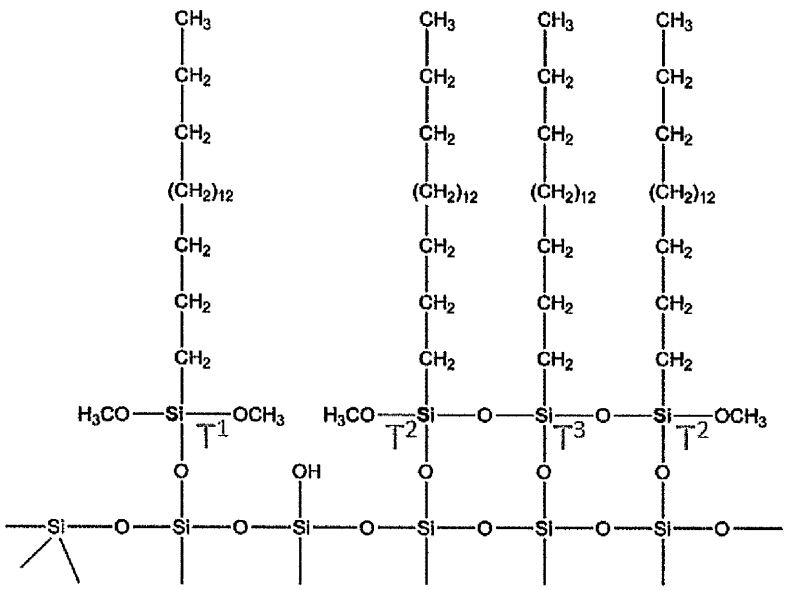

Figure 5.13 Images representing the T sites of Spherisorb ODS2

The 1.7 µm Syncronis and Spherisorb silica have similar pore sizes and both exhibit spherical morphology. The 1.7 µm Syncronis silica has smaller particles sizes and larger surface areas, both of which are beneficial for chromatographic separations. On a molecular level we have shown that although both silicas contain the same functional

groups the 1.7 μm Syncronis silica has monomeric C_{18} chains whereas Spherisorb shows some level of polymerisation on the surface. The effect of the polymerisation has produced a denser packing of C_{18} chains on the surface of the silica. This should increase the retention time of analytes on the Spherisorb column compared to 1.7 μm Syncronis column. However, analysis by ^{1}H-^{29}Si CP / MAS NMR has shown the polymerisation is incomplete with slightly polar $-O-CH_3$ groups remaining near the surface. The presence of these groups can decrease the overall hydrophobicity of the column.

A toluene coating was added to both stationary phases to study how these variations affect the interaction between the stationary phase and analyte. Only then can we relate the molecular properties to the overall efficiency of the column.

5.4 Loading of Silica with Toluene

The toluene coating was added to the 1.7 μm Syncronis, Spherisorb ODS2 and $-CH_2CH_2-$/$-CH_2C_6H_5$ functionalised PMO (discussed in the previous Chapter). The loading level was calculated so as to achieve full surface coverage. As neither the 1.7 μm Syncronis or Spherisorb silica contain aromatic functionalities; the presence of the analyte and the ratio of the analyte to the level of C_{18} functionality incorporated onto the stationary phase can be confirmed using ^{1}H MAS NMR.

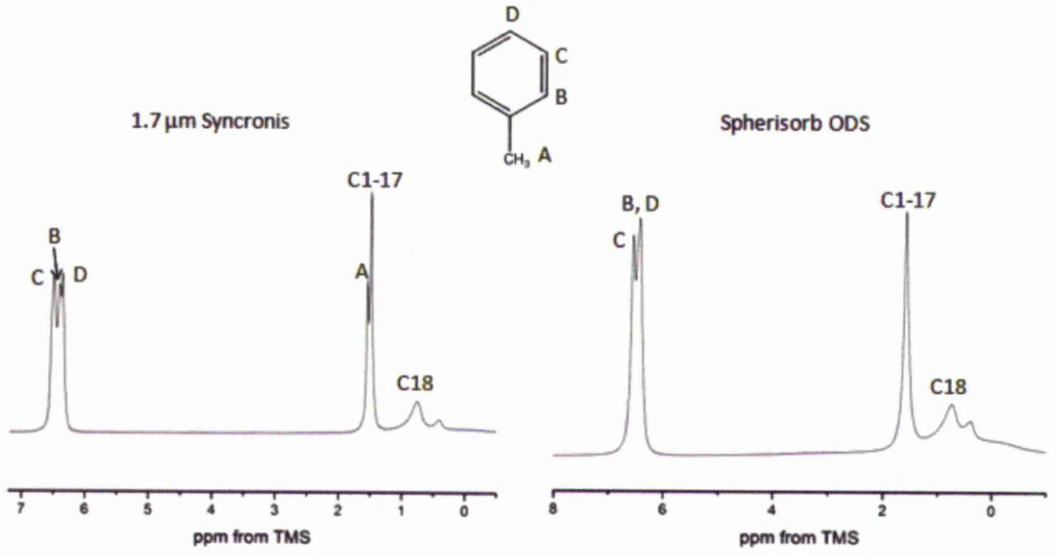

Figure 5.14 ^{1}H MAS NMR spectra of toluene coated 1.7µm Syncronis and Spherisorb ODS2 silica acquired at 10 kHz

The ^{1}H MAS NMR spectra (Figure 5.14) show toluene is present on the surface or within the pores of both stationary phases. The methyl functional group of the toluene resonates at 2.0 ppm and the protons at the ortho, meta and para positions of the benzene ring resonate at 6.8, 6.9 and 6.76 ppm respectively.[234]

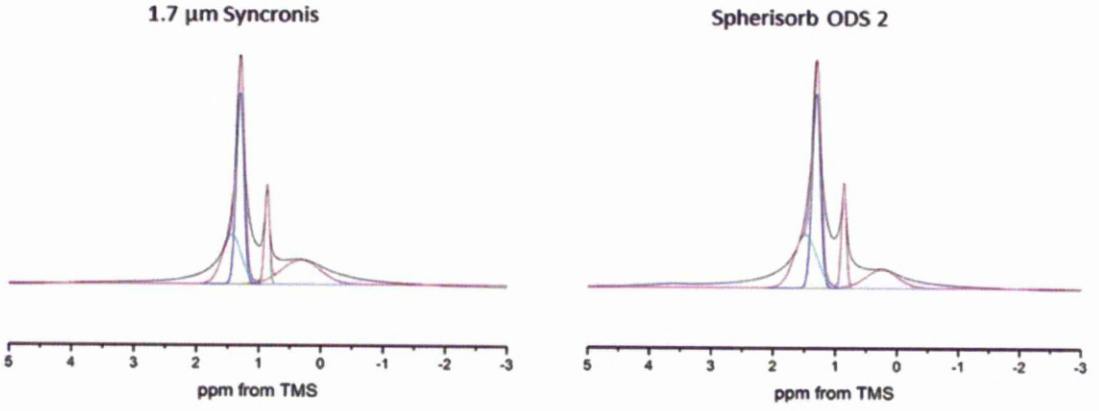

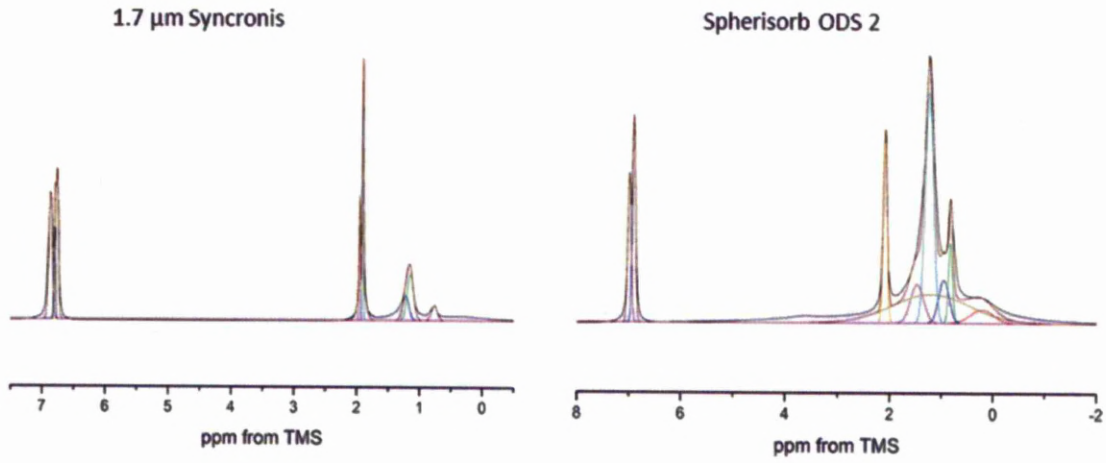

Figure 5.15 Deconvoluted ^{1}H MAS NMR spectra of 1.7 µm Syncronis silica and Spherisorb ODS2 before and after the addition of toluene

Table 5.7 Peak areas for the ^{1}H MAS NMR deconvoluted spectra of 1.7 µm Syncronis silica with toluene

ppm	Functional group	Peak area	Peak Width	Total area	C_{18}/ $CH_2C_6H_5$/ End-capping
C_{18} Chain (without toluene)					
0.32	-Si-$(CH_3)_3$	0.079	0.60		
0.87	C_1/ C_2/ C_{17}/ C_{18}	0.03876	0.076		
1.30/ 1.43	C_3-C_{16} (trans/ gauche)	0.125/ 0.08	0.121/ 0.3		
C_{18} chain (with toluene)					
0.76	-Si-$(CH_3)_3$	0.0065	0.09		
1.145	C_1/ C_{18}	0.0218	0.1		
1.22	C_2/ C_{17}	0.0118	0.1		
1.91	C_3-C_{16}	0.0187	0.017	0.0547	
$CH_3C_6H_5$					
2.0	CH_3-C_6H_5	0.0085	0.019		
6.76	CH_3-C_6H_5 (para)	0.031	0.0435		
6.80	CH_3-C_6H_5 (ortho)	0.0113	0.026		
6.87	CH_3-C_6H_5 (meta)	0.034	0.056	0.0877	
End-capping					
0.76	-Si-$(CH_3)_3$	0.0065		0.0065	
					1/ 1.60/ 0.12

N.B. The broad resonance *c.a.*1.92 ppm corresponds to surface water

Table 5.8 Peak areas of the ^{1}H MAS NMR deconvoluted spectrum of Spherisorb ODS2 silica with toluene

ppm	Functional group	Peak area	Peak Width	Total area	C_{18}/ $CH_2C_6H_5$/ End-capping
C_{18} Chain (without touene)					
0.22	-Si-$(CH_3)_3$	0.028	0.45		
0.82	C_1/ C_2/ C_{17}/C_{18}	0.043	0.075		
1.24/ 1.48	C_3-C_{16} (gauche/ trans)	1.38/ 1.05	0.13/0.36		
C_{18} chain (with toluene)					
0.21	-Si-$(CH_3)_3$	0.028	0.45		
0.82	C_1/ C_{18}	0.029	0.08		
0.95	C_2/ C_{17}	0.040	0.20		
1.24 + 1.48	C_3-C_{16} (gauche/ trans)	0.169/ 0.045	0.158/ 0.25		
$CH_3C_6H_5$					
2.09	CH_3-C_6H_5	0.063	0.08		
6.91	CH_3-C_6H_5 (ortho/para)	0.056	0.06		
7.00	CH_3-C_6H_5 (meta)	0.043	0.07	0.163	
					1/0.48/0.21

N.B. The broad resonance at *c.a.*1.2 ppm corresponds to surface water present

The ^{1}H MAS NMR spectra indicate a higher amount of toluene is incorporated compared to the C_{18} chain for the 1.7 µm Syncronis silica. This is expected as the 1.7 µm Syncronis stationary phase has a much larger surface area compared to Spherisorb though the amount of bonded organic per m^2 for the two materials is similar. The deconvoluted spectra also shows higher amounts of end-capping groups for Spherisorb ODS2 which was unexpected as this stationary phase uses polymeric type bonding of the C_{18} chains.

Comparing the changes observed in the ^{1}H MAS NMR spectra before and after the addition of toluene highlights the differences in mobility of the alkyl chains bonded to the Syncronis and Spherisorb silica. After the addition of toluene a significant decrease in the peak widths for the resonances corresponding to the main body of the C_{18} chain is observed for the Syncronis silica (from 0.121 to 0.017). This indicates an increase in the mobility of the chains, the peak widths are now comparable with those corresponding to toluene.

Unlike the monomeric chains the C_{18} moieties bonded to Spherisorb have some polymerisation restricting their motions. The peak widths of the resonances assigned to the alkyl chain are similar before and after the addition of the solvent, indicating no significant change in mobility.

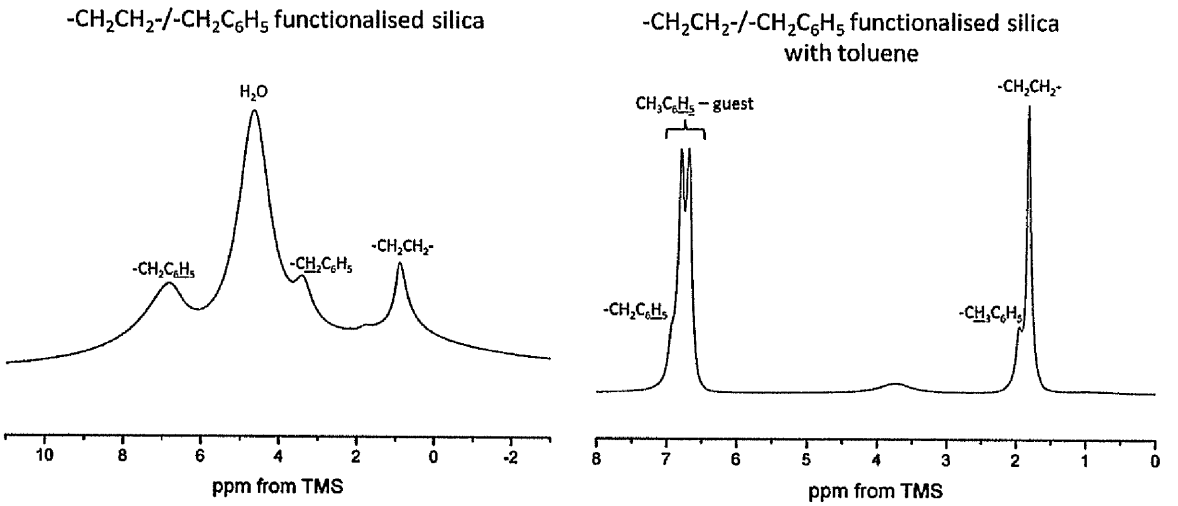

Figure 5.16 ^{1}H NMR spectra CH_2CH_2/ $CH_2C_6H_5$ 80/20 functionalised silica with toluene recorded at an MAS rate of 10 kHz

The increased mobility of the aromatic solvent will produce sharper resonances compared to the bonded $-CH_2C_6H_5$ functional groups. Two sharp resonances and a broad hump can be observed in the aromatic region of the ^{1}H MAS NMR spectrum (Figure 5.16). The sharp resonances (at 6.67 and 6.78 ppm) are most likely due to the guest and a broad hump (at 6.91 ppm) corresponding to the bonded $-CH_2C_6H_5$

functionality. The spectrum shows the presence of both functionalities though the ratio of analyte to stationary phase organic cannot be determined.

To further understand how the stationary phase and analyte interact it is essential to determine how the addition of the analyte affects the bonded organics of the stationary phase. ^{1}H-^{13}C CP/MAS NMR can be used to analyse the affect of toluene on the *trans/ gauche* conformations of the C_{18} chains both at room temperature and 233 K.

5.4.1 Conformation of C_{18} chains after the addition of toluene

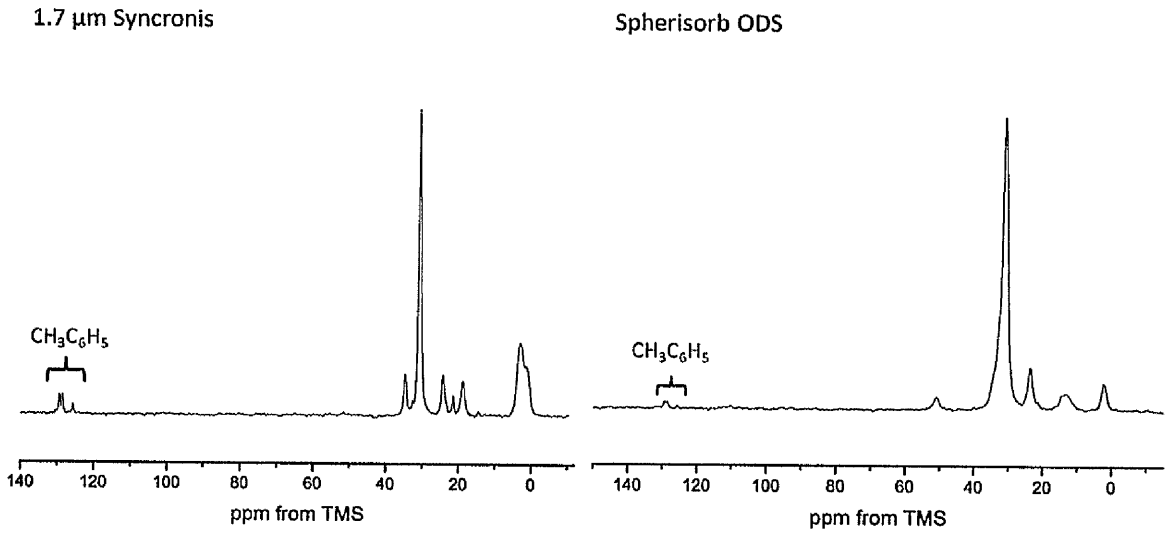

Figure 5.17 ^{1}H-^{13}C CP MAS NMR spectra of 1.7 µm Syncronis and Spheriorb ODS2 with toluene at 298 K

Due to the mobility of toluene at room temperature the corresponding resonances are weak, and therefore longer contact times (3 ms) are needed to observe the peaks of the guest molecule (as shown in Figure 5.17). The methyl functional group of the toluene resonates at 21.4 ppm, the ortho, meta and para (C, D and E) carbons of the benzene ring resonate at 129.4, 128.5 and 125.7 ppm respectively (Figure 5.17). The intensity of the peaks of the protons at the ortho and meta position will be approximately double the intensity of the resonance corresponding to the para positioned protons.[235] Although the resonances corresponding to toluene are weak the effect of the guest on the conformation of the C_{18} chains can still be analysed.

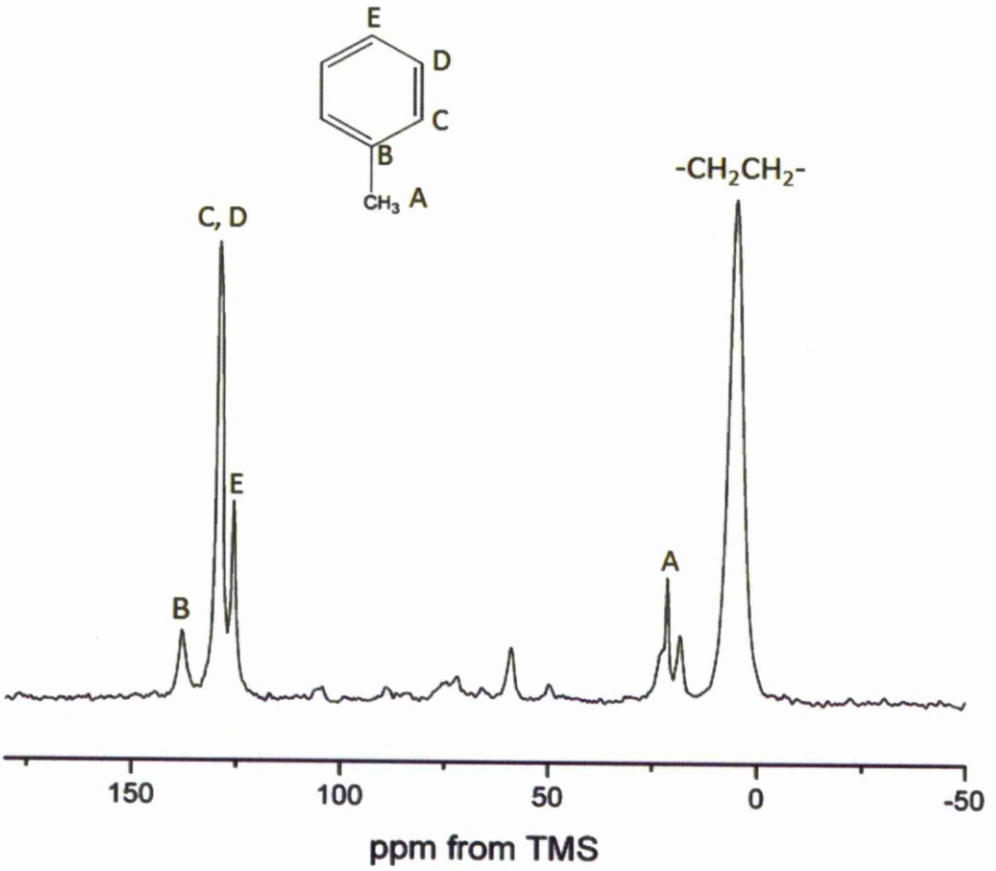

Figure 5.18 ^{1}H-^{13}C CP/MAS NMR spectrum of $-CH_2CH_2-$/ $-CH_2C_6H_5$ 80/20 functionalised silica with toluene at 298K using an MAS rate of 8 kHz

As the benzyl organic group within the framework of the stationary phase resonates at frequencies similar to those of the toluene analyte, the loading level of the guest molecule cannot be determined accurately. An increase of intensity for the resonances corresponding to toluene indicates the analyte is present on the surface or within the pore structure. The incorporation of the solvent can be observed through $^{13}C\{^{1}H\}$ MAS NMR or through studying the ^{1}H-^{13}C kinetics as the mobility of the free toluene would differ from that of the bonded benzyl group.

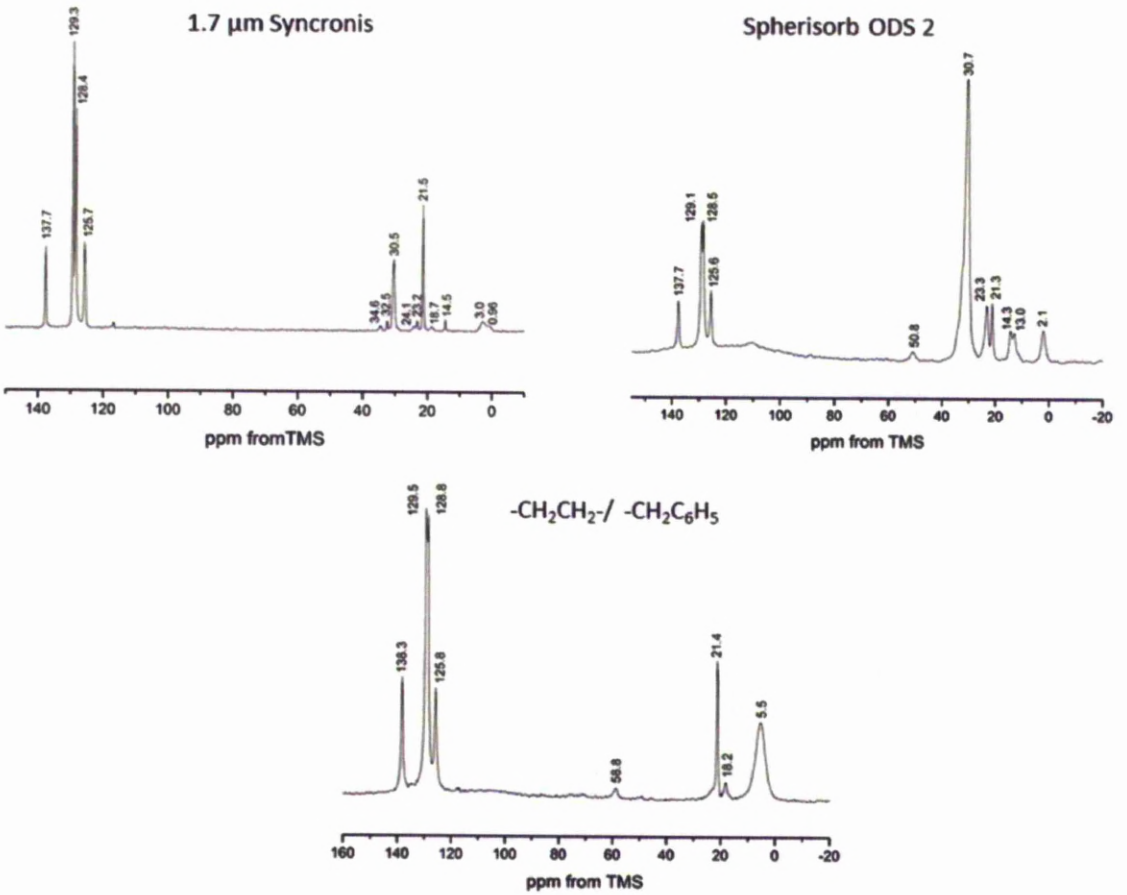

Figure 5.19 $^{13}C\{^{1}H\}$ MAS NMR spectra of toluene coated 1.7 µm Syncronis silica, Spherisorb ODS 2 and $-CH_2CH_2-$/ $-CH_2C_6H_5$ functionalised PMO acquired at 8 kHz

The ^{13}C $\{^{1}H\}$ MAS NMR spectra (Figure 5.19) show that the toluene has been incorporated within the porous structure or on the surface of the stationary phases. The spectra show a significant increase in the intensities of the resonances corresponding to the toluene guest molecule compared to the resonances observed using ^{1}H-^{13}C CP/MAS NMR experiment. An additional resonance ca. 137 ppm can be observed, this is due to the quaternary carbon of the toluene ring. The intensity of the analyte resonances are much higher for Syncronis and $-CH_2CH_2-$/ $-CH_2C_6H_5$ functionalised PMO compared to Spherisorb. This is expected as Spherisorb has a much smaller surface area and therefore a lower loading level of the solvent.

The NMR spectrum of the $-CH_2CH_2-$/ $-CH_2C_6H_5$ PMO shows the presence of both sharp and broad resonances corresponding to toluene and the $-CH_2C_6H_5$ functionality

respectively. The deconvoluted ^{13}C {^{1}H} MAS NMR spectrum (Figure 5.20) shows a significant amount of toluene has been incorporated on to the surface or within the porous structure (bonded phase/ analyte 1/1.64).

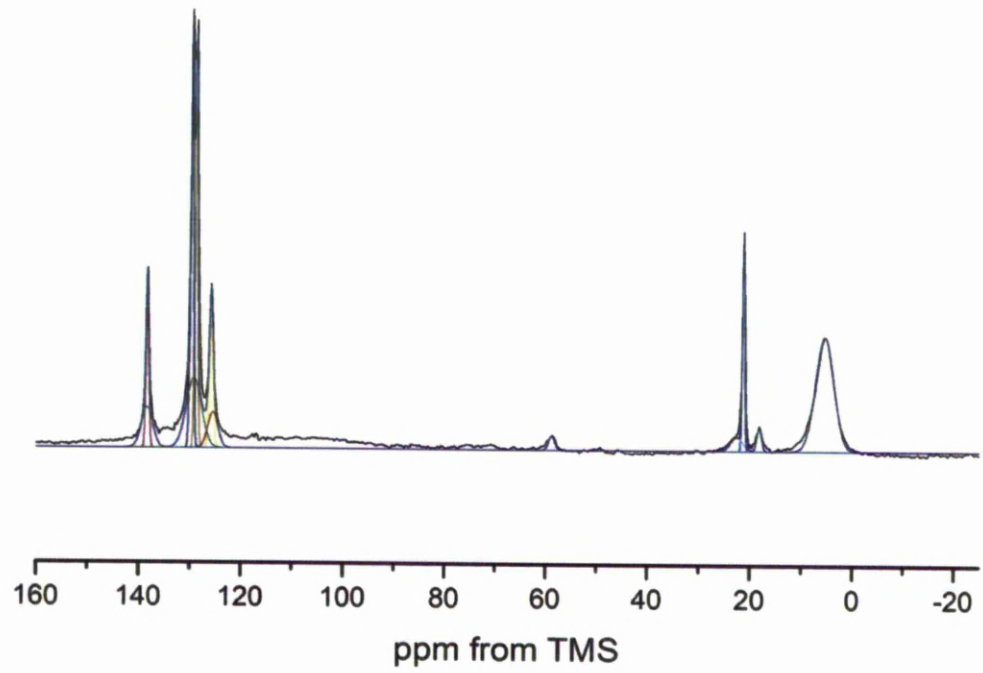

Figure 5.20 Deconvoluted ^{13}C {^{1}H} MAS NMR spectrum of toluene coated $-CH_2CH_2-$/ -$CH_2C_6H_5$ functionalised PMO acquired at 8 kHz

Table 5.9 Peak areas of the ^{13}C {^{1}H} MAS NMR spectrum of toluene coated $-CH_2CH_2-$/ -$CH_2C_6H_5$ functionalised PMO

Functional Group	ppm	Peak area	Width	Ratio of bonded/ analyte
-$CH_2C_6H_5$ (PMO)				
-$\underline{C}H_2C_6H_5$	22.5	0.0984	2.4	
-$CH_2\underline{C}_6H_5$ (para)	125.5	0.206	2.0	
-$CH_2\underline{C}_6H_5$ (ortho/ meta)	129.2	0.60	3.0	
-$CH_2\underline{C}_6H_5$ (Quaternary)	138.3	0.256	2.2	
				1.16
$CH_2C_6H_5$ (toluene)				
$\underline{C}H_2C_6H_5$	21.3	0.259	0.43	
$CH_2\underline{C}_6H_5$ (para)	125.8	0.260	0.75	
$CH_2\underline{C}_6H_5$ (meta)	128.8	0.529	0.55	
$CH_2\underline{C}_6H_5$ (ortho)	129.7	0.619	0.60	
$CH_2\underline{C}_6H_5$ (Quaternary)	138.3	0.229	0.58	1.896
				1/1.64

5.4.2 Conformation of the C_{18} Chain at 233 K

At reduced temperatures (233 K) the mobility of toluene and the C_{18} chain are reduced. This leads to an increase in the strength of the heteronuclear ^{1}H-^{13}C interactions allowing magnetisation to be transferred between atoms close in space and thus determining how the analyte interacts with the stationary phase.

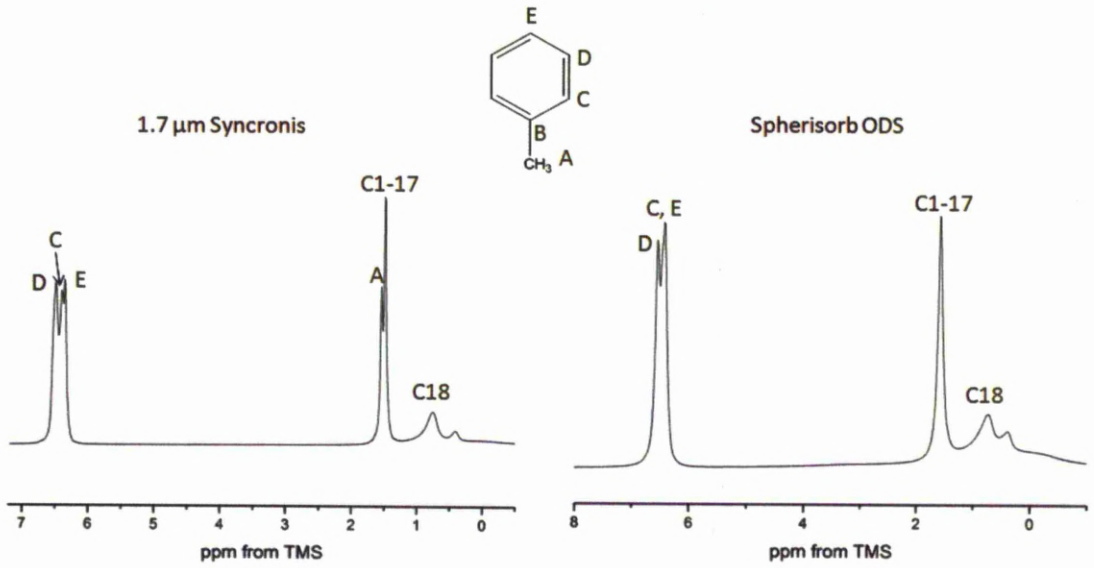

Figure 5.21 ^{1}H MAS NMR spectra of 1.7 µm Syncronis and Spherisorb ODS2 with toluene at 233 K

At the lower temperature the chemical shifts have moved up field, as shown in Figure 5.21. The resonances for the C_{18} carbon chain can be seen at 0.75 ppm for C1, C2, C17 and C18 and at 1.48 ppm corresponding to carbons 3-16. The methyl functional group of the toluene is observed at 1.54 ppm for Syncronis. The two resonances at 1.48 and 1.54 ppm are very close together. Due to the narrow line widths of the Syncronis spectrum both resonances can be observed. The restricted movement of the Spherisorb alkyl chains leads to a broader resonance for C3-C16 (35.6 Hz) compared to Syncronis (13.7 Hz) and so overlaps with the resonance of the toluene methyl group. The peak produced by the methyl group of the toluene guest molecule can no longer be observed due to this effect. The protons at the ortho, meta and para positions of the benzene ring resonate at 6.39, 6.48 and 6.35 ppm respectively for both stationary phases. The end-capping groups can be seen *ca.* 0.40 ppm.

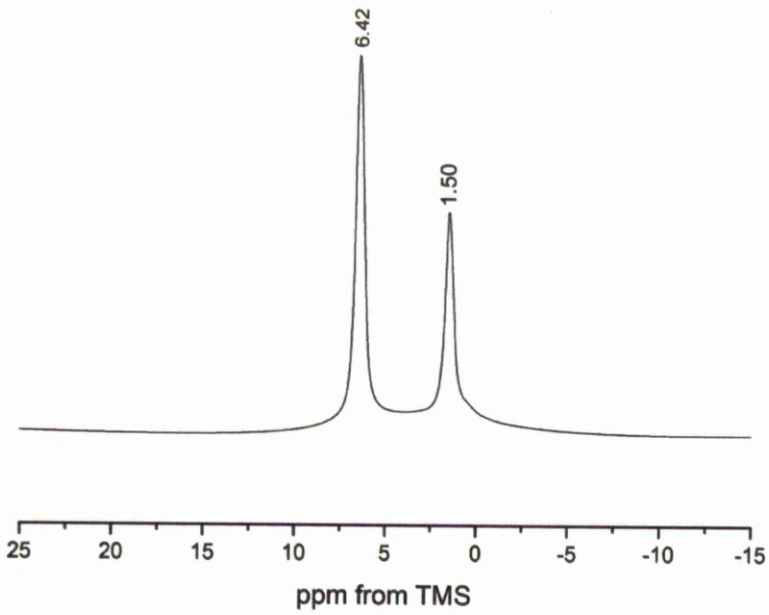

Figure 5.22 ^{1}H MAS NMR spectrum of toluene loaded -CH_2CH_2-/ -$CH_2C_6H_5$ functionalised PMO at 233 K at an MAS rate of 10 kHz

Figure 5.22 shows the NMR spectrum of the toluene loaded –CH_2CH_2-/-$CH_2C_6H_5$ functionalised PMOs, due to the extensive line broadening only two resonances are observed at 233 K corresponding to –CH_2CH_2- and –$C\underline{H}_2C_6H_5$ (1.50 ppm) and –$CH_2C_6\underline{H}_5$ (6.42 ppm). As the proton environments of the toluene resonate at similar frequencies to the –$CH_2C_6H_5$ moiety, the incorporation of the guest can not be observed using this technique.

Conformation of alkyl chain at 233 K

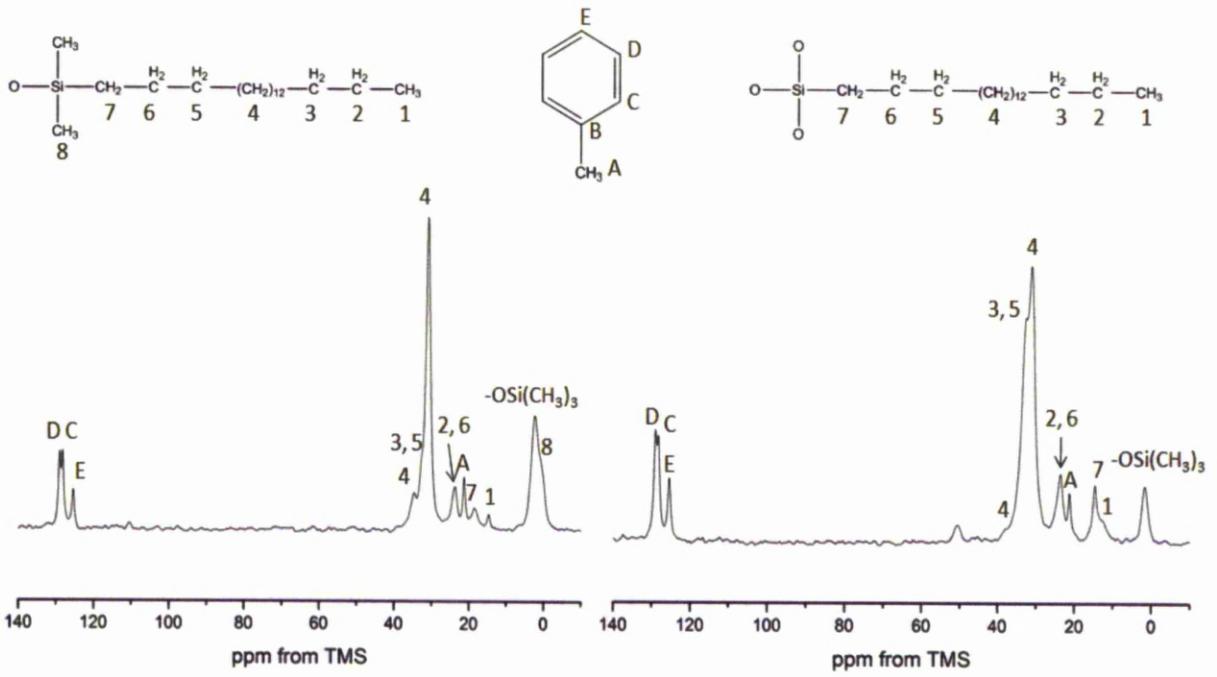

Figure 5.23 ^{1}H-^{13}C CP/MAS NMR spectra of 1.7 µm Syncronis (left) and Spherisorb ODS2 (right) loaded with toluene at 233 K

The ^{1}H – ^{13}C CP/MAS NMR spectra (Figure 5.23) indicate that at 233 K the mobility of toluene has been significantly reduced, as shown by the increase in signal intensity of the corresponding resonances. The spectrum of the $-CH_2CH_2$-/-$CH_2C_6H_5$ PMO (Figure 5.24) shows that at the lower temperature the individual resonances corresponding to the quaternary carbon for both the bonded $-CH_2C_6H_5$ functionality (B) and the toluene analyte (B*) are observed. Reducing the temperature of the stationary phase may alter the mobility of the C_{18} chains. We need to determine the effect of toluene on the conformation of the alkyl chains at lower temperatures.

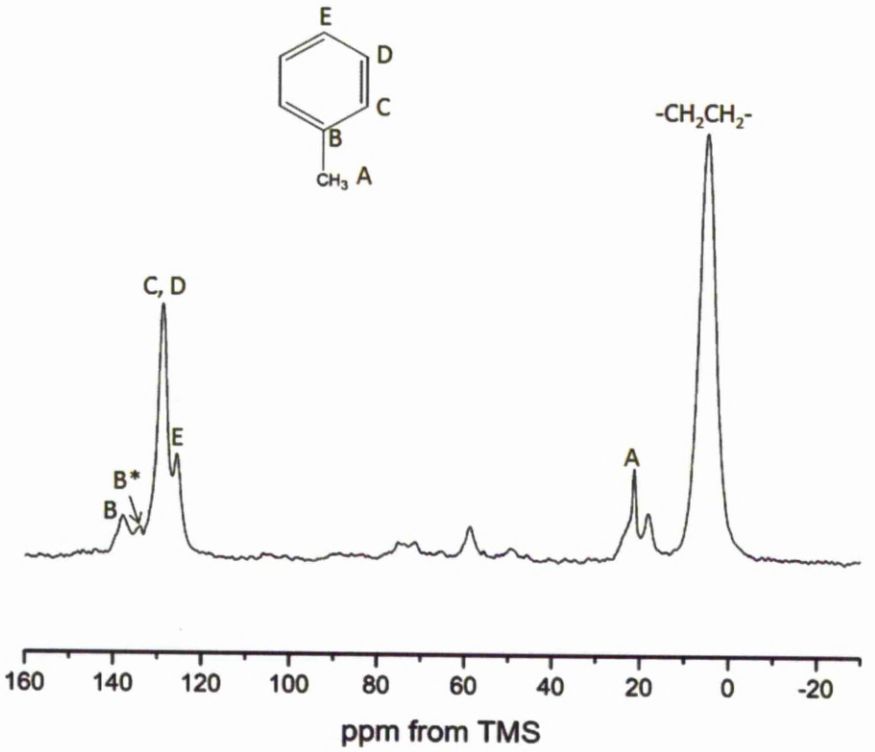

Figure 5.24 $^{1}H - {}^{13}C$ CP/MAS NMR spectrum of $-CH_2CH_2-$/ $-CH_2C_6H_5$ functionalised silica with toluene at 233 K

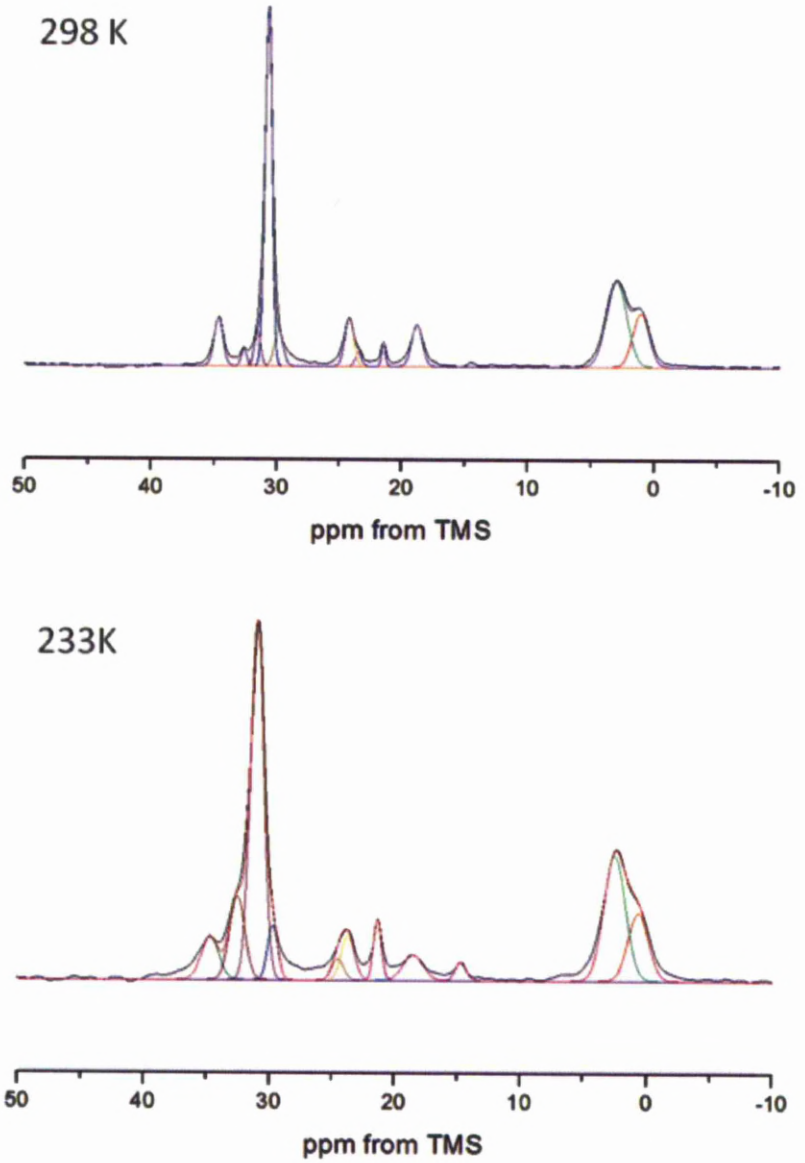

Figure 5.25 Deconvoluted ^{1}H-^{13}C CP/MAS NMR spectrum of 1.7 µm Syncronis silica with toluene at 298 K (top) and 233 K (bottom)

Table 5.10 peak area of *trans/gauche* C_{18} chains in 1.7 µm Syncronis

Temperature (K)	Peak area - *gauche* (30.6 ppm)	Peak width (*gauche*)	Peak area- *trans* (32.0 ppm)	Peak width (*trans*)	*trans/ gauche*
298	0.68	0.55	0.06	0.50	0.09/ 1
233	1.3	1.05	0.345	1.2	0.27/ 1

The ^{1}H-^{13}C CP/MAS NMR spectra show an increased population of the *trans* conformation of the C_{18} chains at 233 K (*trans/ gauche* ratio of 0.27/1) compared to the spectrum recorded at 298 K (*trans/ gauche* ratio of 0.09/ 1). This indicates a reduced mobility of the chains at lower temperatures. At 233 K the spectra also show an increase in the line widths of the resonances corresponding to the alkyl chain consistent with reduced mobility of the chain. The population of *gauche* C_{18} chains is higher for Syncronis with toluene compared to just the Syncronis silica at both 298 K (*trans/ gauche* ratios of 0.13/ 1 (without toluene) and, 0.09/ 1 (with toluene)) and 233 K (*trans/ gauche* ratios of 0.67/ 1 (without toluene) and, 0.27/ 1 (with toluene)). This indicates an increase in the molecular motions of the C_{18} chains with the addition of the quest; this will increase the interaction between the two groups and thus improve the efficiency of the column.[236,230]

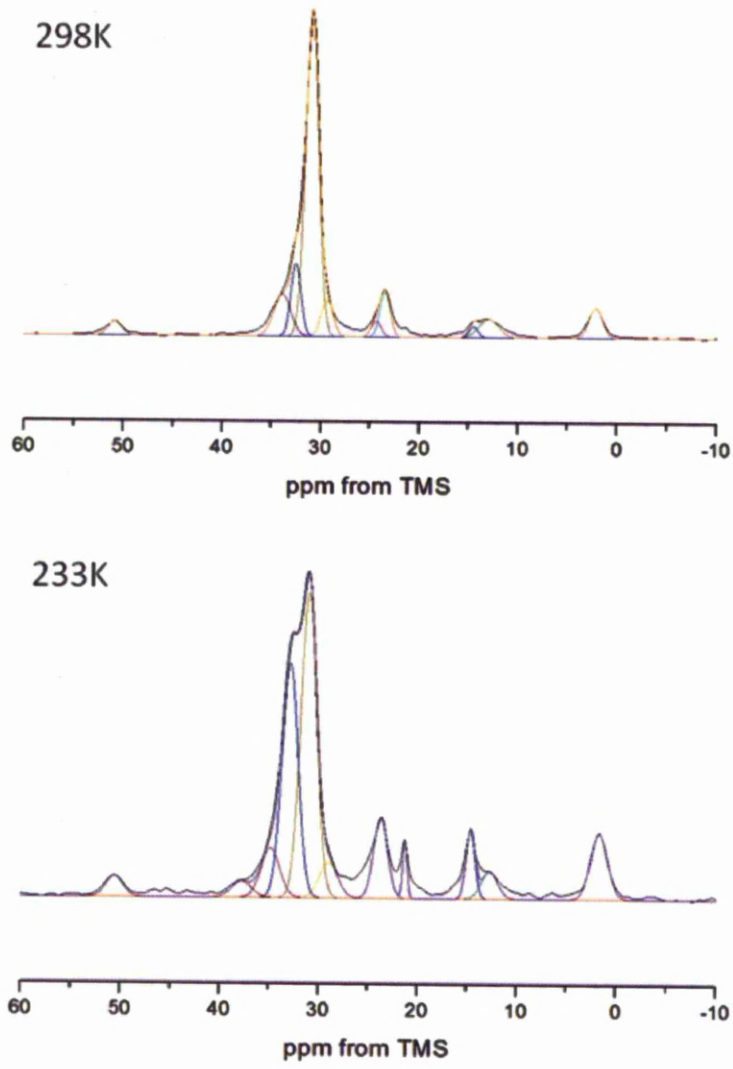

Figure 5.26 Deconvoluted ^{1}H-^{13}C CP/MAS NMR spectrum of Spherisorb ODS2 silica with a surface layer of toluene at 298K (top) and 233K (bottom)

Table 5.11 peak area of trans/gauche C_{18} chains in Spherisorb

Temperature (K)	Peak area - *gauche* (30.6 ppm)	Peak width (*gauche*)	Peak area- *trans* (35.6 ppm)	Peak width (*trans*)	*trans/ gauche*
298	1.62	1.3	0.275	1.0	0.17/ 1
233	1.86	1.6	1.43	1.6	0.79 / 1

The Spherisorb ODS2 silica shows a trend which is similar to that of the 1.7 μm Syncronis silica. An increased population of alkyl chains in *trans* conformation is observed at 233 K (*trans/ gauche* ratio of 0.79/ 1) compared to 298 K (*trans/ gauche* ration of 0.17/1). Increased line broadening at the lower temperatures indicates the change in conformation is due to a decrease in mobility of the alkyl chains. The line widths of Spherisorb ODS 2 are larger than the corresponding resonances for Syncronis. This again highlights the reduced mobility of the polymeric phases compared to the monomer.

The proportion of *gauche* C_{18} chains increases with the addition of toluene at both 298 K (*trans/ gauche* ratios of 0.47/ 1 (without toluene) and, 0.17/ 1 (with toluene)) and 233 K (*trans/ gauche* ratios of 1.8/ 1 (without toluene) and, 0.79/ 1 (with toluene)) which confirms the hydrophobic interaction between the bonded phase and analyte. As both stationary phases have similar loading levels of bonded phases the higher levels of extended *trans* C_{18} chains on Spherisorb silica could produce a higher retentivity compared to Syncronis.

5.4.3 The Effect of Toluene on the Dynamics of the C_{18}chains

^{1}H-^{13}C CP dynamics can be used to determine the mobility of the organic groups incorporated into the RP columns. Longer T_{IS} and $T^{H}_{1\rho}$ times indicate a mobile environment whereas shorter times correspond to a more rigid structure.[237]

^{1}H-^{13}C CP dynamics can be used to determine the mobility of the organic groups incorporated into the RP columns. Longer T_{IS} and $T^{H}_{1\rho}$ times indicate a mobile environment whereas shorter times correspond to a more rigid structure [237].

Both stationary phases exhibit $T^{H}_{1\rho}$ times over 50 ms for the C_{18} chains which are indicative of an extremely mobile environment, though this it to be expected of long alkyl chains. As shown using the ^{1}H-^{13}C CP/MAS NMR the end-methyl group (C18) can not be observed due to the high mobility of this group. C1 (18.6 ppm) was fitted using the IS (two components) model indicating two different environments are present (fast/slow). A faster build up of magnetisation and shorter relaxation is observed for

the more rigid C1 group, this will occur in areas where the functionality is more densely packed. A much longer build up and relaxation time is observed C1 resonances of the more mobile alkyl chains. The CP dynamics of the C4-C16 carbons in trans conformation of both stationary phases are fitted using the I-I*-S model. This model assumes that magnetisation is transferred primarily from protons in close proximity and then from proton further away. The proton spin diffusion rate (T_{df}) is indicative of the strength of the ^{1}H-^{1}H interaction and therefore dependent on distance and can therefore provide information on the packing density of the C_{18} chains within the two stationary phases. The spin diffusion time for the Spherisorb is shorter than that of the 1.7 µm Syncronis. As Spherisorb exhibits a polymeric loading of C_{18} species the alkyl chains will be closer in space and more rigid compared to the monomeric silica. This would be reflected in a decreased spin diffusion time.

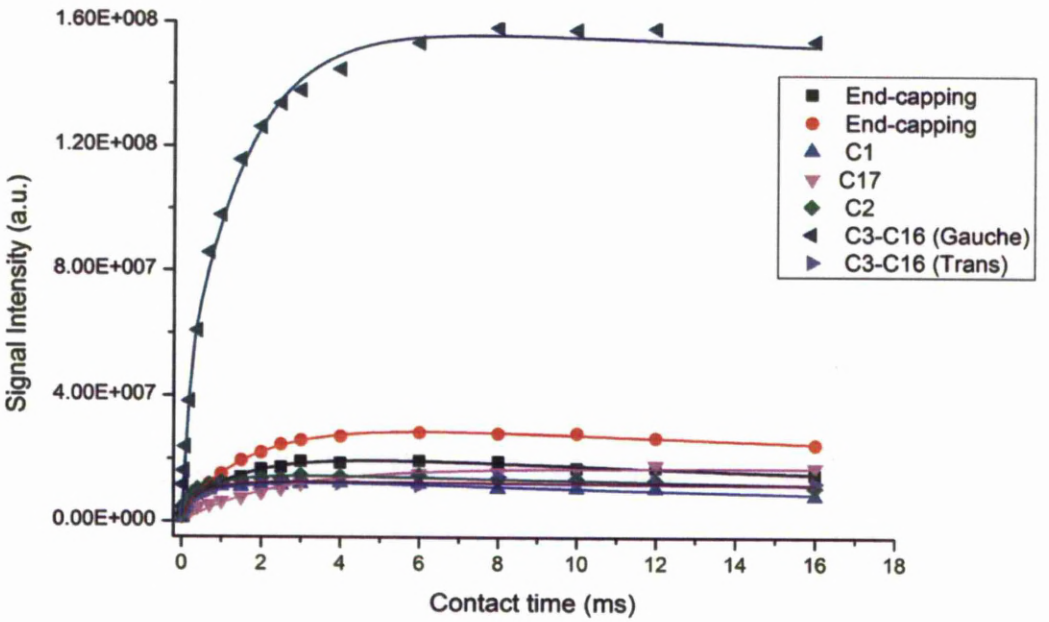

Figure 5.27 ^{1}H-^{13}C CP/MAS kinetics curves of the 1.7 µm Syncronis functional groups

Table 5.12 ^{1}H–^{13}C CP/MAS kinetics parameters for 1.7 μm Syncronis

Resonance (ppm)	^{13}C Site	Model		Signal Intensity (10^7)	T_{IS} (ms)	$T^{H}_{1\rho}$ (ms)	T_{df} (ms)	T^2 (ms)	λ	R^2
0.95	O-Si-$(\underline{C}H_3)_2C_{18}$	I-I*-S		2.29 ± 0.12		39.8 ± 7.86	1.61 ± 0.24	0.09 ± 0.02	0.82 ± 0.03	0.99 1
2.66	End-capping	I-I*-S		3.22 ± 0.10		> 50	1.69 ± 0.12	0.05 ± 0.02	0.93 ± 0.02	0.99 8
18.6	C1	IS (2 components)	Fast	0.71 ±0.10	0.11 ± 0.03	0.80 ± 0.92				0.98 4
			Slow	1.37 ±0.07	1.08 ±0.62	34.4 ± 7.87				
23.1	C17	IS		1.72 ± 0.05	2.41 ± 0.20					0.96 8
24.0	C2	I-I*-S		1.56 ± 0.06		> 50		0.87 ± 0.20	0.60 ± 0.05	0.98 0
30.5	C4-15 (Gauche)	I-I*-S		16.1 ± 0.57		> 50	1.54 ± 0.18	0.12± 0.02	0.78 ± 0.03	0.99 7
34.3	C4-15 (Trans)	I-I*-S		1.29 ±0.06		> 50	0.63 ±0.20	0.07 ±0.02	0.69 ±0.12	0.96 1

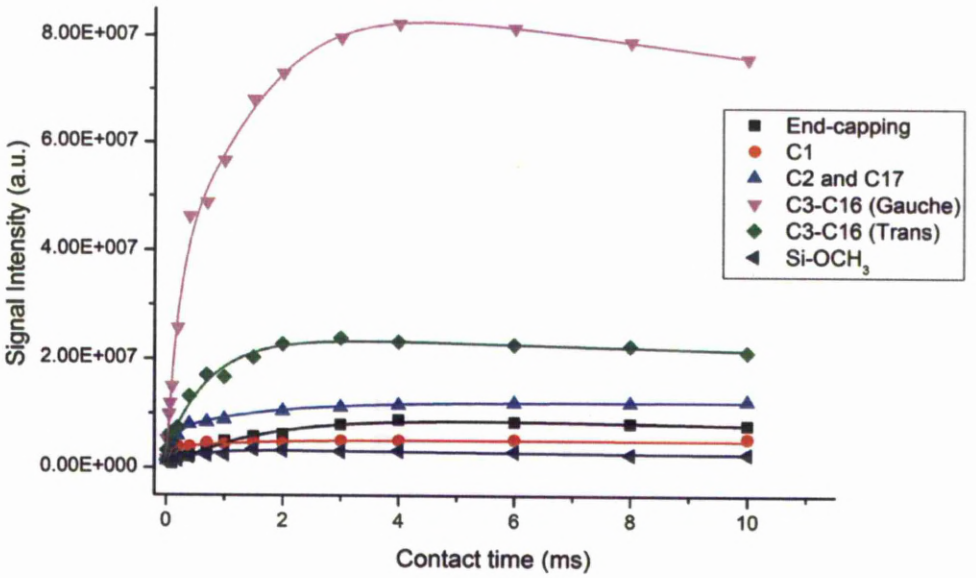

Figure 5.28 ^{1}H-^{13}C CP/MAS kinetic curves of the Spherisorb ODS2 functional groups

Table 5.13 ^{1}H–^{13}C CP/MAS kinetics parameters for Spherisorb ODS2

Resonance (ppm)	^{13}C Site	Model		Signal Intensity (10^7)	T_{IS} (ms)	$T^{H}_{1\rho}$ (ms)	T_{df} (ms)	T^{2} (ms)	λ	R^2
2.1	End-capping	I-S		1.00 ± 0.97	1.64 ±0.26	35.9 ± 20.3				0.982
13.4	C1	IS (2 components)	Fast	0.38 ± 0.02	0.06 ± 0.01	>50				0.967
			Slow	0.16 ± 0.03	2.22 ± 1.00	> 50				
23.5	C2 and C17	IS (2 components)	Fast	0.69 ± 0.04	0.13 ± 0.01	> 50				0.996
			Slow	0.53 ± 0.04	1.90 ± 0.32	> 50				
30.9	C4-C15 (Gauche)	I-I'-S		9.19 ±0.81		> 50	1.41 ±0.36	0.12 ± 0.02	0.72 ± 0.05	0.992
32.5	C4-C15 (Trans)	I-I'-S		2.45 ± 0.14		> 50	0.75 ±0.12	0.01 ± 0.006	0.89 ± 0.03	0.984
51.0	Si-OCH_3	I-S		0.33 ± 0.02	0.43 ±0.08	40.0 ± 20.2				0.867

The ^{1}H-^{13}C CP/MAS NMR shows the addition of toluene to have an effect on the position of the alkyl chain. The ^{1}H-^{13}C CP kinetic data of the C1 carbons for both stationary phases coincide with results obtained from the NMR experiments wherein a Spherisorb ODS2 shows higher percentage of the fast component indicating an increase in C1 groups in a more rigid environment, which is to be expected of a polymer phase. Further the transfer of magnetisation (T_{IS}) for the rigid component is more rapid for Spherisorb ODS 2 (0.06 ms) compared to 1.7 μm Syncronis (0.11 ms) which suggests the polymerisation mechanism has a greater effect on the mobility of the C_{18} chains compared to the higher density packing of the Syncronis phase. ^{1}H-^{13}C CP kinetics can be used to confirm this change in *trans/ gauche* formation but can also be used to determine the effect on the mobility of the C_{18} chain.

Mobility of the C_{18} chain with toluene loaded

The ^{1}H-^{13}C CP/MAS NMR shows the addition of toluene to have an effect on the conformation of the alkyl chain. The mobility of the carbon chain and toluene can be analysed through ^{1}H-^{13}C variable contact time (VCT) MAS NMR and ^{1}H T_1 relaxation NMR

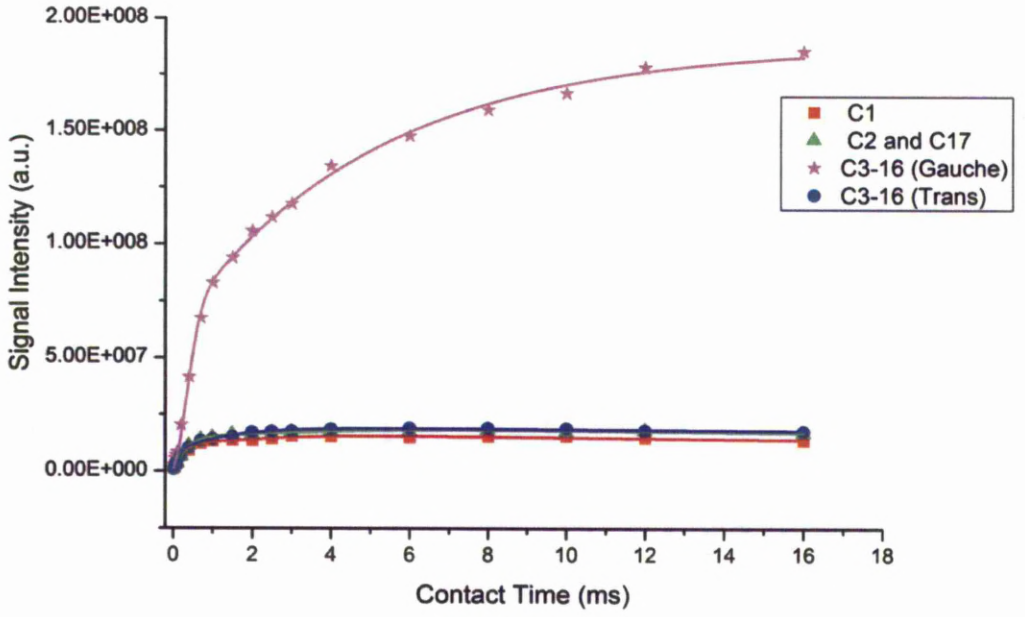

Figure 5.29 ^{1}H -^{13}C CP/MAS kinetics curve for C_{18} chain resonances in 1.7 µm Syncronis silica loaded with toluene

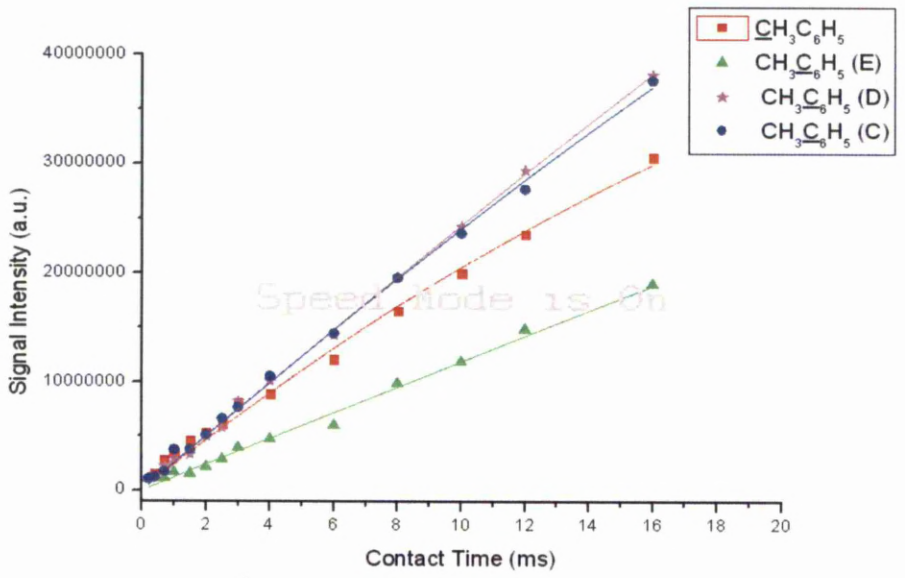

Figure 5.30 ^{1}H -^{13}C CP/ MAS NMR curves for toluene for toluene resonances after loading 1.7 µm Syncronis silica

Table 5.14 ^{1}H-^{13}C CP/ MAS kinetics for the toluene adsorbed onto the 1.7µm Syncronis silica

Resonance (ppm)	^{13}C site	Model		Signal Intensity (10^7)	T_{IS} (ms)	$T^{H}_{1\rho}$ (ms)	T_{df} (ms)	T^2 (ms)	λ	R^2
C_{18} Chain										
18.6	C1	IS (2 components)	Fast	1.05 ± 0.05	0.259 ± 0.025	3.07 ± 0.246				0.994
			Slow	1.70 ± 0.11	3.07 ± 0.301	61.5 ± 25.3				
23.9	C2 and C17	IS (2 components)	Fast	1.30 ± 0.15	0.352 ± 0.063	1.19 ± 0.18				0.994
			Slow	1.94 ± 0.07	1.78 ± 0.12	> 50				
30.6	C3-C16 (Gauche)	I-I*-S		18.8 ± 0.35		>50	5.09 ± 0.47	0.37 ± 0.03	0.67 ± 0.02	0.998
35.5	C3-C16 (Trans)	I-I*S		1.96 ± 0.86		>50	1.29 ± 0.28	0.16 ± 0.02	0.61 ± 0.06	0.992
Toluene										
21.4	$\underline{C}H_3C_6H_5$	IS		7.24 ± 0.15	30.0 ± 0.58					0.992
125.7	$CH_3\underline{C}_6H_5$ (E)	IS		28.0 ± 0.48	227.8 ± 4.03					0.992
128.5	$CH_3C_6H_5$ (D)	IS		39.1 ± 0.26	155.5 ± 1.07					0.999
129.4	$CH_3C_6H_5$ (C)	IS		20.5 ± 7.36	80.4 ± 31.1					0.999

The CP kinetic data show a significant increase in both T_{IS} and $T^{H}_{1\rho}$ for C1. This indicates that the base of the alkyl chain has become more mobile in the presence of toluene. This indicates the guest in penetrating to the base on the alkyl chain. Further an interaction between the alkyl chains and the analyte is also indicated by the change in the *trans/ gauche* ratio. The intensity of the resonance corresponding to the *gauche* position increases with the addition of toluene, indicating a larger proportion of C_{18} chains are in the *gauche* position confirming the conclusions drawn from the ^{1}H-^{13}C CP/MAS NMR (Figure 5.29). The resonances corresponding to toluene do not show any relaxation indicating a high level of mobility.

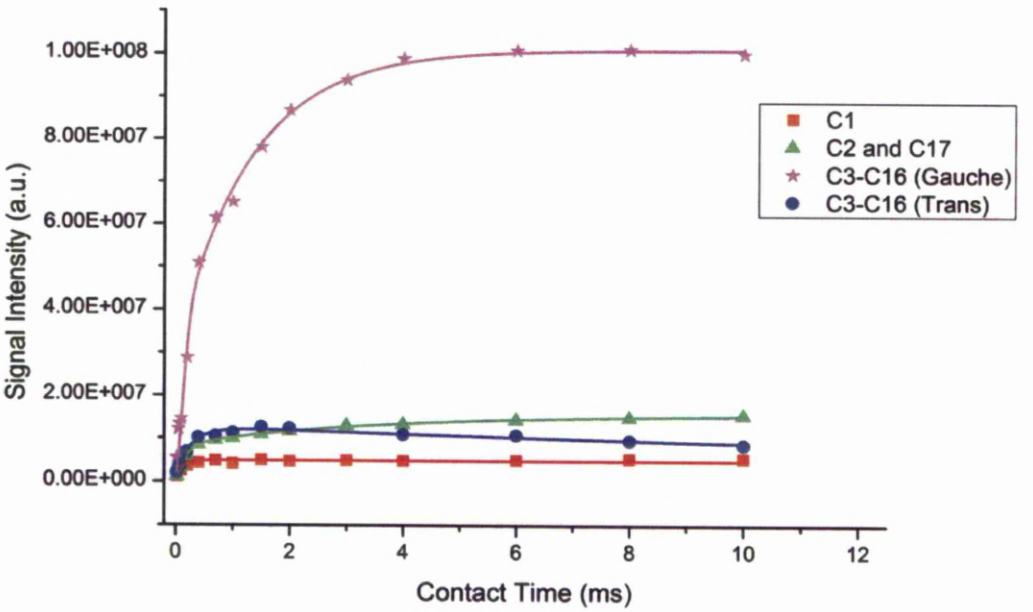

Figure 5.31 ^{1}H-^{13}C CP/MAS kinetics for C_{18} chain and end-capping for the Spherisorb ODS2 silica with toluene

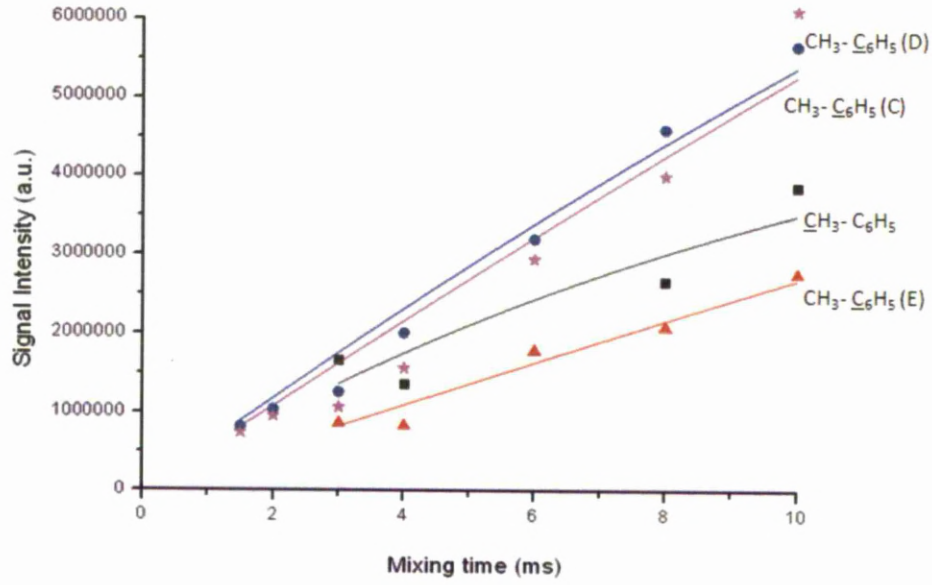

Figure 5.32 ^{1}H-^{13}C CP/MAS NMR kinetics curves for toluene for the Spherisorb silica and toluene sample

Table 5.15 ^{1}H-^{13}C CP/ MAS kinetics for the toluene adsorbed onto Spherisorb ODS2 silica

Resonance (ppm)	^{13}C site	Model		Signal Intensity (10^7)	T_{IS} (ms)	$T^{H}_{1\rho}$ (ms)	T_{df} (ms)	T^{2} (ms)	λ	R^2
2.2	End-capping	No relaxation		1.02 ± 0.03	2.02 ± 0.173					0.980
C_{18} chain										
13.0	C1	No relaxation		0.48 ± 0.01	0.11 ± 0.02					0.885
23.6	C2 and C17	IS (2 components)	Fast	0.78 ± 0.03	0.18 ± 0.02	3.36 ± 0.30				0.995
			Slow	1.56 ± 0.04	3.31 ± 0.183	> 50				
30.9	C3-C16 (Gauche)	I-I*-S		10.1 ± 0.17		>50	1.28 ± 0.17	0.14 ± 0.03	0.70 ± 0.06	0.993
34.4	C3-C16 (Trans)	I-I*-S		1.26 ± 0.06		28.1 ±7.0	0.31 ± 0.17	0.18 ±0.34	0.76 ± 0.70	0.964
Toluene										
21.4	$\underline{C}H_3C_6H_5$	No relaxation		1.57 ± 0.12	37.9 ± 3.11					0.890
125.7	$CH_3\underline{C}_6H_5$ (E)	No relaxation		1.47 ± 0.06	> 50					0.957
128.5	$CH_3C_6H_5$ (D)	No relaxation		1.80 ± 0.08	28.5 ± 1.28					0.970
129.3	$CH_3C_6H_5$ (C)	No relaxation		3.50± 0.03	> 50					0.929

The ^{1}H–^{13}C CP kinetic data for this stationary phase shows a similar trend to the 1.7 µm Syncronis silica. An increase in T_{IS} times are observed for carbons 1, 2 and 17 indicating an increase in mobility with the addition of toluene. Though Spherisorb ODS2 contains a denser packing of C_{18} chains the data still shows long relaxation times for the C_{18} chain and toluene, comparable with 1.7 µm Syncronis (Table 5.14). ^{1}H NOESY NMR can be used to fully analyse the effect of the more densely packed hydrocarbons on the silicon surface.

The ^{1}H T_1 relaxation NMR measurements of 1.7 µm Syncronis with and without toluene were analysed to determine the effect of the analyte on the mobility of the bonded alkyl chains.

Table 5.16 ^{1}H T_1 NMR measurements of 1.7 µm Syncronis silica

ppm	^{13}C site	T_1 (ms)
0.335	End-capping	707.09
0.840	C1, C2, C17	719.63
1.275	C3 – C16	706.59

The ^{1}H T_1 measurement shows the end of the carbon chain to have a slightly longer relaxation time compared to the main body of the chain.

Table 5.17 ^{1}H T_1 NMR measurements of toluene coated 1.7 µm Syncronis silica

ppm	^{13}C site	T_1 (ms)
0.321	End-capping	705.06
0.679	C1, C2, C17	776.34
1.075	C3 – C16	716.69
1.872	$C\underline{H}_3C_6H_5$	3300
6.711	$CH_3C_6\underline{H}_5$ (ortho, para)	3738
6.803	$CH_3C_6\underline{H}_5$ (meta)	1362

The ^{1}H T_1 relaxation measurements show a slight increase in relaxation times for the C_{18} chain after the addition of toluene confirming the results obtained through ^{1}H-^{13}C CP kinetics. The toluene molecule is extremely mobile, which is shown by the long relaxation time (1.4 – 3.7 seconds), as toluene is in a liquid state this is expected. The high mobility of both groups, indicated by the relaxation times, show the need for the interactions to be measured at 233 K whereby the reduced mobility will facilitate the measurement of the interactions between the two compounds.

We have shown that the addition of toluene increases the proportion of C_{18} chains in the *gauche* position for both stationary phases and increased the mobility of the alkyl chains. ^{1}H-^{13}C CP/MAS NMR and CP kinetics have shown that the effects of the addition of the analyte can be observed at room temperature though reducing the mobility of the analyte and the organic groups of the stationary phase increases the dipolar coupling. ^{1}H NOESY NMR can be used to analyse the intermolecular distances between the analyte and stationary phases which can be used to improve our understanding of how the two phases interact.

5.5 ^{1}H NOESY NMR

5.5.1 1.7 µm Syncronis

In solids ^{1}H spin diffusion can occur through dipolar interactions when protons are reasonably close in space, up to 5Å.[162] 2-Dimentional experiments can correlate the different environments, which are distinguished by different chemical shifts, and the structural connectivity of the material through the dipolar interaction.[238] Nuclear Overhauser Effect SpectroscopY (NOESY) experiments can be used to detect cross relaxation between two spins and therefore determine which spins are close in space. The intensity of the cross peaks is dependent on the distance between the two spins as the rate of ^{1}H spin diffusion decreases with distance ($1/r^6$). This technique can be used to determine how the C_{18} chain and toluene molecules interact.

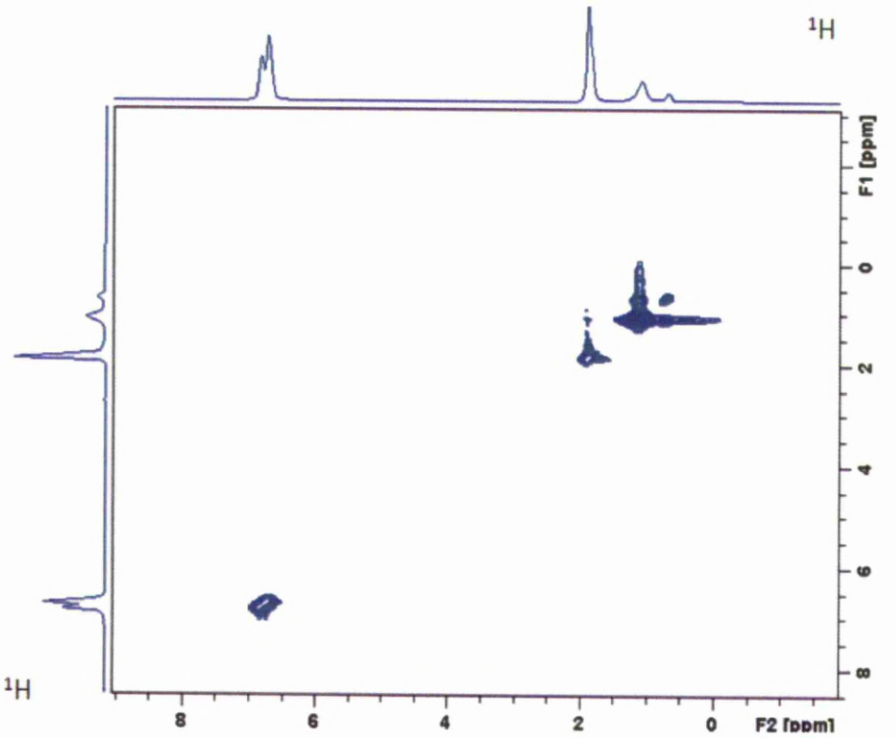

Figure 5.33 ^{1}H NOESY NMR spectrum toluene coated 1.7 µm Syncronis silica. Mixing time of 100 ms and an MAS rate of 10 kHz were used.

Only the auto-correlation (diagonal) peaks are observed for a mixing time of 100 ms, it is the non-diagonal peaks created by the transfer of magnetisation which are used to gain structural information.

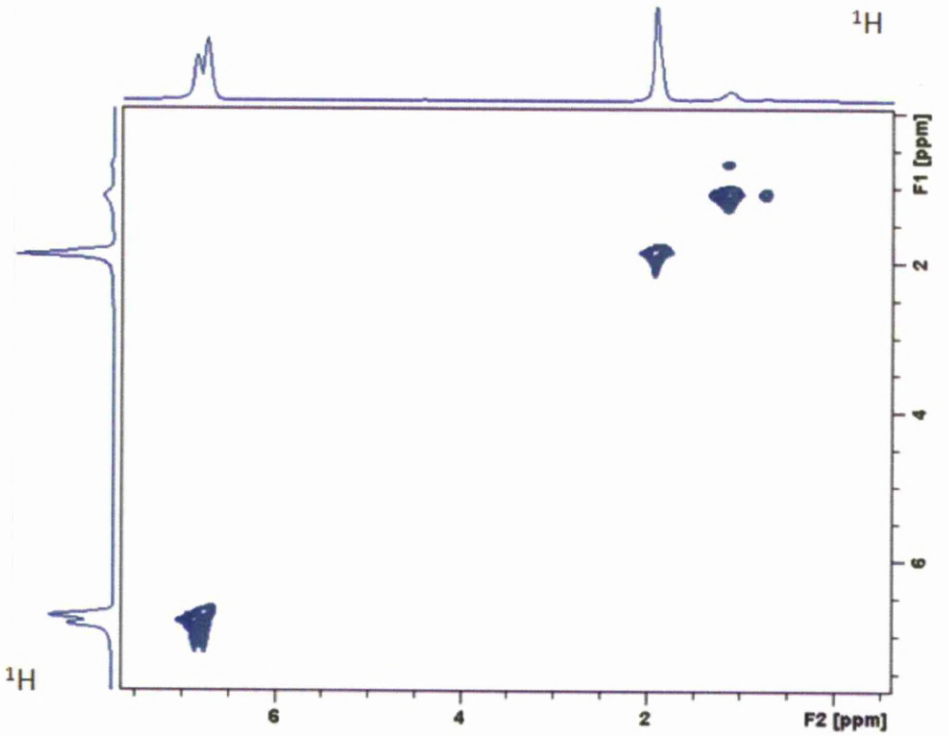

Figure 5.34 ^{1}H NOESY NMR spectrum toluene coated 1.7 µm Syncronis silica. Mixing time of 550 ms and an MAS rate of 10 kHz were used.

Again, only the auto-correlation (diagonal) peaks are observed for the longer mixing time (550 ms). The ^{1}H NOESY spectrum shows no cross peaks (non-diagonal peaks) between the alkyl chain and the toluene guest molecule created by the transfer of magnetisation. One cause may be the high mobility of the two organic groups reducing dipolar interactions. In order to observe the interactions present ^{1}H NOESY NMR spectra were measured at 233 K to reduce the mobility of the organic groups strengthening the dipolar interactions.

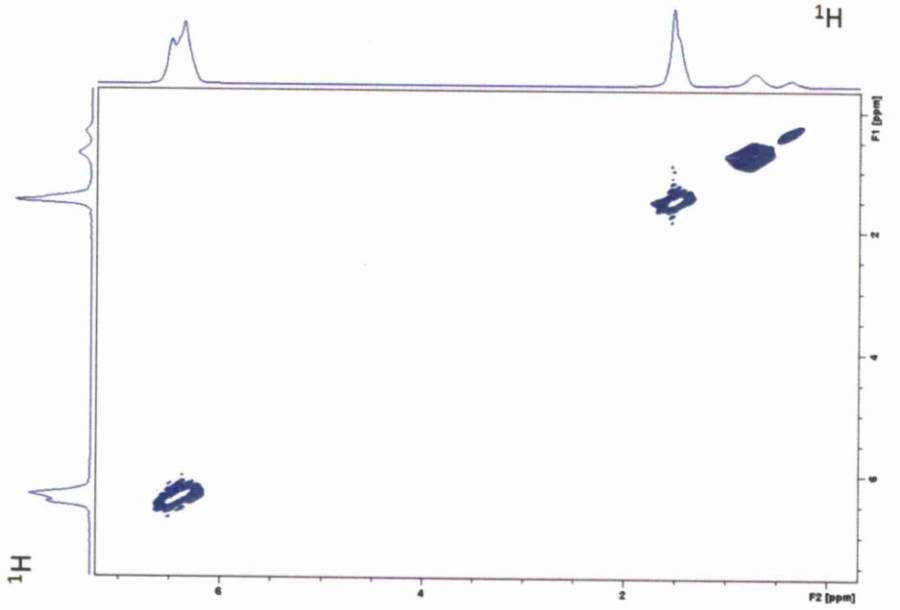

Figure 5.35 ^{1}H NOESY NMR spectrum at 233K of toluene coated 1.7 µm Syncronis silica. Mixing time of 10 ms and an MAS rate of 10 kHz were used.

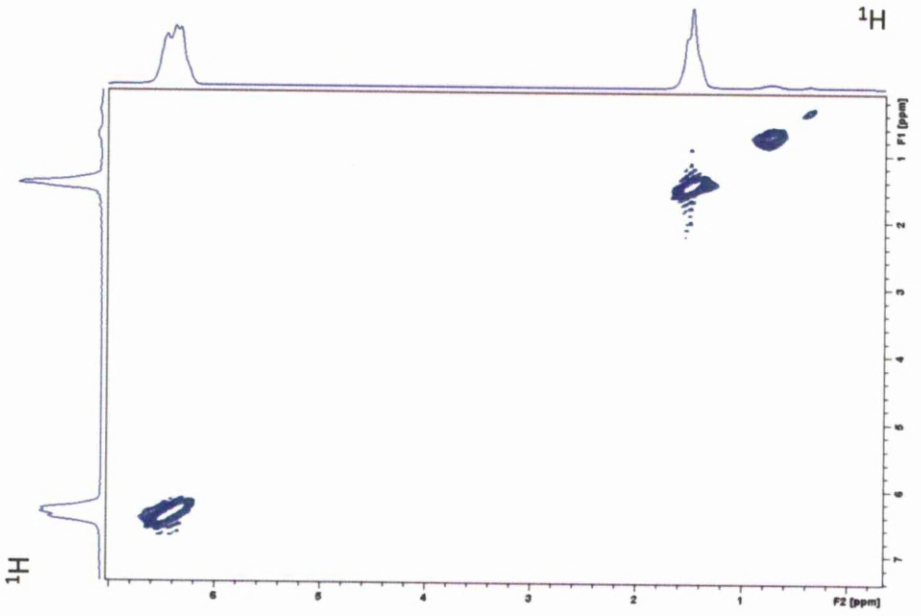

Figure 5.36 ^{1}H NOESY NMR spectrum at 233K of toluene coated 1.7 µm Syncronis silica. Mixing time of 100 ms and an MAS rate of 10 kHz were used.

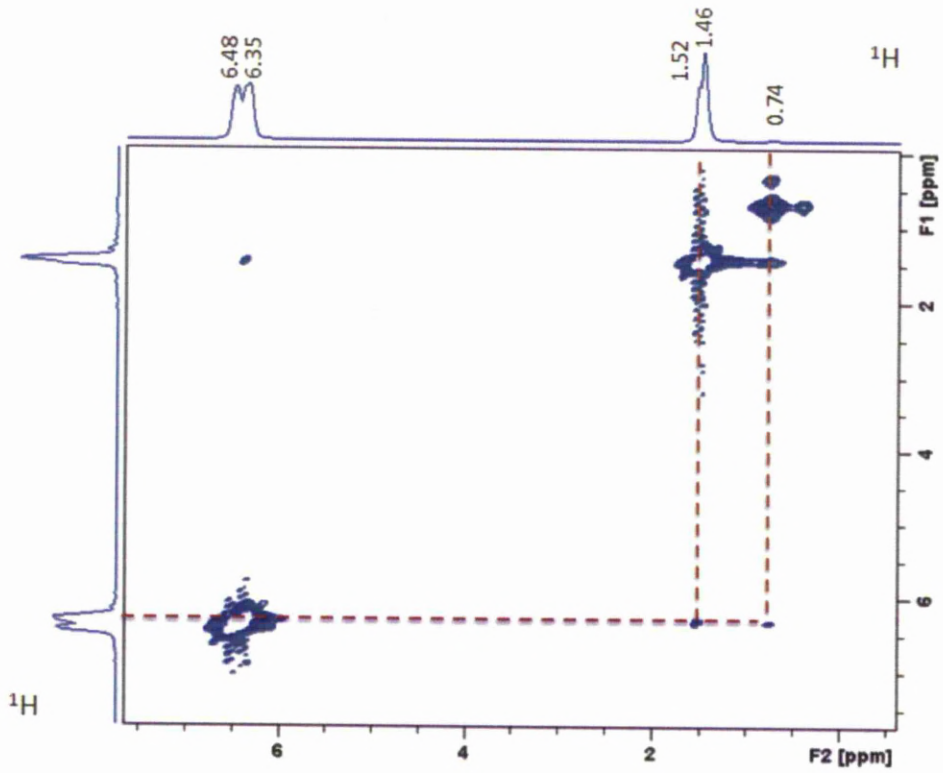

Figure 5.37 ^{1}H NOESY NMR spectrum at 233K of toluene coated 1.7 µm Syncronis silica. Mixing time of 550 ms and an MAS rate of 10 kHz were used.

The ^{1}H NOESY 2D spectrum (Figure 5.37) shows a correlation between the methyl group of toluene and the resonance corresponding to the protons at the ortho/ para position (6.35 ppm) but not at the meta position (6.48 ppm). If the methyl group does not correlate to the whole of the benzene ring it is likely that interaction occurs between the methyl group and the protons at the ortho position only. A correlation is also observed between the end methyl group of the C_{18} chain (0.74 ppm) and both the methyl group of the toluene and the ortho/ para position of the benzene ring. As previously discussed it is likely that the stationary phase/ analyte interaction occurs primarily between the methyl groups of the C_{18} and the methyl group in toluene, though as they are close enough in space some dipolar interaction is observed between the alkyl chain and the protons at the ortho position.

5.5.2 Spherisorb ODS2

At mixing times of 10 ms the ^{1}H NOESY NMR spectrum shows cross peaks between the methyl group of the toluene analyte and $CH_3C_6\underline{H}_5$ at the ortho position. Despite the more densely packed C_{18} no correlation is observed between the aromatic ring and the Syncronis silica at these short mixing times.

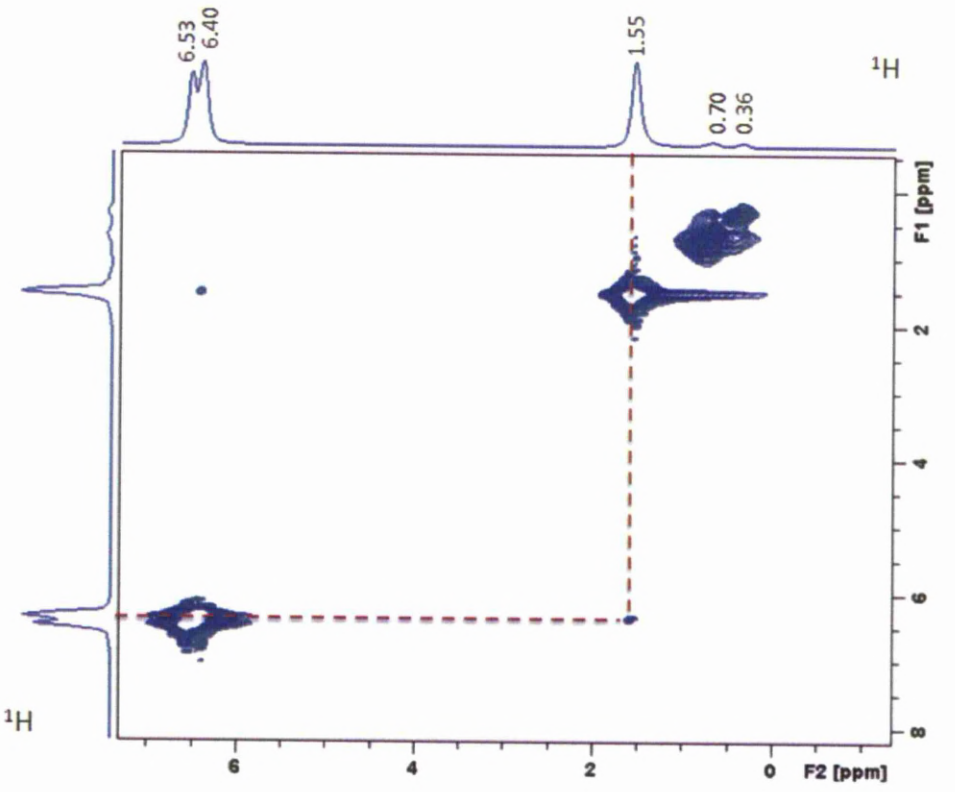

Figure 5.38 ^{1}H NOESY NMR spectrum at 233K of toluene coated Spherisorb ODS2 silica. Mixing time of 10 ms and an MAS rate of 10 kHz were used.

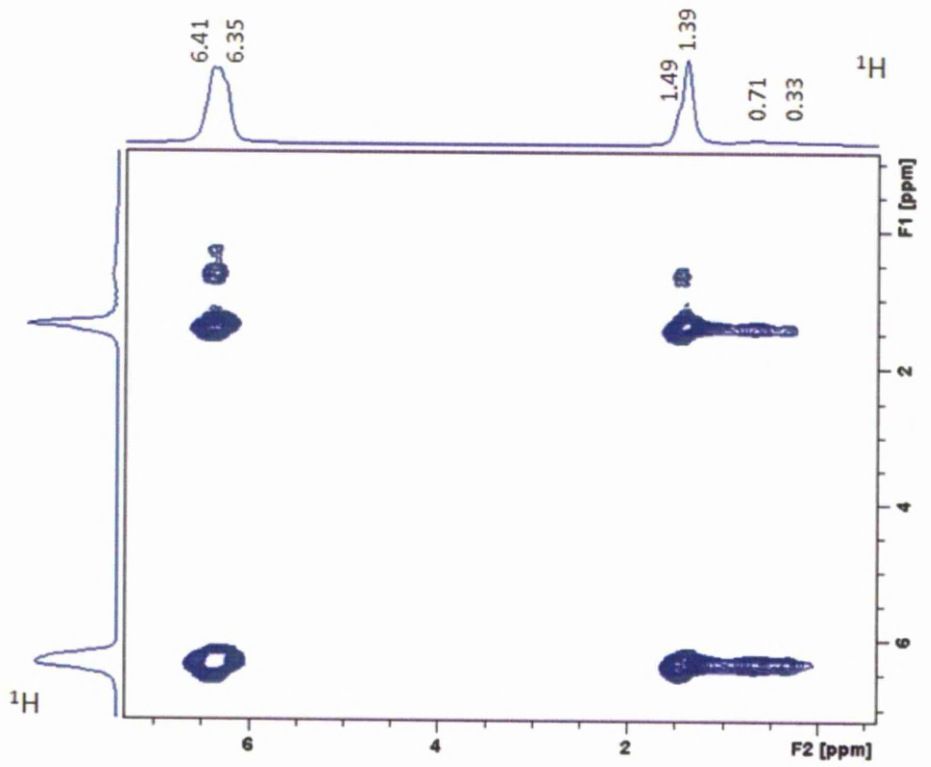

Figure 5.39 ^{1}H NOESY NMR spectrum at 233K of toluene coated Spherisorb ODS2 silica. Mixing time of 550 ms and an MAS rate of 8 kHz were used.

The ^{1}H NOESY experiments using longer mixing time of 550 ms were needed to observed cross peaks. Spherisorb ODS2 at 233 K show clear interactions between the whole of the toluene molecule and both the end and main body of the C_{18} chain. Level of interaction observed for Spherisorb ODS2 at a mixing time of 550 ms is much greater than 1.7 µm Syncronis. The higher levels of interaction observed for Spherisorb are due to the more densely packed C_{18} chains. This indicates that the polymeric chains create a greater interaction with analytes compares to monomeric forms of C_{18}. Though an increase in interaction is observed this does not automatically produce longer retention times as the ^{1}H-^{29}Si CP/ MAS NMR also so the presence of polar Si-OCH_3 groups which can repel non-polar analytes.

As correlations are observed for the whole C_{18} with both the methyl group and the aromatic ring of the toluene analyte primary interactions cannot be determined. By examining the intensity of the cross-peaks with varying mixing times we can analyse how the two groups interact.

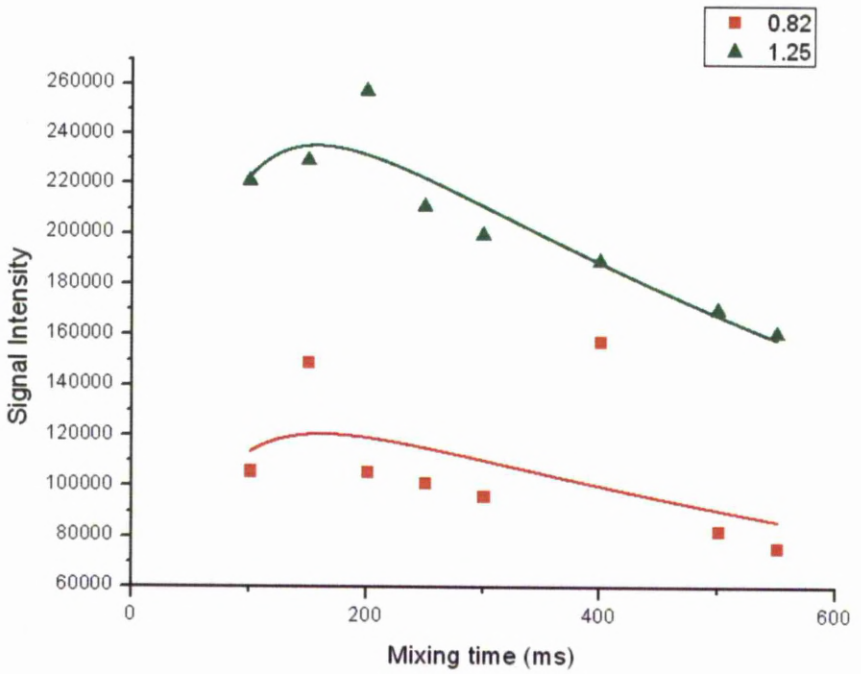

Figure 5.40 Intensity of cross peaks with varying mixing times of compound correlating to $C\underline{H}_3C_6H_5$

We have analysed the intensity of the cross peaks between the methyl group of the toluene and the end methyl groups of the C_{18} chain (0.82 ppm) or the main body of the alkyl group (1.25 ppm). The rate at which the magnetisation increases is very similar for both the end methyl group and the main body of the C_{18} chain. This is due to the high mobility of the chains which are continuously changing in conformation and therefore altering how the alkyl group interacts with the guest molecule. The methyl groups have a slightly faster build up of the magnetisation which indicates toluene interacts primarily with the terminal methyl group of the alkyl chains.

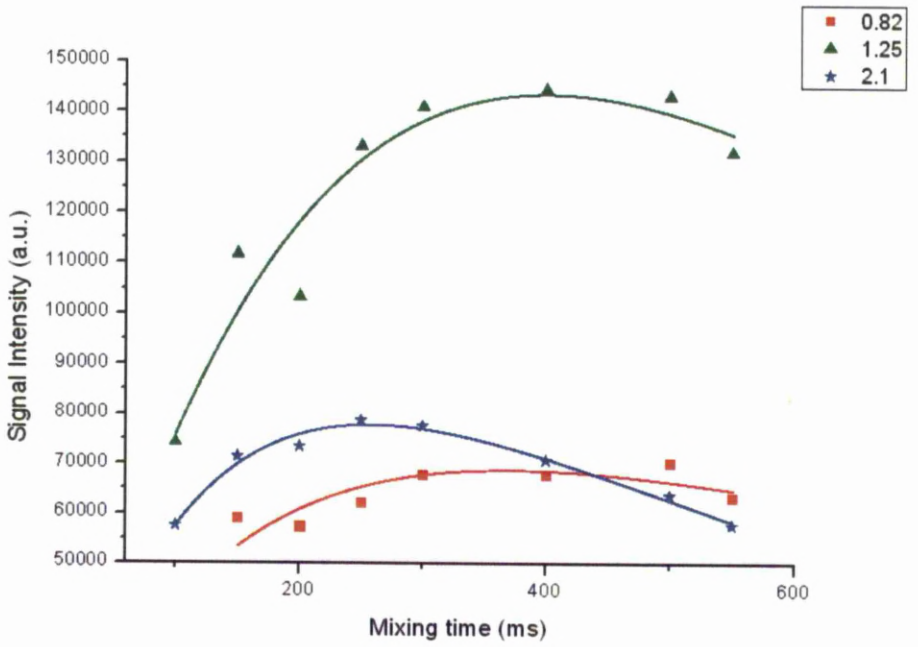

Figure 5.41 Intensity of cross peaks with varying mixing times of compound correlating to $CH_3C_6\underline{H}_5$

The initial interaction occurring between the end of the C_{18} chain and the analyte is further confirmed by analysing the intensity of the cross peaks between $CH_3C_6\underline{H}_5$ and the alkyl chain. Again the build up of magnetisation occurs fastest between the $CH_3C_6\underline{H}_5$ and the end methyl group of the C_{18} chain as opposed to the main body. The fastest increase in intensity occurs between the methyl (2.1 ppm) and aromatic ring of the toluene though this is to be expected as they are part of the same compound and therefore closest in space. We have shown the methyl group of the C_{18} chain is closest in space to the analyte, by comparing the rate of spin diffusion between both the methyl and aromatic ring of toluene to the C_{18} change we can determine what part of the analyte is closer to the alkyl chain. The maximum intensity of the cross peaks between $C\underline{H}_3C_6H_5$ and the methyl group of the C_{18} chain occur below a mixing time of 200 ms. The maximum intensity of the cross peaks between $CH_3C_6\underline{H}_5$ and the main body of the C_{18} chain occur at *ca.* 300-400 ms. As the transfer of magnetisation is fastest between $C\underline{H}_3C_6H_5$ and the C_{18} chain it is logical to conclude that the primary interactions for the Spherisorb column occur between the terminal methyl of the C_{18} chain and the methyl group of toluene.

Table 5.18 Kinetic data for toluene coated Spherisorb ODS2 silica

Resonance correlating with $C\underline{H}_3C_6H_5$	Group	Model	Signal Intensity (10^4)	T_{IS} (ms)	$T^H_{1\rho}$ (ms)	R^2
0.82	C_1, C_2, C_{17}, C_{18}	IS	14.2 ± 5.00	51.6 ± 70.0	> 300	-0.15
1.25	C_3-C_{16}	IS	28.3 ± 2.31	52.8 ± 15.9	> 300	0.809
Resonance correlating with $CH_3C_6\underline{H}_5$						
0.82	C_1, C_2, C_{17}, C_{18}	IS	9.35 ± 4.24	157.5 ± 106.9	> 300	0.250
1.25	C_3-C_{16}	IS	39.0 ± 5.80E6	399.5 ± 5.97E7	> 300	0.871
2.1	$C\underline{H}_3C_6H_5$	IS	12.2 ± 1.10	136.3 ± 18.0	> 300	0.969

5.5.3 $CH_2\underline{CH}_2/CH_2\underline{C}_6H_5$ PMO

The ^{1}H NOESY NMR spectra for the C_{18} functionalised silica have show the predominant interactions with toluene occur between the end methyl group of the C_{18} chain and the methyl group of the toluene, regardless of the density of the alkyl chains. The –CH_2CH_2-/ -$CH_2C_6H_5$ functionalised PMO was also analysed to examine how varying the functional groups on the stationary phase effects the intermolecular interactions and retention of the toluene analyte.

In the aromatic region of the ^{1}H MAS NMR spectrum two sharp resonances can be observed corresponding to the analyte solvent and a broad resonance corresponding to the –$CH_2C_6H_5$ bonded functionality.

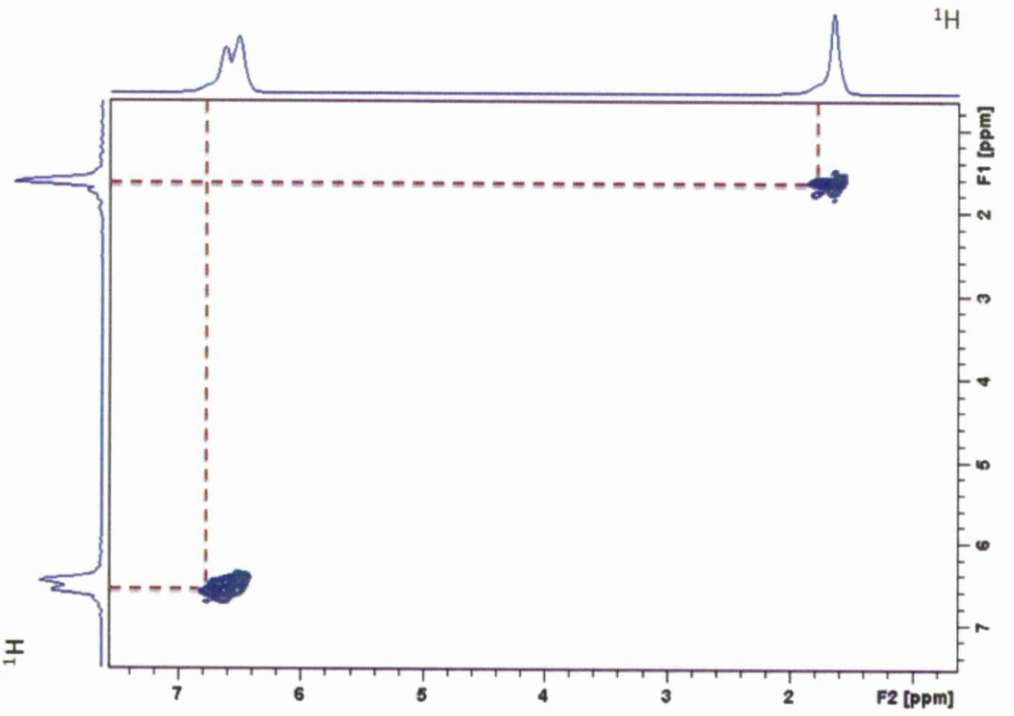

Figure 5.42 ^{1}H NOESY NMR spectrum at 298 K of toluene coated $-CH_2CH_2-$/ $-CH_2C_6H_5$ functionalised PMO. Mixing time of 25 ms and an MAS rate of 10 kHz were used.

The ^{1}H NOESY spectrum shows a correlation between $C\underline{H}_3C_6H_5$ and $-CH_2CH_2-$. An additional correlation is observed between the $-CH_2C_6H_5$ bonded functionality and the protons at the meta position of the toluene ring. This differs from the C_{18} functionalised stationary phase and could be due to the π-π interactions of the two functionalities. Both correlations occur at low mixing times (25 ms) suggesting a strong interaction between toluene and both $-CH_2CH_2-$ and $-CH_2C_6H_5$ functionalities. These initial correlations are observed at much shorter mixing times compared to 1.7μm Syncronis (550 ms) and Spherisorb ODS2. It must also be taken into account that at a mixing time of 25 ms correlations are observed with both the methyl and aromatic ring of the toluene analyte whereas the C_{18} functionalised silica the diffusion is much slower (Figure 5.39) indicating the aromatic ring is at a greater distance to the alkyl chain. Furthermore, due to the functionality being incorporated into the framework and not grafted onto the surface the restricted motions of these moieties have allowed the measurement of these interactions at room temperature not 233 K. As the $-CH_2CH_2-$/ -

$CH_2C_6H_5$ functionalised silica interacts with both the methyl and aromatic ring of toluene, this should lead to longer retention times.

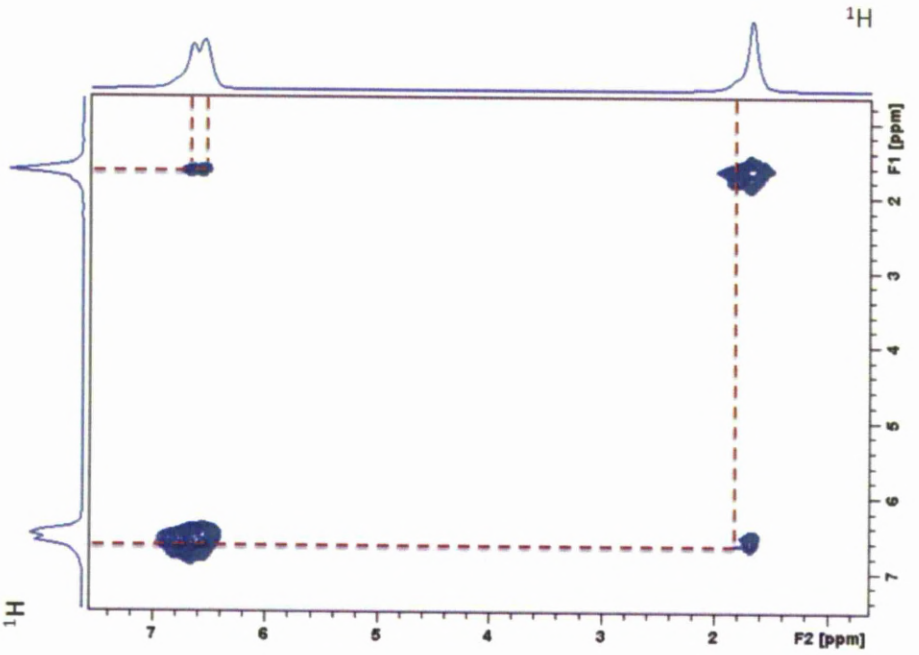

Figure 5.43 ^1H NOESY NMR spectrum at 298 K of toluene coated $-CH_2CH_2-$/ $-CH_2C_6H_5$ functionalised PMO. Mixing time of 100 ms and an MAS rate of 10 kHz were used.

At slightly longer mixing times a correlation can be observed between the $-CH_2CH_2-$ functionality and $CH_3C_6\underline{H}_5$. It is likely that the interaction is between $CH_3C_6\underline{H}_5$ and $-CH_2C_6H_5$ not $CH_3C_6\underline{H}_5$ and $-CH_2CH_2-$ though due to the homogenous distribution of the $-CH_2CH_2-$/$-CH_2C_6H_5$ functionalities in the silica frame work $CH_3C_6\underline{H}_5$ and $-CH_2CH_2-$ will be close in space.

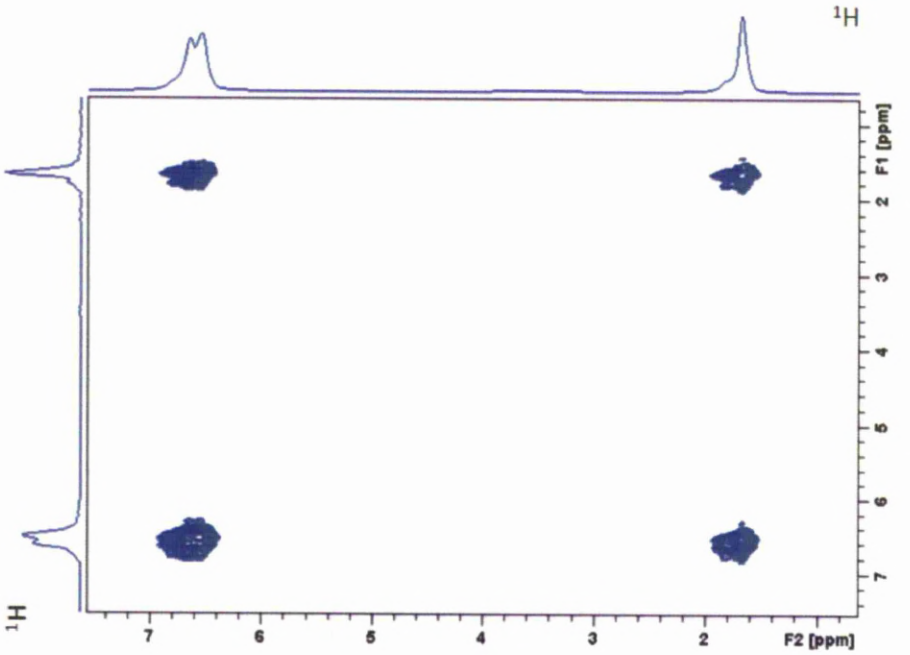

Figure 5.44 ^{1}H NOESY NMR spectrum at 298 K of toluene coated $-CH_2CH_2-$/ $-CH_2C_6H_5$ functionalised PMO. Mixing time of 550 ms and an MAS rate of 10 kHz were used.

At a mixing time of 550 ms correlations can be observed between both functionalities and the toluene analyte. By analysing the interactions between the stationary phases and analyte on a molecular level we have demonstrated that the ends of the C_{18} chains interact with the methyl group of toluene. A correlation between the bonded phase and toluene is observed at shorter mixing times for the more densely packed C_{18} phase (Spherisorb) indicating the two moieties are closer in space. The polar $-SiOCH_3$ groups will also affect retention time of the analyte. The $-CH_2CH_2$/$-CH_2C_6H_5$ functionalised PMO displays strong interactions with both the methyl group and aromatic ring of toluene and therefore should show an increased retention time. It is important to note that as the $-CH_2CH_2-$/ $-CH_2C_6H_5$ PMO is not a commercially available product, it contains no end-capping groups.

5.6 Chromatography

Chromatographic selectivity (α) can be used to probe the retention behaviour of different stationary phases. The selectivity is given by the difference in the change of Gibbs free energy of an analyte moving between the mobile and stationary phase for two different analytes .[239]

$$\alpha = k'_a/k'_b \tag{5.8}$$

Where k'_a and k'_b are the capacity factors for solutes a and b.

$$\ln\alpha = -\Delta(\Delta G)/RT \tag{5.9}$$

Where ΔG is the change in Gibbs free energy, R corresponds to the gas constant and T is the temperature. If the same mobile phase is used with each stationary phase the contribution of the mobile phase to the Gibbs free energy is equivalent for each column and therefore cancelled out. The selectivity is therefore indicative of the differences between the molecular structures of the stationary phases. [240,241,239]

Reversed-phase chromatography is dependent on three main factors, solvophobic interactions, chemical interactions and shape selectivity.

Solvophobic selectivity depends on the hydrophobic interactions between the solute and the stationary phase. Research by Tanaka *et al.*[242] and Jandera *et al.* [243] have shown that the strength of these hydrophobic interactions is the most important parameter for reversed-phase separations.

Chemical selectivity is governed by strong interactions, such as hydrogen bonding, between the solute and specific active sits on the stationary phase (silanol groups). Reversed-phase chromatography is only weakly affected by chemical selectivity, whereas this parameter is much more dominant in normal phase separations.

The third parameter effecting reversed-phase separations is shape selectivity. This parameter is primarily dependent on steric hindrance for rigid and planar molecules.

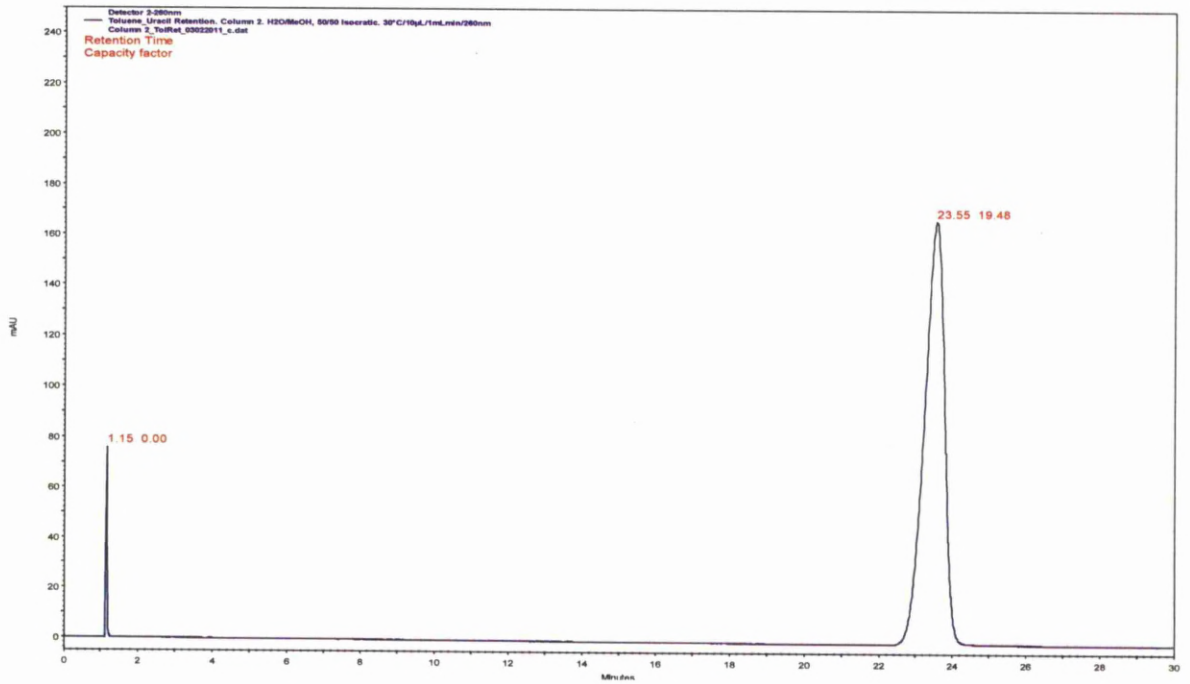

Figure 5.45 Chromatogram of uracil and toluene on a C_{18} functionalised 1.7 µm Syncronis column

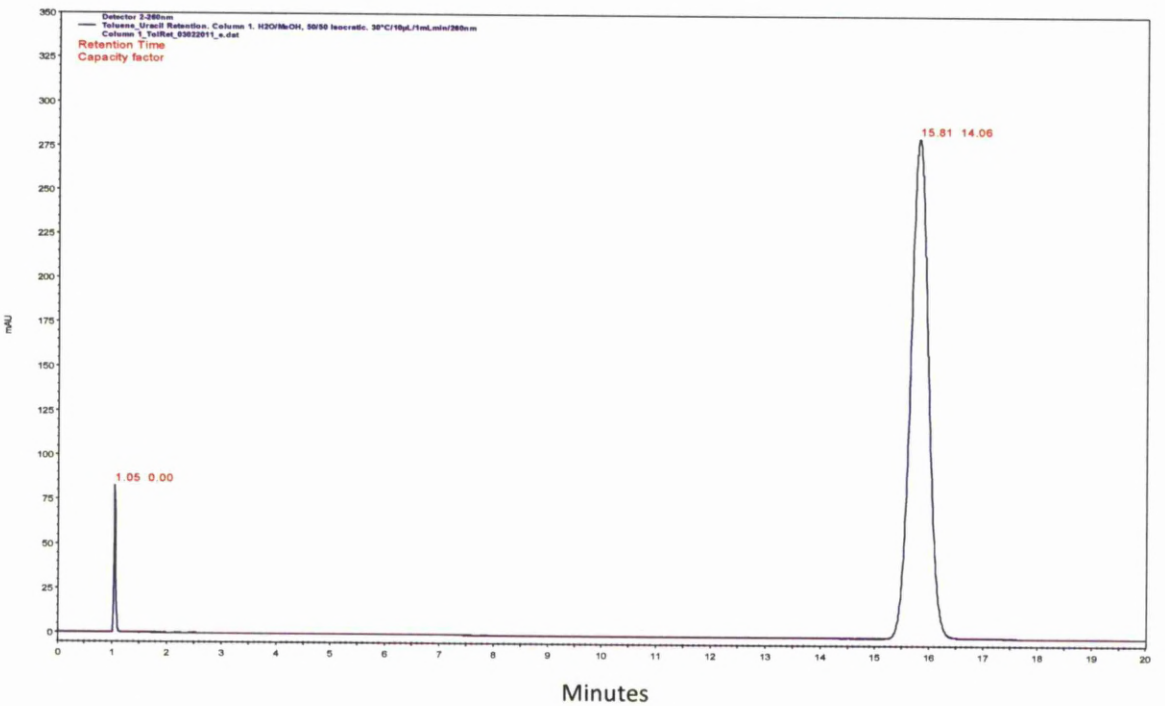

Figure 5.46 Chromatogram of uracil and toluene on a C_{18} functionalised Spherisorb ODS2 column with end-capping

Stationary Phase	Retention Capacity (mins)
1.7 μm Syncronis	19.48
Spherisorb ODS 2	14.06

A higher retention capacity is observed when using the 1.7 μm Syncronis column (19.48) compared to the Spherisorb column (14.06). The occurrence of cross peaks between the bonded phase and guest molecule using ^{1}H NOESY NMR experiments are observed at shorter mixing times for Spherisorb. This indicates toluene is closer in space and therefore interacts more strongly with the alkyl chain. The interaction with the C_{18} chains may be stronger for Spherisorb though as we have shown the bonded phase is not uniform throughout the silica surface. We must also take into consideration that 1.7 μm Syncronis silica not only has a larger surface area (238.2 m^2/g) compared to Spherisorb (110 m^2/g) but also a much smaller particle size (1.76 μm compared to 4.52 μm) leading to more efficient column. The ^{1}H-^{29}Si CP/MAS NMR (Figure 5.12) indicated the presence of T-sites and therefore $-SiOCH_3$ groups on the Spherisorb stationary phase. These polar groups will repel the non-polar analyte reducing the interaction with the stationary phase causing premature elution, reducing the capacity factor. These groups are not present in 1.7 μm Syncronis silica. The effect of polar groups on the silica surface can be explored by comparing the retention capacity factors of Spherisorb ODS2 before and after end-capping the remaining surface silanol groups.

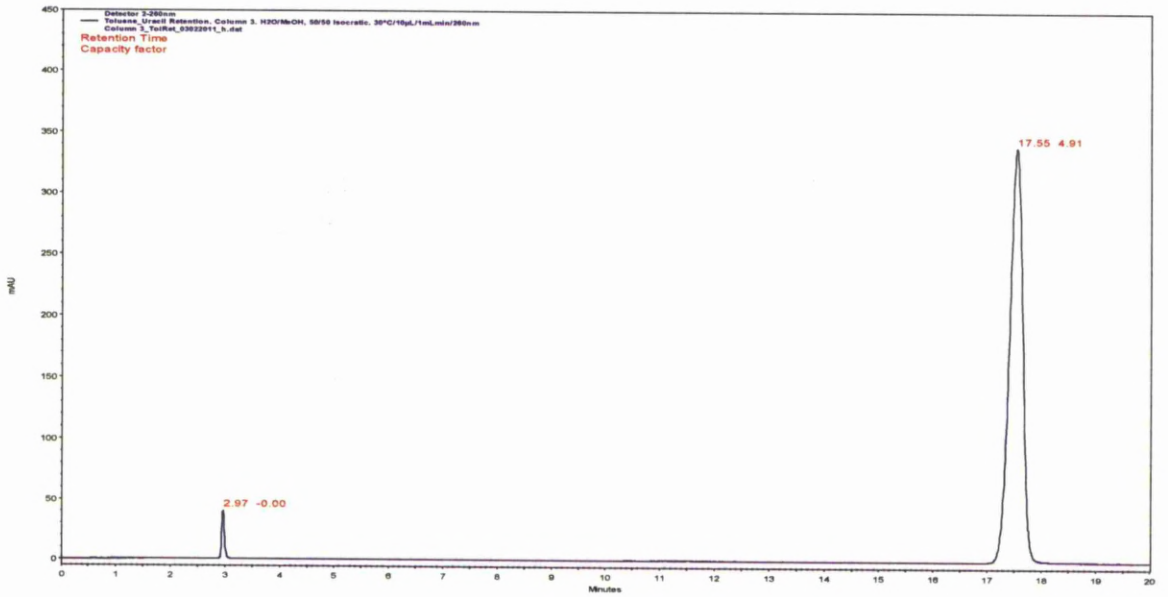

Figure 5.47 Chromatogram of uracil and toluene on a C_{18} functionalised Spherisorb ODS2 column without end-capping

Stationary Phase	Retention Capacity (mins)
Spherisorb ODS 2 (with end-capping)	14.06
Spherisorb ODS 2 (without end-capping)	4.91

The importance of the end-capping is further confirmed by the comparison of the capacity factor of Spherisorb silica before (Figure 5.47) and after (Figure 5.46) the end-capping reaction. The capacity factor is dramatically reduced (4.91) before end-capping Spherisorb silica confirming the surface silanol groups have a detrimental effect of the retentivity of the reversed-phase column. The end-capping of these polar surface groups almost triples the K' factor.

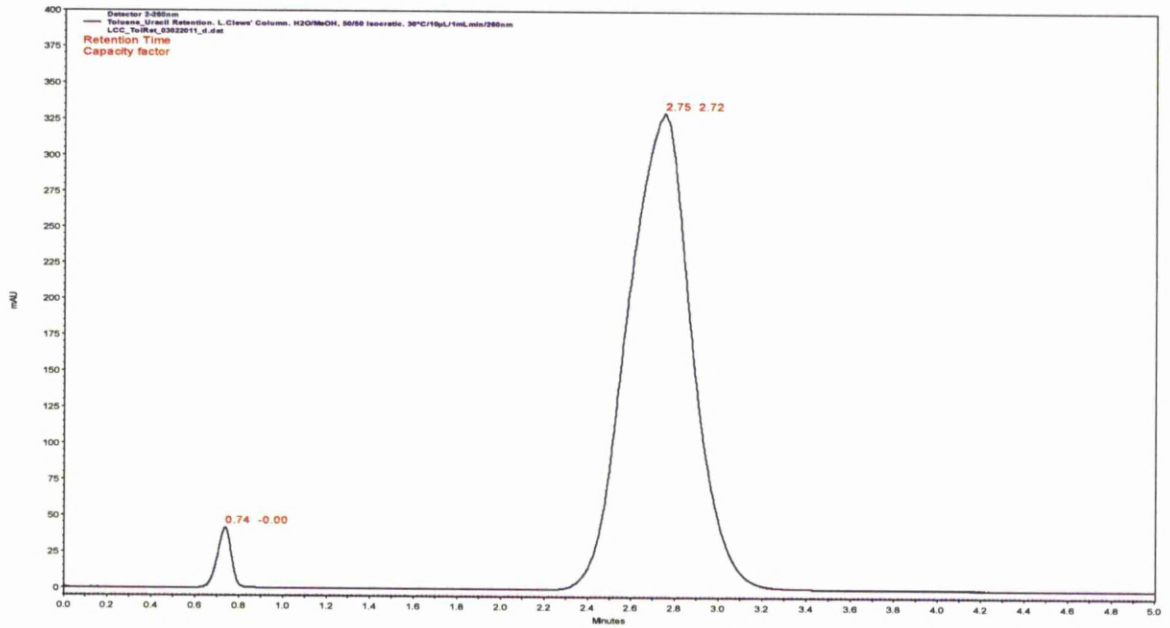

Figure 5.48 Chromatogram of uracil and toluene on a $-CH_2CH_2-$/ $-CH_2C_6H_5$ functionalised column

Stationary Phase	Retention Capacity (mins)
$-CH_2CH_2-$/ $-CH_2C_6H_5$ functionalised silica	2.72

By comparing the capacity factors of the C_{18} functionalised stationary to the $-CH_2CH_2-$/ $-CH_2C_6H_5$ functionalised PMO the effect of different functional groups can be assessed. The chromatograms show the alkyl chain to be more efficient at retaining the toluene compared to the PMO. As this silica is not commercially available the particle size distribution is much larger compared to the other stationary phases, producing a more inefficiently packed column, leading to the band broadening observed. The stationary phase will contain surface silanol groups as there has been no end-capping procedure. The capacity factor is dramatically reduced for C_{18} functionalised silica containing surface silanol groups. The interaction between toluene and the $-CH_2CH_2-$/ $-CH_2C_6H_5$ functional groups occurs in closer proximity to the silanol groups present and therefore creates a greater effect on the retention of the analyte.

5.7 Conclusion and Discussion

There are a wide variety of commercially available reversed-phase materials, though columns containing the same functional groups can produce very different chromatograms. This is a direct result of the varying synthetic conditions used by different manufacturing companies and the use of different grafting and end-capping techniques. There are some publications comparing the selectivity of columns from different manufacturers though a full analysis comparing columns on a mesoscopic and molecular level is not available.

We have shown that on a mesoscopic level the C_{18} functionalised Syncronis column should be more efficient compared to the C_{18} functionalised Spherisorb silica due to the larger surface area, narrower pore size distribution and smaller particle size. Through ^{1}H-^{29}Si CP MAS/NMR spectra we show that Syncronis contains a monomeric form of C_{18} and Spherisorb contains the polymeric form, which produces a denser coverage. As the surface density of organic groups for both silicas are very similar we can conclude the polymeric C_{18} chains must form clusters sporadically distributed throughout the surface.

The effects of the monomeric/ polymeric bonding on the conformation of the C_{18} were analysed using ^{1}H-^{13}C CP/MAS NMR. The increase in *gauche* conformation with the addition of the analyte for both stationary phases indicates the alkyl chains become more mobile. This implies a positive interaction between the bonded phase and toluene, which is essential for the separation of non-polar analytes.

The way in which the bonded phase and toluene molecules interact was analysed using ^{1}H NOESY NMR. If it is possible to further understand how the two groups interact and whether this interaction differs for different bonded phases, RP columns can be tailored to the analytes more effectively. Through these 2-dimentional experiments it is evident that for both Syncronis and Spherisorb it is the methyl group of toluene that interacts with the end of the C_{18} chains. The ^{1}H NOESY experiments show correlations between the bonded groups and analytes at shorter mixing times for Spherisorb ODS2, which suggests the two groups are closer in space and therefore interact more strongly. From this it would be expected that Spherisorb would produce greater retention times though this is not the case. It appears that although the polymeric

nature of the C_{18} on Spherisorb creates a stronger interaction with the analyte the distribution of the bonded phase is not homogeneous throughout the silica. The extent to which the stationary phase retains the analyte will vary throughout the column reducing the capacity factor of the column.

The interaction of toluene with a $-CH_2CH_2-$/ $-CH_2C_6H_5$ functionalised PMO was also investigated. Unlike the C_{18} functionalised columns the primary interactions occurred between the aromatic ring of the toluene analyte and the aromatic ring of the benzyl tether. This is due to the π-π interactions present. The correlations between the two groups occur at much shorter mixing times indicating a stronger interaction. Though again the analysis shows the retention time of toluene is much shorter (2.72). As this stationary phase was not commercially produced it did not contain end-capping groups. By comparing the retentivity of Spherisorb ODS2 before (4.91) and after (14.06) the end-capping procedure the extent to which surface silanol groups effect non-polar compounds is evident. As the analyte / stationary phase interactions occur much closer to the silica surface for $-CH_2CH_2-$/ $-CH_2C_6H_5$ functionalised PMO compared to the C_{18} silicas the effect of the silanol groups will be more pronounced for this phase.

Chapter 6 - Sphere-in-Sphere Silica Beads

Chapter 6. - Sphere-in-Sphere Silica Beads

6.1 Introduction

Large molecules, such as polymers and biomolecules, have a much slower diffusion rate (approximately 1/10th) compared to smaller compounds (Figure 6.3). This causes problems when using conventional totally porous silica particles such as those associated with classical HPLC.[244] Research into increasing the mass transfer of larger solutes has been ongoing for over 40 years.[244] Theoretical work by Purnell, Golay and Knox indicated that using silica beads with an impenetrable core and a thin porous layer (referred to as superficially porous silica) would significantly improve solute mass transfer, as diffusion could only occur in the thin porous layer the diffusion path length is reduced, improving mass transfer (Figure 6.1).[245-247] However it was not until 1964 that Horvath and co-workers put the theory into practice.[248,249] Their research demonstrated the separation of nucleotides using a stationary phase comprised of glass beads coated with a pellicular layer of polystyrene-divinylbenzene polymeric resin. Pellicular silica beads typically consist of a solid core, normally either glass or silica, and a thin porous surface layer. The total diameter of the silica particles are approximately 20 – 40 μm and the porous layer is around 1 – 3 μm.

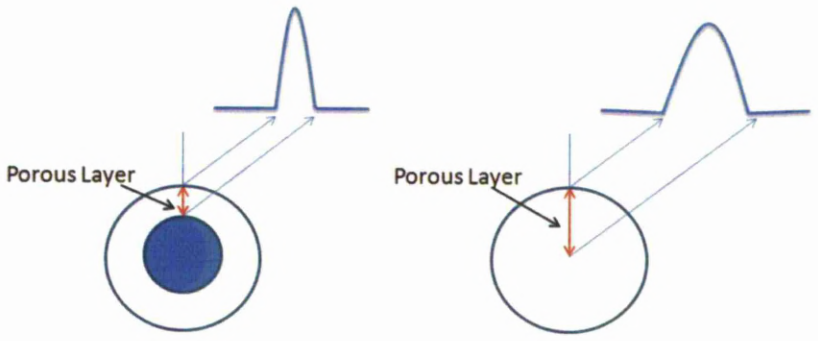

Figure 6.1 Illustration highlighting how restricting the diffusion path length by using superficially porous silica (left) can reduce band broadening compared to totally porous silica

Commercial superficially porous silica (SPS) columns have been available since late 1960's. Soon after, columns containing totally porous silica with particle sizes less than 10 μm were produced displaying greater improvements in efficiency compared to SPSs. This drastically reduced the applications of and therefore the research into 20 μm pellicular and superficially porous silica.

It was not until 1992, when work by Kirkland *et al.* modernised SPSs.[58] Instead of the original 40 μm glass beads with a porous layer between 1-3 μm, Kirkland produced SPSs of *ca.* 5 μm with a 0.25 μm porous layer and 300 Å pores composed entirely of silica (Figure 6.2). The particles were synthesised by using a spray drying method to coat dense silica beads with a porous silica layer.[250] The hard core was produced through sintering 7 μm Zorbax Rx-SIL at 1050°C for four hours, after which, the beads were coated with a polymeric cationic material to ensure the sol adheres to the surface. Optimum ratios of sol/ bead slurry were 0.3-0.4 mg/mL. Kirkland showed a reduced plate height for the SPS column comparable to a porous microsphere column using polymers of 2,000 and 207,000 MW. The thin porous layer allowed rapid mass transfer of larger molecules whilst the reduced particle size creates a more densely packed column, improving efficiency.

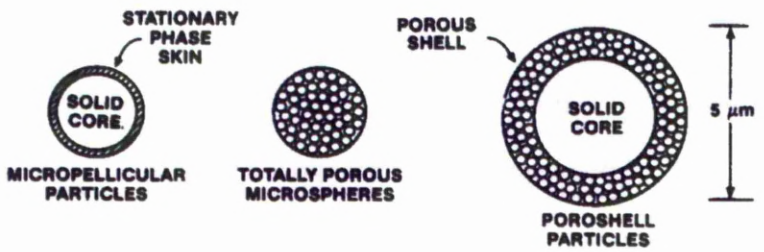

Figure 6.2 Illustration of pellicular particles, totally porous particles and superficially porous particles taken from Kirkland et al.[58]

Modern SPSs have further reduced particle sizes (2.6 – 2.7 μm). The smaller particles also show a reduction in the average pore size of the silica to 90 -120 Å (shown in Table 6.1), which are no longer suitable to facilitate the mass transfer of large biomolecules.

Table 6.1 Commercially available superficially porous silica

Column	Company	Particle Size (µm)	Size of porous shell (µm)	Average Pore Size (Å)
Poroshell 120	Agilent	2.7	0.5	120
Kinetex	Phenomenex	2.6	0.35	100
Halo	AMT	2.7	0.5	90
Ascentis Express	Sigma-Aldrich	2.7	0.5	90

There have been many studies highlighting the increased efficiency of SPSs compared to sub 2 µm porous silica. These reports often analyse molecules such as thiourea, ethylbenzene and naptho[2,3-a]pyrene (Figure 6.3) which are much smaller than the large biomolecules (i.e. molecular weight insulin 5808 Da) these silicas were intended to separate.

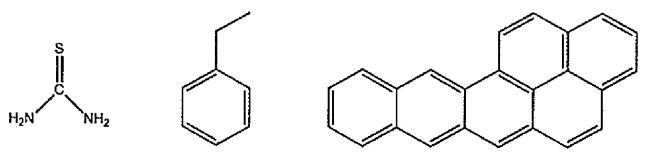

Thiourea Ethylbenzene Naptho[2,3-a]pyrene

Figure 6.3 Examples of molecules used to compare the efficiency of totally porous and superficially porous silica beads

More recent research[251,227] including that of Wang[252] and Gritti[253] have analysed both pellicular and superficially porous silicas focusing on the mass transfer of dipeptides and

proteins, such as insulin (Figure 6.4). Research by Gritti *et al.* presented van Deemter curves for poroshell silica (Agilent) showing a reduction in the A term (eddy diffusion) by 14 %, a reduction in the B term (longitudinal diffusion) by 50 % but a slightly larger C term (mass transfer) (6%) indicating the transfer of compounds through the column is reduced compared to the totally porous silica. The poroshell silica was compared to Zorbax, fully porous silica beads of the same particle size, which were comprised of the same material used to synthesise the porous shell.

Other research indicated that under the same test conditions 2.7 µm Halo silica (AMT analytical) also showed a reduced A term and an increased C term.[12] As SPS silica was synthesised to improve mass transfer of compounds, these results are inconsistent with the principle of core-shell silica (*i.e.* do not increase the mass transfer of the compounds analysed). It has been suggested that the increase in the efficiency of the separation is due to the narrower particle size distribution of the SPS beads which improve the packing of the column (i.e. the A-term) as opposed to increasing the mass transfer of larger compounds (C-term).

Figure 6.4 Hexamer of insulin

Although the C term is increased for superficially porous silica, Gritti *et al.* showed core-shell silica with larger pore volumes provide better mass transfer and increased diffusivity for larger molecules compared to totally porous silica beads.

As recent research has shown, the small pore size and volume of the porous shells hinder the mass transfer of larger compounds. We have synthesised a new stationary phase to improve the mass transfer of larger analytes such as biomolecules and polymers. A stationary phase containing much larger pores (greater than 300 Å) will improve the diffusivity of these molecules, though silica containing large pores often have very low surface areas (*ca.* 10 m^2/g). As there is a smaller area for the molecules to interact with, this can reduce the capacity of the column. By coating the pores and surface of the large pore silica with silica nanoparticles, which have high surface area to volume ratio, we have been able to increase the surface area of the stationary phase significantly without dramatically reducing the pore sizes (as shown in Figure 6.5). Separations of large polymers and biomolecules using size exclusion chromatography require non-polar stationary phases. To create this the SIS silica was functionalised with C_{12} alkyl chains and the remaining silanol groups were end-capped using trimethylchlorosilane.

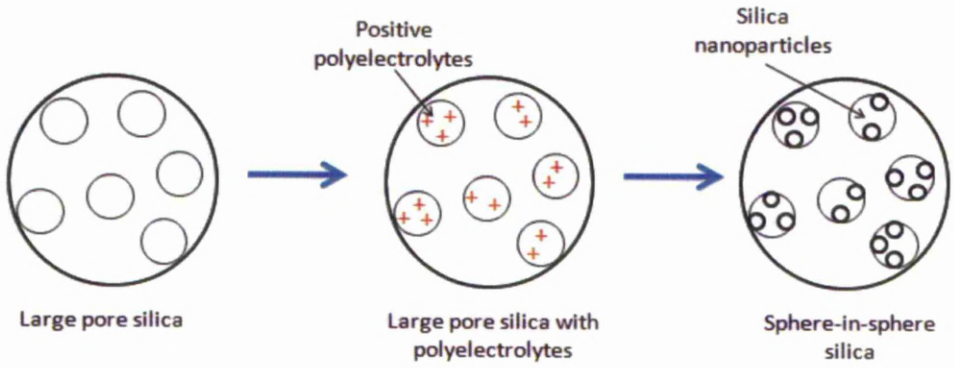

Figure 6.5 Schematic representation of the synthesis of sphere-in-sphere silica beads

In order to incorporate the silica nanoparticles, it has been shown that polyelectrolytes can be used to create a layer-by-layer assembly of silica particles.[254-256] By alternating the adsorption of oppositely charged macromolecules a surface layer of controllable thickness can be achieved (the scheme for this reaction is shown in Figure 6.6). The terminal electrolyte is positively charged to create an electrostatic interaction between the polyelectrolyte layer and the silanol groups of the colloidal silica nanopartilces. Poly(diallydimethylammoniumchloride) which is positively charged ($(CH_3H_5)_2(CH_3)_2N^+$) and poly(styrene sulfonate) which contain negatively charged functional groups ($C_8H_7SO_3^-$), were used to create a monolayer of silica nanoparticles on the surface and within the pores of the large pore silica.

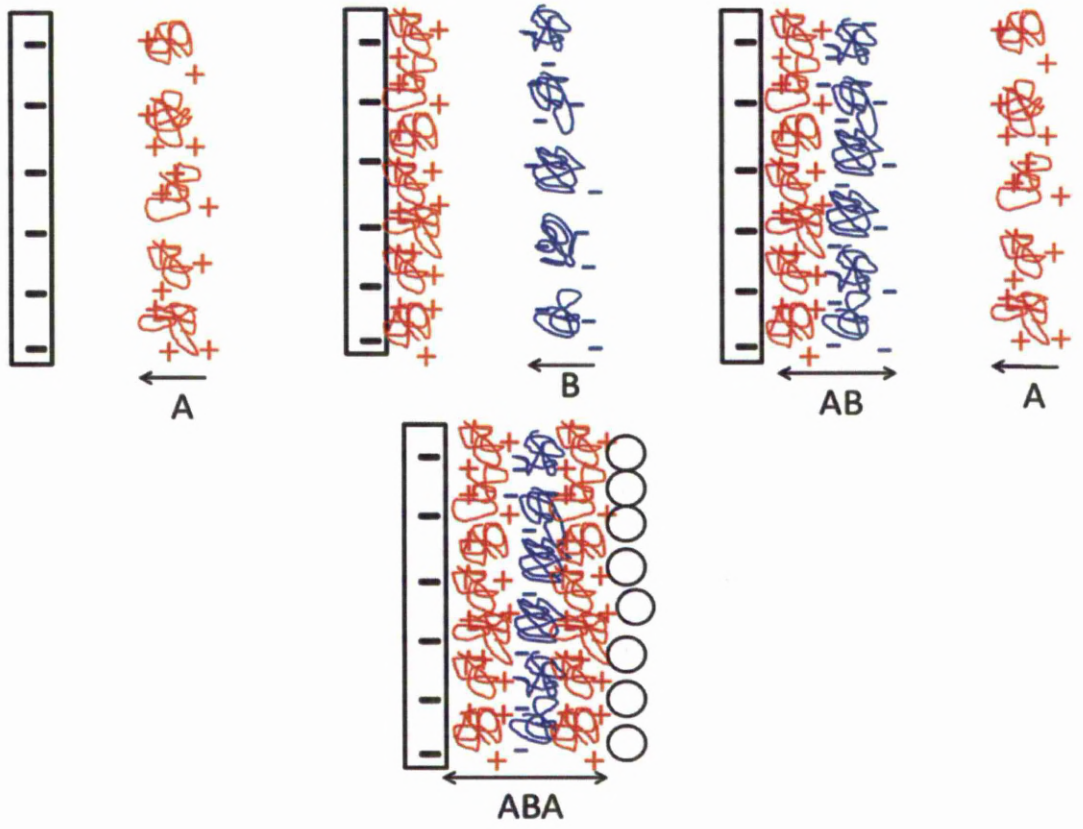

Figure 6.6 Schematic representation of layer-by-layer addition of positively charged (A) and negatively charged (B) polyelectrolytes.

It has also been shown that multiple layers of colloidal silica can be adsorbed onto gold using charged polyelectrolytes. Wherein positively charged polyelectrolytes on the surface of the gold substrate electrostatically interacts with colloidal silica (which is negatively charged at high pH values). The adsorption of the polyelectrolytes occur within a very short time (15 seconds). Using these techniques we have shown polyelectrolytes can be bonded on the surface and within the pores of a macroporous silica bead, and through which, silica nanoparticles can be bonded onto the surface of the macroporous silica.

Immersing the macroporous silica into a solution of poly(diallyldimethyl ammonium chloride) (PDDA) at pH 10 ensures the silica surface is negatively charged and will interact with the positively charged polyelectrolyte. As the polyelectrolytes are not simply bonded onto the flat gold surface but have to be diffused throughout the porous network of the silica, the beads are immersed in the solution for 15 minutes. The product is then immersed in a solution of poly(styrene sulfonate) (PSS) at pH 10, wherein a layer of the polyelectrolyte bonds onto the surface of the product due to the electrostatic interactions between the positive charge of PDDA already on the surface and PSS ($R\text{-}SO_3^-$). A final layer of PDDA is added onto the surface to create a final positive layer which will interact with the negative charges of the silica nanoparticles. The final product is immersed within a solution of the nanoparticles for 30 minutes to ensure the silica nanoparticles are incorporated throughout the porous structure, and not only on the surface of the silica beads.

To silica was then heated to 330^{0}C for 8 hours to ensure the removal of the polyelectrolytes and the silica nanoparticles are sintered to the surface of the macroporous silica.

6.2 Analysis of the Large Pore silica and SIS Silica on a Mesoscopic Level

6.2.1 Changes in Surface Area and Pore Size Distribution.

The addition of the silica nanoparticles can be analysed on a mesoscopic level, as we would expect the surface area of the silica to increase and to observe a decrease in the pore volume when comparing the macroporous silica host and the SIS silica beads.

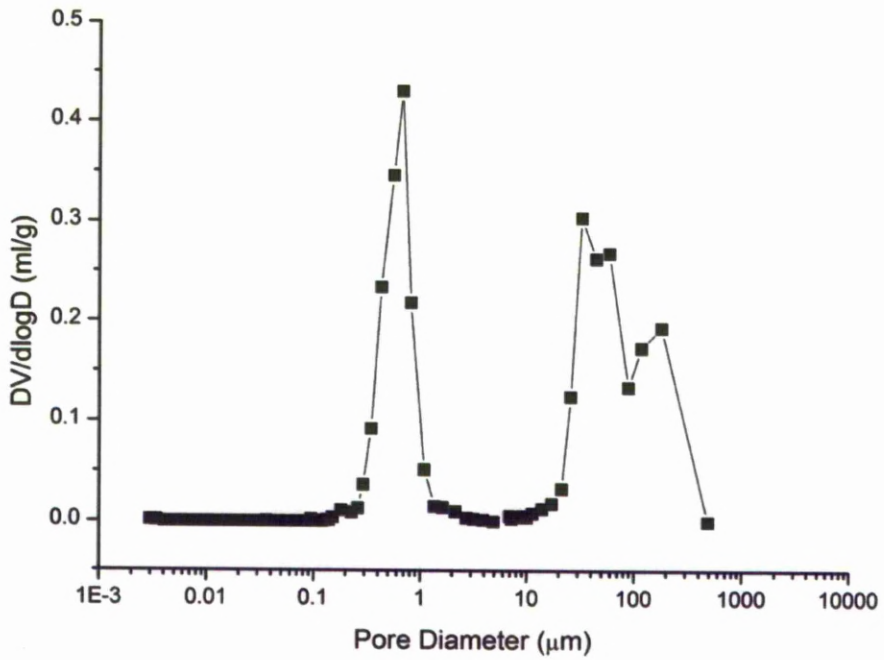

Figure 6.7 Pore size distribution curve derived from Hg porosimetry of macroporous host silica

The Hg analysis of the large pore silica (Figure 6.7) indicates an average pore size of approximately 0.9 μm before creating a surface layer of the silica nanoparticles, which appears to be consistent with the porosity observed using SEM (Figure 6.10). Additional peaks between 50 – 1000 μm are observed though these are due to inter-particulate spacing (Figure 6.7). N_2 adsorption/ desorption isotherms show that the macroporous host

silica has a very low surface area, 38 m^2/g, which is to be expected of material with large pores.

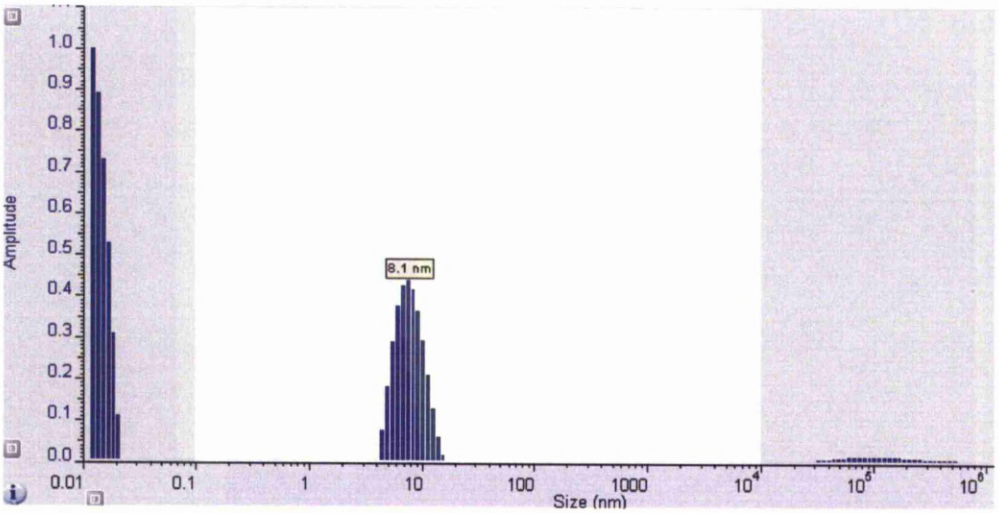

Figure 6.8 Particle size distribution of silica nanoparticles synthesised, determined using DLS

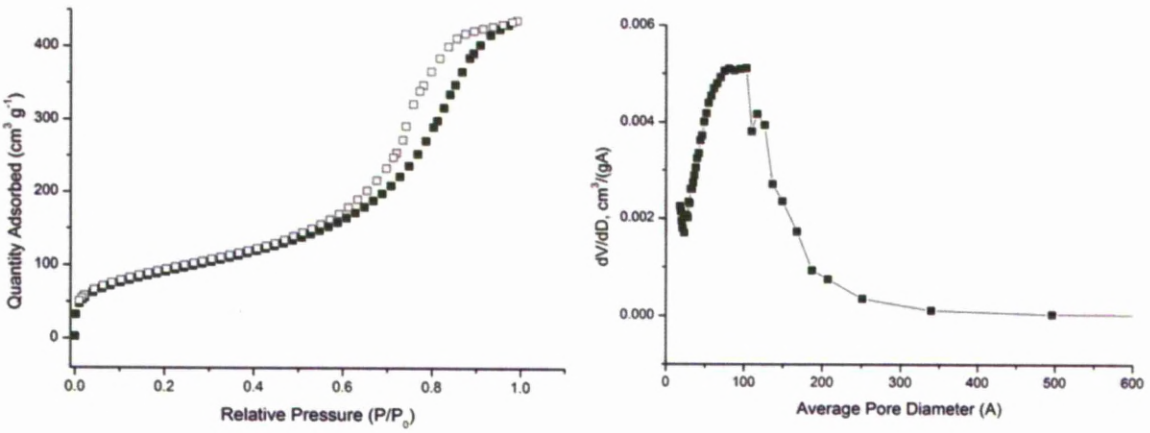

Figure 6.9 N_2 adsorption/desorption isotherm (left) and the pore size distribution (right) for the host silica after the addition of the 16nm silica nanoparticles (calculated from DLS measurements, Figure 6.8), herein referred to as Sphere-in-Sphere (SIS) silica beads (right) wherein the filled symbols represent the adsorption branch and the open symbols the desorption branch

Before the addition of the silica nanoparticles, the particle size and size distribution of the nanoparticles were analysed using Dynamic Light Scattering (DLS), as shown in Figure 6.8. This analysis has shown a very narrow distribution of silica particles with an average diameter of 16.2 nm (Figure 6.8). Also, no aggregation between the nanoparticles is observed.

The N_2 adsorption/ desorption isotherm for the large pore beads after the addition of the nanoparticles is best described as type IV (with elements of type II) which is typical for mesoporous solids (Figure 6.9). This would suggest that the nanoparticles have been incorporated onto both the surface of the silica beads and throughout the porous structure indicated by the reduced pore size (from approximately 0.9 μm (Hg pore size distribution, Figure 6.7) to approximately 100-150 Å (N_2 pore size distribution, Figure 6.9)). The pores of the SIS silica should still be large enough to facilitate the mass transfer of biomolecules. Furthermore, the increased BET surface area of 327 m^2/g implies the presence of the nanoparticles inside the pore system. The increased BET surface area indicating the incorporation of the nanoparticles is also consistent with the change in morphology shown in the SEM images (Figure 6.10). Altering the surface of the silica beads could create aggregation between particles or alter the overall morphology, reducing the packing density and therefore the efficiency of the column. To study any changes to the morphology of the stationary phase, we have used SEM imaging.

6.2.2 Morphology

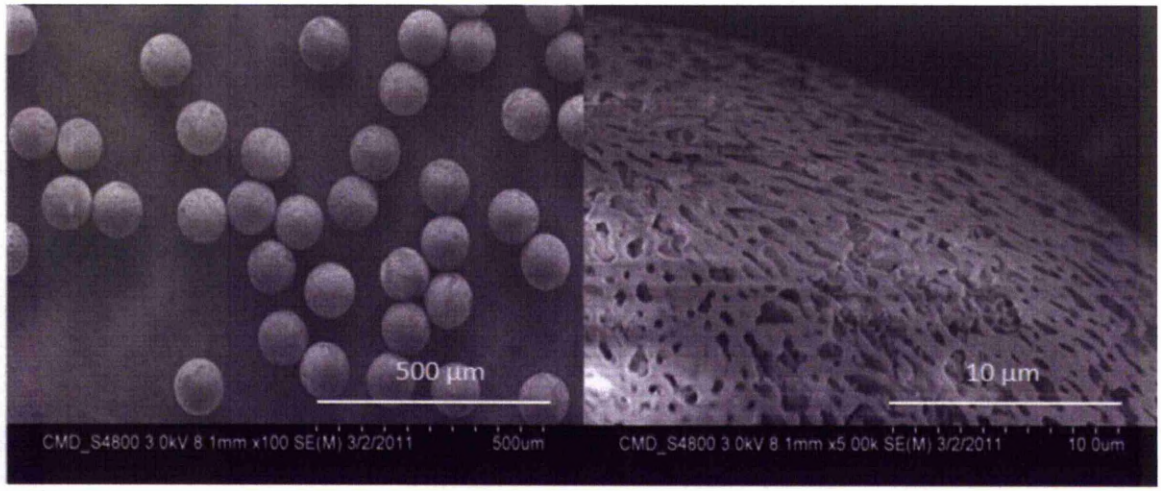

Figure 6.10 SEM images of the large pore silica beads

The SEM images show the spherical monodisperse nature of the parent material. The larger pores (approximately 0.9 µm) within the silica can also be observed. As the SEM used to analyse the material was not able to image individual nanoparticles, due to the size, the overall morphology of the bead has been monitored. This provides an indication as to whether the nanoparticles have been incorporated onto the surface of the large pore silica bead.

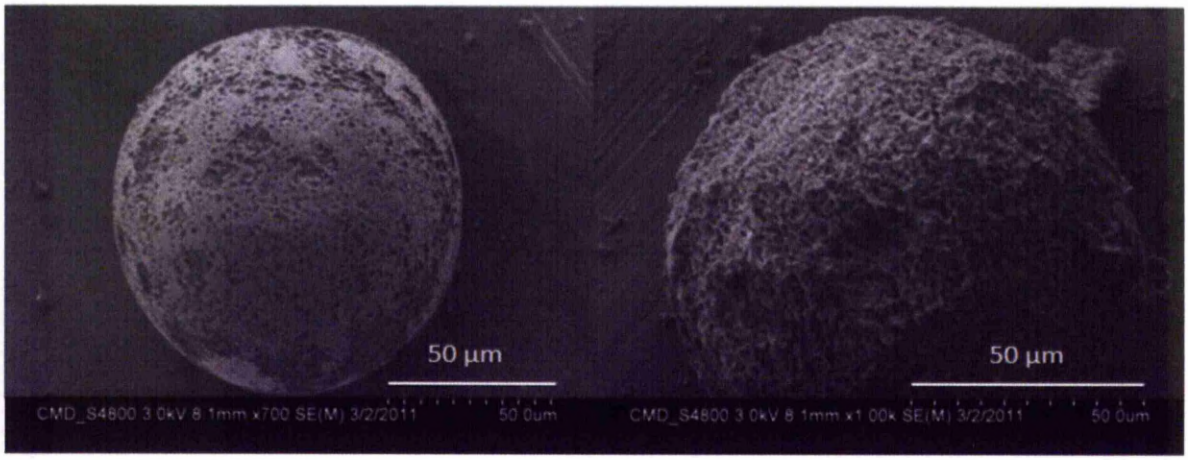

Figure 6.11 SEM image of the large pore silica before (left) and after (right) the incorporation of 16 nm silica particles

The surface roughness and the notable change in the surface morphology of the silica beads observed from the SEM images indicate the silica nanoparticles are present on the surface of the beads. This coincides with the increased BET surface area and narrower pore size distribution indicating the silica nanoparticles have been incorporated throughout the porous network. The images also show that the SIS beads have retained their spherical morphology after the reaction and no apparent aggregation was observed.

6.3 Characterisation of the Large Pore Silica and SIS beads on a Molecular Level

Solid-State NMR can be used to monitor the synthesis of SIS beads through the addition of polyelectolytes which adhere nanoparticles onto the silica surface. We have also studied the effect of the addition of C_{12} functionality on the surface on the resulting silica beads.

6.3.1 Analysis of the Synthesis of Sphere-in Sphere Beads Using ^{1}H NMR Spectroscopy

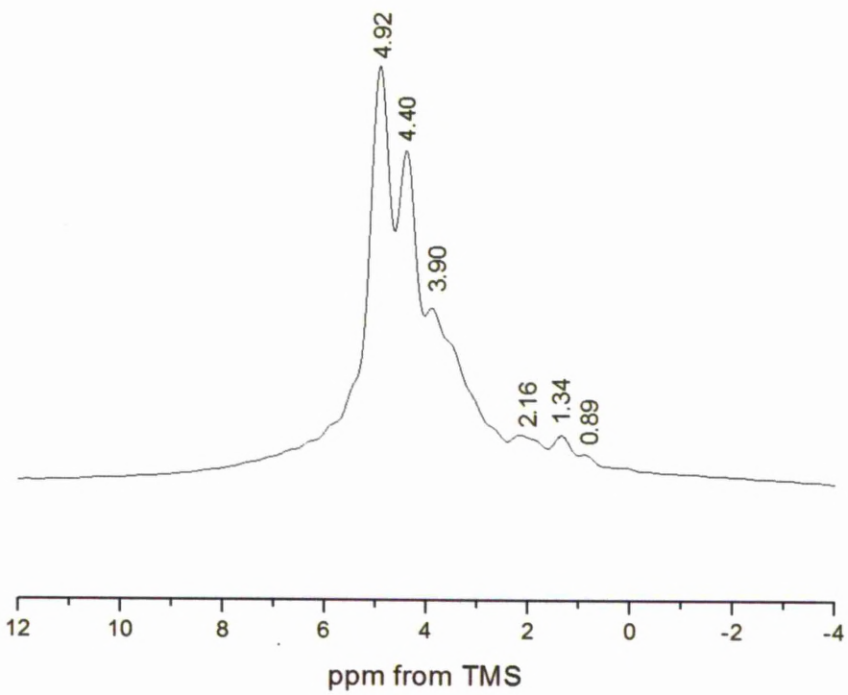

Figure 6.12 ^{1}H MAS NMR spectrum of the large pore silica measured at an MAS rate of 10 kHz

The ^{1}H NMR spectrum of the large pore silica (Figure 6.12) shows the presence of the isolated and hydrogen bonded silanol groups. The broad resonance at 3.90 ppm corresponds to physisorbed water. Si-OH groups which are hydrogen bonded to Si-O-Si bridging groups and to surface water molecules resonate at 4.4 and 4.9 ppm respectively. The spectrum also shows the presence of three smaller resonances between 0.9 – 2.0 ppm. Most likely, the resonances correspond to isolated (2.16 ppm), geminal (1.3 ppm) and associated (0.89 ppm) silanol groups which are not hydrogen bonded to water or Si-O-Si groups. It is likely that these silanols are not at the silica surface but are hidden within the pore walls and, therefore, unable to interact with the water molecules.[154,257-262]

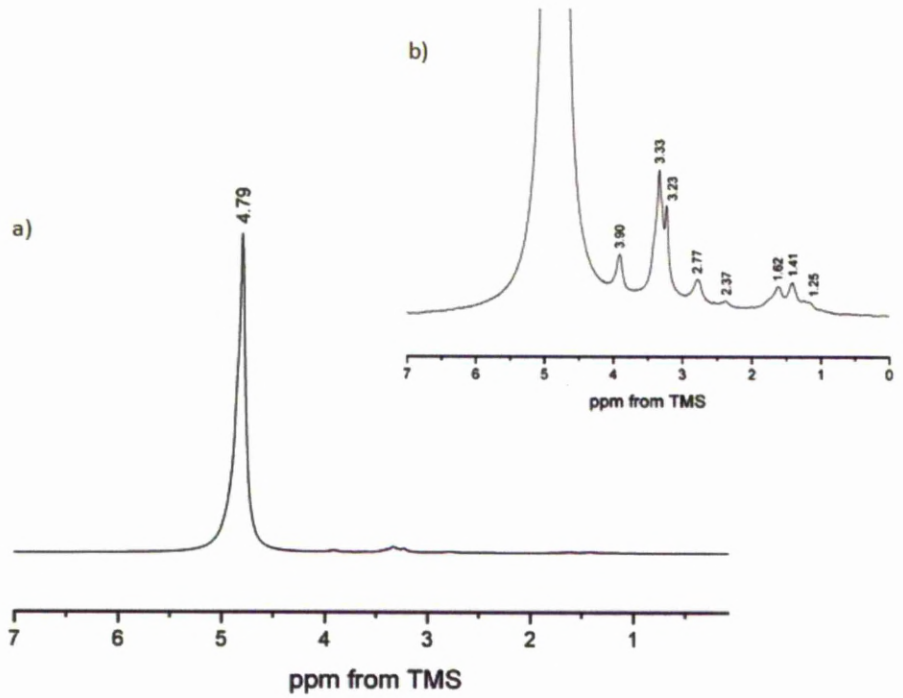

Figure 6.13 a) ^{1}H MAS NMR spectrum of host silica containing silica nanoparticles and adsorbed polyelectrolytes (pH10) acquired at an MAS rate of 10 kHz b) magnified base line of the ^{1}H MAS NMR spectrum of the host silica.

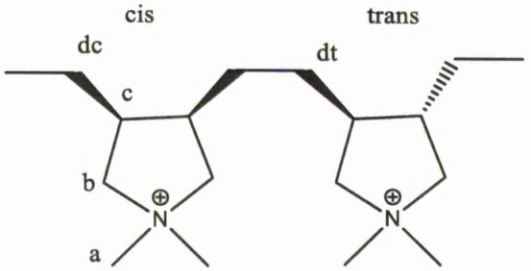

Scheme 6.1 poly(diallyldimethyl ammonium chloride)

The addition of the polyelectrolytes has been analysed using ^{1}H MAS NMR spectroscopy. The spectrum now only appears to show one main resonance corresponding to water physisorbed to the silica surface at 4.79 ppm. The presence of the poly(diallydimethyl ammonium chloride) is observed. The spectrum shows resonances at 1.41 and 1.62 ppm, corresponding to the protons at position (d) for the *cis* and *trans* conformations respectively. The protons of the ring at positions (b) and (c) resonate at 3.9 and 2.77 ppm. The methyl groups (a) are observed at 3.23, 3.33 for the *cis* and *trans* conformations respectively. We would expect the presence of resonances around 7.0 ppm which are characteristic of poly(styrene sulfonate). The absence of these resonances suggest the polyelectrolyte is not adsorbed on the silica surface.[263-265]

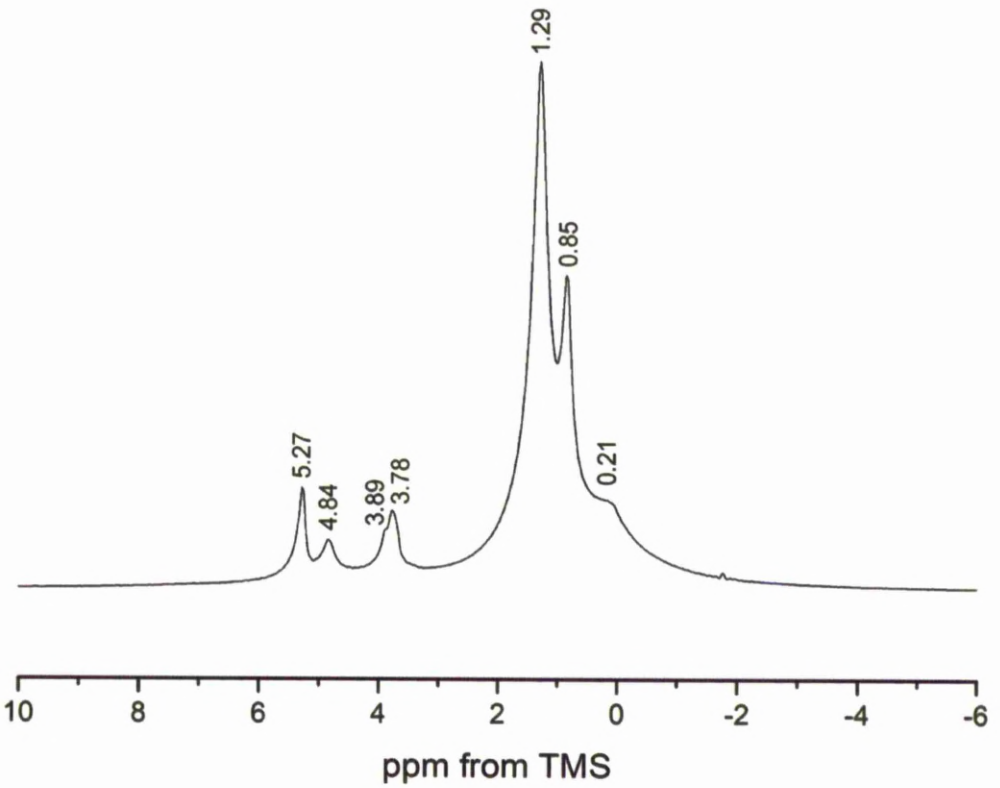

Figure 6.13 ^{1}H MAS NMR spectrum of the Sphere-in-Sphere silica beads containing surface silica nanoparticles functionalised with C_{12} chains. The spectrum was measured using an MAS rate of 10 kHz

The separation of biomolecules and polymers is achieved through size exclusion chromatography. A non-polar surface is required to impede the binding of biomolecules onto the surface of the stationary phase. To create this non-polar stationary phase the SIS silica was functionalised with C_{12} alkyl chains and the remaining silanol groups end capped using trimethylchlorosilane. The protons of the alkyl chain bonded to C1-11 and C12 resonate at 1.29 and 0.85 ppm respectively. The resonance at 0.21 ppm is attributed to the O-Si-($C\underline{H}_3$)$_2$-$C_{12}H_{25}$ and O-Si-$(CH_3)_3$ groups. The spectrum also shows the peaks at 3.78 and 3.89 ppm which are due to a small amount of polyelectrolyte remaining after calcining the silica at 330^{o}C. A small amount of physisorbed water can also observed (4.84 ppm).

6.3.2 Characterisation of the Poly(diallyldimethyl ammonium chloride) on the Silica Surface

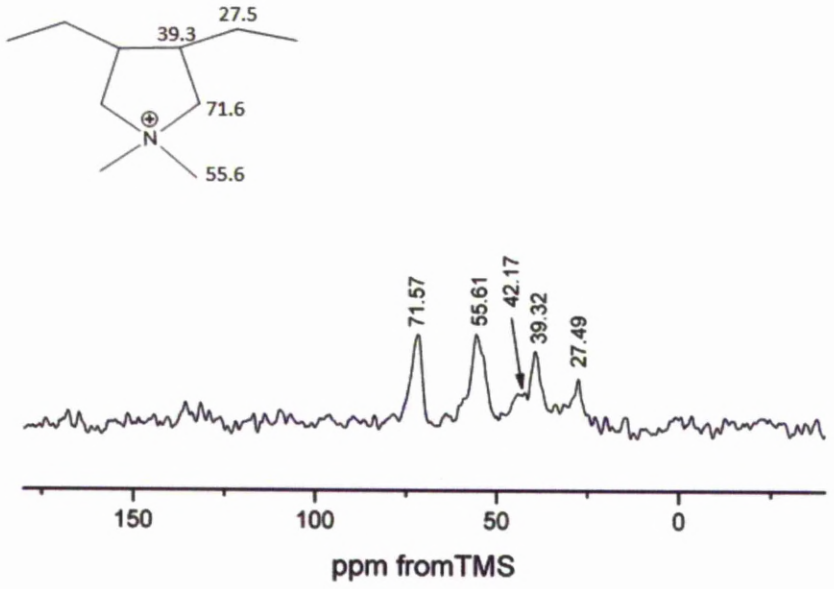

Figure 6.14 ^{1}H-^{13}C CP/MAS NMR spectrum of the large pore silica containing silica nanoparticles and polyelectrolytes (pH =10). An MAS rate of 8 kHz was used.

The ^{1}H-^{13}C CP/MAS NMR spectrum shows the presence of resonances corresponding to the PPDA polyelectrolyte. No resonances are observed which would indicate the presence of poly(styrene sulfonate). Again, this indicates that only one layer of polyelectrolyte was adsorbed onto the surface of the silica. It is likely the low intensity of the resonances observed are due to the high mobility of the polyelectrolytes. No resonances are observed *c.a.* 120 ppm, which are characteristic of poly(styrene sulfonate). The absence of poly(styrene sulfonate) was also confirmed through ^{13}C {^{1}H} MAS NMR experiments.

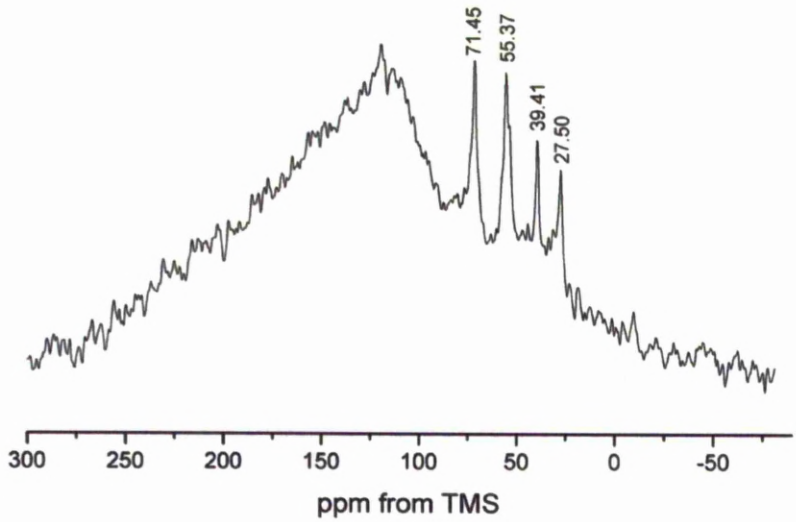

Figure 6.15 $^{13}C\{^{1}H\}$ MAS NMR spectrum of Sphere-in-Sphere silica before the calcinations of the polyelectrolytes (pH10) acquired at an MAS rate of 10 kHz

Research by Dorris *et al*[266] has shown that at high pH values the positively charged polyelectrolyte can be deprotonated, thus removing the positive charge. In this case, it is likely that a proton is removed from one of the methyl groups creating a negative charge ($R\text{-}(CH_3)N^+CH_2^-$) which balances the positive charge of the nitrogen atom, thus producing a neutral polyelectrolyte. The PDDA compounds can still bond to the surface of the silica, though only through very weak hydrogen bonding interactions. This may explain why the negatively charged PSS compounds are not observed on the surface of the macroporous silica. The 16 nm silica nanoparticles are suspended in a methanol solution (pKa of approximately 15.2), wherein the methanol solution is regarded as slightly acidic.

The addition of the silica nanoparticle solution (which is acidic) to the parent silica could restore the positive charge of the PDDA polyelectrolyte. This will facilitate stronger bonding through electrostatic interaction between the silanol groups of the nanoparticles and the positively charged polyelectrolyte, allowing the silica nanoparticles to adhere to the surface of the parent silica.

We have shown that 16 nm silica particles can be held on the surface of the large pore silica with only one layer of PDDA. This significantly reduces the synthesis time required to make the stationary phase.

6.3.3 Conformation of the C_{12} Chain

The *trans/ gauche* ratio of the ≡Si-$C_{12}H_{25}$ alkyl chain can be analysed quantitatively through $^{13}C\{^1H\}$ MAS NMR experiments. It is important to determine the conformation of the C_{12} chains as this will affect the efficiency of the phase. The straighter *trans* conformation will have an increased level of interaction with the analytes compared to the *gauche* conformation and therefore create a more efficient separation.

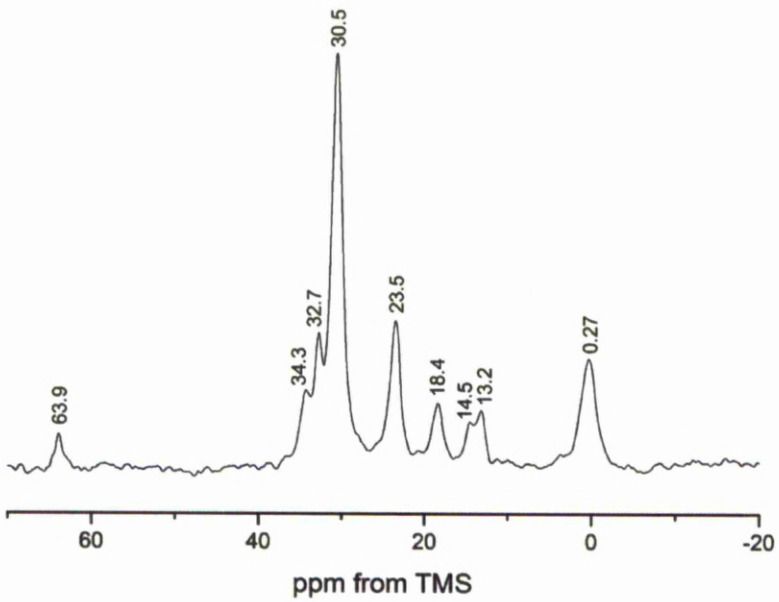

Figure 6.16 $^{13}C\{^1H\}$ MAS NMR spectrum C_{12} functionalised SIS silica measured using an MAS rate of 10 kHz.

Resonances at 30.5 and 34.3 ppm correspond to C4-C9 sites in the *gauche* and *trans* positions respectively. Carbons 2 and 11 are observed at 18.4 and 23.5 ppm. Carbons 3 and 10 resonate at 32.7 ppm. The peaks at 14.5 and 13.2 ppm corresponds to carbon 12 and the terminal methyl group (C1) respectively. The Si-$(CH_3)_3$ end-capping groups are

observed at 0.27 ppm. The spectrum shows the disordered *gauche* conformation is dominant for the alkyl chain. This indicates the C_{12} alkyl chains grafted to the SIS silica have a high level of mobility.

6.3.4 Analysis of the Degree of Condensation of the Silica Framework

The level of cross-linking within the silica framework can affect the mechanical strength of the stationary phase. Also, any remaining surface silanol groups can reduce the efficiency of a reversed-phase column. During the synthesis additional silica is incorporated into the beads in the form of the silica nanoparticles. Consequently, the overall level of framework condensation will change throughout the reaction.

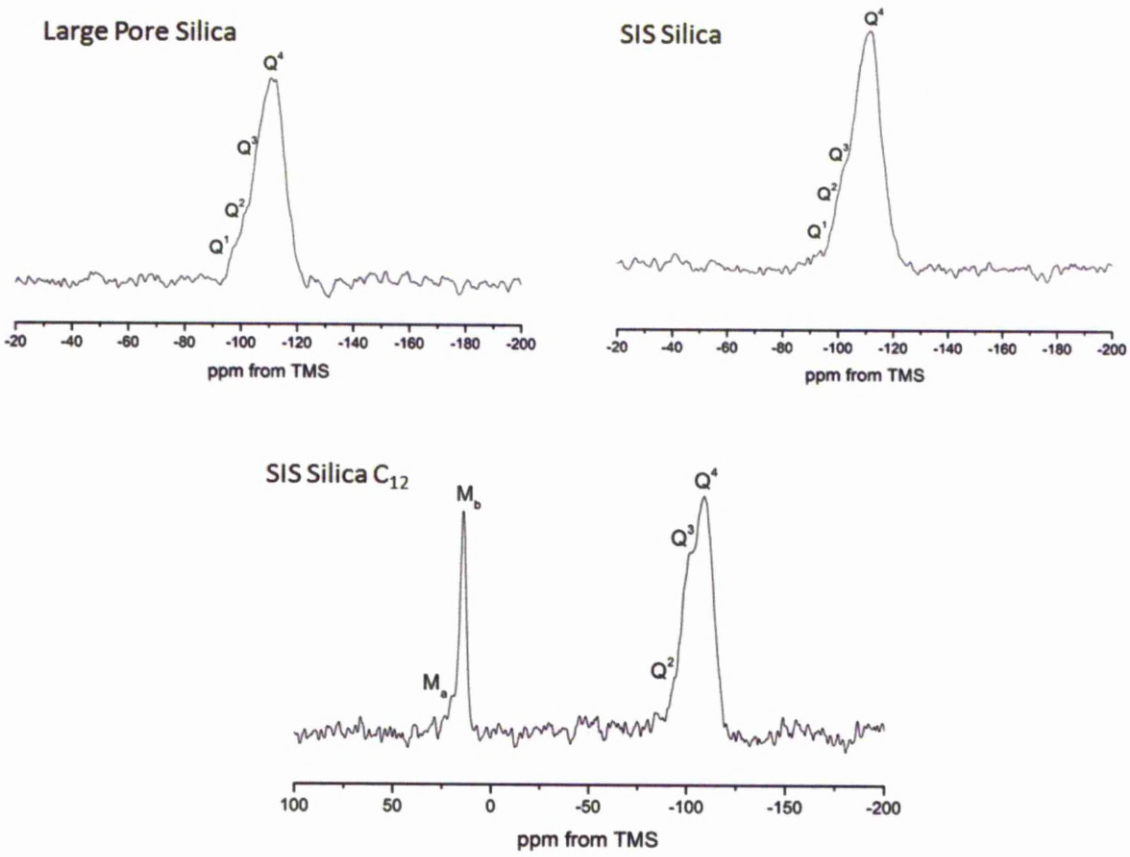

Figure 6.17 ^{29}Si MAS NMR spectra of SIS silica beads throughout the synthesis at an MAS rate of 4 kHz

The ^{29}Si MAS NMR spectra show resonances at *ca.* -97, -101, 108 and -111 ppm indicating the presence of Q^1 ($SiO(OH)_3$), Q^2 ($SiO_2(OH)_2$), Q^3 ($SiO_3(OH)$) and Q^4 (SiO_4) sites. The spectrum indicates the silica is predominantly composed of Q^4 sites inferring the silica is well condensed. The ^{29}Si MAS NMR spectrum of the C_{12} functionalised SIS silica contains two resonances at 14.2 and 19.4 ppm which confirm the incorporation of the C_{12} chain and the Si-$(CH_3)_3$ end-capping groups respectively.

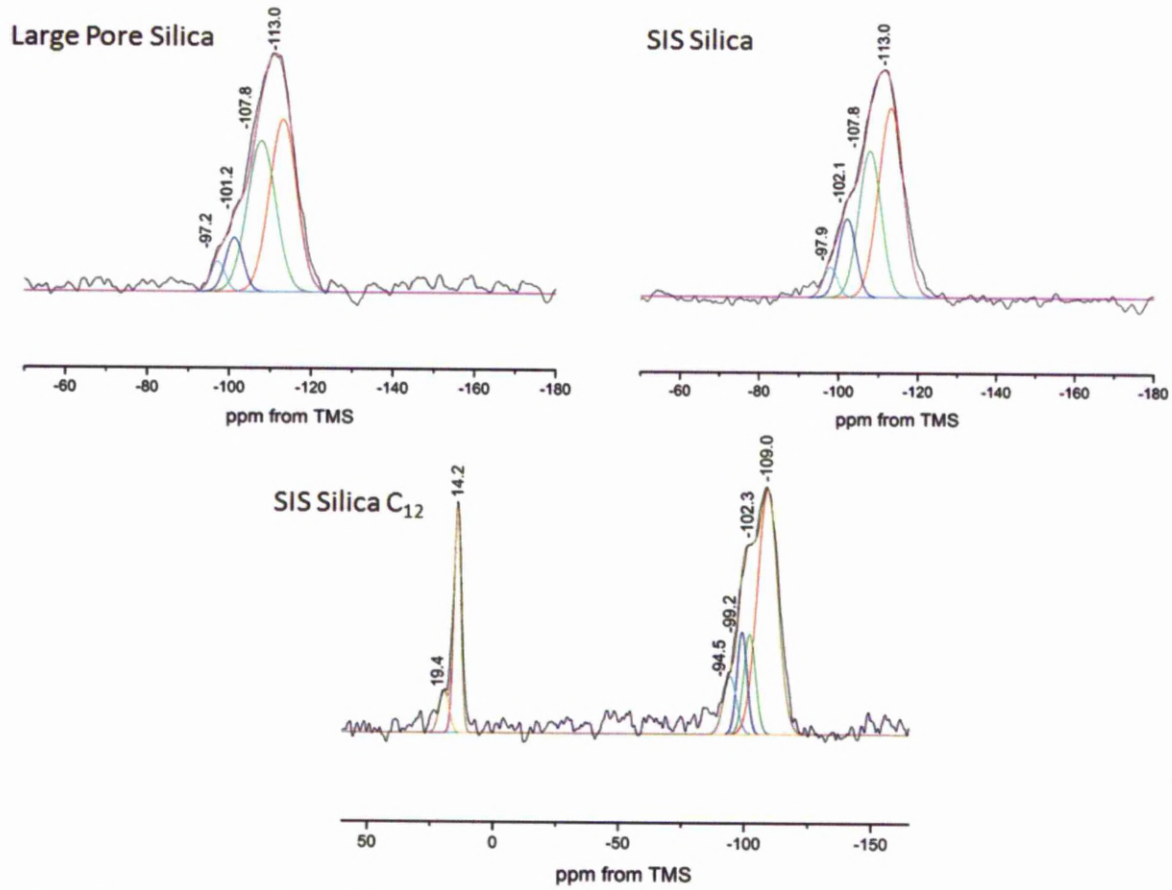

Figure 6.18 Deconvoluted ^{29}Si MAS NMR spectrum of large pore silica, SIS silica and C_{12} functionalised SIS silica.

Table 6.2 peak area of the deconvoluted spectra corresponding to the large pore silica

	Peak area (a.u.)						$(Q^1+Q^2+Q^3)$ / Q^4	M/Q
Sample	Q^1	Q^2	Q^3	Q^4	M_a	M_b		
Large pore silica	0.52	1.12	5.10	5.58			1.208	
SIS Silica	0.54	1.73	4.15	5.97			1.075	
SIS Silica C_{12}	1.409	1.87	2.18	9.10	0.76	2.92	0.609	0.25/ 1.0

The large pore silica is composed predominantly of Q^3 and Q^4 sites indicating a relatively high level of framework interconnectivity. An increase in the overall level of condensation occurs with the incorporation of the silica nanoparticles (large pore silica has a condensation level of 1.208 whereas SIS silica has an overall condensation level of 1.075) this suggests that the nanoparticles contain a significant amount of Q^4 sites. It is evident that the 16 nm silica beads incorporated must be highly condensed to increase the overall condensation level. A further increase is observed with the grafting of the organic moieties (from 1.075 to 0.609), this is to be expected as the organosilanes react with the surface silanol groups.

Analysis on a mesoscopic and molecular level has shown that we have successfully adhered silica nanoparticles onto the surface and throughout the porous structure of a large pore silica bead. Solid-state NMR has also shown that the surface of the SIS silica beads has been functionalised with C_{12} alkyl chains and grafted trimethylsilane moieties in order to cap any remaining silanol groups to create silica with reversed-phase characteristics. This stationary phase was then tested chromatographically on a variety of compounds to

determine whether this material is an effective stationary phase for high molecular weight compounds.

6.4 Chromatography

Traditionally large polymers and biomolecules are separated through size exclusion chromatography (SEC).[267-270] Unlike classical chromatography which relies on differences in the interactions of analytes with the mobile and stationary phase, adsorption has little effect within this separation method.[271] SEC, which can also be referred to as gel-filtration and restricted diffusion chromatography, separates analytes based on their molecular weight. Larger molecules remain in the mobile phase and elute first whereas smaller molecules can penetrate the porous network of the stationary phase and have longer elution times. It is therefore evident that the efficiency of the column is strongly dependent on mass transfer within the pores. The first published separation of macromolecules in order of their molecular weight was by Porath 1959.[272] In the last four decades a lot of research has focused on increasing the mass transfer and improving the separation of macromolecules.[273,274]

The surface silanol groups of the present sphere-in-sphere silica beads where reacted with C_{12} functional groups to create a non-polar stationary phase surface and thereby reduce any interaction between the stationary phase and the analytes. The selectivity of the C_{12} functionalised SIS silica has been tested on a range of molecules with varying molecular weight to determine the selectivity parameters of the stationary phase.

6.4.1 Tanaka Test

As mentioned in Chapter 4, the Tanaka test is a standardised method to analyse the physio-chemical properties of a column, such as the retention, hydrophobicity, steric selectivity, silanol capacity and ion exchange capabilities. These parameters are determined through measuring the retention time and selectivity of analytes such as butylbenzene, o-terphenyl, pentylbenzene, triphenylene, phenol, caffeine and benzylamine. The Tanaka test measures the effect of the column using compounds with molecular weights in the range of 100-230. These are classed as small molecules. The separation of these compounds was also examined using Hypersil Gold C_{18} as a comparison.

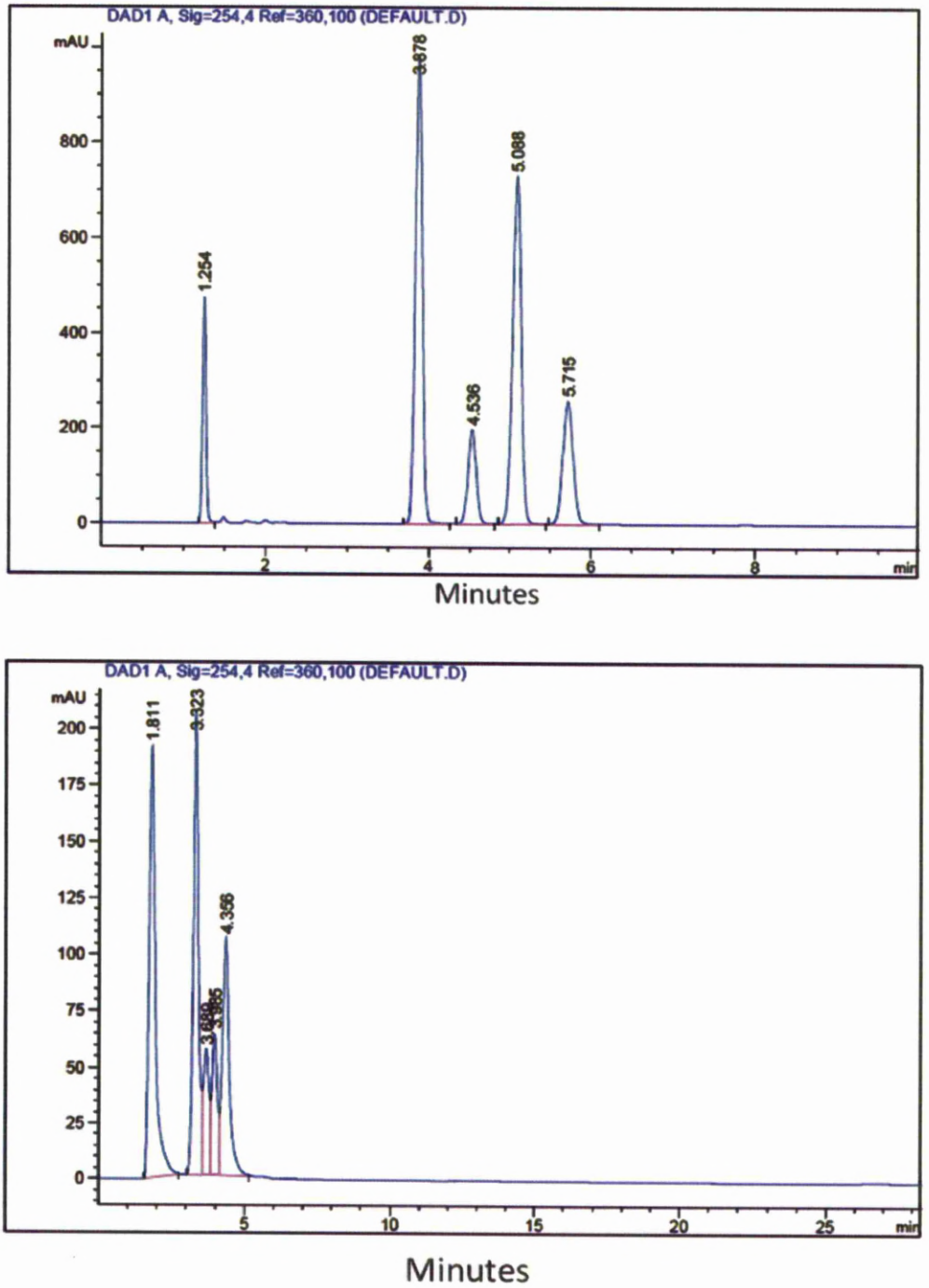

Figure 6.19 Chromatograms of the Tanaka test using Hypersil Gold C_{18} column (4.6 mm x 100 mm) and Hypersil Gold C_{18} microbore column (1.0 mm x 100mm)

The chromatograms show that both columns separate the Tanaka compounds, though the selectivity (K') of the separation is reduced for the microbore column due to its smaller dimensions. As the SIS silica is also packed into a microbore column the separation of the analytes should be similar to the C_{18} microbore separation.

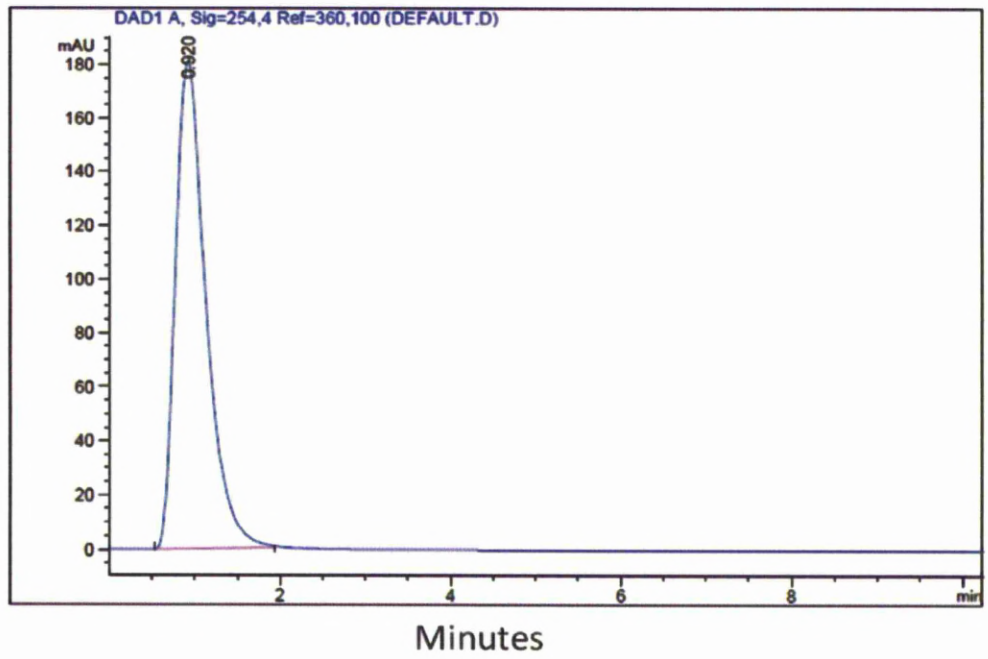

Figure 6.20 Chromatogram showing the retention of the Tanaka test molecules using the C_{12} functionalised SIS silica

The chromatogram shows no separation for these analytes. Separation of analytes through SEC is based on the penetration of some, but not all, analytes into the pores of the stationary phase. If the pores are so large that all analytes permeate the pores of the stationary phase, no separation will occur. On this basis, it is likely that the test compounds are so small in relation the pore size of the SIS material that no separation has occurred, and so all analytes to elute simultaneously.

6.4.2 PAH Test

The PAH test (also mentioned in Chapter 4) is used to determine the selectivity of reversed-phase columns through the separation of polyaromatic hydrocarbons (PAH). As these compounds have a slightly higher range of molecular weights (MW 120 -280) compared to those used in the Tanaka test, they can be used to determine the suitability of the SIS silica stationary phases for separating analytes of this size range. However, when the compounds were loaded onto the column the chromatogram showed the same effect, all analytes elute simultaneously indicating these compounds are also too small in relation to the pore size of the stationary phase to be separated.

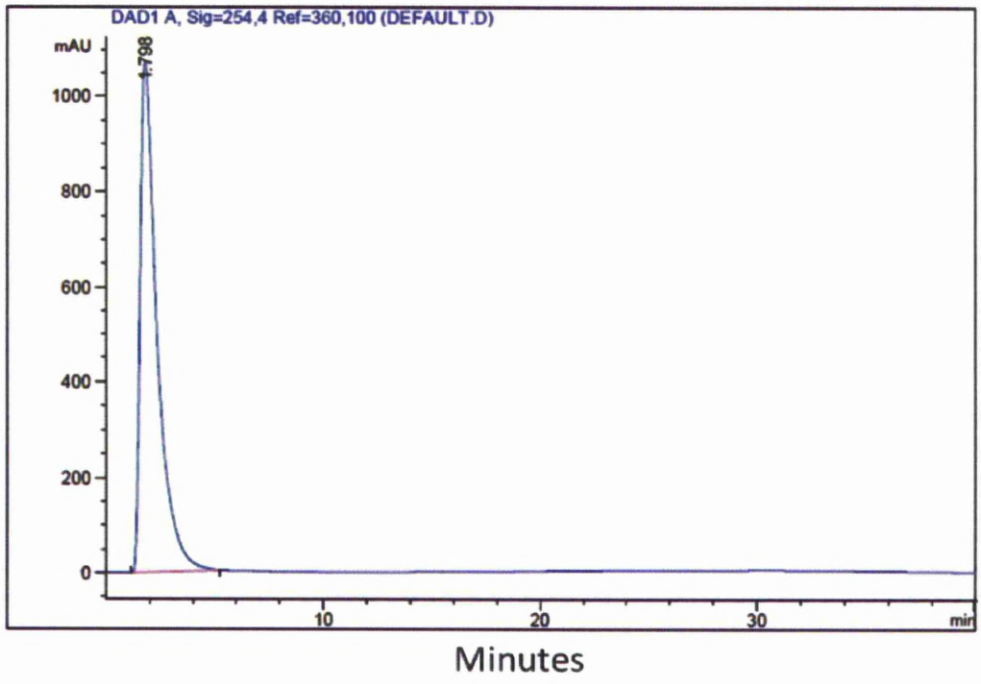

Figure 6.21 Separation of PAH test molecules using the C_{12} functionalised SIS silica stationary phase using the microbore column (1 mm x 100 mm).

6.4.3 Protein Separation

As SIS material was designed specifically to improve the mass transfer of large polymers and biomolecules it is unsurprising the pores within the SIS beads are too large to separate low molecular weight compounds. Lysozyme (MW ca. 14,700) wherein the structural conformation contains five to seven α helixes and an antiparallel β sheet and Bovine serum albumin (BSA) (MW approximately 66,776) in which the structure consists of α-helix and extended chains[275], were used to the test the selectivity of the SIS column for low and high molecular weight macromolecules separations.

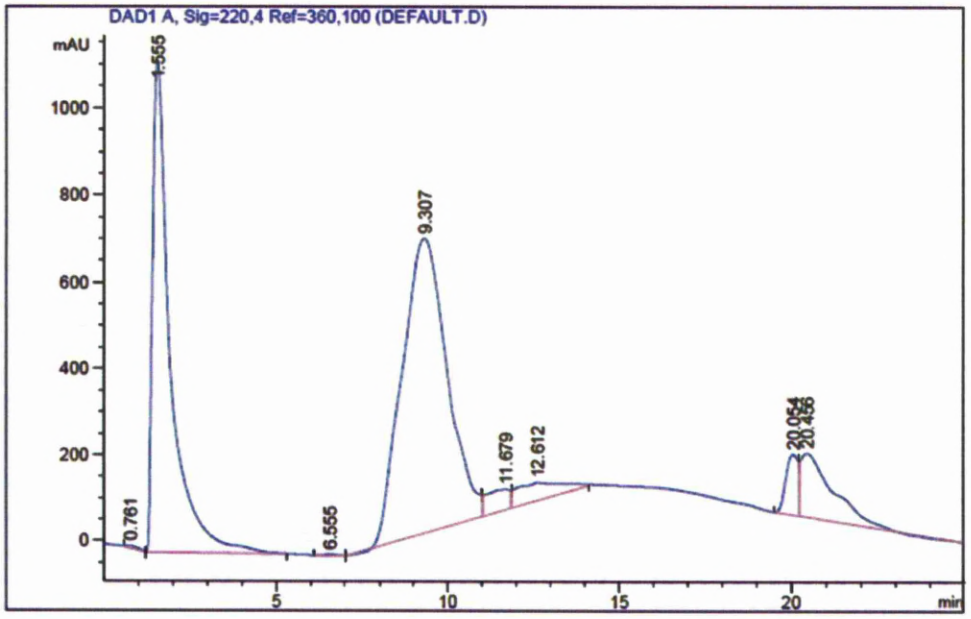

Minutes

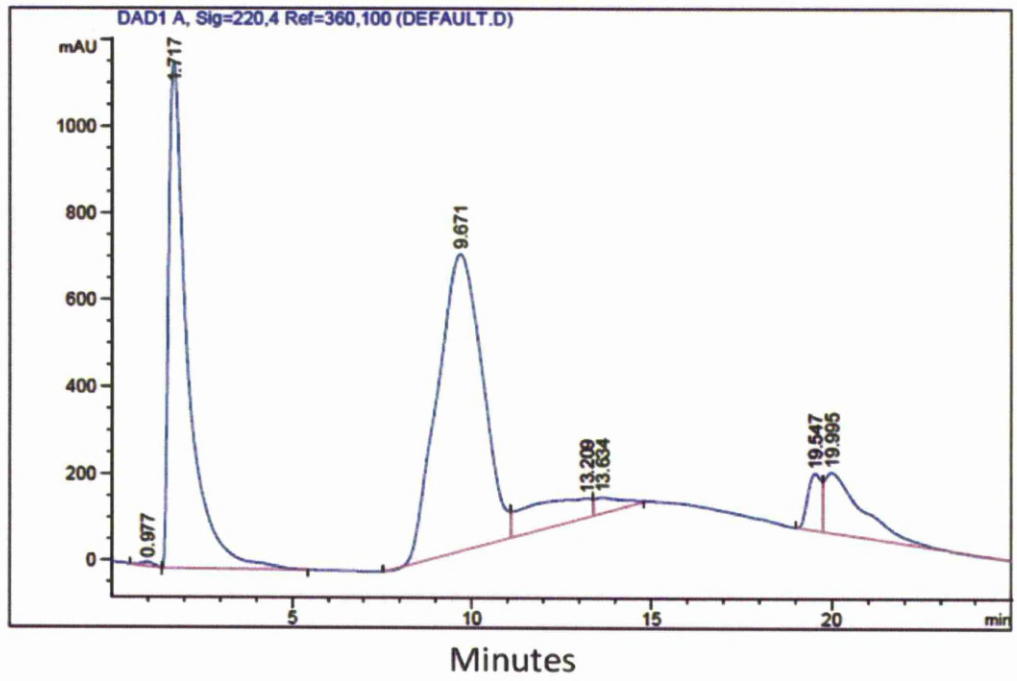

Figure 6.22 Chromatograms illustrating the separation of Lysozyme and BSA using C_{12} functionalised SIS silica.

The chromatograms show the SIS silica has successfully separated the two biomolecules. Three main peaks are observed *ca.* 1.60, 9.5 and 19.0 minutes corresponding to Lysosyme (1.60 minutes) and BSA (9.5 and 19.0 minutes). The analytes were also analysed individually in order to assign the correct elution times. It is likely that the two peaks corresponding to BSA are produced by the protein in the folded and unfolded state. Also, we have shown that the separation is reproducible as the two chromatograms are almost identical. However, Lysozyme (low molecular weight) is the first compound to elute. This is unexpected as the smaller compounds are normally retained longer compared to larger compounds when using SEC chromatography. This indicates that an additional interaction is occurring during this separation. As the silica contains C_{12} alkyl groups it is logical that some reversed-phase type hydrophobic interactions maybe present between the C_{12} chains and proteins. The elution order of the analytes indicate that the SIS material is behaving as a large pore reversed-phase silica as opposed a SEC column as intended.

6.5 Conclusion and Discussion

Large polymers and biomolecules have a slower mass transfer rate through HPLC columns compared to smaller molecules. To improve the separation of these compounds commercially available columns use superficially porous silica beads. By restricting the path length of the analytes it is thought that the hindered movement of the compounds or reduced volume of stagnating analyte within the pores will consequently reduce the band broadening. More recently is has been shown that the use of these stationary phases actually increases the C-term value. It is likely the more uniform particle size of the superficially porous silica beads produces the more efficient separation observed though the smaller pore sizes (90 – 120 Å) of these materials restrict the mass transfer of the analytes as opposed to the shorter diffusion path length having an increasing effect. The synthesis of larger pore silica was used to increase the diffusion rate of the analytes. Though, as the pore size of the silica beads are increased the surface area is decreased, which can affect the efficiency of the stationary phase. To increase the surface area 16 nm silica particles were bonded within the porous framework of the material, creating sphere-in-sphere (SIS) silica beads.

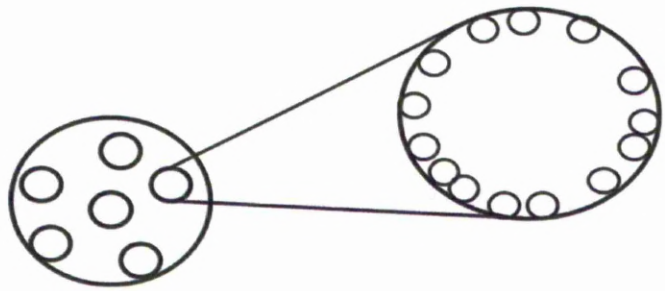

Figure 6.23 Sphere-in-Sphere silica beads

By analysing the different stages of the synthesis of the SIS beads on a molecular level we have shown that the addition of the silica nanoparticles is feasible using only one layer of the poly(diallyldimethyl ammonium chloride). Due to the large pores of the material the

separation of small (MW = 100-280) analytes is not possible. We have shown the stationary phase is able to successfully separate a mixture of small (MW = 14,700) and large (MW = 66, 776) biomolecules. This indicates that not only is the SIS silica a viable stationary phase but also the separation of compounds with a large distribution of molecular weights is possible. Potentially, the prepared SIS silica has many applications for a wide variety of analytes. Furthermore, the column also distinguishes between the large BSA protein in its folded and unfolded state.

Traditionally, for size exclusion chromatography the larger molecules remain in the mobile phase and elute first, whereas the smaller analytes are able to penetrate the porous stationary phase and have longer elution times. The reverse order is shown for the SIS silica, wherein the smaller molecules elute first. This indicates additional interactions are occurring within the column. As the stationary phase was functionalised with C_{12} groups the solvophobic interactions which occur within reversed-phase chromatography may also be present. This would lead to the larger analytes being retained more strongly, producing the chromatogram observed. If some reversed-phase characteristics were present it could be possible to further improve the selectivity of the column by grafting longer alkyl chains (C_{18}, C_{30}) onto the silica surface. Additionally, the elution order of the biomolecules could be controlled depending on the organic group grafted onto the surface of the silica framework.

Further research is needed to fully understand the potential of this new stationary phase. We have shown the incorporation of 16 nm silica beads can increase the surface area of macroporous silica whilst still facilitating the diffusion of large analytes. Research into obtaining the optimum particle size for the silica nanoparticles could increase the efficiency of the column. Further reducing the particle size could increase the resultant surface area of the SIS particles, though as the particle size is decreased it becomes more difficult to control the polydispersity and aggregation of the nanoparticles. Additionally, we have only shown here the result of the addition of one layer of silica nanoparticles, whereas multiple layers can be incorporated using the layer-by-layer technique.

The chromatograms showing the separation of Lysosyme and BSA using the C_{12} functionalised SIS silica indicate the presence of hydrophobic interactions between the stationary phase and the analytes. This indicates the SIS silica retains analytes in the same way as a large pore reversed-phase silica. On this basis, it would be beneficial to investigate the elution order of Lysosyme and BSA on a non-funtionalised SIS silica column. Removing the C_{12} functionality should reverse the elution order of the analytes, creating a true SEC separation.

7.0 General conclusions and Outlook

The synthesis of new reversed-phase and size exclusion columns has been presented in this work. Analysis of the new columns was undertaken on a mesoscopic level using x-ray diffraction, N_2 adsorption/ desorption isotherms, microanalysis and SEM imaging. The organosilicas were also characterised on a molecular level using various solid-state NMR techniques. Finally, the new HPLC columns were characterised and compared chromatographically to commercially available columns using PAH and Tanaka tests.

The synthesis of bi-functionalised PMOs (Chapter 4) has been used to create a new stationary phase containing high carbon loading levels (*ca.* 22%). This was achieved by incorporating organic moieties into the silica framework which produces a stationary phase with a higher thermal stability compared to the grafting technique. It has demonstrated the complexity of the synthesis, wherein small changes of the organosilane silica precursors create very different stationary phases. The Tanaka test highlighted the ion exchange capacity and steric selectivity of the column. The Tanaka analysis also showed the silica surface to have a large number of remaining surface silanol groups. The selectivity of the column could be further improved by reacting the silanol with an end-capping functionality (-Si-$(CH_3)_3$). This research could also be extended by varying other synthetic parameters such as the ethanol content and Si/H_2O ratio to determine whether the polydispersity of the silica particles could be further improved. This in turn would improve the efficiency of the column.

We have demonstrated the ability of the SIS silica to separate large biomolecules (Chapter 6). As we have shown the stationary phase is unable to separate small molecules the boundaries of the upper and lower molecular weight of the molecules which can be separated needs to be investigated. Using solid-state NMR we have shown the addition of silica nanoparticles can be achieved using only one layer of poly(diallyldimethylammonium chloride) which significantly reduces the reaction time.

The elution order of the biomolecules using the SIS stationary phase indicates the SIS material behaves more like a large pore reverse-phase silica. In view of this, further experiments could be under taken to evaluate the elution order of the same analytes using a non-functionalised SIS silica material. These changes to the stationary phase should reverse the elution order of the large analytes and produce a true SEC column.

This research has demonstrated the importance of analysing stationary phases on a molecular level and the significance of solid-state NMR as a characterisation technique for amorphous materials. The incorporation of the grafted functionality and end-capping groups can be confirmed using ^{1}H-^{13}C CP MAS NMR and the position of the moieties (on the pore surface or within the pore wall) through ^{1}H-^{13}C CP kinetics and ^{1}H-^{13}C WISE NMR experiments. The chromatograms of Spherisorb ODS2 (Chapter 5) have demonstrated the importance of a homogeneous distribution of the bonded phase on the selectivity of the column, and the homogeneity can be probed using a 2D ^{1}H-^{29}Si HETCOR NMR. ^{1}H-^{29}Si CP MAS NMR was used to distinguish between the monomeric Syncronis and polymeric Spherisorb silica.

Additionally we have shown that solid-state NMR analysis can also be used to determine how a toluene analyte interacts with different bonded phases. This work could be extended by studying how different analytes interact with a C_{18} bonded stationary phases. Through this we can gain a greater understanding of the separation process and improve methods for producing efficient HPLC columns.

8.References

1. Meyer, V. R. *Practical High-Performance Liquid Chromatography*; Wiley, 2004.
2. Hanai, T. *HPLC A Practical Guide*; The Royal Society of Chemistry, 1999.
3. Unger, K. K.; Kumar, D.; Grun, M.; Buchel, G.; Ludtke, S.; Adam, T.; Schumacher, K.; Renker, S. *Journal of Chromatography A* **2000,** *892*, 47-55.
4. Deemter, J. J. V. *Chemical Engineering Science* **1956,** *5*, 271-289.
5. Giddings, J. C. *Journal of Chromatography* **1964,** *16*, 444-&.
6. Done, J. N.; Knox, J. H. *Journal of Chromatographic Science* **1972,** *10*, 606.
7. Knox, J. H.; Parcher, J. F. *Analytical Chemistry* **1969,** *41*, 1599-1606.
8. Knox, J. H.; Pryde, A. *Journal of Chromatography* **1975,** *112*, 171-188.
9. Knox, J. H.; Saleem, M. *Journal of Chromatographic Science* **1969,** *7*, 614-622.
10. Desmet, G.; Clicq, D.; Gzil, P. *Analytical Chemistry* **2005,** *77*, 4058-4070.
11. Desmet, G.; Gzil, P.; Clicq, D. *Lc Gc Europe* **2005,** *18*, 403-409.
12. Fanigliulo, A.; Cabooter, D.; Bellazzi, G.; Tramarin, D.; Allieri, B.; Rottigni, A.; Desmet, G. *Journal of Separation Science*, *33*, 3655-3665.
13. Nawrocki, J. *Journal of Chromatography A* **1997,** *779*, 29-71.
14. Treuherz, B. A.; Khimyak, Y. Z. *Microporous and Mesoporous Materials* **2007,** *106*, 236-245.
15. Mesa, M.; Sierra, L.; Guth, J. L. *Microporous and Mesoporous Materials* **2008,** *112*, 338-350.
16. Naik, S. P.; Elangovan, S. P.; Okubo, T.; Sokolov, I. *Journal of Physical Chemistry C* **2007,** *111*, 11168-11173.
17. Alexandridis, P.; Holzwarth, J. F.; Hatton, T. A. *Macromolecules* **1994,** *27*, 2414-2425.
18. Patel, T.; Bahadur, P.; Mata, J. *Journal of Colloid and Interface Science*, *345*, 346-350.
19. Alexandridis, P.; Hatton, T. A. *Colloids and Surfaces a-Physicochemical and Engineering Aspects* **1995,** *96*, 1-46.
20. Brown, W.; Schillen, K.; Almgren, M.; Hvidt, S.; Bahadur, P. *Journal of Physical Chemistry* **1991,** *95*, 1850-1858.
21. Kipkemboi, P.; Fogden, A.; Alfredsson, V.; Flodstrom, K. *Langmuir* **2001,** *17*, 5398-5402.
22. Wanka, G.; Hoffmann, H.; Ulbricht, W. *Macromolecules* **1994,** *27*, 4145-4159.
23. Mortensen, K.; Brown, W. *Macromolecules* **1993,** *26*, 4128-4135.
24. Mortensen, K.; Brown, W.; Norden, B. *Physical Review Letters* **1992,** *68*, 2340-2343.
25. Mortensen, K.; Pedersen, J. S. *Macromolecules* **1993,** *26*, 805-812.
26. Na, W.; Wei, Q.; Zou, Z. C.; Li, Q. Y.; Nie, Z. R. *Journal of Colloid and Interface Science*, *346*, 61-65.
27. Ballem, M. A.; Cordoba, J. M.; Oden, M. *Microporous and Mesoporous Materials*, *129*, 106-111.
28. Huo, Q. S.; Margolese, D. I.; Stucky, G. D. *Chemistry of Materials* **1996,** *8*, 1147-1160.
29. Bahadur, P.; Pandya, K.; Almgren, M.; Li, P.; Stilbs, P. *Colloid and Polymer Science* **1993,** *271*, 657-667.
30. Bahadur, P.; Li, P. Y.; Almgren, M.; Brown, W. *Langmuir* **1992,** *8*, 1903-1907.
31. Florin, E.; Kjellander, R.; Eriksson, J. C. *Journal of the Chemical Society-Faraday Transactions I* **1984,** *80*, 2889-2910.
32. Karlstrom, G. *Journal of Physical Chemistry* **1985,** *89*, 4962-4964.
33. Qiao, S. Z.; Yu, C. Z.; Hu, Q. H.; Jin, Y. G.; Zhou, X. F.; Zhao, X. S.; Lu, G. Q. *Microporous and Mesoporous Materials* **2006,** *91*, 59-69.

34. Wu, Y. J.; Ren, X. Q.; Wang, J. *Materials Chemistry and Physics* **2009,** *113*, 773-779.
35. Bao, X. Y.; Zhao, X. S.; Qiao, S. Z.; Bhatia, S. K. *Journal of Physical Chemistry B* **2004,** *108*, 16441-16450.
36. Bao, X. Y.; Zhao, X. S.; Li, X.; Chia, P. A.; Li, J. *Journal of Physical Chemistry B* **2004,** *108*, 4684-4689.
37. Beck, J. S.; Vartuli, J. C.; Roth, W. J.; Leonowicz, M. E.; Kresge, C. T.; Schmitt, K. D.; Chu, C. T. W.; Olson, D. H.; Sheppard, E. W.; McCullen, S. B.; Higgins, J. B.; Schlenker, J. L. *Journal of the American Chemical Society* **1992,** *114*, 10834-10843.
38. Unger, K. K.; Skudas, R.; Schulte, M. M. *Journal of Chromatography A* **2008,** *1184*, 393-415.
39. Endele, R.; Halasz, I.; Unger, K. *Journal of Chromatography* **1974,** *99*, 377-393.
40. Unger, K.; Schickka.J; Krebs, K. F. *Journal of Chromatography* **1973,** *83*, 5-9.
41. Kolbe, G., Das komplexchemische Verhalten der Kieselsäure, *Dissertation*, Friedrich-Schiller Universität Jena, 1956.
42. Stober, W.; Fink, A.; Bohn, E. *Journal of Colloid and Interface Science* **1968,** *26*, 62-69.
43. Bogush, G. H.; Tracy, M. A.; Zukoski, C. F. *Journal of Non-Crystalline Solids* **1988,** *104*, 95-106.
44. Barder, T. J. In *Allied-Signal Inc*, 1991.
45. Boscott, R. J. *Nature* **1947,** *159*, 342-342.
46. Boldingh, J. *Experientia* **1948,** *4*, 270-271.
47. Horvath, C., Ed. *High-Performance Liquid Chromatography - Advances and Perspectives*; Academic Press, 1980.
48. Howard, G. A.; Martin, A. J. P. *Biochemical Journal* **1950,** *46*, 532-538.
49. Hoffmann, F.; Cornelius, M.; Morell, J.; Froba, M. *Angewandte Chemie-International Edition* **2006,** *45*, 3216-3251.
50. Jones, J. T. A.; Wood, C. D.; Dickinson, C.; Khimyak, Y. Z. *Chemistry of Materials* **2008,** *20*, 3385-3397.
51. Asefa, T.; MacLachlan, M. J.; Coombs, N.; Ozin, G. A. *Nature* **1999,** *402*, 867-871.
52. Inagaki, S.; Guan, S.; Fukushima, Y.; Ohsuna, T.; Terasaki, O. *Journal of the American Chemical Society* **1999,** *121*, 9611-9614.
53. Melde, B. J.; Holland, B. T.; Blanford, C. F.; Stein, A. *Chemistry of Materials* **1999,** *11*, 3302-3308.
54. Inagaki, S.; Guan, S.; Ohsuna, T.; Terasaki, O. *Nature* **2002,** *416*, 304-307.
55. Kirkland, J. J. *Modern Practice Of Liquid Chromatography*; Wiley-Interscience, 1971.
56. Scott, R. P. W., Ed. *Gas Chromatography*; Butterworths 1960.
57. Bohemen, J.; Purnell, J. H. *Journal of the Chemical Society* **1961**, 360-367.
58. Kirkland, J. J. *Analytical Chemistry* **1992,** *64*, 1239-1245.
59. Lvov, Y.; Ariga, K.; Onda, M.; Ichinose, I.; Kunitake, T. *Langmuir* **1997,** *13*, 6195-6203.
60. Horvath, C.; Melander, W.; Molnar, I. *Journal of Chromatography* **1976,** *125*, 129-156.
61. Karger, B. L.; Gant, J. R.; Hartkopf, A.; Weiner, P. H. *Journal of Chromatography* **1976,** *128*, 65-78.
62. Dill, K. A. *Journal of Physical Chemistry* **1987,** *91*, 1980-1988.
63. Dorsey, J. G.; Dill, K. A. *Chemical Reviews* **1989,** *89*, 331-346.
64. Martire, D. E.; Boehm, R. E. *Journal of Physical Chemistry* **1983,** *87*, 1045-1062.
65. Wise, S. A.; Sander, L. C.; Chang, H. C. K.; Markides, K. E.; Lee, M. L. *Chromatographia* **1988,** *25*, 473-479.
66. Yasmin, T.; Muller, K. *Journal of chromatography. A*, *1218*, 6464-75.
67. Zhang, F.; Li, Y.; Guo, Z.; Liang, T.; Yang, B.; Zhou, Y.; Liang, X. *Talanta*, *85*, 112-116.

68. Scully, N. M.; Ashu-Arrah, B. A.; Nagle, A. P.; Omamogho, J. O.; O'Sullivan, G. P.; Friebolin, V.; Dietrich, B.; Albert, K.; Glennon, J. D. *Journal of Chromatography A*, *1218*, 1974-1982.
69. Mallik, A. K.; Sawada, T.; Takafuji, M.; Ihara, H. *Journal of Separation Science*, *33*, 2977-2989.
70. Ansarian, H. R.; Derakhshan, M.; Rahman, M. M.; Sakurai, T.; Takafuji, M.; Taniguchi, I.; Ihara, H. *Analytica Chimica Acta* **2005,** *547*, 179-187.
71. Pursch, M.; Sander, L. C.; Egelhaaf, H. J.; Raitza, M.; Wise, S. A.; Oelkrug, D.; Albert, K. *Journal of the American Chemical Society* **1999,** *121*, 3201-3213.
72. Chagolla, D.; Mathias, E. V.; Ba, Y. *Journal of Chromatography A* **2006,** *1121*, 23-31.
73. Sentell, K. B. *Journal of Chromatography A* **1993,** *656*, 231-263.
74. Dabre, R.; Schwammle, A.; Lammerhofer, M.; Lindner, W. *Journal of Chromatography A* **2009,** *1216*, 3473-3479.
75. Kailasam, K.; Muller, K. *Journal of Chromatography A* **2008,** *1191*, 125-135.
76. Kailasam, K.; Natile, M. M.; Glisenti, A.; Muller, K. *Journal of Chromatography A* **2009,** *1216*, 2345-2354.
77. Kuehnle, M.; Friebolin, V.; Albert, K.; Rimmer, C. A.; Lippa, K. A.; Sander, L. C. *Analytical Chemistry* **2009,** *81*, 10136-10142.
78. Pursch, M.; Brindle, R.; Ellwanger, A.; Sander, L. C.; Bell, C. M.; Handel, H.; Albert, K. *Solid State Nuclear Magnetic Resonance* **1997,** *9*, 191-201.
79. Albert, K. *Journal of Separation Science* **2003,** *26*, 215-224.
80. Sander, L. C.; Lippa, K. A.; Wise, S. A. *Analytical and Bioanalytical Chemistry* **2005,** *382*, 646-668.
81. Rabi, Ii; Zacharias, J. R.; Millman, S.; Kusch, P. *Physical Review* **1938,** *53*, 318-318.
82. Bloch, F. *Physical Review* **1946,** *70*, 460-474.
83. Purcell, E. M.; Torrey, H. C.; Pound, R. V. *Physical Review* **1946,** *69*, 37-38.
84. Bloch, F. *Principles of Nuclear Induction - Nobel Lecture*, 1952.
85. Levitt, M. H. *Spin Dynamics - Basics of Muclear Magnetic Resonance*, Second ed.; Wiley, 2008.
86. K.J.D Mackenzie, M. E. S. *Multinuclear Solid-State NMR of Inorganic Materials*; PERGAMON, 2002.
87. Laws, D. D.; Bitter, H. M. L.; Jerschow, A. *Angewandte Chemie-International Edition* **2002,** *41*, 3096-3129.
88. Duer, M. J. *Introduction to Solid-State NMR Spectroscopy*; Blackwell Publishing, 2004.
89. Hunter, J. K. M. S. a. B. K. *Modern NMR Spectroscopy - A Guide For Chemists*, Second ed.; Oxford University Press, 1993.
90. Kolodziejski, W.; Klinowski, J. *Chemical Reviews* **2002,** *102*, 613-628.
91. Weller, M. T. *Inorganic Materials Chemistry*; Oxford University Press, 1996.
92. Pecharsky, V. K. *Fundamentals of Powder Diffraction and Structural Characterisation*; Springer.
93. Mitra, S. *Fundamentals of optical, spectroscopic and x-ray mineralogy*; New Age International (P) Limited, 1996.
94. Alexander J. Blake, W. C., Jacqueline M Cole *Crystal structure analysis: principles and practice*; Oxford University Press, 2009.
95. Fitzgerald, R. *Physics Today* **2001,** *54*, 21-23.
96. Marler, B.; Oberhagemann, U.; Vortmann, S.; Gies, H. *Microporous Materials* **1996,** *6*, 375-383.

97. C. J. Glinka, J. M. N., G. D. Stucky, E. Ramli, D. I. Margolese and Q. Hou. *Mater. Res. Symp Proc* **1995,** *37*, 47.
98. Kresge, C. T.; Leonowicz, M. E.; Roth, W. J.; Vartuli, J. C.; Beck, J. S. *Nature* **1992,** *359*, 710-712.
99. Leofanti, G.; Padovan, M.; Tozzola, G.; Venturelli, B. *Catalysis Today* **1998,** *41*, 207-219.
100. Sing, K. S. W.; Everett, D. H.; Haul, R. A. W.; Moscou, L.; Pierotti, R. A.; Rouquerol, J.; Siemieniewska, T. *Pure and Applied Chemistry* **1985,** *57*, 603-619.
101. Brunauer, S.; Emmett, P. H.; Teller, E. *Journal of the American Chemical Society* **1938,** *60*, 309-319.
102. Barrett, E. P.; Joyner, L. G.; Halenda, P. P. *Journal of the American Chemical Society* **1951,** *73*, 373-380.
103. Joyner, L. G.; Barrett, E. P.; Skold, R. *Journal of the American Chemical Society* **1951,** *73*, 3155-3158.
104. Knoll, M. *Physikalische Zeitschrift* **1935,** *36*, 861-869.
105. Oatley, C. W. *Journal of Applied Physics* **1982,** *53*, R1-R13.
106. www.fei.com; Malvern Instruments.
107. Syvitski, J. P. M. *Principles, Methods and Applications of Particle Size Analysis*; Cambridge University Press, 1991.
108. Pecora, B. B. a. R. *Dynamic Light Scattering with Applications to Chemistry, Biology and Physics*; John Wiley & Sons, 1976.
109. www.chnanalysis.com, 2009.
110. Srinivasan, G.; Meyer, C.; Welsch, N.; Albert, K.; Muller, K. *Journal of Chromatography A* **2006,** *1113*, 45-54.
111. V.R, M. *Practical High-Performance Liquid Chromatography*; Wiley, 2004.
112. Seifar, R. M.; Heemstra, S.; Kok, W. T.; Kraak, J. C.; Poppe, H. *Biomedical Chromatography* **1998,** *12*, 140.
113. Choi, M.; Kleitz, F.; Liu, D. N.; Lee, H. Y.; Ahn, W. S.; Ryoo, R. *Journal of the American Chemical Society* **2005,** *127*, 1924-1932.
114. Deng, T. S.; Zhang, Q. F.; Zhang, J. Y.; Shen, X.; Zhu, K. T.; Wu, J. L. *Journal of Colloid and Interface Science* **2009,** *329*, 292-299.
115. Yu, J. G.; Zhao, L.; Cheng, B. *Journal of Solid State Chemistry* **2006,** *179*, 226-232.
116. Hartono, S. B.; Qiao, S. Z.; Jack, K.; Ladewig, B. P.; Hao, Z. P.; Lu, G. Q. *Langmuir* **2009,** *25*, 6413-6424.
117. Lefevre, B.; Galarneau, A.; Iapichella, J.; Petitto, C.; Di Renzo, F.; Fajula, F.; Bayram-Hahn, Z.; Skudas, R.; Unger, K. *Chemistry of Materials* **2005,** *17*, 601-607.
118. Beesley, T. E. *Lc Gc Europe*, *24*, 270-276.
119. Lai, X. H.; Tang, W. H.; Ng, S. C. *Journal of Chromatography A*, *1218*, 3496-3501.
120. Zhang, T.; Kientzy, C.; Franco, P.; Ohnishi, A.; Kagamihara, Y.; Kurosawa, H. *Journal of Chromatography A* **2005,** *1075*, 65-75.
121. Zhang, T.; Nguyen, D.; Franco, P.; Murakami, T.; Ohnishi, A.; Kurosawa, H. *Analytica Chimica Acta* **2006,** *557*, 221-228.
122. Zheng, M. M.; Ruan, G. D.; Feng, Y. Q. *Journal of Chromatography A* **2009,** *1216*, 7739-7746.
123. Wang, X. M.; Du, X. Z.; Li, C. L.; Cao, X. *Applied Surface Science* **2008,** *254*, 3753-3757.
124. Yang, L. M.; Wang, Y. J.; Luo, G. S.; Dai, Y. Y. *Particuology* **2008,** *6*, 143-148.
125. Ko, J. H.; Baik, Y. S.; Park, S. T.; Cheong, W. J. *Journal of Chromatography A* **2007,** *1144*, 269-274.

126. Hamoudi, S.; El-Nemr, A.; Belkacemi, K. *Journal of Colloid and Interface Science*, **343**, 615-621.
127. Yokoi, T.; Yoshitake, H.; Yamada, T.; Kubota, Y.; Tatsumi, T. *Journal of Materials Chemistry* **2006**, *16*, 1125-1135.
128. Huang, L.; Dolai, S.; Raja, K.; Kruk, M. *Langmuir*, **26**, 2688-2693.
129. Goto, Y.; Inagaki, S. *Chemical Communications* **2002**, 2410-2411.
130. Dewaele, C.; Verzele, M. *Journal of Chromatography* **1983**, *260*, 13-21.
131. Halasz, I.; Naefe, M. *Analytical Chemistry* **1972**, *44*, 76-&.
132. Han, Y.; Lee, S. S.; Ying, J. Y. *Journal of Chromatography A*, *1217*, 4337-4343.
133. Martin, T.; Galarneau, A.; Di Renzo, F.; Brunel, D.; Fajula, F.; Heinisch, S.; Cretier, G.; Rocca, J. L. *Chemistry of Materials* **2004**, *16*, 1725-1731.
134. Kirkland, J. J.; Truszkowski, F. A.; Dilks, C. H.; Engel, G. S. *Journal of Chromatography A* **2000**, *890*, 3-13.
135. Berggren, A.; Palmqvist, A. E. C.; Holmberg, K. *Soft Matter* **2005**, *1*, 219-226.
136. Huo, Q. S.; Margolese, D. I.; Ciesla, U.; Demuth, D. G.; Feng, P. Y.; Gier, T. E.; Sieger, P.; Firouzi, A.; Chmelka, B. F.; Schuth, F.; Stucky, G. D. *Chemistry of Materials* **1994**, *6*, 1176-1191.
137. Han, S. H.; Hou, W. G.; Dang, W. X.; Xu, J.; Hu, J. F.; Li, D. Q. *Colloid and Polymer Science* **2004**, *282*, 761-765.
138. Han, S. H.; Hou, W. G.; Xu, J.; Li, Z. M. *Colloid and Polymer Science* **2004**, *282*, 1286-1291.
139. Chao, M. C.; Chang, C. H.; Lin, H. P.; Tang, C. Y.; Lin, C. Y. *Journal of Materials Science* **2009**, *44*, 6453-6462.
140. Wang, W. Q.; Wang, J. G.; Sun, P. C.; Ding, D. T.; Chen, T. H. *Journal of Colloid and Interface Science* **2009**, *331*, 156-162.
141. Vercaemst, C.; Ide, M.; Friedrich, H.; de Jong, K. P.; Verpoort, F.; Van der Voort, P. *Journal of Materials Chemistry* **2009**, *19*, 8839-8845.
142. Lin, H. P.; Kao, C. P.; Mou, C. Y.; Liu, S. B. *Journal of Physical Chemistry B* **2000**, *104*, 7885-7894.
143. Kumar, D.; Schumacher, K.; von Hohenesche, C. D. F.; Grun, M.; Unger, K. K. *Colloids and Surfaces a-Physicochemical and Engineering Aspects* **2001**, *187*, 109-116.
144. Yoldas, B. E. *Journal of Non-Crystalline Solids* **1986**, *82*, 11-23.
145. Yoldas, B. E. *Journal of Non-Crystalline Solids* **1986**, *83*, 375-390.
146. Livage, J.; Henry, M.; Sanchez, C. *Progress in Solid State Chemistry* **1988**, *18*, 259-341.
147. Shirai, S.; Goto, Y.; Mizoshita, N.; Ohashi, M.; Tani, T.; Shimada, T.; Hyodo, S.; Inagaki, S. *Journal of Physical Chemistry A*, *114*, 6047-6054.
148. Miao, J. B.; Qian, J. S.; Wang, X. H.; Zhang, Y. C.; Yang, H. Y.; He, P. S. *Materials Letters* **2009**, *63*, 989-990.
149. Hunks, W. J.; Ozin, G. A. *Journal of Materials Chemistry* **2005**, *15*, 3716-3724.
150. Huh, S.; Wiench, J. W.; Yoo, J. C.; Pruski, M.; Lin, V. S. Y. *Chemistry of Materials* **2003**, *15*, 4247-4256.
151. Zhao, D. Y.; Sun, J. Y.; Li, Q. Z.; Stucky, G. D. *Chemistry of Materials* **2000**, *12*, 275-279.
152. Wan, Y.; Shi, Y. F.; Zhao, D. Y. *Chemical Communications* **2007**, 897-926.
153. Yang, B.; Guo, C.; Chen, S.; Ma, J. H.; Wang, J.; Liang, X. F.; Zheng, L.; Liu, H. Z. *Journal of Physical Chemistry B* **2006**, *110*, 23068-23074.
154. Bronnimann, C. E.; Zeigler, R. C.; Maciel, G. E. *Journal of the American Chemical Society* **1988**, *110*, 2023-2026.

155. Kao, H. M.; Liao, C. H.; Hung, T. T.; Pan, Y. C.; Chiang, A. S. T. *Chemistry of Materials* **2008,** *20*, 2412-2422.
156. Kapoor, M. P.; Inagaki, S. *Chemistry of Materials* **2002,** *14*, 3509-3514.
157. Ying, J. Y.; Mehnert, C. P.; Wong, M. S. *Angewandte Chemie-International Edition* **1999,** *38*, 56-77.
158. Monnier, A.; Schuth, F.; Huo, Q.; Kumar, D.; Margolese, D.; Maxwell, R. S.; Stucky, G. D.; Krishnamurty, M.; Petroff, P.; Firouzi, A.; Janicke, M.; Chmelka, B. F. *Science* **1993,** *261*, 1299-1303.
159. Xu, J.; Luan, Z. H.; He, H. Y.; Zhou, W. Z.; Kevan, L. *Chemistry of Materials* **1998,** *10*, 3690-3698.
160. Dire, S.; Tagliazucca, V.; Callone, E.; Quaranta, A. *Materials Chemistry and Physics*, *126*, 909-917.
161. Han, D. I.; Hah, H. J.; Park, H. W.; Koo, S. M. *Journal of Sol-Gel Science and Technology* **2004,** *32*, 47-51.
162. Keeler, J. *Understanding NMR spectroscopy*; Wiley, 2005.
163. Lin, Y. C.; Chou, H. L.; Sarma, L. S.; Hwang, B. J. *Chemistry-a European Journal* **2009,** *15*, 10658-10665.
164. Jones, J. T., University of Liverpool, 2009.
165. K. Schmidt-Rohr, J. C., and H. W. Spiess. *Macromolecules* **1992**, 3273-3277.
166. Schmit, J. A.; Henry, R. A.; Williams, R. C.; Dieckman, J. F. *Journal of Chromatographic Science* **1971,** *9*, 645.
167. Wise, S. A.; Sander, L. C.; May, W. E. *Journal of Chromatography* **1993,** *642*, 329-349.
168. Cruz, E.; Euerby, M. R.; Johnson, C. M.; Hackett, C. A. *Chromatographia* **1997,** *44*, 151-161.
169. Welch, C. J.; Brkovic, T.; Schafer, W.; Gong, X. Y. *Green Chemistry* **2009,** *11*, 1232-1238.
170. Capello, C.; Fischer, U.; Hungerbuhler, K. *Green Chemistry* **2007,** *9*, 927-934.
171. Hesselink, W.; Schiffer, R.; Kootstra, P. R. *Journal of Chromatography A* **1995,** *697*, 165-174.
172. Jinno, K.; Ibuki, T.; Tanaka, N.; Okamoto, M.; Fetzer, J. C.; Biggs, W. R.; Griffiths, P. R.; Olinger, J. M. *Journal of Chromatography* **1989,** *461*, 209-227.
173. Wise, S. A.; Sander, L. C. *Journal of High Resolution Chromatography & Chromatography Communications* **1985,** *8*, 248-255.
174. Saito, Y.; Jinno, K.; Pesek, J. J.; Chen, Y. L.; Luehr, G.; Archer, J.; Fetzer, J. C.; Biggs, W. R. *Chromatographia* **1994,** *38*, 295-303.
175. Claessens, H. A.; van Straten, M. A.; Cramers, C. A.; Jezierska, M.; Buszewski, B. *Journal of Chromatography A* **1998,** *826*, 135-156.
176. Jandera, P.; Novotna, K.; Beldean-Galea, M. S.; Jisa, K. *Journal of Separation Science* **2006,** *29*, 856-871.
177. Kulikov, A. U.; Galat, M. N. *Journal of Separation Science* **2009,** *32*, 1340-1350.
178. MacNair, J. E.; Patel, K. D.; Jorgenson, J. W. *Analytical Chemistry* **1999,** *71*, 700-708.
179. Melander, W.; Stoveken, J.; Horvath, C. *Journal of Chromatography* **1980,** *199*, 35-56.
180. Euerby, M. R.; Petersson, P.; Campbell, W.; Roe, W. *Journal of Chromatography A* **2007,** *1154*, 138-151.
181. Stevenson, P. G.; Mayfield, K. J.; Soliven, A.; Dennis, G. R.; Gritti, F.; Guiochon, G.; Shalliker, R. A. *Journal of Chromatography A*, *1217*, 5358-5364.
182. Zhang, Y. P.; Jin, Y.; Dai, P.; Yu, H.; Yu, D. H.; Ke, Y. X.; Liang, X. M. *Analytical Methods* **2009,** *1*, 123-127.
183. Vailaya, A.; Horvath, C. *Journal of Chromatography A* **1998,** *829*, 1-27.

184. Simpson, R. J. *Proteins and Proteomics - A Laboratory Manual*; Cold Spring Harbor Laboratory Press, 2003.
185. McCalley, D. V. *Journal of Chromatography A* **1997,** *769*, 169-178.
186. Olsen, B. A.; Sullivan, G. R. *Journal of Chromatography A* **1995,** *692*, 147-159.
187. Vervoort, R. J. M.; Derksen, M. W. J.; Maris, F. A. *Journal of Chromatography A* **1994,** *678*, 1-15.
188. McCalley, D. V. *Journal of Chromatography* **1993,** *636*, 213-220.
189. Paesen, J.; Claeys, P.; Roets, E.; Hoogmartens, J. *Journal of Chromatography* **1993,** *630*, 117-122.
190. Vervoort, R. J. M.; Maris, F. A.; Hindriks, H. *Journal of Chromatography* **1992,** *623*, 207-220.
191. Vernemismer, J.; Lamard, M.; Wagner, J. *Journal of Chromatography* **1993,** *645*, 251-258.
192. Vervoort, R. J. M.; Derksen, M. W. J.; Debets, A. J. J. *Journal of Chromatography A* **1997,** *765*, 157-168.
193. Dams, R.; Lambert, W. E.; Clauwaert, K. M.; De Leenheer, A. P. *Journal of Chromatography A* **2000,** *896*, 311-319.
194. Epler, K. S.; Sander, L. C.; Ziegler, R. G.; Wise, S. A.; Craft, N. E. *Journal of Chromatography* **1992,** *595*, 89-101.
195. Petersson, P.; Euerby, M. R. *Journal of Separation Science* **2007,** *30*, 2012-2024.
196. Buszewski, B.; Kowalska, S.; Stepnowski, P. *Journal of Separation Science* **2006,** *29*, 1116-1125.
197. Claessens, H. A. *Trac-Trends in Analytical Chemistry* **2001,** *20*, 563-583.
198. Dehouck, P.; Visky, D.; Vander Heyden, Y.; Adams, E.; Kovacs, Z.; Noszal, B.; Massart, D. L.; Hoogmartens, J. *Journal of Chromatography A* **2004,** *1025*, 189-200.
199. Euerby, M. R.; Petersson, P. *Journal of Chromatography A* **2005,** *1088*, 1-15.
200. Horak, J.; Lindner, W. *Journal of Chromatography A* **2004,** *1043*, 177-194.
201. Sander, L. C.; Wise, S. A. *Journal of Separation Science* **2003,** *26*, 283-294.
202. Grun, M.; Unger, K. K.; Matsumoto, A.; Tsutsumi, K. *Microporous and Mesoporous Materials* **1999,** *27*, 207-216.
203. Guan, H.; Guiochon, G. *Journal of Chromatography A* **1994,** *687*, 201-212.
204. Guan, H.; Guiochon, G.; Coffey, D.; Davis, E.; Gulakowski, K.; Smith, D. W. *Journal of Chromatography A* **1996,** *736*, 21-30.
205. Ide, M.; Wallaert, E.; Van Driessche, I.; Lynen, F.; Sandra, P.; Van Der Voort, P. *Microporous and Mesoporous Materials*, *142*, 282-291.
206. Albert, K. *Trac-Trends in Analytical Chemistry* **1998,** *17*, 648-658.
207. Buszewski, B.; Krupczynska, K.; Gadzala-Kopciuch, R. M.; Rychlicki, G.; Kaliszan, R. *Journal of Separation Science* **2003,** *26*, 313-321.
208. Buszewski, B.; Schmid, J.; Albert, K.; Bayer, E. *Journal of Chromatography* **1991,** *552*, 415-427.
209. Dietrich, B.; Holtin, K.; Bayer, M.; Friebolin, V.; Kuhnle, M.; Albert, K. *Analytical and Bioanalytical Chemistry* **2008,** *391*, 2627-2633.
210. Fatunmbi, H. O.; Bruch, M. D.; Wirth, M. J. *Analytical Chemistry* **1993,** *65*, 2048-2054.
211. Pursch, M.; Jager, A.; Schneller, T.; Brindle, R.; Albert, K.; Lindner, E. *Chemistry of Materials* **1996,** *8*, 1245-1249.
212. Schmid, J.; Albert, K.; Bayer, E. *Journal of Chromatography A* **1995,** *694*, 333-345.
213. Scholten, A. B.; deHaan, J. W.; Claessens, H. A.; vandeVen, L. J. M.; Cramers, C. A. *Langmuir* **1996,** *12*, 4741-4747.

214. Silva, C. R.; Bachmann, S.; Schefer, R. R.; Albert, K.; Jardim, I.; Airoldi, C. *Journal of Chromatography A* **2002,** *948*, 85-95.
215. Gadzala-Kopciuch, R.; Buszewski, B. *Journal of Separation Science* **2003,** *26*, 1273-1283.
216. Dearing, A. W.; Reid, E. E. *Journal of the American Chemical Society* **1928,** *50*, 3058-3062.
217. Kaiser, A.; Schmidt, H. *Journal of Non-Crystalline Solids* **1984,** *63*, 261-271.
218. Philipp, G.; Schmidt, H. *Journal of Non-Crystalline Solids* **1984,** *63*, 283-292.
219. Wen, J. Y.; Wilkes, G. L. *Chemistry of Materials* **1996,** *8*, 1667-1681.
220. Yoldas, B. E. *Journal of Non-Crystalline Solids* **1984,** *63*, 145-154.
221. Schmidt, H.; Scholze, H.; Kaiser, A. *Journal of Non-Crystalline Solids* **1984,** *63*, 1-11.
222. Sander, L. C.; Sharpless, K. E.; Pursch, M. *Journal of Chromatography A* **2000,** *880*, 189-202.
223. Sander, L. C.; Sharpless, K. E.; Craft, N. E.; Wise, S. A. *Analytical Chemistry* **1994,** *66*, 1667-1674.
224. Yang, C.; Ikegami, T.; Hara, T.; Tanaka, N. *Journal of Chromatography A* **2006,** *1130*, 175-181.
225. Bayram-Hahn, Z.; Grimes, B. A.; Lind, A. M.; Skudas, R.; Unger, K. K.; Galarneau, A.; Lapichella, J.; Fajula, F. *Journal of Separation Science* **2007,** *30*, 3089-3103.
226. Majors, R. E. *Lc Gc North America* **2005,** *23*, 1248-1255.
227. McCalley, D. V. *Journal of Chromatography A* **2008,** *1193*, 85-91.
228. JD, S., The Florida International University College of Arts and Sciences University College of Arts and Sciences 2003.
229. Coen, M.; Lindon, J. C.; Gavaghan, C.; Holmes, E.; Humpfer, E.; Wilson, I. D.; Stanley, P. D.; Nicholson, J. K. *Analyst* **2001,** *126*, 548-550.
230. Shah, P.; Rogers, L. B.; Fetzer, J. C. *Journal of Chromatography* **1987,** *388*, 411-419.
231. Pesek, J. J.; Matyska, M. T.; Yu, R. J. *Journal of Chromatography A* **2002,** *947*, 195-203.
232. Ducey, M. W.; Orendorff, C. J.; Pemberton, J. E.; Sander, L. C. *Analytical Chemistry* **2002,** *74*, 5576-5584.
233. Liao, Z. H.; Orendorff, C. J.; Sander, L. C.; Pemberton, J. E. *Analytical Chemistry* **2006,** *78*, 5813-5822.
234. Gottlieb, H. E.; Kotlyar, V.; Nudelman, A. *Journal of Organic Chemistry* **1997,** *62*, 7512-7515.
235. Shimizu, I.; Okabayashi, H.; Hattori, N.; Taga, K.; Yoshino, A.; Oconnor, C. J. *Colloid and Polymer Science* **1997,** *275*, 293-297.
236. Albert, K.; Evers, B.; Bayer, E. *Journal of Magnetic Resonance* **1985,** *62*, 428-436.
237. Khimyak, Y. Z.; Klinowski, J. *Physical Chemistry Chemical Physics* **2001,** *3*, 616-626.
238. Brown, S. P. *Progress in Nuclear Magnetic Resonance Spectroscopy* **2007,** *50*, 199-251.
239. Sentell, K. B.; Dorsey, J. G. *Journal of Chromatography* **1989,** *461*, 193-207.
240. Lochmuller, C. H.; Hunnicutt, M. L.; Mullaney, J. F. *Journal of Physical Chemistry* **1985,** *89*, 5770-5772.
241. Sandi, A.; Szepesy, L. *Journal of Chromatography A* **1998,** *818*, 19-30.
242. Tanaka, N.; Goodell, H.; Karger, B. L. *Journal of Chromatography* **1978,** *158*, 233-248.
243. Jandera, P. *Journal of Chromatography* **1986,** *352*, 91-110.
244. Majors, R. E. *Lc Gc North America*, *28*, 1014-1020.
245. Golay, M. J. E. *Nature* **1963,** *199*, 370-371.
246. Knox, J. H.; McLaren, L. *Analytical Chemistry* **1963,** *35*, 449-454.
247. Purnell, J. H. *Nature* **1959,** *184*, 2009-2009.
248. Halasz, I.; Horvath, C. *Analytical Chemistry* **1964,** *36*, 1178-1186

249. Kirkland, J. J. *Analytical Chemistry* **1969,** *41*, 218-220.
250. Bergna, U.S patent 4,131,542., 1984.
251. Cabooter, D.; Fanigliulo, A.; Bellazzi, G.; Allieri, B.; Rottigni, A.; Desmet, G. *Journal of Chromatography A*, *1217*, 7074-7081.
252. Wang, X. L.; Barber, W. E.; Carr, P. W. *Journal of Chromatography A* **2006,** *1107*, 139-151.
253. Gritti, F.; Leonardis, I.; Abia, J.; Guiochon, G. *Journal of Chromatography A*, *1217*, 3819-3843.
254. Guan, G.; Liu, R.; Wu, M.; Li, Z.; Liu, B.; Wang, Z.; Gao, D.; Zhang, Z. *Analyst* **2009,** *134*, 1880-6.
255. Lvov, Y.; Ariga, K.; Ichinose, I.; Kunitake, T. *Journal of the American Chemical Society* **1995,** *117*, 6117-6123.
256. Ariga, K.; Lvov, Y.; Kunitake, T. *Journal of the American Chemical Society* **1997,** *119*, 2224-2231.
257. Civalleri, B.; Garrone, E.; Ugliengo, P. *Chemical Physics Letters* **1999,** *299*, 443-450.
258. Hu, J. Z.; Kwak, J. H.; Herrera, J. E.; Wang, Y.; Peden, C. H. F. *Solid State Nuclear Magnetic Resonance* **2005,** *27*, 200-205.
259. Kinney, D. R.; Chuang, I. S.; Maciel, G. E. *Journal of the American Chemical Society* **1993,** *115*, 6786-6794.
260. Legrand, A. P.; Hommel, H.; de la Caillerie, J. B. D. *Colloids and Surfaces a-Physicochemical and Engineering Aspects* **1999,** *158*, 157-163.
261. Leonardelli, S.; Facchini, L.; Fretigny, C.; Tougne, P.; Legrand, A. P. *Journal of the American Chemical Society* **1992,** *114*, 6412-6418.
262. Zhou, Y. H. *Glass Physics and Chemistry* **2009,** *35*, 384-388.
263. Kriz, J.; Dybal, J.; Kurkova, D. *Journal of Physical Chemistry A* **2002,** *106*, 7971-7981.
264. Pont, A. L.; Marcilla, R.; De Meatza, I.; Grande, H.; Mecerreyes, D. *Journal of Power Sources* **2009,** *188*, 558-563.
265. Trzcinski, S.; Varum, K. M.; Staszewska, D. U.; Smidsrod, O.; Bohdanecky, M. *Carbohydrate Polymers* **2002,** *48*, 171-178.
266. Dorris, A.; Rucareanu, S.; Reven, L.; Barrett, C. J.; Lennox, R. B. *Langmuir* **2008,** *24*, 2532-2538.
267. Loa, C. C.; Lin, T. L.; Wu, C. C.; Bryan, T. A.; Thacker, H. L.; Hooper, T.; Schrader, D. *Journal of Virological Methods* **2002,** *104*, 187-194.
268. Mant, C. T.; Parker, J. M. R.; Hodges, R. S. *Journal of Chromatography* **1987,** *397*, 99-112.
269. Patrickios, C. S.; Strittmatter, J. A.; Hertler, W. R.; Hatton, T. A. *Journal of Colloid and Interface Science* **1996,** *182*, 326-329.
270. Shalliker, R. A.; Kavanagh, P. E.; Russell, I. M.; Hawthorne, D. G. *Chromatographia* **1992,** *33*, 427-433.
271. Haller, W. *Nature* **1965,** *206*, 693-696.
272. Porath, J.; Flodin, P. *Nature* **1959,** *183*, 1657-1659.
273. Barth, H. G.; Boyes, B. E.; Jackson, C. *Analytical Chemistry* **1994,** *66*, R595-R620.
274. Ricker, R. D.; Sandoval, L. A. *Journal of Chromatography A* **1996,** *743*, 43-50.
275. Murayama, K.; Tomida, M. *Biochemistry* **2004,** *43*, 11526-11532.